

# Next Generation Wireless Receiver Architecture Design in Deep-Sub-Micron CMOS Technology

*Chaoying Wu*



Electrical Engineering and Computer Sciences  
University of California at Berkeley

Technical Report No. UCB/EECS-2016-181

<http://www2.eecs.berkeley.edu/Pubs/TechRpts/2016/EECS-2016-181.html>

December 1, 2016

Copyright © 2016, by the author(s).  
All rights reserved.

Permission to make digital or hard copies of all or part of this work for personal or classroom use is granted without fee provided that copies are not made or distributed for profit or commercial advantage and that copies bear this notice and the full citation on the first page. To copy otherwise, to republish, to post on servers or to redistribute to lists, requires prior specific permission.

Copyright @ 2014

by

Chaoying Wu

**The Dissertation Committee for Chaoying (Charles) Wu Certifies that this is the  
approved version of the following dissertation:**

**Next Generation Wireless Receiver Architecture Design in  
Deep-Sub-Micron CMOS Technology**

**Committee:**

---

Prof. Borivoje Nikolic, Chair

---

Prof. Ali M. Niknejad

---

Prof. David J. Allstot

---

Prof. Paul K. Wright

**Next Generation Wireless Receiver Architecture Design in  
Deep-Sub-Micron CMOS Technology**

**by**

**Chaoying (Charles) Wu**

A dissertation submitted in partial satisfaction of the  
requirements for the degree of

**Doctor of Philosophy**

in

Engineering – Electrical Engineering and Computer Sciences

in the

Graduate Division

of the

University of California, Berkeley

Committee in charge:

Professor Borivoje Nikolic, Chair

Professor Ali M. Niknejad

Professor David J. Allstot

Professor Paul K. Wright

**May, 2014**

Day before yesterday I saw a rabbit, and yesterday a deer, and today, you.

--- *The Dandelion Girl*, Robert F. Young

To my parents, Uncle Shaw and Sherri.

## **Abstract**

Next Generation Wireless Receiver Architecture Design in  
Deep-Sub-Micron CMOS Technology

by

Chaoying Wu

Doctor of Philosophy in Engineering-Electrical Engineering and Computer Sciences

The University of California, Berkeley

Professor Borivoje Nikolic, Chair

Current advances in wireless receiver technologies are primarily driven by the need for cost reduction through (1) integration of a radio, an ADC and a digital processor on a single CMOS die, and (2) the design of low-power multi-standard capable receivers. However, due to the spectrum scarcity, future wireless standards, such as LTE, present a whole new set of challenges for radio system design. For example, LTE's highly fragmented spectrum requires multiple chipsets for support. Due to this cost overhead, there is no global LTE-enabled device available in the market now. Moreover, while carrier aggregation (CA) added to LTE brings unparalleled data rate improvement, it seriously complicates the RF frontend design. Modern commercial LTE solutions include multiple chipsets to support various scenarios of CA, which is not cost effective.

This work focuses on novel receiver architectures that address the design challenges associated with LTE-Advance from two perspectives: (1) a receiver that is capable of wide-frequency range of operation to cover all the LTE bands and (2) a single highly linear RF frontend to support non-contiguous-in-band CA. A novel sigma-delta-based direct-RF-to-digital receiver architecture is introduced in this work as an example of a complete integrated RF-to-digital frontend design capable to cover all the LTE bands. The design is implemented in 65 nm CMOS technology and the SNDR of the receiver exceeds 68 dB for a 4 MHz signal, and is better than 60 dB over the 400 MHz to 4 GHz frequency range. In a different example, we propose a passive-mixer-first receiver system to provide CA support in a cost-effective and power-efficient manner. Mixer-first receiver's superb linearity performance enables the possibility of a single receiver processing the entire LTE RX band, while most of the signal conditioning can be pushed into DSP to enjoy the benefit of process scaling. This design has been demonstrated in a 28 nm bulk CMOS technology, and the overall system achieves <3 dB NF, >15 dBm IIP3 and 35 dB gain with 60 mW of power.

## Acknowledgements

I have had the honor to work and interact with a group of very intelligent and talented individuals at Berkeley. Without them, my stay in Berkeley would not be as memorable.

First and upmost, I can take this opportunity to express my gratitude to my advisor, Professor Bora Nikolic, for his vision and his dedication to research.

I would like to thank members of my project group, Professor Ali Niknejad for the most insightful discussions, Professor David Allstot for constant encouragement, Professor Elad Alon for always upholding the highest standards.

I have had many lengthy discussions with Christopher Hull and Ken Nishimura during my internships as well as formative stages of my research. My internship experience with Intel and Agilent enriched my knowledge, and widened my view in many perspective. I thank Haideh Khorramabadi, Tom Kwan and David Sobel for many constructive suggestions on research and career. Also, I thank Michael Reiha for his countless effort on teaching me how to properly write a scientific paper. I also appreciate all the helps from Professor Jason Stauth and Professor Seth Sanders.

I was based in BWRC for the most part of my Ph.D. career. I consider it a privilege to be associated with the center. The resource and level of collaboration is unmatched. Senior students and staff laid the foundation that made my research possible. I learned how to use the HFSS emulation platform from Ling kai Kong. I appreciate his effort in listening to me and providing the best solutions. I thank Brian Richards for his supports with my chip design. I was also lucky to have a period of overlap with Jiashu Chen and Jun-Chau Chien, who shared their great depth of design experience. Many thanks go to Yue Lu for always being patient with my questions and helps in emulation and design. Special thanks go to Gary Kelson, Tom Boot, Kevin Zimmerman and other staff members for making BWRC such a pleasant place to work.

The friendship of many peers in Berkeley is perhaps one of the best memories that I will take with me of my graduate studies. I have very much enjoyed being part of DCDG/Bora's group. Zheng Guo, Seng-Oon Toh, Ji-Hoon Park, Dusan Stepanovic, Vinayak Nagpal, Milos Jorgovanovic, Matt Weiner, Sharon Xiao, Katerina Papadopoulou, Jawhwa Kwak and Brian Zimmer have made my stay very memorable. For outside of the group, I appreciate Amin Arbabian's perspective in life, career and in research and most importantly I am thankful for his friendship throughout the years. I thank Siva Thyagarajan for being a loyal friend and for giving me many constructive and critical feedback and support on my research; I have benefited much from our



discussions. I also thank Steven Callender and Shinwon Kang for discussions regarding our common research interests.

Finally, my gratitude goes to my family, who has been a perpetual source of comfort and encouragement. They taught me the values of life, the importance of integrity and work ethics, which I only learn to appreciate gradually over time. They always valued my honest effort, no matter how minuscule. They provided the best cushion to allow me to recover from each setback and become more determined. I dedicate this work to them for their love and support that made it possible.

## Table of Contents

<b>List of Tables</b> .....	xi
<b>List of Figures</b> .....	xii
<b>Chapter 1 Introduction</b> .....	1
1.1 Related Work .....	6
1.2 Thesis Organization .....	8
<b>Chapter 2 Software-Defined Radio Receiver Design</b> .....	11
2.1 RF Receiver Design Principles .....	11
2.2 RF Convertor Receiver Design .....	14
2.2.1 Overview on $\Delta\Sigma$ ADC Design .....	15
2.2.2 $\Delta\Sigma$ ADC in RF Receivers .....	19
2.3 Digital-Assist Receiver Architecture .....	20
2.3.1 Passive Mixer-First Receiver Design.....	20
2.4 Understanding the Wireless Standards .....	21
2.5 Performance Comparison of Existing Designs.....	31
2.5.1 Software-Defined Radio Implementation .....	35
<b>Chapter 3 <math>\Delta\Sigma</math> Receiver System Architecture</b> .....	36
3.1 Introduction.....	36
3.2 Receiver Architecture .....	37
3.2.1 System Level Design .....	37
3.2.2 Loop Filter Structure.....	40
3.2.3 Jitter Sensitivity .....	46
3.2.4 Current-Mode-Integration Mixing/Sampling.....	52
3.3 Summary .....	59
Appendix A Derivation of Multi-Bit RZ and NRZ DAC Jitter Sensitivity ..	60
<b>Chapter 4 <math>\Delta\Sigma</math> Receiver Experimental Prototype</b> .....	63
4.1 Introduction to System Implementation.....	63

4.2 Circuit Design Details.....	65
4.2.1 Sub-Channel Design .....	65
4.2.2 Low Noise Transconductance Amplifier .....	67
4.2.3 Feedback DAC Designs.....	74
4.2.4 Comparator Design .....	77
4.2.5 LO Generation and Distribution .....	80
4.3 Measurement Results.....	82
4.4 Conclusion .....	91
<b>Chapter 5 Mixer-First Receiver Design Considerations .....</b>	<b>92</b>
5.1 Introduction to Passive CMOS Mixer.....	92
5.2 Passive-Mixer First Receiver Design.....	93
5.3 Baseband Trans-Impedance Amplifier (BB-TIA) Design.....	97
5.3.1 Noise Analysis for BB-TIA .....	99
5.3.2 Analysis for BB-TIA Out-of-Band Linearity .....	102
5.4 Harmonic Rejection System .....	105
5.4.1 Harmonic Folding and Noise Figure Performance .....	105
5.4.1 Harmonic Rejection System Design .....	107
Appendix B Mixer Linearity Analysis.....	116
<b>Chapter 6 Circuit Prototype for a Mixer-First Receiver Design.....</b>	<b>125</b>
6.1 Introduction.....	125
6.2 System Overview .....	125
6.3 Circuit Design Details.....	127
6.4 Optimizing Noise Figure Performance .....	133
6.5 Measurement Results.....	136
6.6 Summary .....	152
<b>Chapter 7 Conclusion .....</b>	<b>153</b>
7.1 Significant Contribution.....	154
7.2 Future Work.....	155

**Bibliography** .....158

## List of Tables

Table 2.1:	RF receiver performance summary .....	32
Table 2.2:	A summary for modern multi-mode multi-radio designs .....	34
Table 3.1:	Comparision of $P_y$ $P_{yd}$ on different levels of DACs .....	46
Table 3.2:	SNR comprision between RZ and NRZ DACs with different DAC levels .....	47
Table 4.1:	Parasitic capacitor extraction result for different capcaitor layout topology .....	68
Table 4.2:	Performance comparison table .....	87
Table 5.1:	Gain allocation and $G_m$ requirement for different value of $R_{FB}$ ...	98
Table 5.2:	Filtering Versus out-of-band IIP3 .....	100
Table 6.1	Noise power breakdowns for noise integrated over different bandwidth.....	120
Table 6.2	Comparison table with other state-of-art receiver designs.....	137
Table 6.3	Comparison table with designs for LTE .....	138

## List of Figures

Fig 1.1:	Spectrum allocation for United States .....	2
Fig 1.2:	The UK frequency allocations .....	3
Fig 1.3:	Hong Kong frequency allocation chart .....	4
Fig 1.4:	Australian frequency allocation chart.....	4
Fig 2.1:	The scenario of the near-far problem .....	11
Fig 2.2.a:	A blocking mask for GSM .....	12
Fig 2.2.b:	A blocking mask for UMTS .....	12
Fig 2.3:	Recent evolution of the RF receiver design .....	14
Fig 2.4:	A simple $\Delta\Sigma$ modulator .....	16
Fig 2.5:	Signal and noise transfer function of a second-order modulator.....	16
Fig 2.6:	Evolution of the wireless communication in the past thirty years .....	23
Fig 2.7:	Non-overlapping LO waveforms.....	18
Fig 2.8:	LTE spectrum allocation across the world .....	24
Fig 2.9:	Supporting LTE together with other wireless standards .....	24
Fig 2.10:	Five different models of iPhone 5 for global support .....	25
Fig 2.11:	Five sub-carrier carrier aggregation to generate a higher bandwidth..	26
Fig 2.12:	LTE carrier aggregation between the licensed and unlicensed bands.	27
Fig 2.13:	System requirement for a device supporting LTE CA .....	27
Fig 2.14:	Samples of the supported channels from a commercial design.....	28
Fig 2.15:	Three different scenarios for carrier aggregations .....	29
Fig 2.16:	Channel bonding for two 20 MHz channels.....	30
Fig 3.1:	Band-pass $\Delta\Sigma$ modulator loop filter in Z transform .....	38
Fig 3.2:	Band-pass feedback created with two SD Modulator .....	39
Fig 3.3:	A second order CIFB $\Delta\Sigma$ loop filter .....	40
Fig 3.4:	Signal and noise transfer functions of a second order modulator .....	41
Fig 3.5:	Simulation results with complex zeroes .....	41
Fig 3.6:	A simplified $\Delta\Sigma$ loop filter .....	42
Fig 3.7:	Signal transfer function peaking in CIFF architecture .....	44
Fig 3.8:	A simplified $\Delta\Sigma$ loop model for FIR DAC .....	45
Fig 3.9:	A simplified $\Delta\Sigma$ loop model with phase noise .....	46

Fig 3.10:	Simulated output spectrum with phase noise model .....	47
Fig 3.11:	Time domain output waveform for $\Delta\Sigma$ ADCs with different quantizer levels .....	48
Fig 3.12:	Comparison of jitter impact on RZ and NRZ DACs.....	50
Fig 3.13:	Equivalent sampling model in time domain.....	53
Fig 3.14:	Equivalent sampling model in frequency domain.....	53
Fig 3.15:	Effect of frequency domain of using sampling to downconvert RF signal .....	54
Fig 3.16:	Equivalent mixing model in time domain .....	55
Fig 3.17:	Equivalent mixing model in frequency domain .....	55
Fig 3.18:	Effect of frequency domain of using mixing to downconvert RF signal .....	56
Fig 3.19:	Current-mode integration sampler with single-ended output.....	57
Fig 3.20:	Equivalent model for CMIS to downconvert RF signal in frequency domain .....	58
Fig 4.1:	Simplified block diagram of the entire receiver .....	63
Fig 4.2:	Simplified schematic of the I-channel.....	65
Fig 4.3:	Low noise trans-conductance front-end design with bias .....	67
Fig 4.4:	Transformer-based output combining network .....	68
Fig 4.5:	Noise simulation result of LNTA under different blocker level .....	69
Fig 4.6:	LNTA linearity simulation results.....	70
Fig 4.7:	Graphical explanation of the LNTA under large blocker transient.....	70
Fig 4.8:	Detail schematic and clocking scheme for FB-DAC1 .....	72
Fig 4.9:	System model including the effects of feedback DAC finite output resistance.....	73
Fig 4.10:	Schematic for the quantizer design .....	75
Fig 4.11:	Quantizer area comparison with and without calibration.....	76
Fig 4.12:	Quantizer area breakdown with calibration.....	76
Fig 4.13:	Quantizer power comparison with and without calibration .....	77
Fig 4.14:	LO generation and distribution network .....	78
Fig 4.15:	Chip microphotograph.....	79
Fig 4.16:	Measurement setup for data capturing and system control .....	80
Fig 4.17:	Measured SNR at 2 GHz carrier frequency.....	81

Fig 4.18:	Measured SNR and SNDR at 2 GHz carrier frequency .....	82
Fig 4.19:	Output spectrum at 2 GHz center frequency with input signal offset by 1MHz .....	82
Fig 4.20:	Flicker noise from LO chain upconversion and downconversion.....	83
Fig 4.21:	Two tone tests with 1 MHz tone spacing around 2 GHz center frequency .....	83
Fig 4.22:	IIP3 versus two-tone spacing at 2 GHz .....	84
Fig 4.23:	SNR, SNDR vs. Signal Bandwidth .....	84
Fig 4.24:	SNDR versus carrier frequency.....	85
Fig 4.25:	Power breakdown for the entire receiver system .....	86
Fig 5.1:	Simplified circuit model of passive mixer .....	91
Fig 5.2:	Non-overlapping LO waveforms.....	91
Fig 5.3:	Passive Mixer-first receiver with baseband TIA .....	93
Fig 5.4:	Equivalent noise model for mixer-first design .....	93
Fig 5.5:	Different amplifier structure candidates for BB-TIA design .....	94
Fig 5.6:	Noise figure (NF) for OTA and Op-amp with different feedback Resistors .....	96
Fig 5.7:	Noise figure with the second stage amplification stage .....	97
Fig 5.8:	BB-TIA with CL and CFB .....	101
Fig 5.9:	Input Impedance with CL and CFB. ....	101
Fig 5.10:	Harmonic noise folding.....	103
Fig 5.11:	The idea of harmonic rejection.....	104
Fig 5.12:	System level implementation of harmonic rejection .....	104
Fig 5.13:	Oversampling and time domain interleaving sampling.....	105
Fig 5.14:	Time-domain interleaving sampling with different duty cycle .....	105
Fig 5.15:	Aliasing content within one slower sampling path .....	106
Fig 5.16:	Aliasing contents in each of the paths .....	106
Fig 5.17:	Imperfect alignment due to the presence of mismatch.....	108
Fig 5.18:	Incomplete harmonic cancelation due phase and gain mismatch.....	109
Fig 5.19:	Performance limitation due to mismatches .....	109
Fig 5.20:	Behavior model for time-interleave system with phase and gain mismatches.....	109
Fig 5.21:	Gain and phase mismatches degrade the HR performance .....	110



Fig 5.22:	Phase mismatches simulation .....	111
Fig 5.23:	HR ratio measured with 50%, 25% and 12.5% duty cycle LO .....	111
Fig 5.24:	LO with different duty cycle for harmonic rejection.....	112
Fig 6.1:	Top-level system overview for mixer-first design .....	114
Fig 6.2:	Schematic for the mixer core and unit cell in the mixer DAC. ....	114
Fig 6.3:	Layout for the differential mixer cells.....	115
Fig 6.4:	Inverter-based amplifier design with CMFB and its bias scheme.....	116
Fig 6.5:	Instability of a two-stage amplifier design. ....	117
Fig 6.6:	AC-boosting compensation (ACBC) scheme.....	118
Fig 6.7:	Detail schematic design for second stage amplifier design.....	118
Fig 6.8:	Floor planning for the entire system.....	119
Fig 6.9:	Noise power breakdown during large signal transient .....	121
Fig 6.10:	Mixer noise power break down. ....	122
Fig 6.11:	Chip Microphotograph .....	123
Fig 6.12:	LO leakage before calibration. ....	124
Fig 6.13:	LO leakage after calibration. ....	125
Fig 6.14:	S11 over wide range of frequencies .....	126
Fig 6.15:	Measured noise figure performance from 250 MHz to 3.5 GHz .....	127
Fig 6.16:	Measured NF performance with different baseband bandwidth .....	129
Fig 6.17:	Noise figure measurement result with various blocker power level .....	130
Fig 6.18:	Test setup for measuring far-out IIP3.....	131
Fig 6.19:	Test setup for measuring close-in IIP3.....	132
Fig 6.20:	In-band and out-of-band IIP3 measured.....	133
Fig 6.21:	Measured P1dB for in-band and out-of-band.....	134
Fig 6.22:	Measured in-band P1dB .....	135
Fig 6.23:	Power break down for major circuit blocks .....	136
Fig 7.1:	Sigma delta receiver with interference cancellation.....	141



# Chapter 1

## Introduction

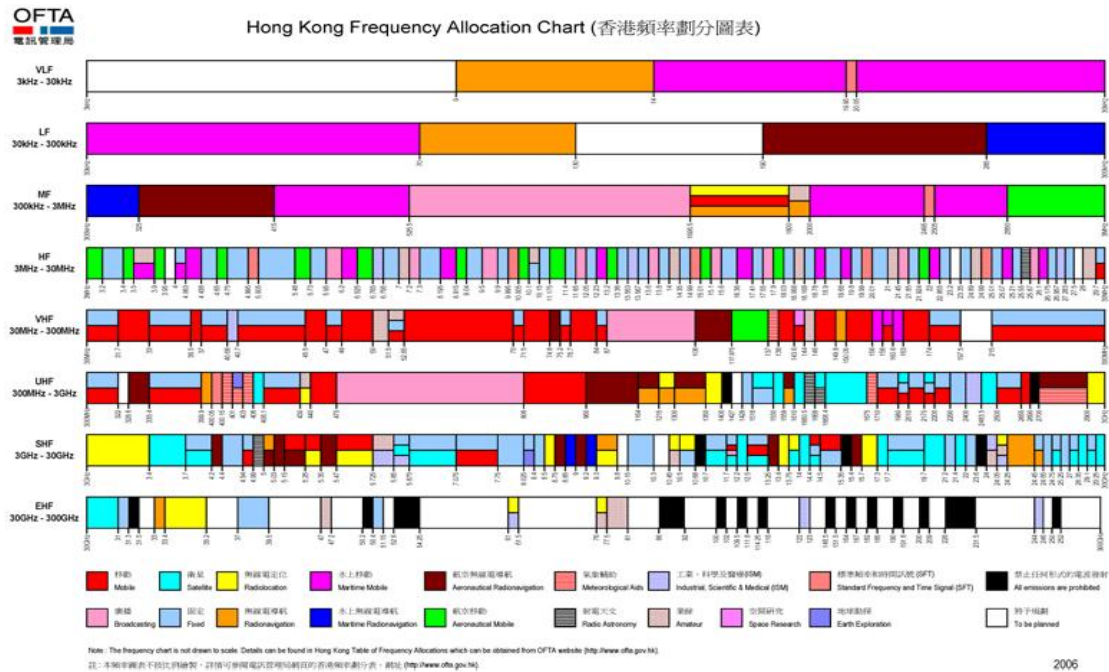
Wireless connectivity has shown its immense significance in the past decade. The continued technology scaling behind the very large system integration (VLSI) has enabled multi-radio system design for mobile applications, which has not been possible in the past century. This highly integrated system on chip (SoC) solution not only allows mobile devices to achieve smaller form factors, but also make the latest wireless technologies more affordable and accessible than they ever were in the past. Coupled with the unending desire for a faster data connection, the wireless connectivity continues to grow, as new wireless standards are introduced to address different needs every year. By now, a wide range of wireless standards exist. Each is highly optimized for power and cost for its own applications, and hence they support different in data rate requirement and cover different range.

It is challenging to support such a multitude of wireless standards with each of them being so drastically different from another. To add to the matter, different countries around the world allocate their spectrum in different ways, and even in the same country, different service providers are operating at different frequency bands. A high-end cellular handset device can support up to a dozen handful of different wireless standards such as GSM, CDMA, UMTS, HSPA, WiFi, Bluetooth as well as LTE, and it is able to operate over more than ten different frequency bands[1]. Up till now, transceiver ICs are often designed with a particular wireless standard in mind, due to the huge difference in system requirement between different standards. To achieve the desired support of the multitude of wireless standards support, multiple chipsets are often required. Given the apparent increase in the design complexity for wireless handset devices and the cost reduction possibility offered by the continuous scaling of the modern CMOS technology, the demand for a single uniform transceiver system which is capable for multi-standard and multi-band operation is highly desired, but not yet available.

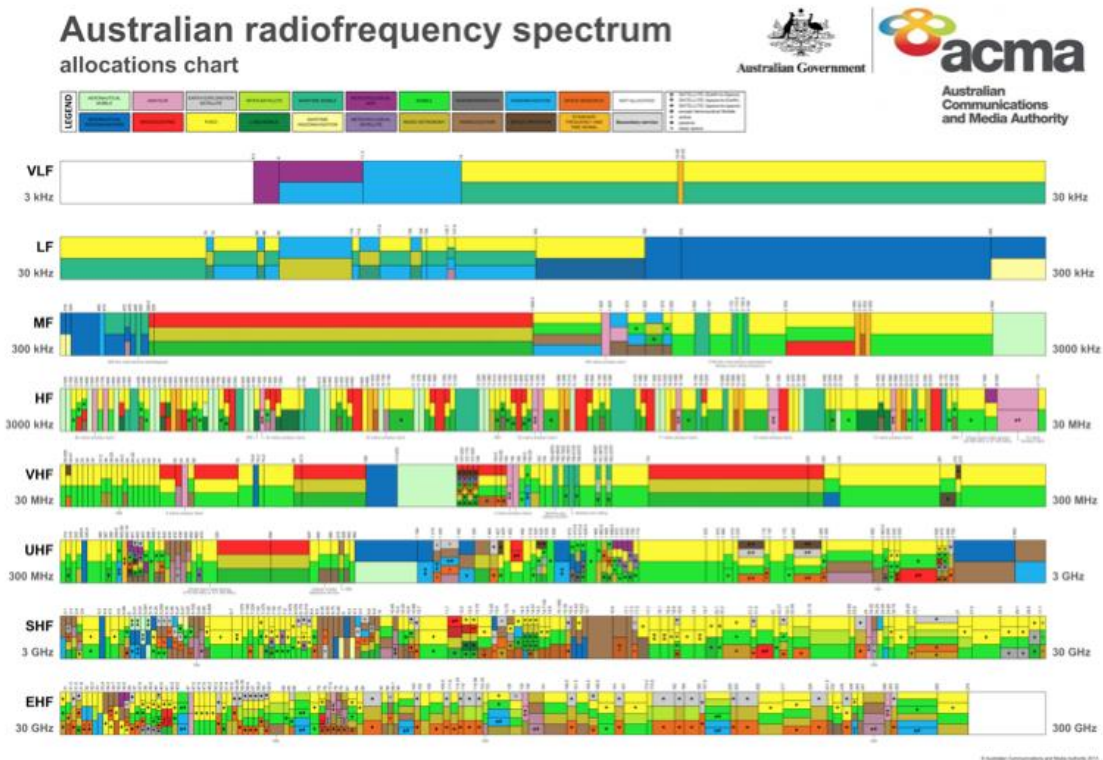
Moreover, spectrum scarcity is an increasingly important issue for the decade, and therefore a flexible and dynamic spectrum allocation is preferable. Due to the proliferation of the wireless standards in the past decade, a majority of the commercial bands have been allocated to different standards (Fig. 1.1). As a result, the remaining available frequency bands that can be allocated for future standards are quite limited, while future wireless standards are still striving for a faster data rate and wider bandwidth.

Fig. 1.1 Spectrum allocations for United States.





Courtesy of Office of the Communication Authority (ofca.gov.hk)  
Fig. 1.3 Hong Kong frequency allocation chart



Courtesy of Australian Communications and Media Authority (acma.gov.au)  
Fig. 1.3 Australian frequency allocation chart



Cognitive radio (CR) is one technology under research that could potentially allow a more efficient use of the existing spectrum. While spectrum is auctioned off at high price, researchers have noticed that most of the licensed frequency bands are being under-utilized for most of the time [2], which suggest there is a potential to improve efficiency of the spectrum usage by sharing it among other systems. The advantage of cognitive radio is its feature of dynamic spectrum access (DSA), which allows different system to look for the unused channels and time-share it.

Regulatory efforts from governments around the world also aim to solve the issue. Cognitive radio is expected to operate in a large portion of the commercial spectrum in the future. As for now, vacant channels have been or plan to be released by governments for different applications. The new devices, known as TV band devices (TVBD) would operate in those frequency bands. Japan, Singapore, the United Kingdom as well the as the United States have been working on to support devices like this. For instance, the European Conference of Postal and Telecommunications Administrations have opened up the 470 to 790 MHz band for TVBD use.

In U.S, the FCC has established the fixed and the portable devices categories for TVBDs. Fixed devices can transmit with a power up to 1 watt, and they may use any of the vacant U.S. TV bands as 2, 5 to 36, and 38 to 51. On the other hand, the portable devices shall operate in TV channels from 21 to 36 and from 38 to 51. The permitted output is 100 mW EIRP, or at a reduced power level of 40 mW when there is an adjacent TV channel.

While research and regulatory efforts aim to solve the issue of the spectrum scarcity, the envisioned implementation of the CR poses a series of serious challenges on the RF transmitter and receiver design. The RF transceiver system needs to be flexible enough to adapt to different frequency band and different standards upon request, which is a huge deviation from the conventional wireless design methodology, where RF transceiver design is highly optimized by one set of application. On the other hand, a faster and more affordable network is always desired, which puts a lot of pressure on the future wireless standard in the absence of the CR. Before CR can be widely deployed, all the future standards would have to struggle between the limited remaining spectrum and the desire for higher data rate.

Long-Term Evolution (LTE) is the latest radio platform technology introduced to the family of the commercial wireless systems. As the result of the increasing global spectrum scarcity, LTE standard is a compromise that consists of total 43 separate bands ranging from 450 MHz all the way up to 3.8GHz. All 43 bands of LTE are separated to fit in the narrow available channels in different geographical regions, and the end result is a highly fragmented spectrum over a wide frequency range, which makes LTE the most difficult standard to provide world-wide support.

Another issue associated with the future wireless system is how to provide a higher throughput with limited bandwidth available. A similar idea as CR has been introduced to the latest wireless technologies, which is known as in-channel spectrum re-

allocation. The recent wireless standards, such as 802.11.ac and LTE all adopted similar schemes. LTE Advanced introduces the idea of carrier aggregation, where multiple in-channel sub-carriers can be allocated for the same user or different users in a wide range of manners, while the 802.11.ac (5G WiFi) includes the idea of channel binding, where the channel bandwidth allocated to a user can be expanded to achieve a much faster data rate when it is possible.

A reconfigurable transceiver is desired because of its ease to cover wide range of wireless standards and frequency bands, in particular it can be a cost-effective solution to support the LTE fragmented spectrum. Moreover, it can be extended to support future dynamic spectrum allocation, such as required by the cognitive radio. The final goal is a single uniform transceiver system, which is sufficiently flexible to support the existing as well as the future standards over a wide-range of frequency bands. The system would ease on the difficulties to support multitude of existing standards as well as open up a path for flexible spectrum allocation scheme for demanded to address the spectrum scarcity issue.

## 1.1 Related Work

The idea of software-define radio (SDR) is first proposed by Joseph Mitola in 1992 [3]. A software-defined radio is a radio system such that most of its components are implemented by means of software on a general purpose computing device or embedded system. The ideal concept envisions a system which can monitor and transmit over the entire RF spectrum. Since then, there are a few notable examples known as the reconfigurable, or software-defined, RF receivers (SDR) such as references [4][5][6][7][17][27][30]. All the listed designs adapted the convectional chain of elements design, where the systems begin with an RF amplification stage (LNA), followed by a frequency conversion state (mixer). Then the down-converted signal is filtered by a high-order low-pass filter prior to it reaches the ADC.

Throughout the years, there are a wide range of system implementation proposed to fulfill the grand vision of SDR. In particular, one thing that stands out in the UCLA design [5] is that it contains a low-power discrete-time low-pass filter. This filter makes use of an old and yet well-known concept: the passive switched-capacitor filter, which is popular choice for the baseband filter in RF receiver designs such as [5][7][8] and [9]. The passive switched-capacitor technique has several advantages, such as its precision in the filter cut-off frequency, relaxed requirement on the amplifier settling time as opposed to an active switched-capacitor filter design.

As demonstrated in [10], the passive switched-capacitor filter design can be better combined with the idea of current mode integration sampling mixer. This sampling mixer



provides the necessary down-conversion feature for a RF receiver system, while avoiding the otherwise power-hungry sample-and-hold circuit that is often required for any discrete-time circuit. Since it was first introduced in 2000, the idea of sampling mixer are widely adopted in a few different designs such as [7][8][5][11] and [12].

In this first design, a sampling mixer is used to down-convert the signal from radio-frequency down to base band, and integrated the converted charge on the sampling capacitor. The sample and held signal charge is then digitized by a fast-sampled  $\Delta\Sigma$  ADC. Most of the signal processing are removed from the analog domain and pushed into the digital domain, to take full advantage of the technology scaling.

To be able to support the various existing and future standards, a high-resolution and a high-speed ADC is always preferred for any software-defined radio system [3]. The high-resolution conversion not only can cover the different SNR requirements posed by the different wireless standards, but also ease the interference performance of the front-end circuits. On the other hand, the high-speed feature helps to reduce noise folding and blocker folding down to the band of interest, especially for a sub-sampling receiver system such as [13][14] and [15]. The issue of such an ADC is that its design is not feasible, given the limited power and area budget of a cellular device [16].

As proposed in [17], an alternative is a fast-sample, high-resolution but low-signal-bandwidth  $\Delta\Sigma$  ADC. Even though a high-speed ADC is preferable, wide-band digitizing is not really necessary. As a matter of fact, most of the wireless standards have data concentrated only in a narrow band centered around their carrier frequencies.  $\Delta\Sigma$  ADC is therefore perfect candidate for such an application. It samples the input RF signal at a fast rate, in the case of [17] which would be the RF carrier frequency. This meets the high-speed feature mentioned above. Moreover,  $\Delta\Sigma$  ADC utilizes the large OSR between the data bandwidth and its carrier frequency to produce the desired high resolution conversion within the signal bandwidth, which is essential to cover the SNR requirements for various wireless standards.

Historically, different  $\Delta\Sigma$  ADC based converter designs have been reported in the literature such as [17][18][19][20] and [21]. Some of the reported works have the mixer embedded in the loop design [17][20][21]. However, besides [17], the other two designs can only achieve limited bandwidths such as 40 KHz and 200 KHz, which are clearly not enough to support modern wireless standards. The designs as [18][19] are structured more like a conventional type of  $\Delta\Sigma$  ADC with the exception that a mixer is included ahead of the ADC. As will be discussed later in this work, embedding the mixer inside the  $\Delta\Sigma$  ADC loop filter can effectively improve the overall linearity performance, a better linearity performance is always preferred for SDR sign.

On the other hand, passive-mixers based on CMOS technology can be dated back in early 2000 [57][58]. The recent improvement the CMOS technology really empowers the passive mixer, as it replaces the active mixer designs in industrial system and academia endeavors [59][60]. Compared to the active mixers, passive mixer is known for its bi-directionality. Equivalently speaking, the passive mixer lacks of the reverse

isolation. Bi-directionality makes the analysis for a passive mixer more difficult, so engineering intuition is hard to obtain. Fortunately, recent research efforts such as [59] show an in-depth analysis of the circuit. It has been shown that its two-way frequency translation feature provides passive mixers with a series of benefits over active mixers, therefore, new opportunities together with unique design challenges arise.

Recent research has shown that by utilizing a multiple non-overlapping LO waveforms, the passive mixer designs can be better optimized compared with the use of a more traditional sinusoidal or simple square-wave LO waveforms [58][60][63][64][65]. Each of the clock pulses drives different mixer switch. Together, a series of phase-shifted baseband output can be generated, and they can later be summed with the baseband trans-impedance amplifier (TIA) to reconstruct the complete baseband output.

The idea of passive mixer-first design is first proposed by Berkeley Sensor and Actuator Lab in 2004 as a low-power RF frontend for sensor network applications [24]. Limited by the understanding on the passive mixer at the time, the idea was considered too radical and didn't fare too well. Six year after it was first introduced, it has been brought back to the public attention by its original author, Alyosha Molnar and his student Caroline Andrews in ISSCC 2008 [25]. Since then, the idea of the passive mixer-first design has gaining a lot of attention.

## 1.2 Thesis Scope and Organization

This work focuses on the exploration of highly reconfigurable RF receiver designs with the intention to cover multi-band and multi-standard operations. The stress would be on the 0.4-4-GHz frequency-range where most of the commercial wireless communication standards take places.

Flexibility and re-configurability of the RF receiver should be achieved with minimum performance sacrifice as well as maintain the overall design in an economical manners from the silicon area's perspective. Thanks to the continuous technology scaling, digital signal processing (DSP) is getting more powerful and more affordable every day. One of the focuses of this work is to shift part of the signal processing features from the analog domain into the digital world to enjoy the precision and the affordability offered by the DSP core.

Two separate receiver architectures are proposed in this work. The first one is a high performance analog-to-digital converter design aiming at directly digitizing the RF signal and down-convert it to baseband in one step. In this proposed architecture, an analog signal residing at the radio frequency is converted directly into the digital domain using a second order down-converting sigma-delta ( $\Sigma\Delta$ ) modulator. The  $\Sigma\Delta$  ADC architecture is a good fit for such an application since it takes full advantage of the high oversampling ratio (OSR) to provide a wide dynamic range in the frequency band of

interest. Channel selection and bandwidth adjustment is pushed into the digital domain to enjoy the precision and affordability of the DSP offered by the latest CMOS technology scaling. A direct-down-conversion receiver design eliminates problem of with image frequency content folding which is always the issue for superheterodyne design.

A circuit prototype demonstrating the above concept has been designed and measured. The test-chip prototype is able to achieve an SNDR of close to +70dB across a 4-MHz bandwidth with a programmable center frequency spanning from 400MHz up to 4GHz. As will be illustrated in this work, the entire design is based on current mode operation, and the tight integration of the  $\Sigma\Delta$  receiver ensures the overall the system to maintain a very good linearity performance. A wideband IIP3 better than +10dBm is measured in this test-chip prototype.

A second architecture, based on the mixer-first design is proposed in this work, where the first stage of amplification, which is considered as necessary for conventional designs, is removed for better wide-band linearity performance. In this proposed architecture, the RF signal is directly sent to the passive mixers, and it is then down-converted to the baseband directly. A reasonable noise figure can be ensured through careful sizing the passive mixer size as well as optimizing the baseband amplifier's gain. Without the LNA up front, the entire system achieves a better linearity performance over a wide range of frequency both in-band and out-of-band. This is essential to support carrier aggregation introduced in the LTE Advanced.

A passive-mixer-first receiver prototype is designed in 28 nm high-K metal-gate CMOS technology. The frontend 5-bit mixer-DAC provides a wide-band tunable impedance match to suppress the LO leakage. Baseband LNA together with the AC-boosting compensation amplifier provides a 50 MHz baseband bandwidth, which provides support for non-contiguous carrier aggregation for LTE in power efficient manners. The overall design achieves < 3 dB NF, > 15 dBm IIP3 and 35 dB gain with 55 mW power.

Chapter 2 of this dissertation centers on the overview of the issues presented by the upcoming standards. A set of system requirement is derived; a survey of the state-of-art solutions from the conventional receiver design as well as band-pass  $\Delta\Sigma$  ADCs is presented. Finally a few practical performance issues are examined.

Chapter 3 of this dissertation focuses on the system level design of the  $\Delta\Sigma$ . The  $\Delta\Sigma$  based receiver architecture is first introduced. Some of the highlighted analysis from reference [44] is summarized, and new analysis which is essential for performance improvement is also presented.

Chapter 4 of this dissertation discusses the detail implementation of the  $\Delta\Sigma$ -based receiver design. Details of a few core circuit blocks are revealed and explained. A novel class-AB LNTA circuit is presented, along with the pertinent analysis. This chapter concludes with  $\Delta\Sigma$  receiver's measurement results recorded from the test chips.

Chapter 5 of this dissertation addresses the system level trade-off for the mixer-first design. The structure of a mixer-first receiver is first explained, followed all pertinent analysis associated with the design.

Chapter 6 of this dissertation presents implementation detail of the mixer-first design. Detail descriptions of the important circuit blocks are discussed, together with detail analysis for the design. The latter part of this chapter is dedicated to the measurement results from the test chips.

Chapter 7 of this dissertation summarizes the important contribution of this work and suggested potential topics for future improvements and research.

# Chapter 2

## Software-defined Radio Receiver Design

This section starts with an introduction of general design principles of a RF receiver. Derivations of an ADC specification for a receiver are then demonstrated. After that, the basic of  $\Delta\Sigma$  ADC is introduced. Specifications for a reconfigurable receiver are then introduced with the intention to cover some of modern wireless standards. Finally, a survey of state-of-art integrated circuit solutions is presented.

### 2.1 RF Receiver Design Principles

One well-known issue in the wireless receiver community is the near-far problem. The case is depicted in Figure 2.1. It can be described as a device try to receive a weak signal sent by a faraway signal source (system A) in the presence of a strong interference presented by another nearby signal source (system B). Often times, the desired signal and the interference might reside at different frequencies, but they may still be at a close proximity in frequency. As the result, instead of detecting the desired signal, the device might be overwhelmed by the undesired blocker, given the fact that the blocker might be orders of magnitude larger than the desired signal.

The RF receiver has to be able to endure this scenario and maintain the link robustly. In order to do this, a minimum amount of signal to noise ratio (SNR) has to be maintained. The actual required number varies from one standard to another. This minimum SNR does not always need to be positive. For example, some standards such as CDMA can even function properly with a negative SNR down to certain number.

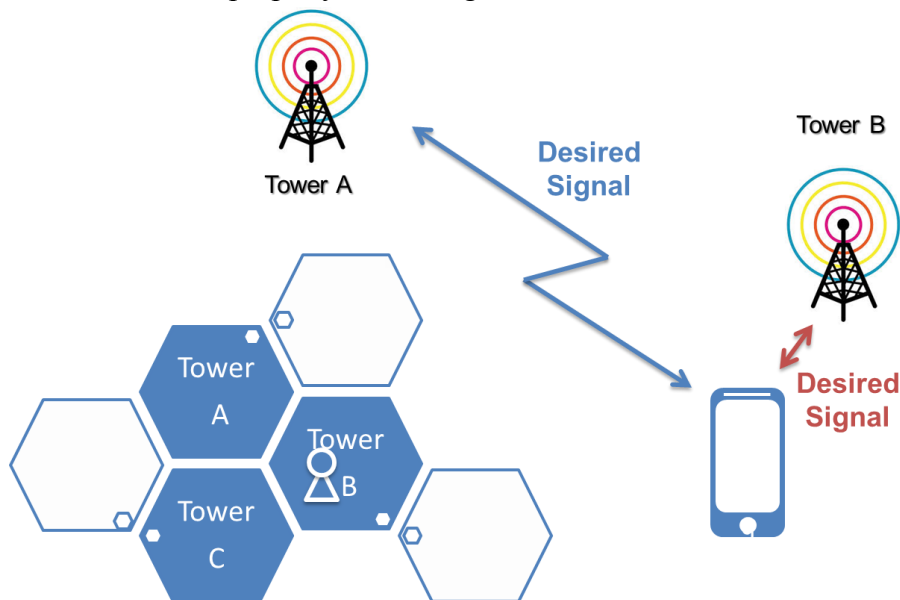


Fig. 2.1. The scenario of the near-far problem

Different from the ADC designers, RF community likes to characterize SNR performance from the noise perspective. The metric used in this case is known as noise figure. Noise measured at the RF receiver has three common sources: 1. the thermal noise; 2. the thermal incident noise due to the antenna and 3. the added noise from the RF receiver circuit. Out of these three noise components, the first two are unavoidable. Therefore, the noise figure is mostly related to the receiver added noise. For the same amount of the SNR desired, a receiver with lower noise figure would be more sensitive to pick up a weaker signal, therefore perform better in the far-near scenario. The minimum signal power level for a particular receiver that ensures correctly demodulation is defined as the receiver sensitivity level.

Beside noise figure or sensitivity level which would impact how a receiver to handle the near-far problem, the blocking mask requirement is also important. Two blocking masks for GSM and UMTS are shown in Fig. 2.2.a and b. The masks describe the worst case of near-far problems that should be supported in each of the standards. For the GSM case (Fig 2.2.a), while the signal can be as low as -104 dBm, a blocker which is only 3 MHz away can be at a power level as high as -13 dBm. The difference between the strongest 3 MHz blocker and the desired signal can be as large as 90 dBm. If it is

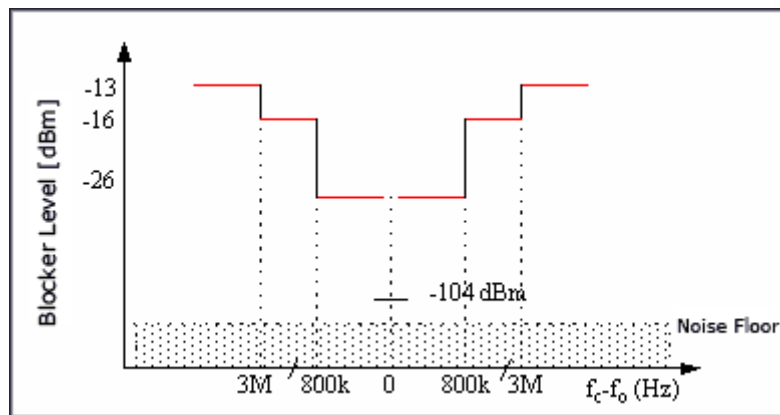


Fig. 2.2.a The blocking mask for GSM

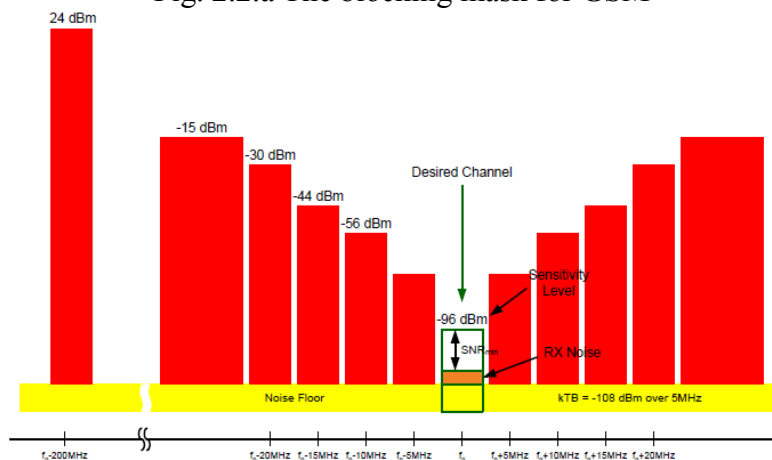


Fig. 2.2.b The blocking mask for UMTS

translated to a voltage swing, the blocker would be on the order of  $10^4$  times larger than the desired signal.

Compared Fig. 2.2.a and Fig 2.2.b, it should be apparent that GSM and UMTS are quite different from each other. Not only the required receiver sensitivities differ by  $\sim 10\text{dBm}$ , but the blocking masks are different too. Therefore, it poses serious challenges to software-define radio system, as it needs to meet the sensitivity and the blocking mask requirement for various standards.

Given this understanding, it helps to explore different strategies in partitioning the analog and the digital components for the optimal implementation of a software-defined radio system. First off, a conventional type of the receiver structure is introduced. Classical receiver design consist a series of amplification stages, filter stages and mixing stages in cascade as shown in Fig. 2.3. For direct-conversion receiver implementation as shown in Figure 2.3, the system has a LNA to provide early amplification which improves the noise figure performance. A down-conversion mixer then translates the signal content from the carrier frequency down to DC or to a low intermediate frequency (IF). Depending on the actual implementation, the filters might occur prior or after the mixing stage to meet the particular blocking mask requirement demanded by the standard. Finally, there is an ADC digitizing the analog signal, and digital output would then be sent to the DSP for demodulation and further processing. As the desired signal travels down this mixed-signal path, it is amplified gradually until it satisfies the minimum SNR requirement demanded by the demodulation process. On the other hand, the blockers or interferences would be attenuated stage after stage so that the components in the receiver chain would not be upset by their presence. As the combine result of these two processes, receiver can handle the near-and-far problem with confidence, and the received signal can demodulated successively even in the minimum signal level.

One major change in direction in the RF receiver design is in the filtering. The channel selection filter, is migrated into the digital domain as shown in figure 2.3 thanks to the technology scaling. Digital assisted design not only helps reduce the silicon area, but also helps achieve a more flexible design. However, the amount of signal processing can be shifted into the digital backend is dictated by the achievable dynamic range and the sampling rate of the ADC. The larger the ADC's dynamic range can be, more signal conditioning can be pushed into the digital domain, and hence the RF frontend is more flexible. From the sampling point of view, if an ADC can sample at faster rate, a less stringent anti-aliasing filter is required. Taking these two points to extreme, it yields to Mitola's vision of the software-defined radio receiver.

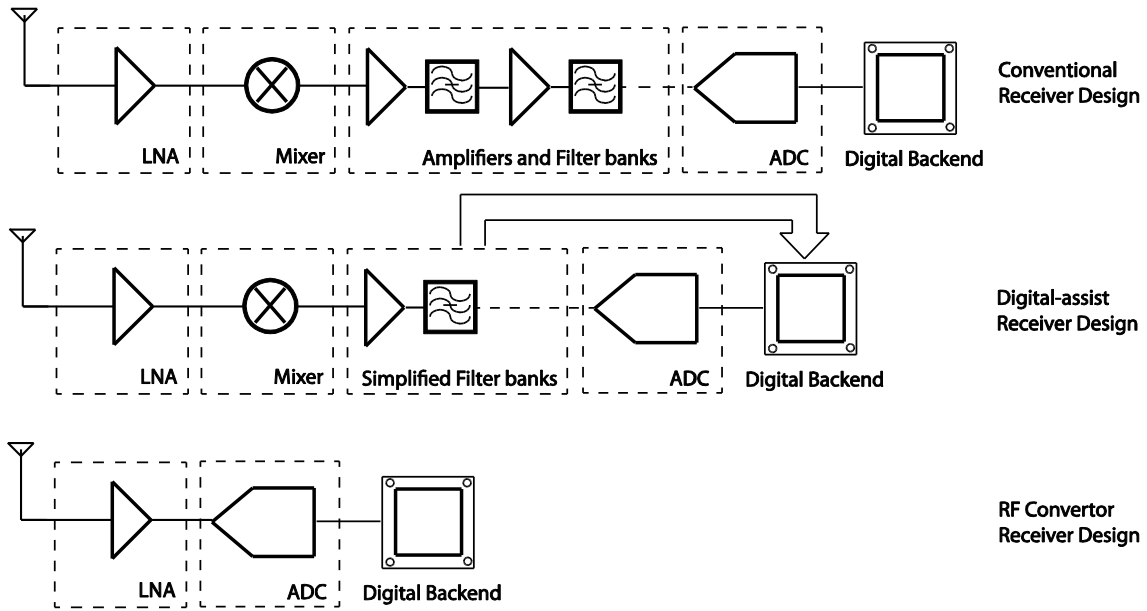


Fig. 2.3. Recent evolution of the RF receiver design

To accommodate the vast majority of existing wireless standards as well as the standards that shall be introduced in the next decade, digital-focus design methodology can enable the otherwise fixated RF design with great flexibility. Therefore, this work mostly focuses on the digitally-assisted receiver and the RF convertor architectures.

## 2.2 RF Convertor Receiver Design

At the core of Mitola's vision of SDR, it is a wide-range high-resolution ADC. One might be curious how high a resolution is needed to achieve the software-define radio. In GSM, for example (Fig 2.2.a), if one aims to migrate the all the filtering stage into the digital core, they would need an ADC with at least 102 dB dynamic range (17 bit ENOB) to handle the case where the minimum signal level coexist with 0 dBm out-of-band blocker.

ADC architectures can be categorized into three groups: flash, multi-step and oversampled ADC. Flash ADC can operate at a very high sampling rate, and introduces



the lowest latency among all. However, its resolution is limited and its design is power hungry. Multi-step ADC such as pipeline and SAR digitizes the input signal in a few cycles. They are good fit for applications with medium resolution and medium bandwidth requirement, but they fail to meet the speed and resolution requirements for SDR system. For a Nyquist-rate ADC design, a one-bit resolution improvement requires four times more power, therefore, designing a high-speed Nyquist-rate ADC whose resolution is capable of meeting the near-far requirement is too power hungry to be practical. As the result, Mitola's vision of digitizing at the antenna is not realizable.

To circumvent this fundamental issue, one needs to recognize that the ADC doesn't need to maintain its high dynamic range over the entire half-Nyquist bandwidth. The high dynamic range is needed only within the narrow band where the modulated signal resides. For the rest of the Nyquist bandwidth, the ADC can have a more relaxed dynamic range. The ADC still has to maintain a large full-scale range over a wide range of frequencies to handle the out-of-band blocker. This makes oversampling ADC, in particular  $\Delta\Sigma$  ADC, a potent candidate for software-defined radio application.

## 2.2.1 Overview on $\Delta\Sigma$ ADC Design

$\Delta\Sigma$  ADC is most well-known for its high resolution achieved over a narrow signal bandwidth in a power efficient manner. Moreover, it also ease on the front-end anti-aliasing filter requirements, hence reduces the overall power consumptions. There are many detail references on  $\Delta\Sigma$  ADC in the literature [22][23]. For completeness of this work, a brief overview of  $\Delta\Sigma$  ADC is included here.

$\Delta\Sigma$  modulator as shown in figure 2.4 features two powerful concepts: oversampling and noise-shaping. Taking advantage of these two concepts,  $\Delta\Sigma$  ADC can achieve a high resolution even with a one-bit quantizer design.

Oversampling helps to increase the in-band SNR of a  $\Delta\Sigma$  ADC by spreading the quantization noise over a wider bandwidth. The signal content outside of the desired bandwidth  $BW$  would be cut off by the digital decimation filter. The oversampling ratio (OSR) can be described as the ratio between the Nyquist-rate ( $f_s/2$ ) of the quantizer and the desired signal bandwidth ( $BW$ ):

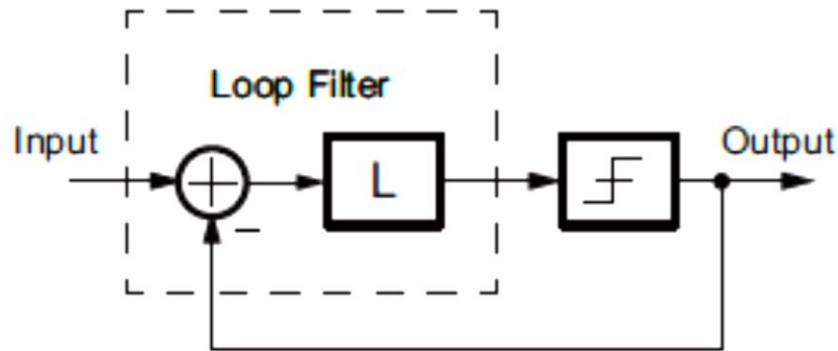


Fig. 2.4. A simple  $\Delta\Sigma$  modulator

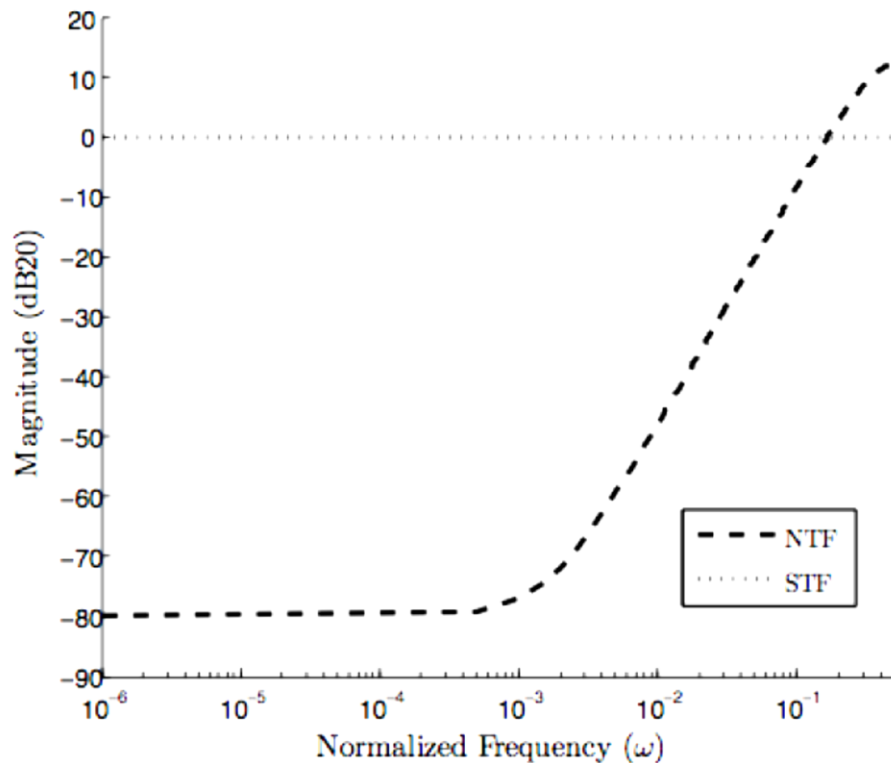


Fig. 2.5. Signal and noise transfer functions of a second-order modulator

$$OSR = \frac{f_s}{2 \cdot BW} \quad (1)$$

For a quantizer with N-bit resolution, its SNR is  $(1.76+6.02N)$  dB. Since the quantization noise is spread over a wider bandwidth, if we assume the quantization noise is white, then the overall in-band SNR with an oversampling ratio can be described as:

$$SNR = 1.76 + 6.02 \cdot N + 10 \cdot \log_{10}(OSR) \quad (2)$$

As OSR is doubled, the overall SNR would increase by 3 dB.

The overall SNR can be further improved by pushing most of the quantization noise out of the band of interest, which is known as the noise shaping. Noise shaping is implemented by enclosing a loop filter inside the  $\Delta\Sigma$  modulator loop as shown in the figure 2.4. This loop filter should have minimum impact on the desired signal, but it high-pass filters the in-band quantization noise, and pushes them out of the band as demonstrated in figure 2.5. The actual loop filter implementation varies from design to design, and it can either take the form of a low-pass structure or a band-pass structure. By combining the techniques of oversampling and noise shaping, a much larger SNR improvement can be achieved

Without a loss in generality, assume a low-pass filter is chosen as the  $\Delta\Sigma$  loop filter. The loop filter should have minimum impact on the desired signal, therefore the signal transfer function (STF) is flat in this case. The loop filter's low-frequency gain forces the feedback signal to follow the input signal with high fidelity. The quantization noise content in those frequencies is rejected by the low-frequency gain of the entire loop structure. For short, the large loop gain of the feedback system helps to suppress the in band noise. As the loop gain diminishes at higher frequency, the effect of the noise suppression degrades as well. Therefore the noise transfer function (NTF) rises as the frequency increases, as shown in figure 2.5.

For example, in the case from figure 2.5, a second order low-pass filter is chosen as the  $\Delta\Sigma$  loop filter. The STF and the NTF can be described as:

$$STF = 1 \quad (3)$$

$$NTF = 1 - z^{-2} \quad (4)$$

The STF is truly flat over the entire frequency, and the NTF has a high-pass nature compared to the low-pass loop filter. Given this particular nature of the NTF, the quantization noise is lower at the low frequencies, and hence a higher dynamic range can be assured there. Moreover, NTF has a second order high-pass response, therefore, the out-of-band quantization noise rises with a 40dB-per-decade slope, which is typically described as a second-order noise shaping. In such a way, the  $\Delta\Sigma$  manages to achieve a high resolution in a narrow frequency band, while maintaining a high-sampling frequency which helps to ease the anti-aliasing filter design.

Higher-order  $\Delta\Sigma$  ADC enjoys the benefit of higher order noise shaping, therefore, to achieve the same resolution, lower OSR is required, which helps to reduce the power consumption of the system and simplify the quantizer and feedback DAC design. However, higher-order  $\Delta\Sigma$  ADCs demand higher-order loop filter, which contains more poles and zeroes. Just as every other feedback system, it is much harder to maintain the overall stability when the system becomes more complicated. ADC designers often have to trade off favorably between the orders of the system with a reasonable OSR. In general, most of the commercial  $\Delta\Sigma$  ADC designs refrain to an order less than five, due to the stability and complexity reasons.

As mentioned above,  $\Delta\Sigma$  ADC's output spectrum contains not only the desired signal, but also a wide-frequency of the shaped noise. This suggests its output needs to be filtered and down-sampled before the digital signal processor can demodulate the desired signal efficiently. The digital decimation filter can be implemented in the digital domain without causing too much power consumption. Modern CMOS technology allows for a very power and area-efficient implementation of such digital design. Even better, digital decimation filter can scale with the process, which further reduces its impact on the overall power and area budget.

## 2.2.2 $\Delta\Sigma$ ADC in RF Receivers

As discussed earlier, an ADC that meets the SDR requirements needs to have a high resolution and fast sampling rate at the same time.  $\Delta\Sigma$  ADC offers a unique alternative, compared to other topologies to meet both of these two criteria, while maintaining a reasonable power and cost budget.  $\Delta\Sigma$  ADC is able to avoid the some of the fundamental trade-offs facing by the Nyquist rate ADC designs.

$\Delta\Sigma$  modulator design is promising for RF receiver design is mostly due to its two prominent features: oversampling and noise-shaping. Oversampling raises the Nyquist rate, and hence it eases on the anti-aliasing filter design. For a Nyquist rate ADC design, increasing the sampling-rate is really challenging, since this ADC needs maintain its noise floor over the widened bandwidth. To add to the matter, as the ADC can handle a wider range of input, it is susceptible for the out-of-band interferences, which could be a few times or order of magnitude bigger than the desired signal. Therefore, the required dynamic range and sampling speed requirement makes a Nyquist-ADC design highly impractical.

It is really important to realize that high resolution conversion is not necessary over the entire frequency range, but only for narrow frequency band of interest, where the desired signal resides. For frequencies other than that band of interest, the ADC only needs to tolerate a large input level such as that the large out-of-band blockers are not going to rail out the ADC. Given these two important observations,  $\Delta\Sigma$  ADC truly shines in the SDR application, as it can provide a high dynamic range only over a narrow frequency band, while maintaining a high sampling rate. The narrow-band high-resolution conversion ensures the conversion process of the  $\Delta\Sigma$  ADC is as efficient as possible. Compared to Nyquist-rate designs, where all the signals (both in-band and out-of-band) are still being converted in high resolution, large amount of the power is wasted in converting signals which has little use for demodulation process.  $\Delta\Sigma$  ADC data conversion process is much more energy efficient.

Aliasing is a major issue that plagues any type of the ADC design. However, for RF receiver design, an explicit anti-aliasing filter might not be necessary. First, RF components such as antenna SAW filters, TR switches and duplexers all have limited operational bandwidth.  $\Delta\Sigma$  ADC's sampling rate is often much higher than the narrow band of interest, then, the first aliasing Nyquist zone is quite faraway. Hence, the limited operational bandwidth of various RF components can serve as implicit filtering for aliasing contents. Even better, bondwire has limited operation bandwidth as well, which further helps to suppress the aliasing content. Moreover, as shall be discussed later in this work, other techniques can effectively alleviate the issue of aliasing in an ADC-based RF receiver design. Overall, the removal of an explicit analog anti-aliasing filter not only helps to maintain a better power and area budget of the overall design, but it also enables great flexibility of the design, as the signal bandwidth is no longer explicitly defined in the analog domain. The final signal selection can be pushed into the digital domain, in the

form of the application of digital filters. Combined with a programmable digital system such as FPGA, it allows a possibility of on-the-fly re-programming the digital filters to accommodate the change of signal bandwidths and applications. This feature is very amenable and appealing as a concept for reconfigurable RF receiver.

## 2.3 Digitally-Assisted Receiver Architecture

The beauty of the digitally-assisted Receiver is that a part of the filtering network is shifted into the digital domain. The analog/RF components can be reduced to its minimum to enhance the flexibility and better performance vs. power tradeoff for the overall system. To carry this idea to the extreme, it will very well be an ideal ADC that fits the idea of software-defined radio. Throughout the past decade, technology scaling has been marching into the sub-micrometer region, and it enables devices with sizes 100<sup>th</sup> of micrometers to come into production. At this point of time, realization of devices size even down to single digit nanometer is not that far at all. This improvement in the process shrinking not only makes the digital backend more capable and power efficient than any time before, but also allows many mixed signal blocks, such as ADC, to evolve at the same time. In particular, ADC design for wireless applications has experienced major change in the past decade. In most of the wireless applications, the once dominant Pipeline architecture has become obsolete. Its throne is now claimed by architectures such as  $\Delta\Sigma$  ADC and SAR ADC. SAR ADC architecture scales more naturally with the technology shrinking, while the  $\Delta\Sigma$  ADC draws great benefits from a more capable digital backend enabled by the latest technology improvement. In the literature, SAR ADCs and  $\Delta\Sigma$  ADCs have been reported efficiency that is ten times better than Pipeline ADCs. Because of the more powerful digital core as well as a more capable data convertor, the conventional way of partitioning between the analog/RF domain and digital domain is obsolete, and cannot provide the best performance vs. power tradeoff. In the recent decade, a great amount of research effort has been made in reshaping the boundary between the digital and analog/RF. Many analog/RF components, which used to be deemed as essential or critical for the applications, have been removed from the receiver chain successively. The overall result is a much simpler design with much better power efficiency.

### 2.3.1 Passive Mixer-first Receiver Design

The passive mixer-first receiver design centers on the idea of the passive mixer, which has been reported in 2000 [57][58]. For a fairly long time, active Gilbert mixers have been the mainstay for the integrated receiver system, because of their gain performance. However, they suffer from high flicker noise. Passive mixers, on the other hand, has higher conversion losses but outstanding flicker noise performance [119][120]. Several studies have addressed passive mixer design converts in great detail from the

perspective of noise, dc offset, second-order distortion and third-order distortion[120][121][122][123]. Over the years, it has become the mainstream design for modern commercial integrated receiver systems [59][60].

Also, it has been shown that by utilizing a multiple non-overlapping LO waveforms, the passive mixer designs can be further optimized [58][60][63][64][65]. Recent mixer-first receiver designs have demonstrated that the architecture can achieve excellent noise and linearity performance: reference [25] has shown a sample design with a record-high 25 dBm IIP3, while in [68] a mixer-first system with a 1.9 dB noise figure is reported with the aid of noise cancellation.

## 2.4 Wireless Standards

A survey of requirements of a few modern wireless standards is presented in this section in order to shed light on the basic requirements for a reconfigurable RF receiver. Some of the RF signal requirement for different standards can be simplified into a blocker mask and a sensitivity requirement. A short summary between blocker mask requirements from three existing wireless standards is shown in figure 2.6. The blocker mask gives a good understanding about the signal level the receiver needs to tolerate at different frequency offsets. Another requirement is based on the minimum SNR for successful demodulation as well as the sensitivity requirement of a particular wireless standard.

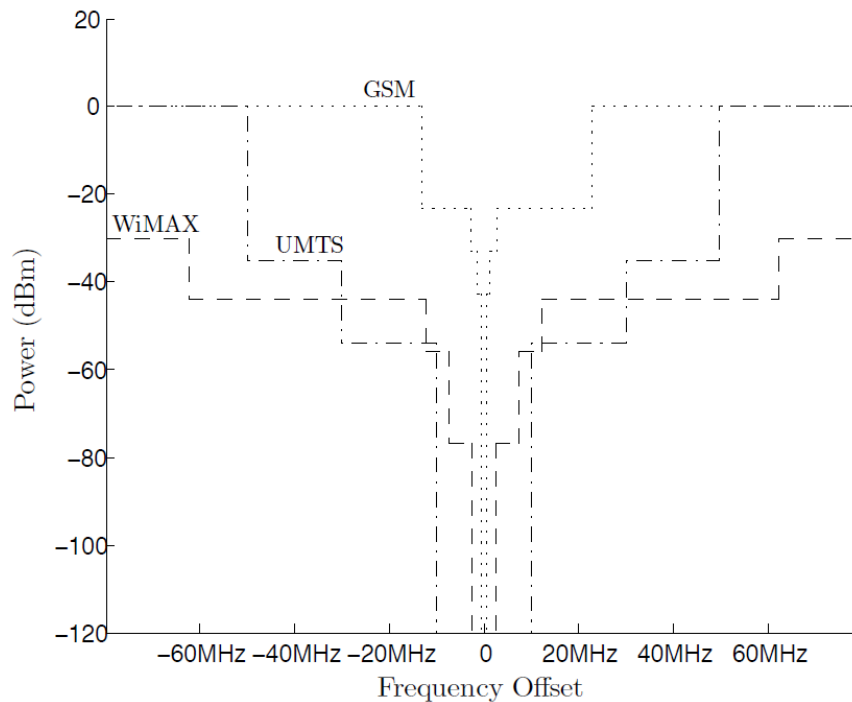


Fig. 2.6.a. Blocker masks for three different wireless standards

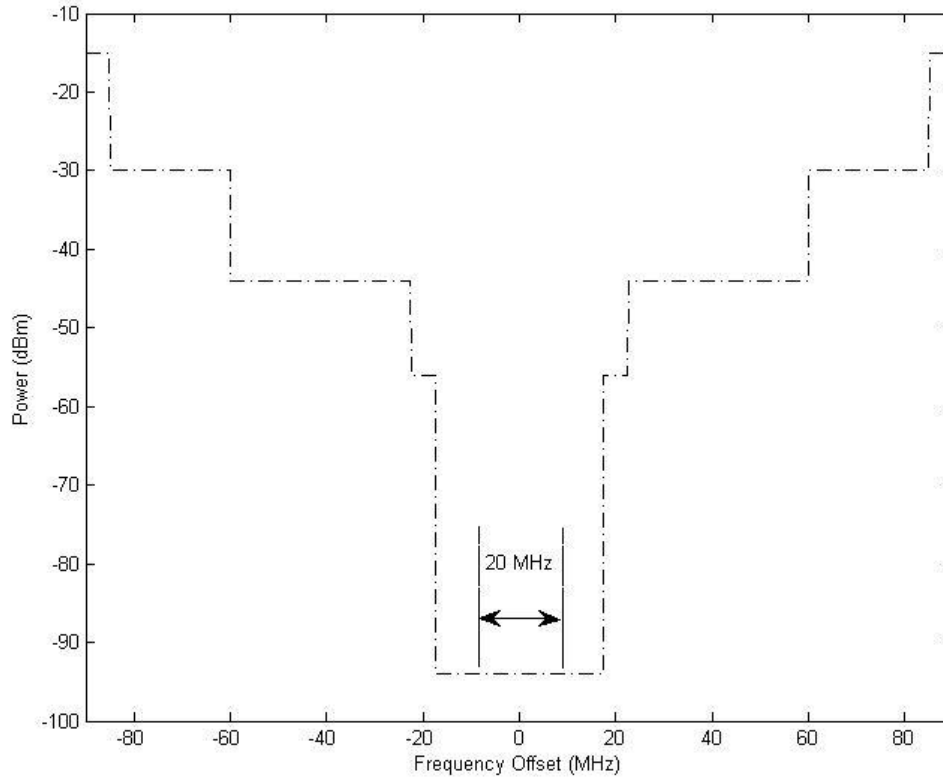


Fig. 2.6.b. Blocker masks for LTE with 20 MHz channel bandwidth

The three standards shown figure 2.6 have quite different range of requirements, which is why a reconfigurable RF receiver is so hard to implement. For instance, the GSM standard has the narrowest signal bandwidth of 200 KHz. However, it has some of the toughest blocker mask requirement among the three. In particular, a blocker which is 80 MHz away could be as high as +100 dB larger than the wanted signal. In absolute scale, it means the blocker can be  $10^5$  times larger than the desired signal. On the other hand, standards like WiMAX have much wider bandwidth to provide a higher throughput. Even though WiMAX mandates 20 MHz signal bandwidth, which is 100 times larger than GSM, its blocker mask requirement is much more relaxed compared to GSM. A reconfigurable RF receiver frontend will have to put up with different requirements demanded by the different standards.

Ever since the introduction of AMPS in 1983 in Chicago, there are more than a dozen different wireless standards introduced in the past thirty years as shown in figure 2.7. With each of them presenting unique requirements on the radio system design, it is impossible and unnecessary to design a flexible radio front-end to address the requirements for every one of them. Instead, this work is only going to focus on to address the needs for LTE Advanced only, since most likely the future wireless standards would face the same challenges that associate with LTE Advanced today.



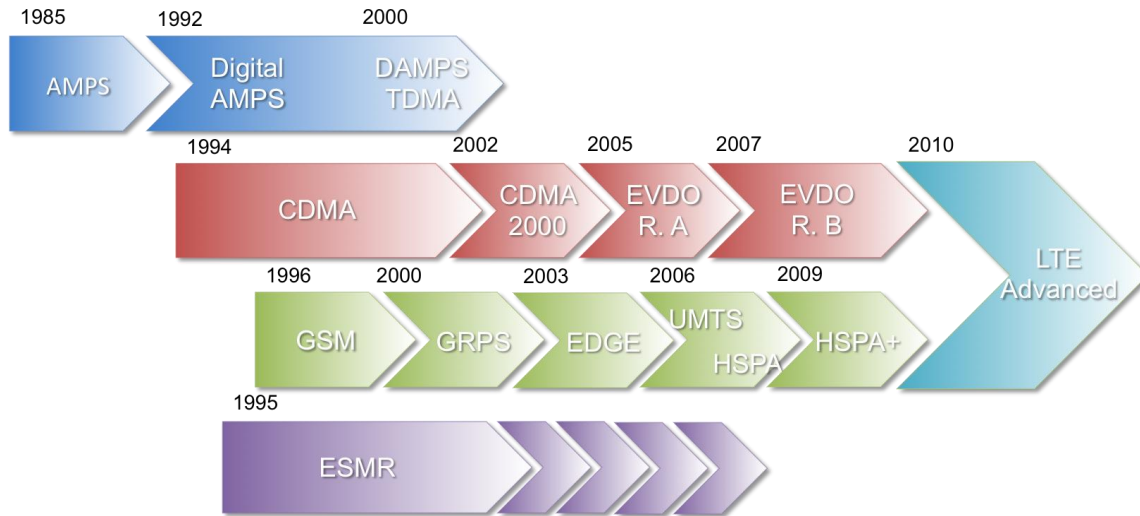


Fig. 2.7 Evolution of the wireless communication in the past thirty years.

LTE Advanced presented two major challenges to RF receiver design. The first one is its fragmented spectrum. Due to the history of spectrum allocation and political reasons, the availability of spectrum in different countries and regions is fragmented, which has a profound impact on the deployment of LTE internationally. The availability of spectrum for 4G varies widely from country to country and by region with some bands only available in particular countries as shown in figure 2.8. For example, the 700 MHz band, which is popular band in the U.S., is only going to be adopted by a handful of operators outside the America. The 1900 MHz band, on the other hand, would have confined usage only within in the U.S. and Argentina, while the 1500 MHz band would only be limited in Japan.

The spectrum fragmentation is not an issue in the past, since most of the older standards are confined to one or limited bands across the world. For instance, GSM is operating in three bands globally: 900 MHz, 1800 MHz (PCS) and 1900 MHz (DCS). Receiver designs that support LTE in different countries requires different hardware inside and outside of the chip, which makes it impossible to achieve an universal design for international LTE support.

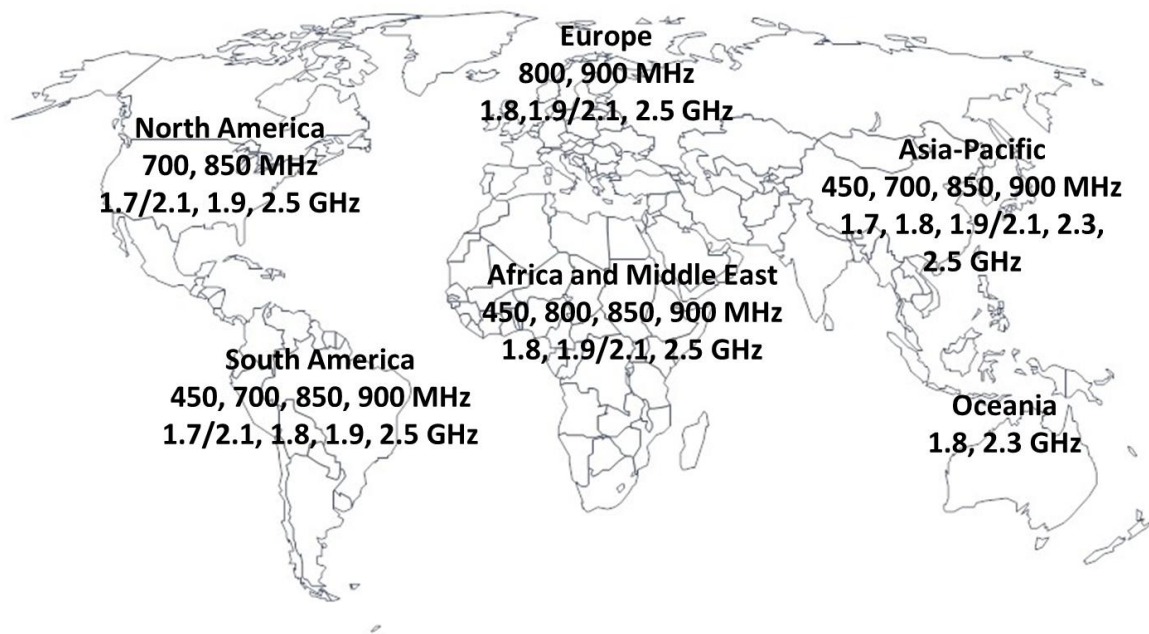


Fig. 2.8 LTE spectrum allocation across the world.

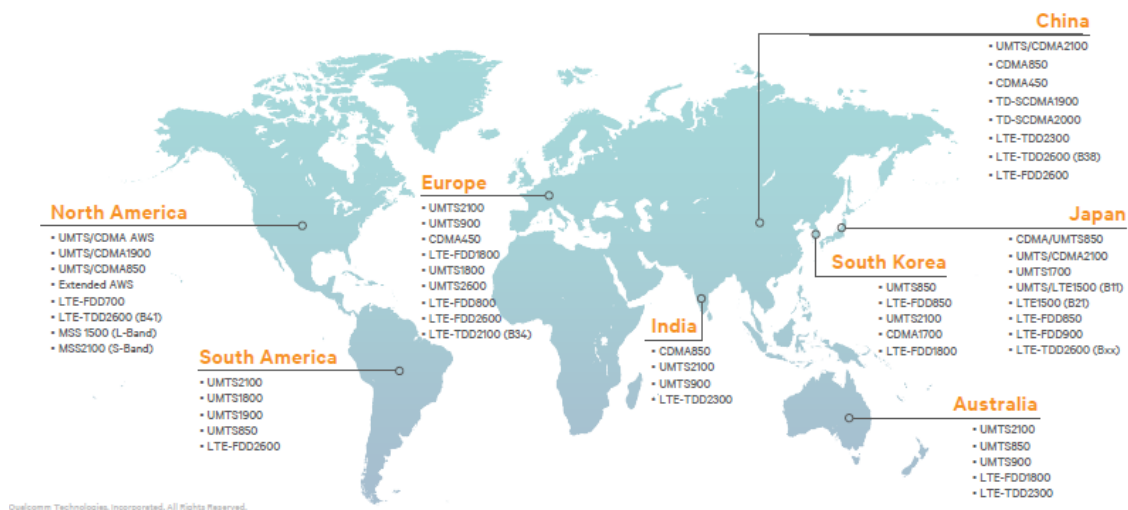


Fig. 2.9 Supporting LTE together with other existing wireless standards

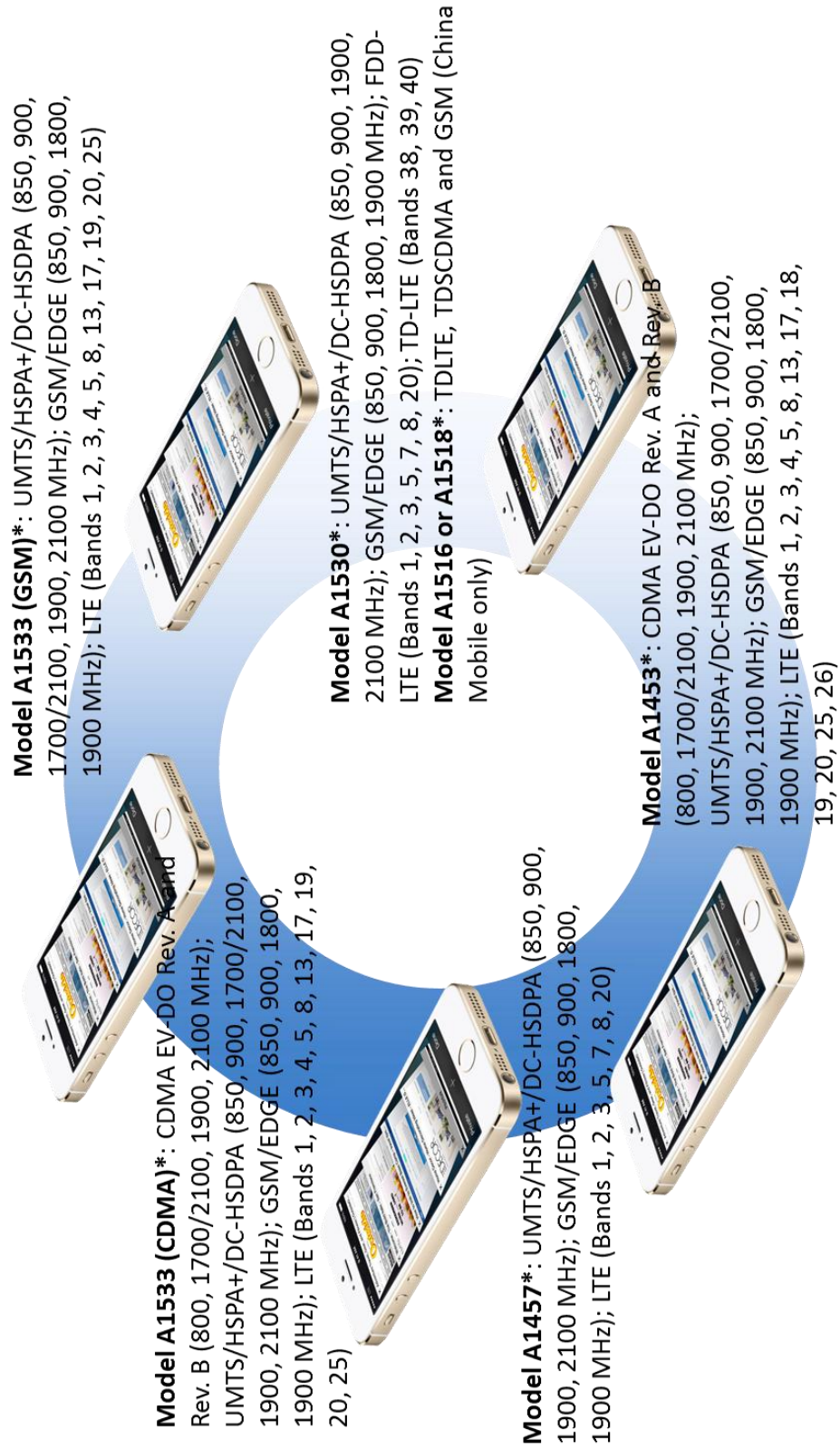


Fig. 2.10 Five different models of iPhone 5 for global support.

The problem gets even worse, when we consider the backward compatibility for legacy wireless standards. Figure 2.9 shows an example of what different wireless standards need to be supported for different part of the world. There are a total of over 40 different RF bands required. As the result, mobile device manufacturers are facing serious challenges in supporting LTE. The highly fragmented spectrum requirement makes it impossible for standardizing devices for a global market. Virtually all countries regulate their radio spectrum in a different way and large portions of the spectrum that could be aggregated for LTE are already in use for other devices or services. Therefore, given the technology limitation, one device for one dedicated region seems to be the cell-phone manufactures best strategy so far. For example, the iPhone 5 has five different models to provide the support for different regions and different carriers as shown in figure 2.10. For the reason given above, there are two models dedicated to the U.S. market alone to provide coverage for AT&T and Verizon Wireless.

LTE Advanced provides additional improvement in user data rates through carrier aggregation (CA). LTE Advanced can aggregate up to five carriers (up to 100 MHz bandwidth) to a single user and increase capacity for different applications as illustrated in figure 2.11. As a first step, the current LTE Advanced (Cat 4) can support the aggregation of two 10 MHz carriers, which allows a peak 150 Mbps data rate.

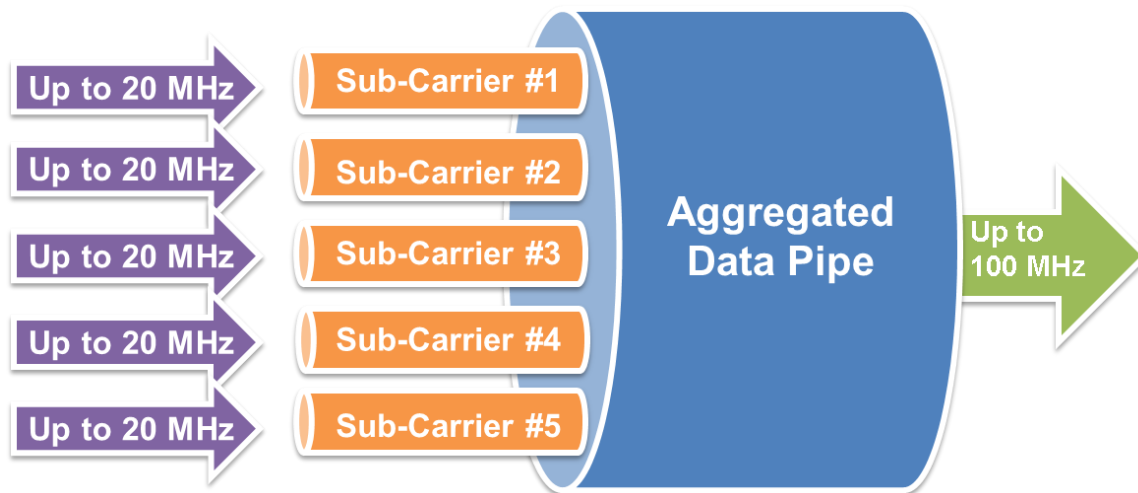


Fig. 2.11 Five sub-carrier carrier aggregation to generate a higher bandwidth.

At this time, the 3GPP alliance is aiming on to provide up-to-5 carrier aggregation with up to 100 MHz total bandwidth support to LTE in the future. They also aim to open up an unlicensed spectrum at 5 GHz band for further user data rate improvement, as shown in figure 2.12. Figure 2.13 summarizes the requirement for the modern mobile devices posed by the LTE Advanced, and figure 2.14 lists some of the supported carrier aggregation bands by a modern commercial design.

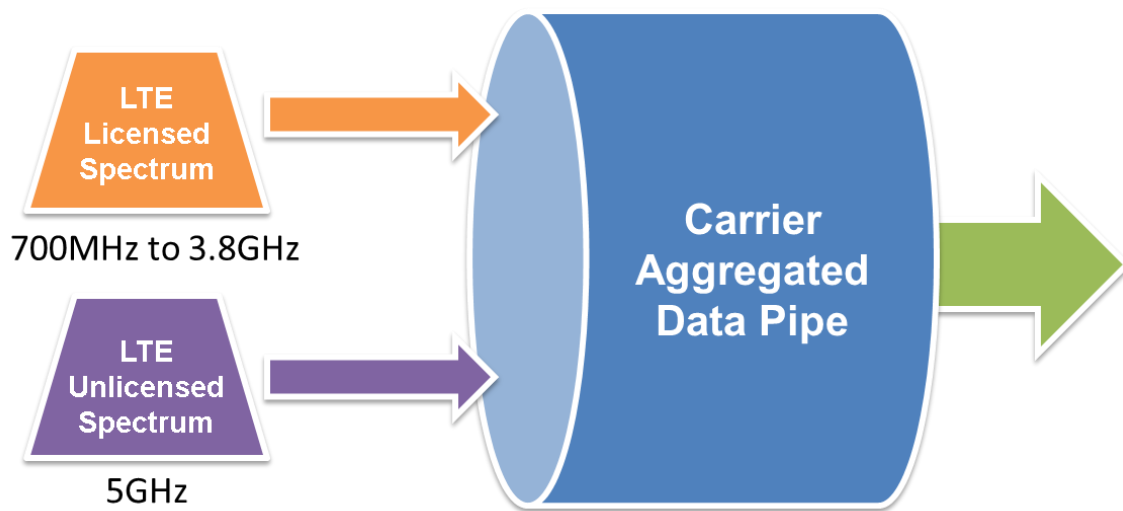


Fig. 2.12 LTE carrier aggregation between the licensed and unlicensed bands.

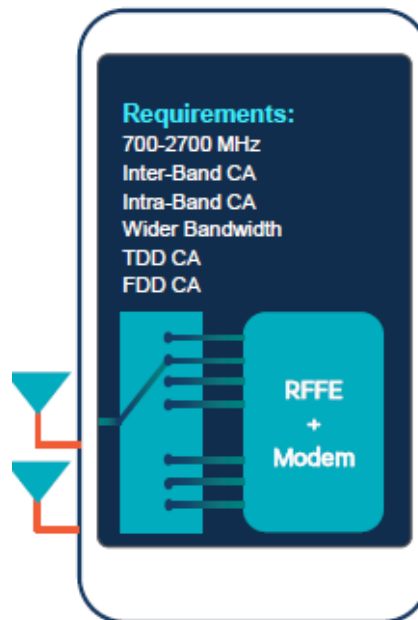


Fig. 2.13 System requirement for a device supporting LTE CA.

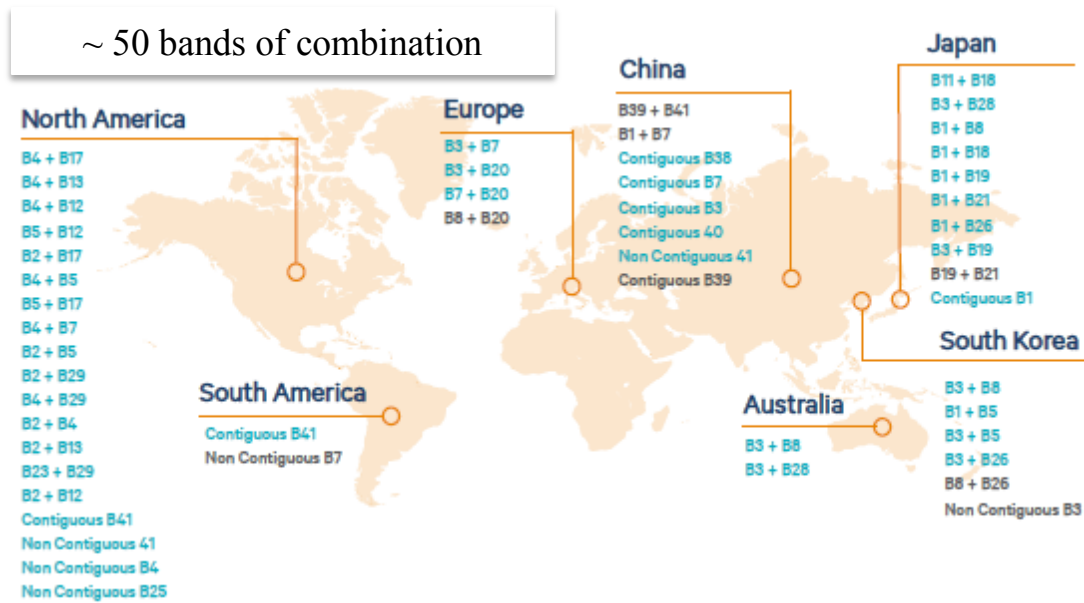


Fig. 2.14 Samples of the supported LTE CA channels from a commercial design.

Each aggregated carrier is often referred to as a component carrier (CC). The CC can have bandwidth varies from 1.4, 3, 5, 10, 15 and 20 MHz. Up to five of component carriers can be combined, the maximum resulting bandwidth can be provided is therefore 100 MHz. Carrier aggregation can be used in both the cases of FDD and TDD. As demonstrated in figure 2.14, there are three ways to arrange aggregations. The most straightforward way is to use carriers right next to each other from the same operating frequency spectrum. It is called intra-band contiguous carrier aggregation. However, this might not always be possible since the adjacent carriers might not be the available carrier that can be reallocated. Therefore, LTE-Advanced also requires support for non-contiguous aggregations, which provides the system with wider degree of freedom in combing different component carriers under different operator allocation scenarios. The non-contiguous carrier aggregations can be broken down in two cases: the intra-band non-contiguous case and the inter-band non-contiguous case. The difference between the above two cases are that the allocated component carriers are from the same operating frequency spectrum or from two separate frequency bands as detailed in figure 2.15.



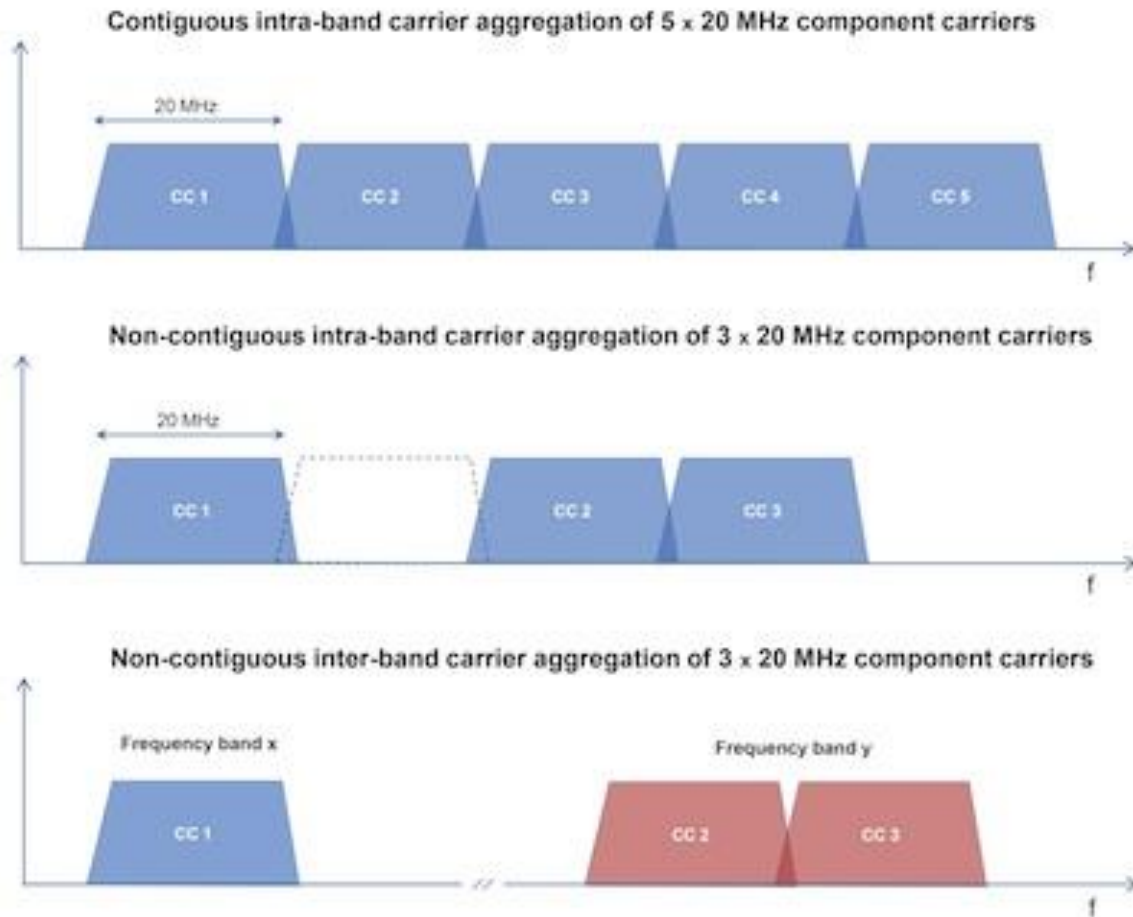


Fig. 2.15 Three different scenarios for carrier aggregations.

In earlier part in this section, we mentioned that there is another modern standard, 802.11.ac (or 5G Wi-Fi), based on a similar idea of the bandwidth reallocation scheme as the LTE Advanced. One example of channel bonding is shown in figure 2.16, where two 20 MHz channels are combined to form a 40 MHz channel to provide faster data throughput. Compared to the case of LTE Advanced, where each of the component carriers maintains its own spectrum mask, the channel bonding eliminates the original channels before combining and takes all the resulted spectrum to form a wider channel. From the spectrum perspective, channel bonding is more efficient, since it removes all physical frequency separation, such as guard bands between adjacent channels. However, it is not as flexible as the carrier aggregation in the LTE Advanced case, since it can only combine nearby channels, while LTE Advanced can even reallocate sub-carriers from different frequency bands for the same users. Also, 802.11.ac poses stringent requirement

on the physical hardware, since the channels can have different spectrum shape with various bandwidth, while LTE Advanced can work with the same physical layer since each component carrier doesn't change its spectrum identity with or without being allocated.

It should not be surprising that the future wireless standards would have to share many of the same design challenges such as LTE Advanced. The struggle between limited spectrum and the never-enough bandwidth demand will get worse as the remaining commercial spectrums become even more scarce over time. A reconfigurable receiver, therefore, would be highly preferable in the future. A reconfigurable frontend not only needs to be able to hop around different bands to support different standards, but more importantly, its flexibility should also be able to support the same standard such as LTE over its fragmented spectrums. In addition, compared to the conventional definition of the reconfigurable frontend, the new generation of SDR receiver also has to be able to reconfigure within the signal bandwidth to provide support for carrier aggregation or channel bonding.

This work is to explore novel architectures for the new generation of SDR receiver designs, which can be reconfigurable inside and outside of the signal bandwidth to address the needs and challenges presented by the future wireless standards.

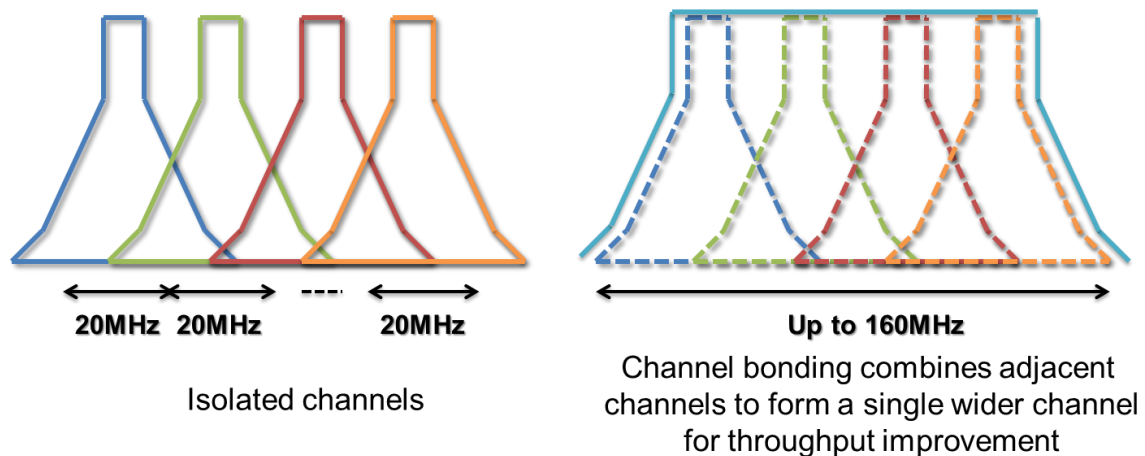


Fig. 2.16 Channel bonding for two 20 MHz channels.



## 2.5 Performance Comparison of Existing Designs

The major technology advancement in the past decade is the realization of a multi-standard multi-radio on a single monolithic die design, which was initially deemed as impossible due to signal isolation issues. At first, short-range standards, such as Wi-Fi and Bluetooth were integrated onto a single piece of silicon, for their more forgiving performance requirements. Today, single piece of system on chip (SoC) solutions can provide support for even the long-range cellular standards. The performance of state-of-art designs are summarized in table 2.1. The listed performance metrics such as noise figure, IIP2 and IIP3 reveals the trade-offs made to address the different requirements posed by different standards. For example, GPS receivers have lower noise figure since the signal level from the GPS satellites can potentially be lower than the thermal noise floor. On the other hand, wireless LAN solutions stress more on the bandwidth it can provide as the data rate is the most important metric. Furthermore, the reported performance in table 2.1 also highlights how technology is evolving over the past decade. Take GPS receiver designs for example. As the technology scaled from 90nm down to 40nm, the reported GPS designs manage to achieve more than 8 times power reduction, while maintaining the same noise figure performance. On the other side, WCDMA receivers also experience a factor of two power reduction. Another important improvement in the receiver designs which is not covered in the table 2.1 is the reduction of the external components. For instance, GSM is the standard known for its stringent spectrum mask requirement. Conventional GSM receivers require multiple stages of external SAW filters to meet the spectrum mask requirement. In the recent years, multiple works has reported GSM receivers required less external filtering and sometimes even no filtering at all, such as [106]. SAW-less GSM and WCDMA receiver systems can now be found in wide-range of cellular devices, which improves the form-factor of the mobile devices as well as makes the wireless technology more affordable.

Also, multiple receivers reported in table 2.1 can support more than one standard. For example, the EDGE standard is a standard built on top the GPRS to provide a better spectral efficiency. It operates on the same spectrum as the GPRS, but it requires a more linear frontend as the advanced modulation scheme it adopted. In this case, a receiver which can support EDGE will be able to meet the GPRS requirements with ease. Therefore, most of the EDGE receivers are back-ward compatible with GPRS as well. This is an enforcing statement that reconfigurable receiver is preferable, and its performance is also set by the standards with more stringent requirements.

	Year	Standard	Technology	Power (mW)	NF (dB)	IIP3 (dBm)	IIP2 (dBm)
[8]	2004	Bluetooth	0.13 $\mu$ m	60	-	-	-
[77]	2007	Bluetooth	0.13 $\mu$ m	48	-	-18	-
[104]	2010	Bluetooth	65nm	21	5	-	-
[111]	2012	Bluetooth	65nm	23	4	3	-
[2]	2005	802.11g	0.18 $\mu$ m	324	5.5	-	-
[78]	2006	802.11a/b/g	0.18 $\mu$ m	310	5.5	-	-
[79]	2006	802.11n	90nm	170	6	-	-
[80]	2007	802.11n	0.13 $\mu$ m	275	4.5	5	-
[81]	2008	802.11a/g/n	90nm	270	4	-	-
[104]	2010	WLAN	65nm	72	4.5	-	-
[116]	2011	802.11n	65nm	103	4	-	-
[111]	2012	WLAN	65nm	72	4	14	-
[112]	2013	WLAN	45nm	75	-	-	-
[117]	2014	802.11a/b/g/n/ac	40nm	320	3	-	-
[82]	2001	GSM	0.35 $\mu$ m	75	5	-16	-
[8]	2006	GSM/GPRS	90nm	84	2	-25	46
[83]	2005	GSM/GPRS	0.18 $\mu$ m	256	2.7	-15	40
[84]	2005	GPRS/EDGE	BiCMOS	202	3	-9	-
[85]	2008	GPRS/EDGE	0.13 $\mu$ m	140	2.5	-12	45
[102]	2010	EDGE	0.13 $\mu$ m	70	2.9	-0.5	55
[106]	2011	GSM/GPRS/EDGE	65nm	75	2.7	0	50
[86]	2005	CDMA	BiCMOS	151	3	-	-
[87]	2006	WCDMA	BiCMOS	50	9	0	55
[88]	2008	WCDMA	0.18 $\mu$ m	105	2.8	-2	65
[101]	2010	WCDMA/HSPA	0.13 $\mu$ m	60	2.5	-5	55
[110]	2011	WCDMA/GSM	65nm	50	2.4	-3	50
[89]	2007	CDMA2000	0.13 $\mu$ m	150	9.2	1	51
[90]	2007	TD-SCDMA	BiCMOS	95	3.5	-14	25
[118]	2014	TD-SCDMA	40nm	30	1.7/2.4	0.4	55
[91]	2005	GPS	90nm	84	2	5	-
[92]	2006	GPS	BiCMOS	20	5	-	-
[103]	2010	GPS	65nm	23	2.3	-	-
[109]	2011	GPS	45nm	12	2.7	1.5	60
[111]	2012	GPS	65nm	6.5	2	-5	-
[113]	2013	GPS	40nm	10	2.1	-	-
[105]	2010	Wi-MAX	65nm	126	3.8	-7	-
[71]	2013	LTE-Advanced	65nm	155	4.5	2.4	58

Table 2.1 RF receiver performance summary

Multi-mode and multi-standard receivers are more capable than just to provide backward compatibility for older standards. From the late 80s, very large system integration (VLSI) is always the driving force of the silicon industry. There is always the desire to expend success of VLSI from the digital domain into the RF field to achieve a better cost reduction in the RF designs. Integration of multi-radio on a single die, however, was deemed impossible initially, since it is challenging to provide enough isolation for different radio systems on single piece of silicon so that each radio system can maintain its functionality. Fortunately, it has been demonstrated that with careful layout planning and novel design techniques, multi-radio on single die design is achievable. Table 2.2 shows a list of multi-mode radios that have been published in the literature.

Table 2.2 reveals the development progress of the integration of multi-mode radio in the past decade. Initially, only standards with less stringent performance requirement, such as GPS, Bluetooth, and FM, are integrated into a single chip. Today, single-chip commercial solutions can easily long-range cellular standards, such as WCDMA and GSM, and support for GPS at the same time.

Table 2.2 also highlights the improvement in the number of frequency bands can be supported by a single chip solution. At first, receiver design is frequency band specific. The design is highly optimized for one standard and one band only. Later on, the receivers are more flexible to provide multi-band support for one standard. Nowadays, a WCDMA receiver can support more than 10 different bands. This again underlines the importance of a reconfigurable receiver design. Due to spectrum scarcity, future standards might have an even more fragmented spectrum than LTE, a reconfigurable receiver design can greatly reduce the design overhead, and consequently achieve cost-effective solution.

Entry		Supported Standards	Frequency Bands
[93]	Broadcom BCM 2075	Bluetooth (EDR)	1
		GPS	1
		FM	1
[94]	Broadcom BCM 4329	802.11n	2
		Bluetooth (EDR)	1
		FM	1
[104]	Broadcom BCM (2010)	802.11a/b/g/n	2
		Bluetooth (EDR)	1
		FM	1
[95]	Marvell (2009)	802.11	1
		WiMAX	1
[117]	Marvell (2014)	3-stream 802.11a/b/g/n/ac	6
		MIMO	
[96]	Freescale	WCDMA/HSDPA	10
		GSM/GPRS/EDGE	4
[97]	TI	GSM/GPRS/EDGE	3
		CDMA2000	1
[112]	TI (2013)	802.11n 2X2 b/g-band	2
		802.11n 2X2 a-band	1
[98]	Skyworks	WCDMA/HSDPA/HSUPA	11
		GSM/GPRS/EDGE	4
[99]	Qualcomm (2009)	WCDMA/HSDPA/HSUPA	10
		GSM/GPRS/EDGE	4
		GPS	1
[108]	Qualcomm (2011)	WCDMA/HSDPA/HSUPA	8
		GSM/GPRS/EDGE	4
		GPS	1
[116]	Atheros (2011)	3 Stream 802.11n MIMO	6
[107]	ST-Ericsson (2011)	WCDMA	9
		EDGE	4
[111]	MediaTek (2012)	WiFi a/b/g/n	-
		Bluetooth	-
		FM	-
		GPS	-
[118]	MediaTek (2014)	2G/3G TD-SCDMA	7
[71]	Ericsson (2013)	LTE Advanced	2
		with up to 3 carrier aggregations	

Table 2.2. A summary for modern multi-mode multi-radio designs.

## 2.5.1 Software-Defined Radio Implementation

Last but not the least, there are also a number of demonstrations of software-defined radio implementations reported in the literature, such as [102][27][66]. All the designs have flexible forward signal paths that can be reconfigured in different ways. All of the designs employ a single-down-conversion architecture followed by a series of baseband filters where the filters' corner frequencies can be adjusted to support different modulation scheme used by the different standards.

# Chapter 3

## $\Delta\Sigma$ Receiver System Architecture

### 3.1. Introduction

Continued evolution of wideband wireless communications drives the need for flexible receivers capable of multi-mode, multi-standard operation [27][28]. A universal 4G-LTE device, for example, is anticipated to operate from 450 MHz to 3800 MHz with varying bandwidths. A downconverting analog-to-digital converter (ADC) is an architecture capable of such operation [29][30]. By embedding the mixer inside the feedback loop, a highly linear design is achievable. By utilizing a low-noise transconductance amplifier (LNTA) in front of the ADC, this architecture can perform a low noise direct RF-to-digital conversion. The center frequency is tuned by an external oscillator, and the bandwidth is set by the decimation filter. With large dynamic range, this architecture enables the ADC to migrate closer to the antenna, enabling many signal conditioning features to be implemented in the digital domain, thus benefiting from technology scaling.

While the direct-conversion architecture is still prevalent in commercial mobile handsets, significant research effort has been shifted towards novel schemes that employ bandpass or downconverting ADCs. Previous implementations of downconverting receivers with switched-capacitor loop filters have demonstrated wide-tuning range or high dynamic range, but not both [29][30]. In general, the dynamic range has been limited by the clock jitter injected at high frequencies from the feedback digital-to-analog converter (DAC). Jitter directly degrades the SNDR of the receiver, since it cannot be distinguished from input noise. A non-return-to-zero (NRZ) signal waveform helps reduce the jitter sensitivity by reducing the transitions, while a multi-level DAC improves the jitter immunity by reducing the transition steps. However, both techniques are challenging to implement at high frequencies. This thesis demonstrates a system that achieves a high dynamic range together with a wide-tuning range, enabled by the implementation of a four-level NRZ DAC. The overall system linearity is further enhanced by a highly-linear class-AB LNTA.

This chapter is organized as follows. Section 3.2 discusses various architecture design tradeoffs in order to motivate the choices made in this design. Section 3.3 presents

circuit implementation details, and Section 3.4 presents measurement results. The chapter is concluded in Section 3.5.

## 3.2 Receiver Architecture

In the following discussion, various system architectures are evaluated and compared, and the impact of clock jitter is studied and analyzed. In addition, a behavioral model of a current-mode integration sampler (CMIS) mixer is derived. Finally, an architecture capable of addressing the desired specifications is proposed.

### 3.2.1 System Level Design

To meet the requirements of software-defined radio (SDR) applications, an ADC has to meet two major challenges. The first is that its dynamic range has to be large enough to process the input signal together with the blockers. The other is that it needs to downconvert the input signal from the carrier frequency to baseband. A bandpass  $\Delta\Sigma$  ADC Fig. 1 is seemingly an ideal candidate for this application. However its design requires resonators with high quality factors, which are difficult to realize in CMOS technology. Passive resonator designs offer higher Q, but come with a large area overhead and limited tuning range. On the other hand, active resonators are tunable but suffer from limited quality factors. In addition, active designs lead to large power overhead and limit the system's linearity.

An alternative design of a bandpass  $\Delta\Sigma$  system is proposed in [32]. By summing the feedback signals from the two interleaved channels, it forms a bandpass feedback structure as illustrated in Fig. 2(a). Taking advantage the idea of current mode integration sampling which would be elaborated later, the sampler in Fig. 3.2(a) can be transformed into a mixer and be moved inside of the  $\Delta\Sigma$  loop as in Fig. 3.2(b). The bandpass feedback suppresses the swing at the RF nodes, and enhances the linearity of both the LNTA as well as the baseband  $\Delta\Sigma$  ADCs). The two channels of the  $\Delta\Sigma$  ADCs also serve to oversample the input data by a factor of two, thus providing a 3dB SNR improvement.

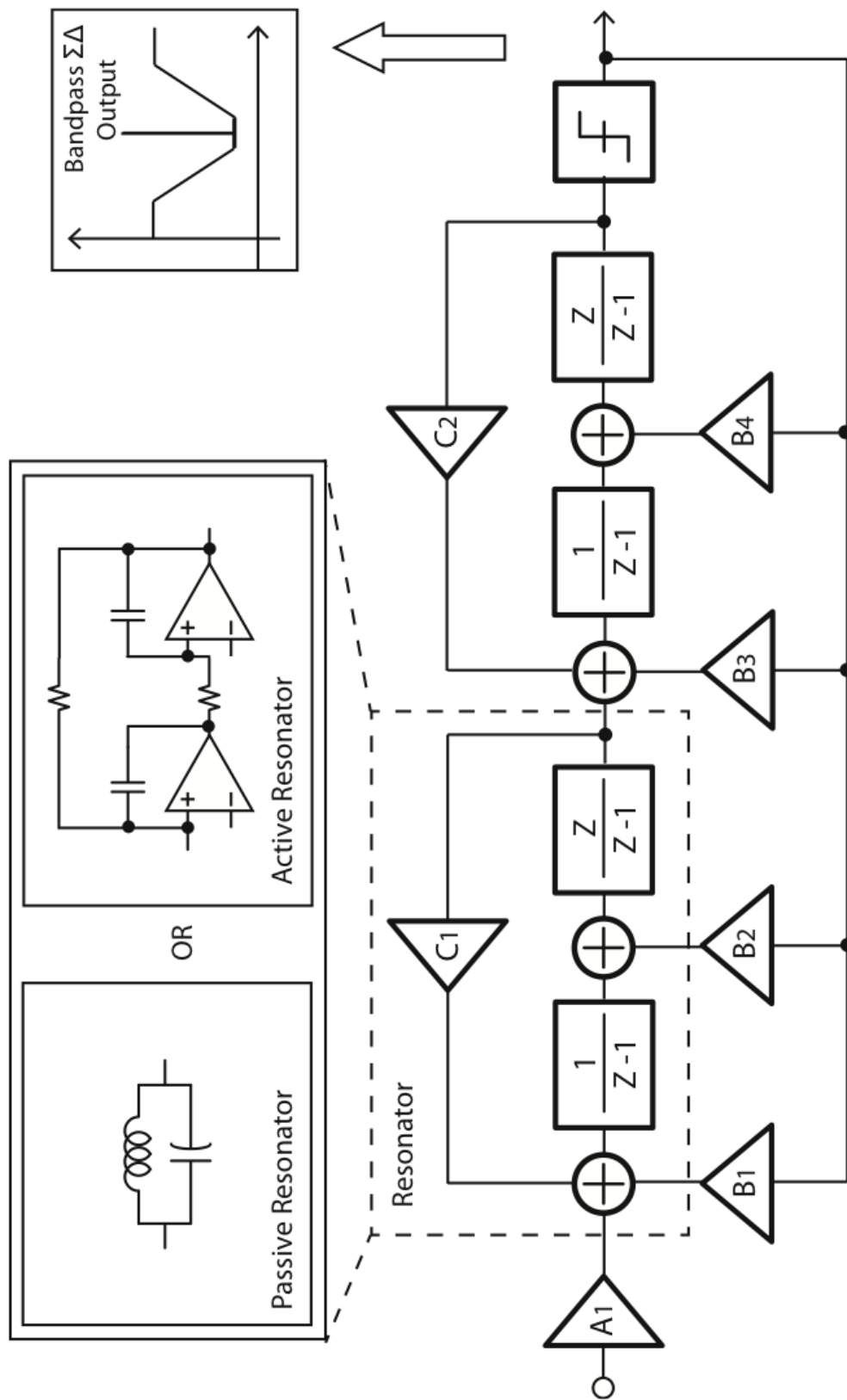


Fig. 3.1. Band-pass  $\Delta\Sigma$  modulator loop filter in Z transform.



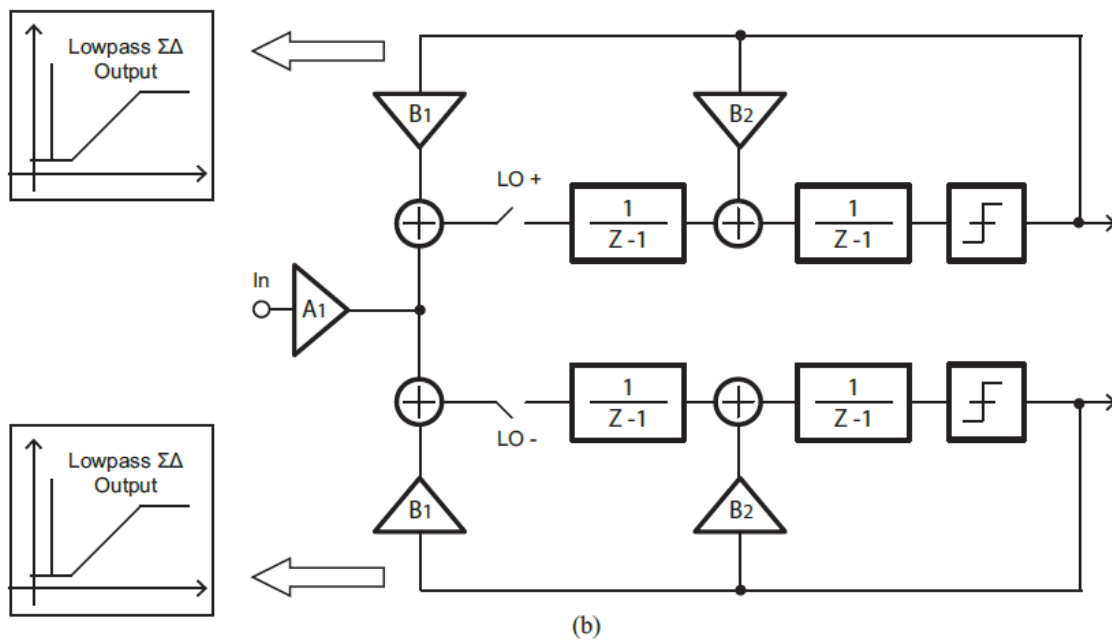
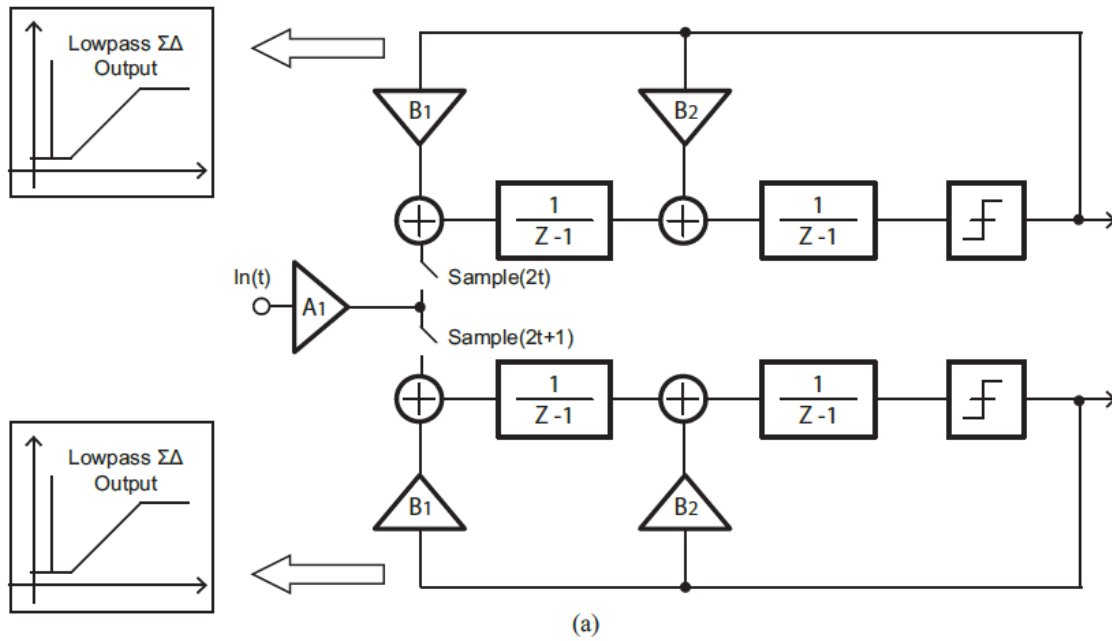


Fig. 3.2. Bandpass feedback created with two  $\Delta\Sigma$  modulators.

### 3.2.2 Loop Filter Structure

There are numerous  $\Delta\Sigma$  loop filter structures reported in the literature [33][7]. As shown in Fig. 3.3 a second order all feedback cascaded integrators with distributed feedback (CIFB) structure is chosen for this design because of concerns for stability and peaking in signal transfer function (STF). The STF and noise transfer function (NTF) of the chosen loop structure is shown in Fig. 3.4. The STF is ensured to be maximally flat for the entire band to maintain better wide-band blocker resilience. The NTF takes advantage of the large over-sampling ratio (OSR) between the baseband bandwidth of the wireless standards and the much higher carrier frequencies to provide the aforementioned large dynamic range desired.

1) *Loop Stability*: A major tradeoff in  $\Delta\Sigma$  ADC design is the one between loop stability and the aggressiveness of the noise shaping. As demonstrated in [33], by optimizing complex poles and zeroes, a more aggressive NTF can be achieved without raising the order of the loop filter or increasing the OSR, as shown in Fig 3.5.

For ADC designs which are only targeted for a fixed sampling frequency, their loop stability can be well compensated with additional tuning range in the feedback and feedforward factors [34][35]. However, for SDR applications, the desired frequency of operation can spread over a decade, which results complex loop structures such as CRFB (chain of resonators with weighted feedforward summation) or CIFF (chain of integrators with feedforward summation and local resonator feedback), far less appealing.

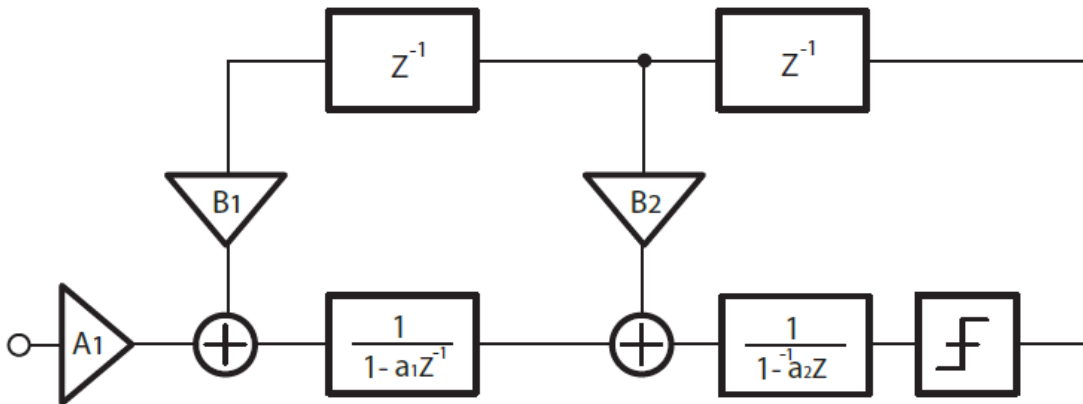


Fig. 3.3. A second order CIFB  $\Delta\Sigma$  loop filter.

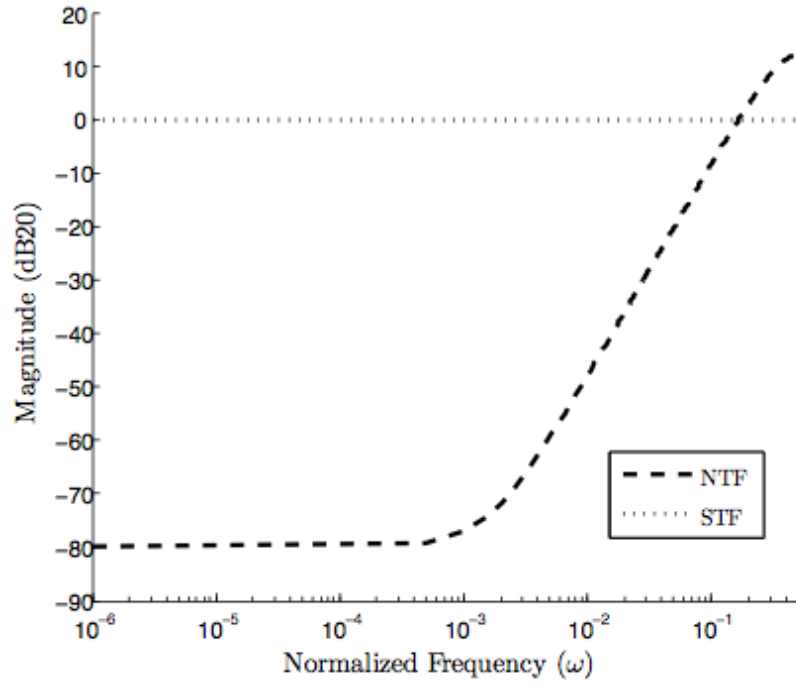


Fig. 3.4. Signal and noise transfer functions of a second-order modulator.

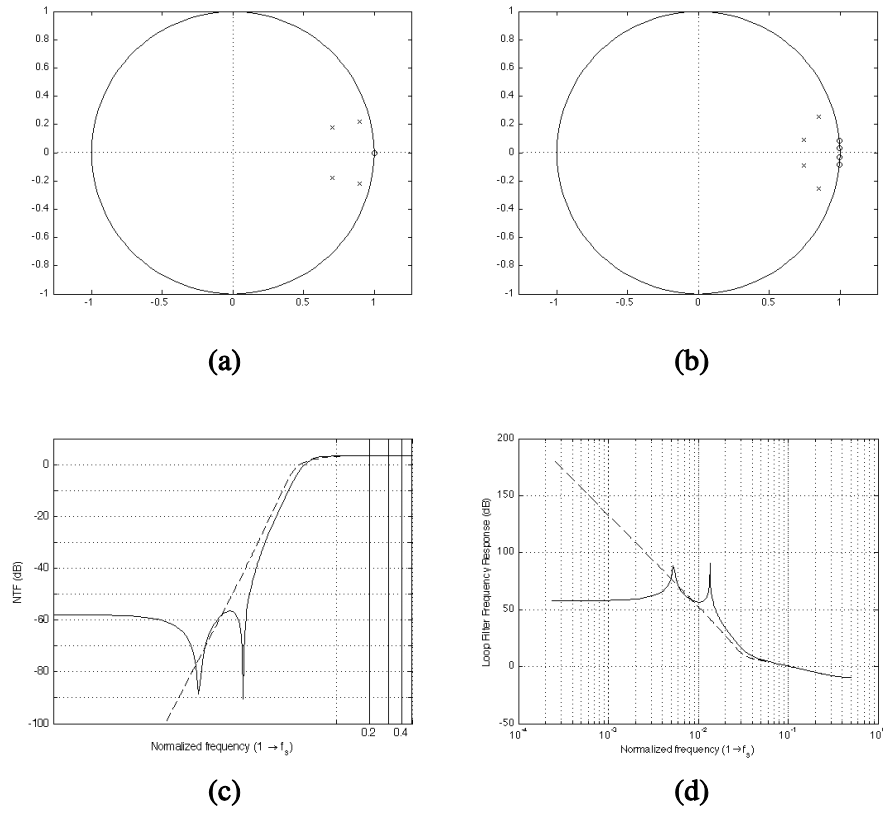


Fig. 3.5. Simulation results with complex zeros.

2) *Peaking in STF*: Another challenge for the RF  $\Delta\Sigma$  design is the flatness of the STF. As summarized in [33],  $\Delta\Sigma$  loop filter architectures can be summarized as: CIFB, CIFF, CRFB and CRFF (chain of resonators with weighted feedforward summation and local resonator feedback). CIFF and CRFF are popular choices in  $\Delta\Sigma$  ADC design because a smaller number of feedback DACs are required; these DACs are often the bottlenecks in the designs. However, a major drawback for CIFF or CRFF design is ripple in the STF. Without a loss of generality, from the simple loop shown in Fig. 3.6, it can be shown as:

$$NTF(z) = \frac{1}{1 + L(z)} \quad (9)$$

$$STF(z) = \frac{L(z)}{1 + L(z)} \quad (10)$$

$$L(z) = \frac{1}{NTF(z)} - 1 \quad (11)$$

$$STF(z) = NTF(z)L(z) \quad (12)$$

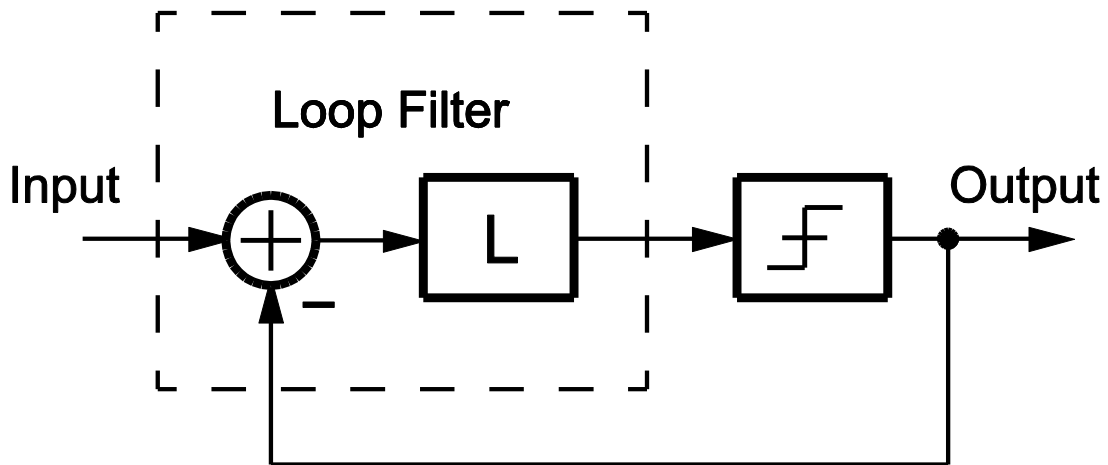


Fig. 3.6. A simplified  $\Delta\Sigma$  loop filter.

From the equations (11) and (12), poles in  $NTF(z)$  become zero(es) in  $L(z)$ , and hence show up as zero(es) in  $STF(z)$ . This in turn results in peaking in the STF. One graphical example for CIFF architecture is shown in Fig. 3.7.

In some applications such as audio CODEC out-of-band STF peaking can be tolerated due to the frontend anti-aliasing filters or microphone wind filters. However, in SDR applications, peaking in the STF degrades the receiver's out-of-band interference resilience. Due to the absence of any front-end filtering, interference that coincides with the STF peaks would be "amplified" and hence desensitize the receiver. In the worst case scenario, it might exceed the ADC's full scale range, causing the  $\Delta\Sigma$  ADC to clip.

Recent  $\Delta\Sigma$  ADCs [31][34][36] have reported loop architectures with a FIR-feedback-DAC design. Embedding an FIR filter into the DAC is a low-power technique that effectively alleviates the jitter sensitivity of a high-speed  $\Delta\Sigma$  system, which is a major factor limiting the dynamic range. However, loop filters with an FIR DAC result in large out-of-band peaking in the STF, which makes this technique unsuitable for SDR applications. For a FIR filter  $F(z)$

$$NTF(z) = \frac{1}{1 + F(z)G(z)} \quad (13)$$

$$STF(z) = \frac{G(z)}{1 + F(z)G(z)} \quad (14)$$

where  $G(z)$  is the loop filter of the  $\Delta\Sigma$  system as shown in Fig. 3.6. Then for the FIR filter in the DAC

$$F(z) = \sum_{i=0}^n a_i z^{-i} = \frac{\sum_{i=0}^n a_i z^{n-i}}{z^n} \quad (15)$$

where  $a$  is the weighting factors for the taps in the FIR DAC. Most of the FIR DAC based designs have small number of taps such as 4 to 8 taps ([31][34][37]), therefore the equation (14) is quite manageable. In the frequency range where  $F(z)G(z) \gg 1$ , (5) reduces to  $NTF(z) \approx 0$ , and (14) yields

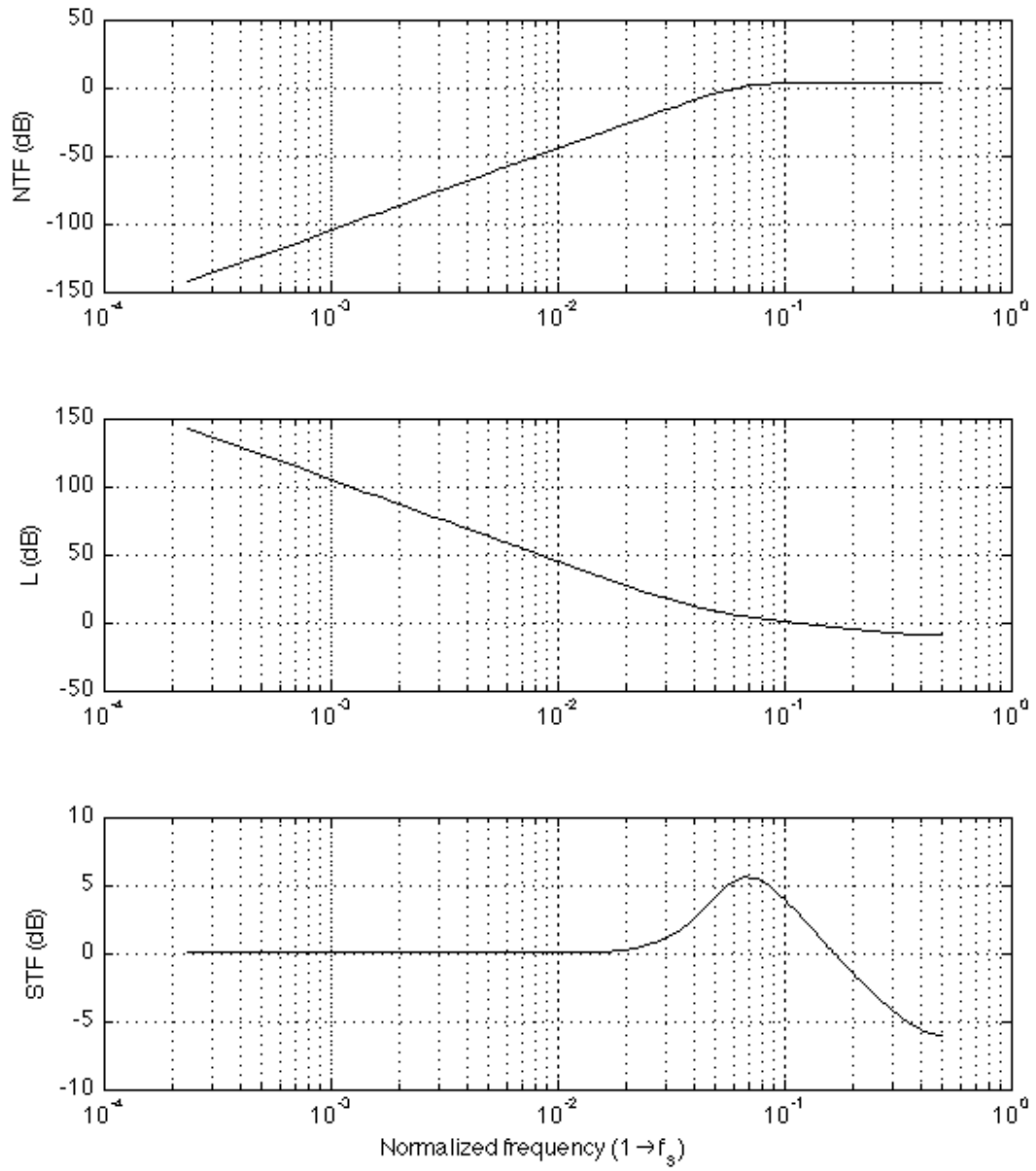


Fig. 3.7. Signal transfer function peaking in CIFF architecture.

$$STF(z) \approx \frac{1}{F(z)} \quad (16)$$

In general,  $F(z)G(z) \gg 1$  at low frequency, since  $NTF(z)$  should filter out most of the quantization noise at the low frequency. On the other hand, STF would be flat if  $F(z)$  is just a short. Or by (14), then

$$STF(z) = \frac{z^n}{\sum_{i=0}^n a_i z^{n-i}} \quad (17)$$

Since  $F(z)$  is a FIR function, it has nulls at different frequencies. By (17), these nulls results in peaking in the STF. The actual height of such peaks relates to the loop structure as well as the number of taps in the FIR filter. In [34][36], peaking levels higher than 10 dB have been reported with 4-tap and 8-tap.

The STF and NTF of the chosen second-order all feedback CIFB structure is shown in Fig. 3.3. The STF is flat for the entire bandwidth to ensure better blocker resilience.

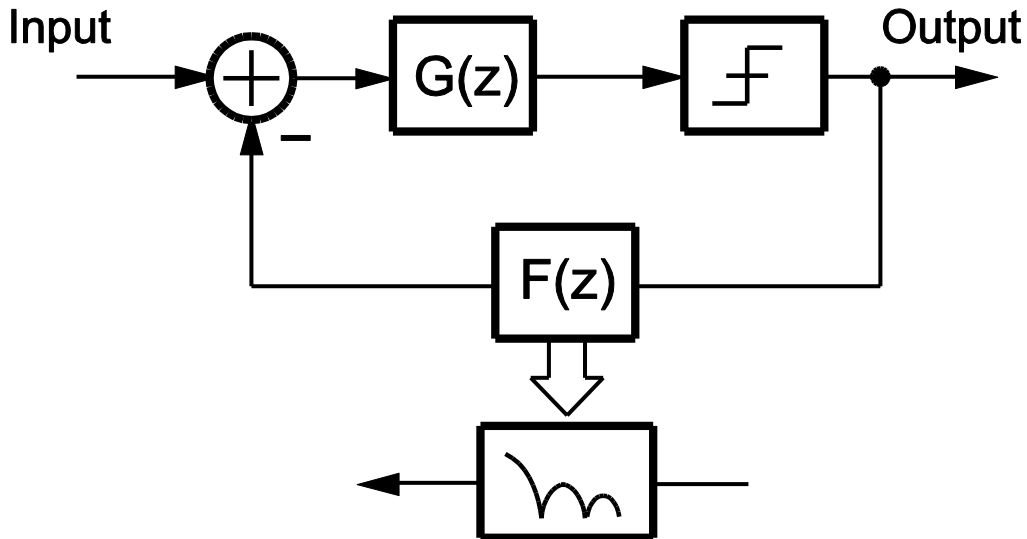


Fig. 3.8. A simplified  $\Delta\Sigma$  loop model for FIR DAC.

### 3.2.3. Jitter Sensitivity

Clock jitter is a major performance limiting factor for any high speed ADC design. It has been reported in [38] that clock jitter perturbs the amount of the charge from the feedback DAC and degrades the in-band SNR, but the actual mechanism as to how clock jitter compromises the high speed in-band performance has not been analyzed in detail.

One widely held belief is that the side skirt of the phase noise of the source clock is the cause of the SNR degradation for high-speed  $\Delta\Sigma$  ADC, since it reciprocal downconverts the quantization noise which previously has been pushed to a higher frequencies due to the noise-shaping feature of a  $\Delta\Sigma$  modulator. A simplified loop model with the effect of phase noise can be built as shown in Fig. 3.9. Fig. 3.10 shows the simulated added noise from an approximated phase noise spectrum with noise-shaped output spectrum from a second-order  $\Delta\Sigma$  modulator. This approximated phase noise profile results a 1 ps rms clock jitter. The added noise, which is shown as the dashed line in Fig. 3.10, is at least 20 dB below the in-band noise floor, which suggests that the impact of 1 ps rms jitter should have minor effect on the overall noise performance, which is clearly contradicting reported results in the literature.

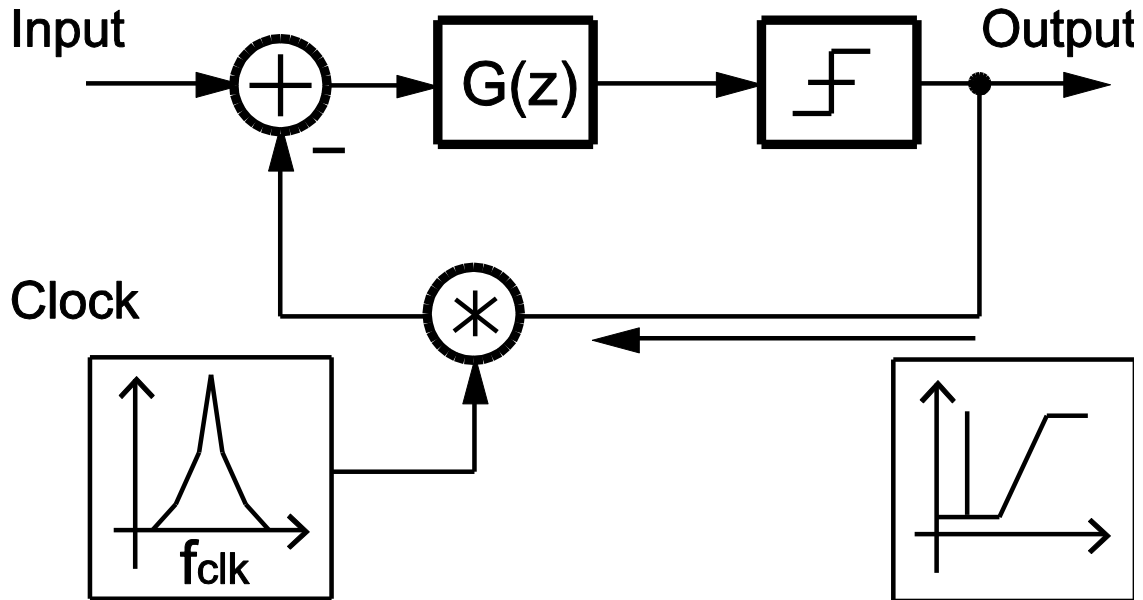


Fig. 3.9. A simplified  $\Delta\Sigma$  loop model with phase noise.



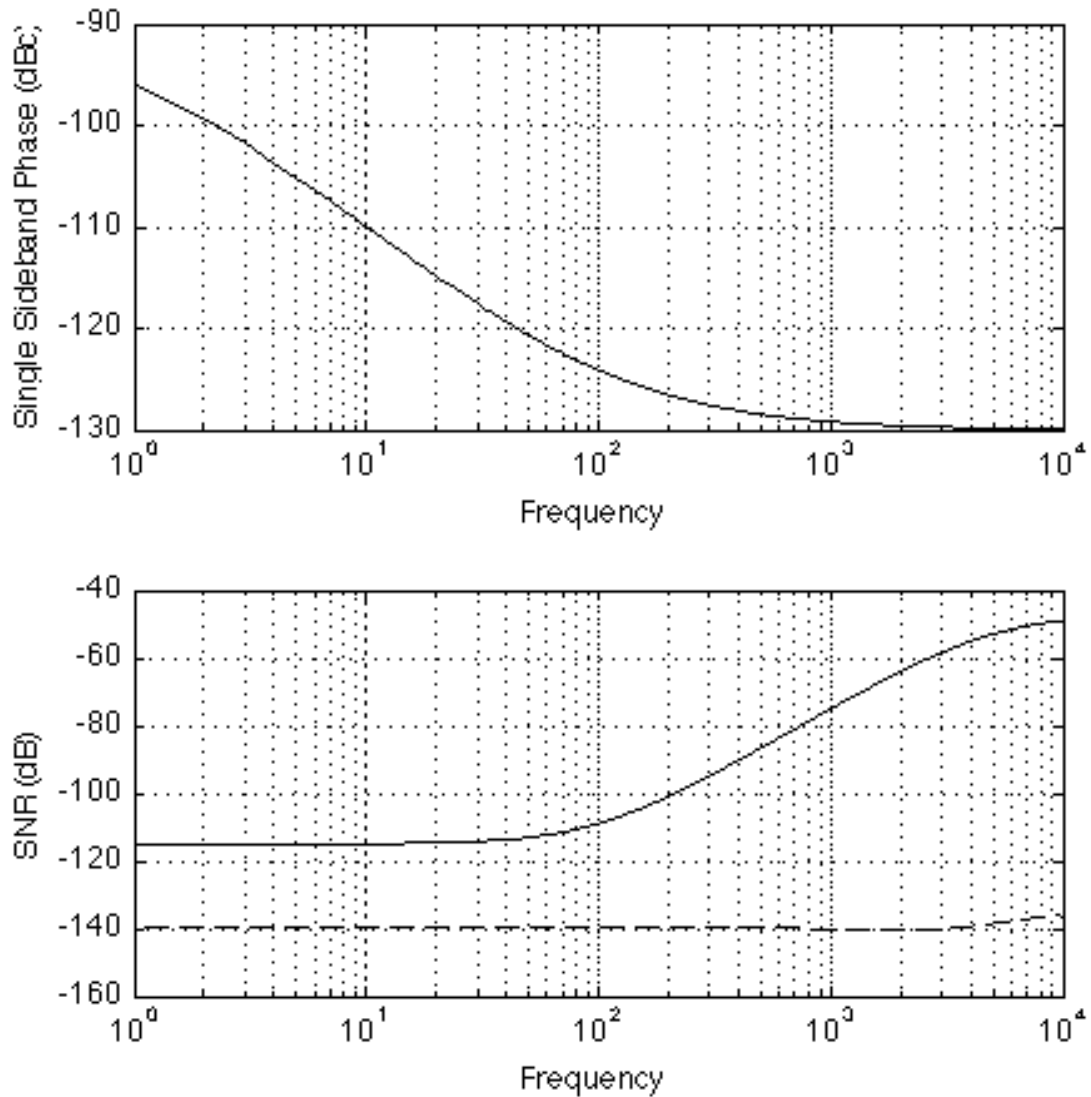


Fig. 3.10. Simulated output spectrum with phase noise model.

The physical origin of the jitter sensitivity of high-speed systems is the nonlinear nature of the loop. A  $\Delta\Sigma$  modulator can provide a dynamic range far exceeding the limit of its low-resolution quantizer. In the time domain, the  $\Delta\Sigma$ 's output is a pulse-density-modulated (PDM) bit sequence as shown in Fig. 3.11. The PDM nature of the bit sequence provides an additional dimension to encode data, so a  $\Delta\Sigma$  ADC's dynamic range is not limited by its quantizer. When lower resolution is designated for the quantizer, the modulator has to modulate the output density more aggressively to maintain the same dynamic range compared to the case when the quantizer has higher resolution. This result is more frequent switching between different levels in the output sequence.

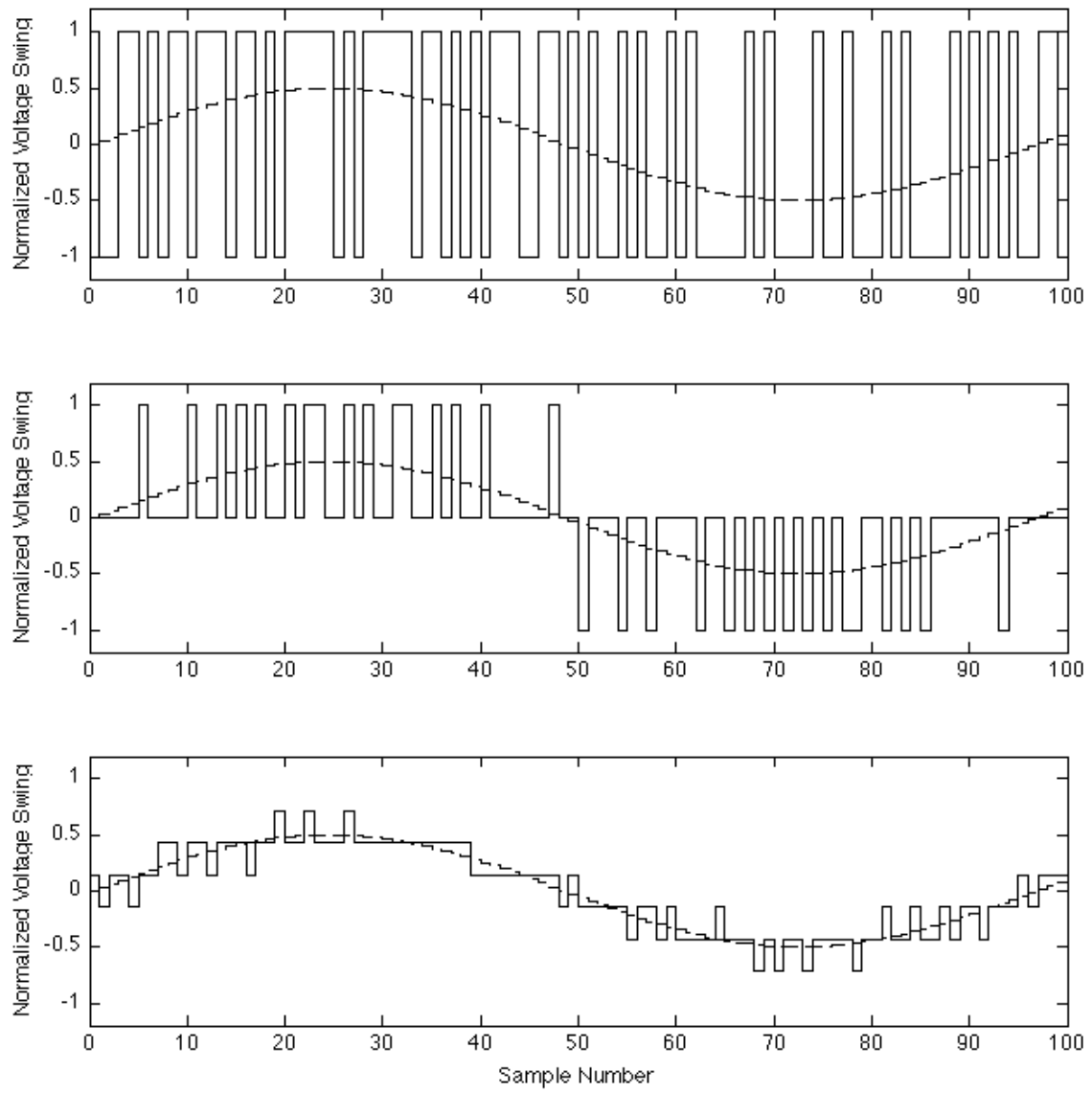


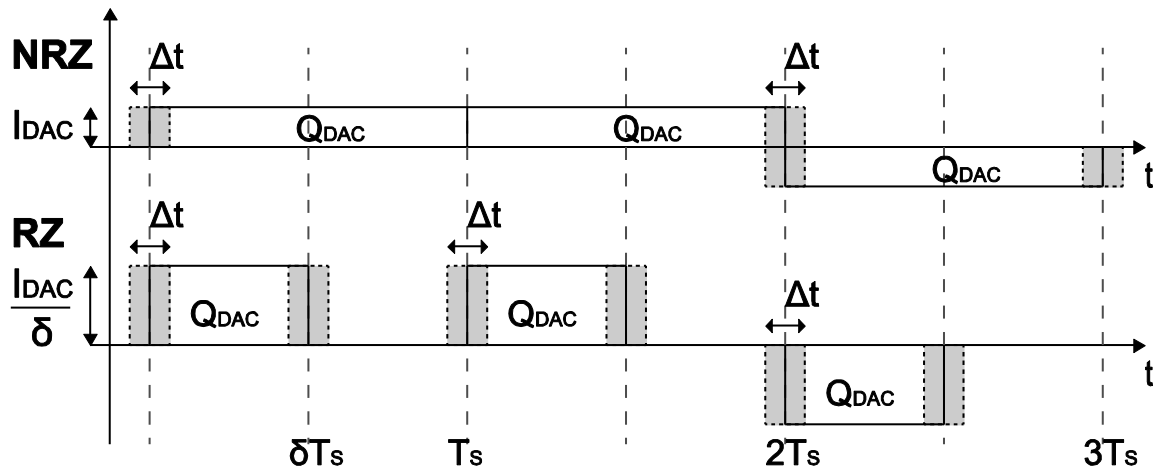
Fig. 3.11. Time domain output waveform for  $\Delta\Sigma$  ADCs with different quantizer levels.

Clock jitter introduces noise every time there is a switching event in the output sequence. The more frequently the output switches, the more noise would be added, then the in-band SNR suffers. Therefore, a quantizer with higher resolution is preferred for high-speed  $\Delta\Sigma$  modulator designs.

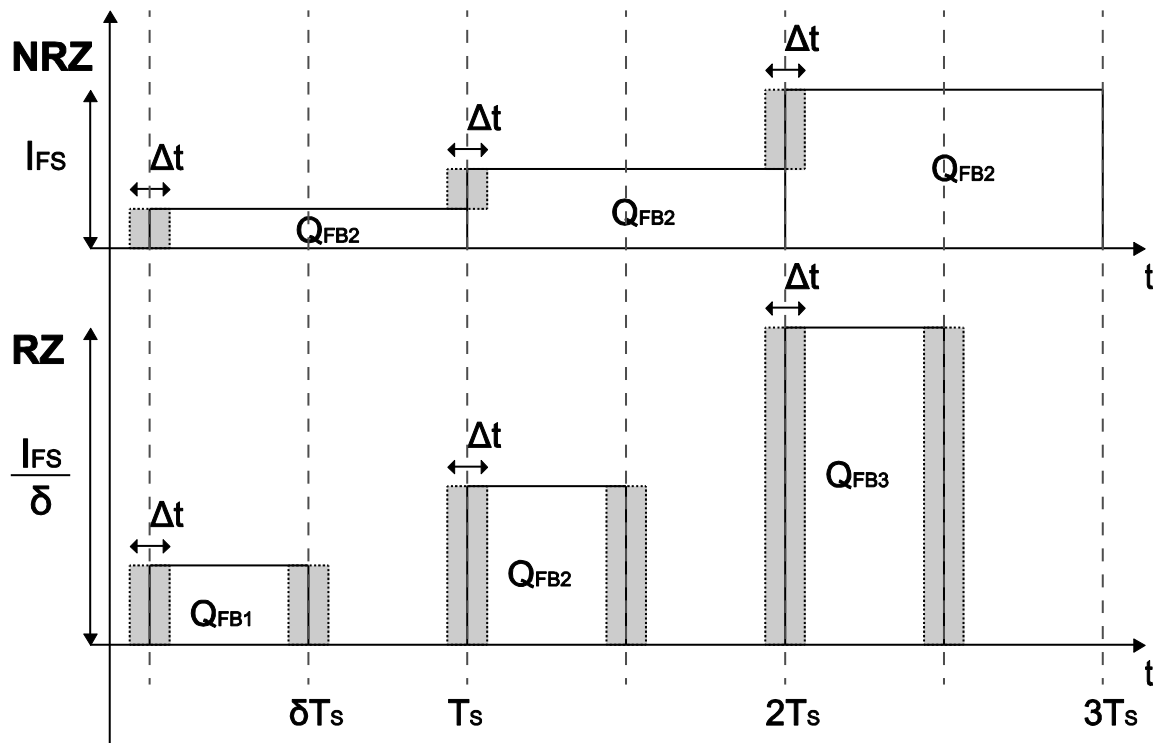
1) *Comparison of DAC implementations:* Most common feedback DAC pulse shapes reported in the literature can be summarized as non-return-to-zero (NRZ), return-to-zero (RZ), exponential and half-sinusoid [39]. As reported in [40], even though raised-cosine DACs looks promising, the complexity of such a design poses implementation challenges. A switch-capacitor DAC, which has a exponential pulse shape, is a popular choice for discrete-time ADC design. To first order, the feedback charge is set by the reference voltage and the capacitor size, so it should not be affected by the clock jitter. In reality, due to slewing and settling, the system is still sensitive to clock jitter. Furthermore, since the SC DAC's feedback level is fixed by the reference voltage and capacitor sizes, the design lacks the flexibility to support wide frequency range, making it less appealing for SDR applications. In comparison, current DACs, such as RZ and NRZ DACs, feedback charge can scale naturally with the clock frequency, thus enables a wide frequency range of operation for the overall system. Therefore, RZ and NRZ DACs are the only clear choices.

Reference [39] discusses how single-bit RZ and NRZ DACs are affected by timing uncertainties. Figure 3.12 shows how clock jitter impacts the RZ and NRZ DACs output pulses. Timing uncertainties are modeled as a zero-mean random white noise process with a variance  $\sigma_j^2$ . As illustrated in Fig. 3.12, clock jitter modulates the pulse width of the feedback signal, hence introduces a noise charge of a size of  $I_{Feedback}\Delta t$ . In the single-bit DAC case, the feedback current  $I_{Feedback}$  is the feedback DAC current  $I_{DAC}$ , as shown in the Fig. 3.12, while in the multi-bit case,  $I_{Feedback}$  is related to the feedback level resolved by the quantizer. One major difference between the RZ and NRZ designs is that the feedback current of the RZ DAC is larger than the NRZ DAC, due to the fact that pulse width is narrower, as shown in Fig. 3.12. Therefore, RZ DACs are more sensitive to timing uncertainties, as more noise charge is injected than the NRZ DAC case. Shown in Fig. 3.12 (a), the noise charge in the RZ DAC has the same width as in the NRZ DAC case, but a factor of  $\delta$  taller, therefore the noise charge is a factor of  $\delta$  larger in the RZ DAC case. Also, RZ DAC has worse jitter performance because of one more transition edge in every cycle, therefore the dynamic range is approximately 3 dB worse [40].

Fig. 3.12 (b) compares the effect of jitter on multi-bit RZ and NRZ DACs. Compared to single-bit DACs, the multi-bit DACs are less sensitive to jitter since the DACs don't always operate at the full-scale range as do single-bit DACs. The noise charge Fig. 7 (a) and (b) still have the same width for the same amount of jitter. However, the height of the noise charge varies with the input signal statistics. The more levels the DAC has, the less often or likely it would operate at the full scale output, so the less noise charge would be dumped into the integrators. In summary, more levels in the DAC reduce the jitter sensitivity.



a) Single Bit Case



b) Multi-bit Case

Fig. 3.12. Comparison of jitter impact on RZ and NRZ DACs.

2) *Jitter analysis and simulation models*: The jitter sensitivity of ADCs with single-bit feedback DACs have been studied in the literature in the past. References [38] [42] offer derivations of jitter sensitivity for systems with single-bit DACs for both the RZ and NRZ cases. With some modification on [42] which would be detailed in the appendix A at the end of this chapter, the SNR for a multi-bit NRZ and RZ DAC can be written as

$$SNR_{NRZ} \approx 10 \log_{10} \left[ \frac{OSR}{\left(\frac{\sigma_j}{T}\right)^2} \left(\frac{A}{P_{yd}}\right)^2 \right] + 3 \quad (18)$$

$$SNR_{RZ} \approx 10 \log_{10} \left[ \frac{OSR}{\left(\frac{\sigma_j}{T}\right)^2} \left(\frac{A}{P_y}\right)^2 \right] \quad (19)$$

where the  $A$  is the amplitude for a sinusoidal input, and  $P_y = \sqrt{2}E[y[n]y[n+k]]$ , which is the power in the modulator's output sequence. The  $P_y$  in the RZ case and  $P_{yd}$  in the NRZ case can be extracted from behavioral simulations. Table 3.1 lists different values of  $P_y$  and  $P_{yd}$  for a second-order modulator, assuming a 1 ps rms jitter for a 2 GHz clock. The numbers from Table 3.1 are then substituted into equations (18) and (19) to calculate the effective SNR, which are summarized in Table 3.2. Based on simulation and previous measurement result [44], 1 ps rms jitter roughly corresponds to 60 dB SNR.

<b>Number of Levels</b>	<b><math>P_y</math> RZ DAC</b>	<b><math>P_{yd}</math> NRZ DAC</b>
2	0.5000	0.6584
3	0.3628	0.3574
4	0.3250	0.2429
8	0.2950	0.0983

Table 3.1. Value of  $P_y$  and  $P_{yd}$  with different number of levels of DACs.

<b>Number of Levels</b>	<b>RZ DAC</b>	<b>NRZ DAC</b>
2	Ref.	0.6 dB
3	2.8 dB	5.9 dB
4	3.7 dB	9.3 dB
8	4.6 dB	17.1 dB

Table 3.2. SNR improvement between RZ and NRZ DACs with different DAC levels.

One difference between the RZ DAC and the NRZ DAC from Table 3.2 is that at a higher number of levels, the improvement of the RZ DAC saturates, while the NRZ DAC's SNR keeps increasing. As shown in Fig. 3.12, the NRZ DAC's output waveform is smoother as more levels are introduced. In theory, when the NRZ DAC approaches infinite resolution, the output waveform approaches a sine wave for a sinusoidal input. The difference between DAC levels from adjacent cycles would be reduced, hence the jitter induced noise charge can be reduced as well. In reality, implementing a linear DAC with resolution beyond 3 bits comes with substantial design challenges as well as a large power and area penalty.

On the other hand, for the RZ DAC, the improvement in SNR saturates because the increment in the DAC's levels doesn't help to reduce the step size. Due to its nature, the RZ DAC has transitions as large as the output full-scale of the DAC, so the noise charge induced would not scale as nicely as in the NRZ DAC case. For this implementation, it saturates roughly at the 2-bit level, as listed in Table 3.2.

### 3.2.4. Current-Mode-Integration Mixing/Sampling

This design, similar to [30], relies on current mode integration sampling (CMIS) [43] to provide frequency translation within the loop. A graphical representation of sampling is shown in Fig. 13 and Fig. 3.14. In the time domain (Fig. 3.13), the input signal is multiplied with an impulse train  $s(t)$ , which translates to a convolution between the input signal and an impulse train in the frequency domain as in Fig. 3.14. The results are shown in Fig. 3.15. Because of aliasing, the signal, DC offset and blockers at

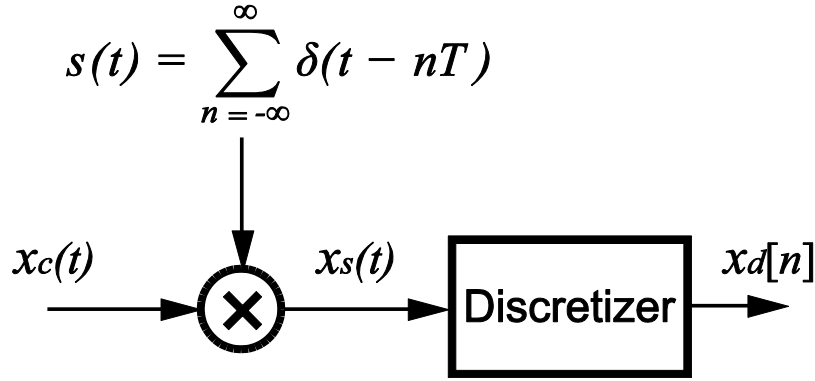


Fig. 3.13. Equivalent sampling model in time domain.

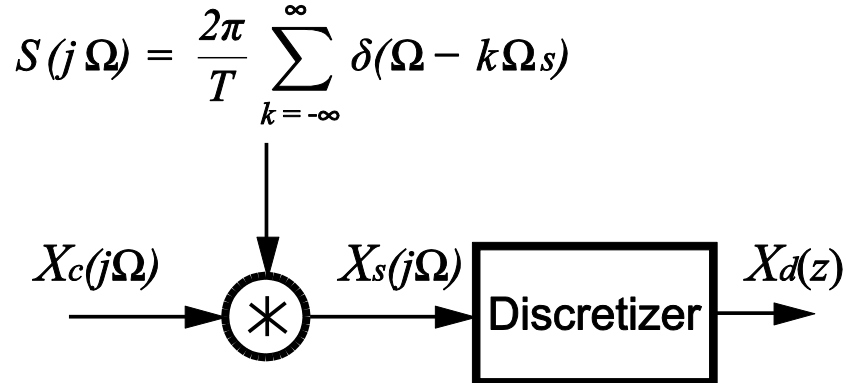


Fig. 3.14. Equivalent sampling model in frequency domain.

harmonics of the carrier frequency would fold down to baseband. In practical cases, the desired signal cannot be resolved properly.

On the other hand, Fig. 3.16 and Fig. 3.17 shows simplified models of the input signal mixed with a square-wave clock with a 50% duty cycle. The sinc filter in Fig. 3.17 is due to the square shape of the clock. For a clock with 50% duty cycle, this sinc filter nulls out the even-order harmonic contents of the clock frequency. Note that in Fig. 3.16  $a_0 = 0$ . This is because most of mixer circuit designs employ differential structures, that help to reject common-mode noise or DC offsets. The mixing process is illustrated in Fig. 13. Compared with the sampling case shown in Fig. 3.15, the additional sinc filter rejects contents at the even-order harmonics, and attenuates the odd-order harmonics except for

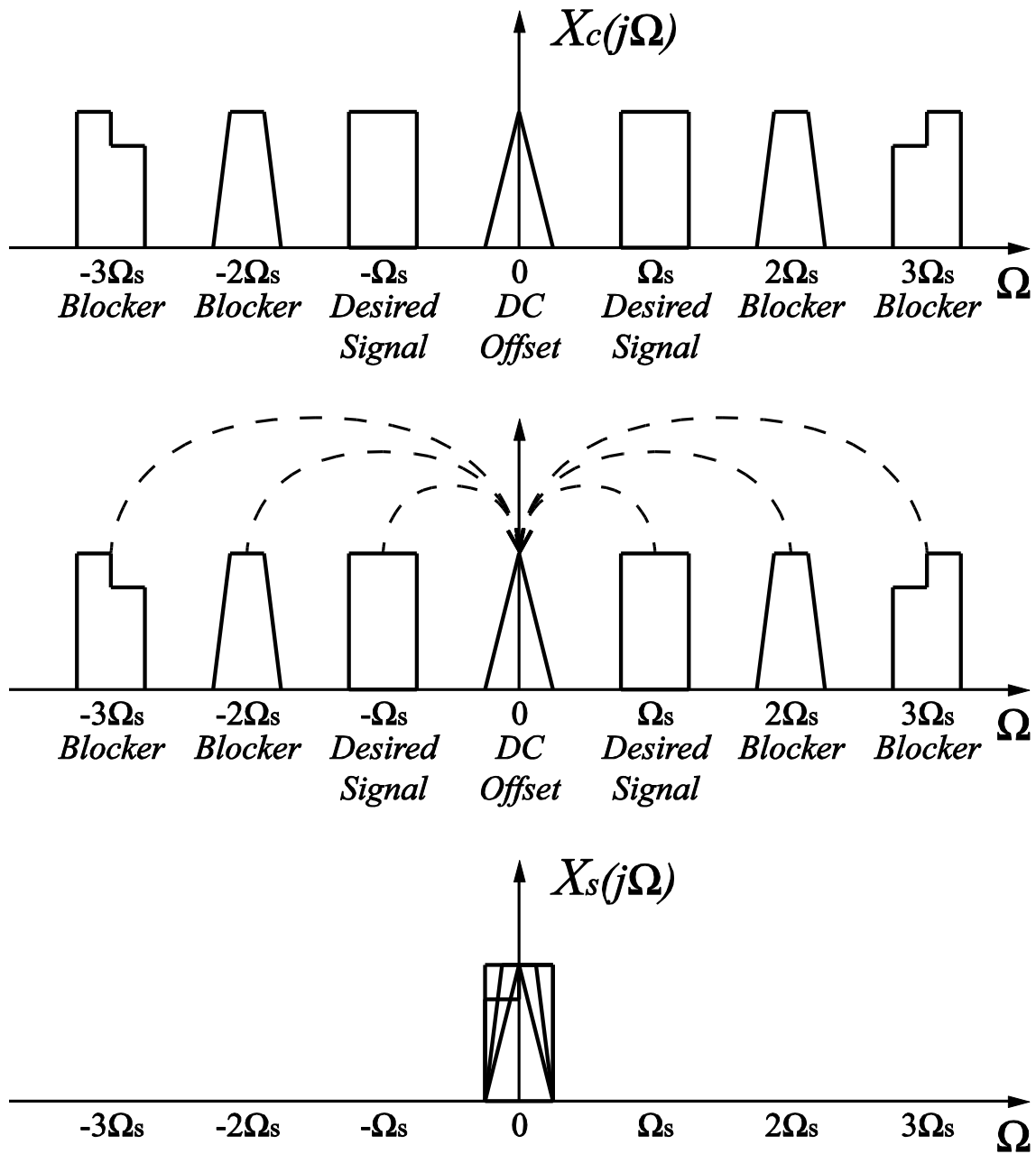


Fig. 3.15. Effect in the frequency domain of using sampling to downconvert RF signal.



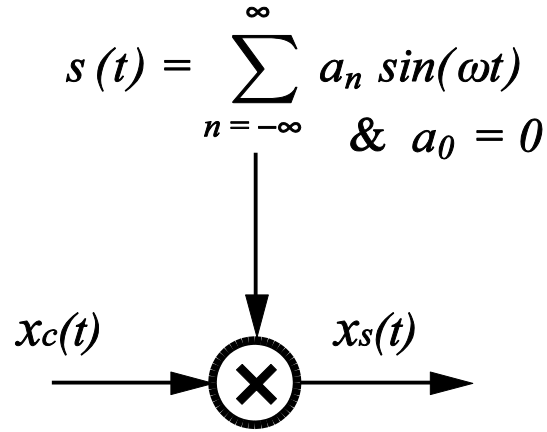


Fig. 3.16. Equivalent mixing model in time domain.

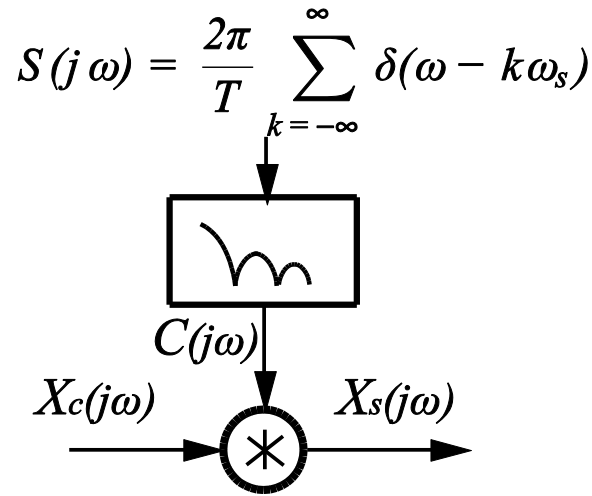


Fig. 3.17. Equivalent mixing model in frequency domain.

the one at DC. It can be shown that the attenuation at  $\omega_s$  is  $\frac{2}{\pi}$ , which is commonly described as conversion loss in the RF-community. Fig. 3.18 also exposes that the scheme is susceptible to higher order odd-order harmonics, such as the third-order harmonic shown here, when mixing with a 50% duty-cycle clock.

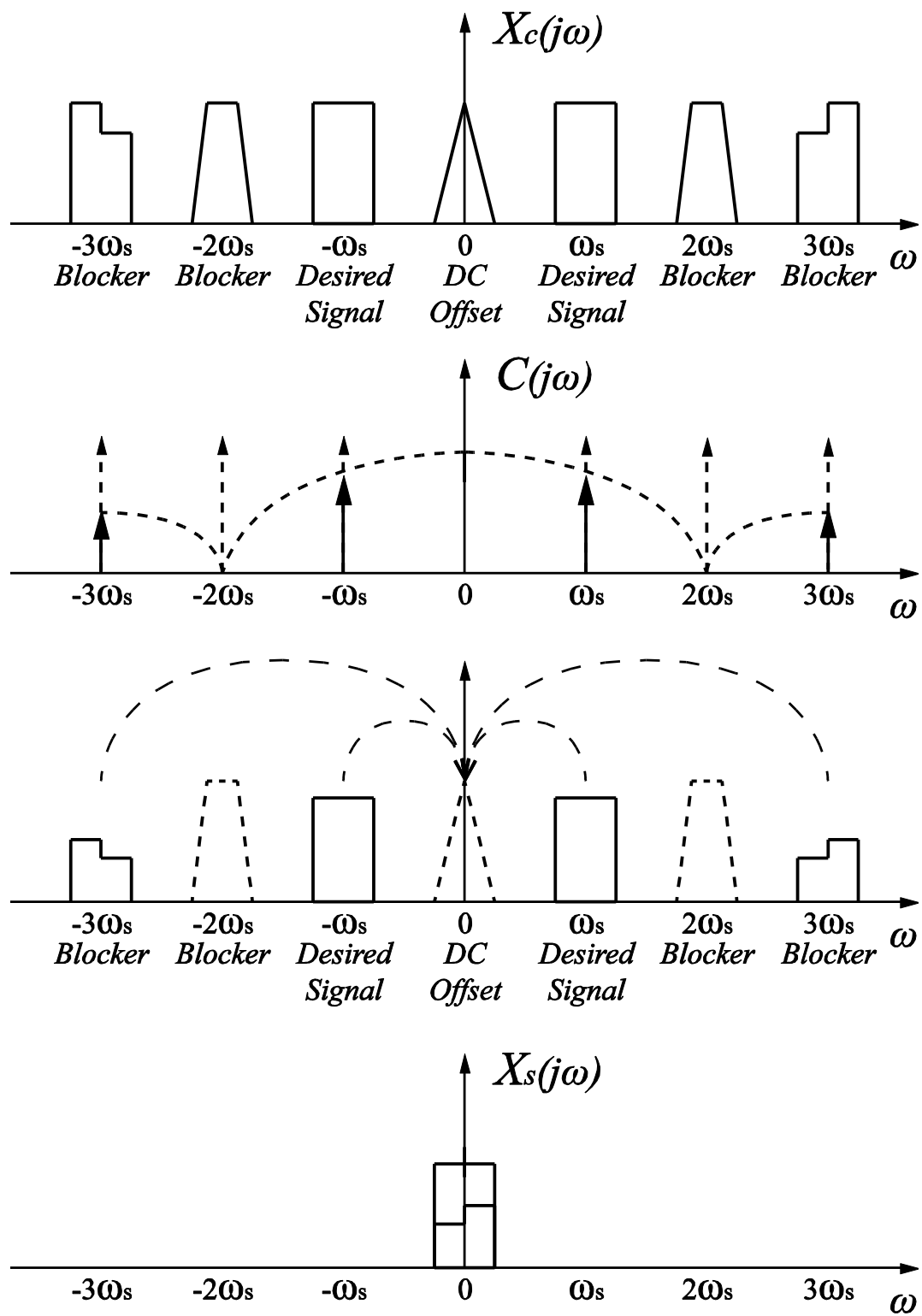


Fig. 3.18. Effect in the frequency domain of using mixing to downconvert RF signal.

Current-mode integration sampling (CMIS) behaves like mixing [44]. Consider a CMI sampler shown in Fig. 3.19. Instead of capturing the instantaneous voltage at the moment that switch  $M_1$  turns off, capacitor  $C_H$  integrates the input current over a period of time set by the LO. It can then be shown [44] that,

$$q_{in}[n] = \frac{T_{LO}}{2} \int_{-\infty}^{nT_{LO} + \frac{T_{LO}}{2}} I_{RF}(\tau) p\left(\left(nT_{LO} + \frac{T_{LO}}{2}\right) - \tau\right) d\tau \quad (20)$$

where  $p(x) = \frac{T_{LO}}{2}$  for  $0 \leq t \leq \frac{2}{T_{LO}}$  and  $p(x) = 0$  elsewhere.  $T_{LO}$  is the integration period.

Fig. 3.20 gives a graphical representation of the above equation. While a sinc filter is in the clock path in the mixing case as shown in Fig. 3.16 CMIS has the sinc filter in the signal path as shown in Fig. 3.17. Therefore, for a LO clock with the same 50% duty cycle, the output from mixing and CMIS is identical for the reasoning shown in Fig. 3.18. Also, the DC offset in the case of CMIS can be rejected by a differential implementation. CMIS is also susceptible to higher odd-order harmonics folding as in the mixing case.

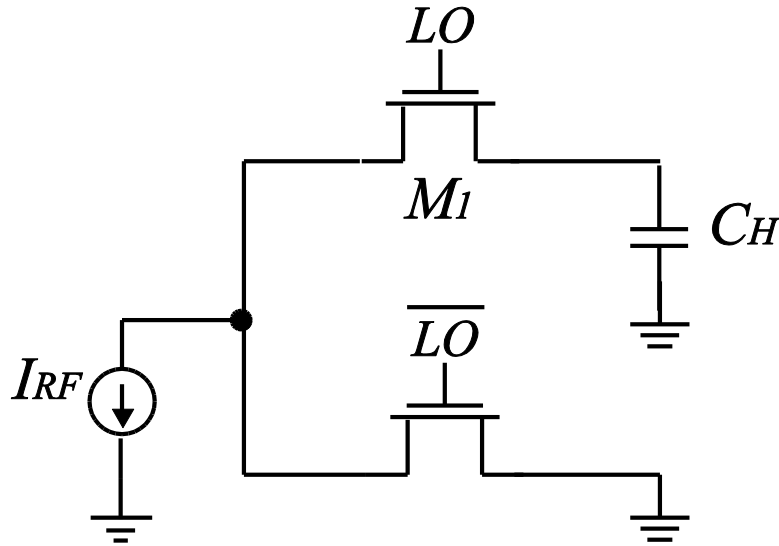


Fig. 3.19. Current-mode integration sampler with single-ended output.

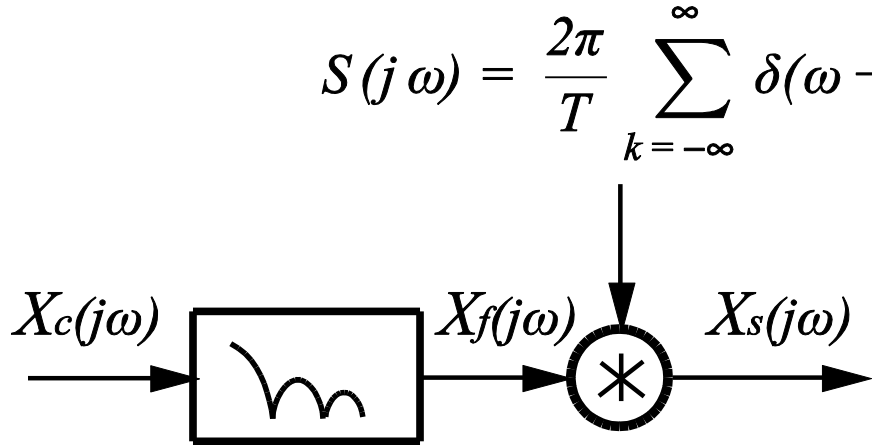


Fig. 3.20. Equivalent model for CMIS to downconvert RF signal in frequency domain.

For this particular design, a CMIS design with 50% duty cycle is chosen for its ease to integrate with the rest of the system. As demonstrated in figure 3.21, the current-mode nature of the CMIS mixer allows most parts of the system remained in current mode operation, except at the input of the low noise trans-conductance amplifier and the input of the comparators. As the result, large voltage swing in the intermediate nodes are completely avoided, and hence a much better linearity performance is ensured, which would be further elaborated in the Chapter 4.

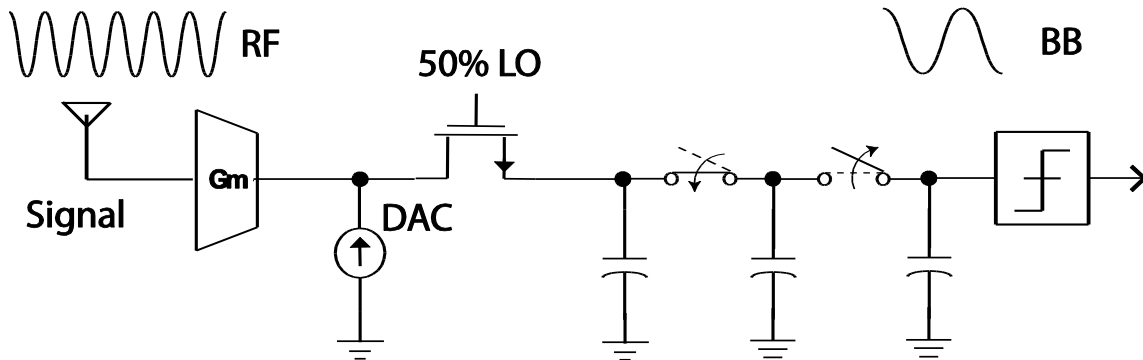


Fig. 3.21. Simplified model for CMIS integrated with rest of the system.

### 3.2.5. Summary

A four channel second-order ADC with CIFB all-feedback loop structure has been chosen for this work in order to achieve a maximally flat STF response and flexibility to support a wide frequency range. Also, a 2-bit NRZ DAC is selected for better jitter immunity and lower power consumption compared to higher resolution options. Finally, each of the ADCs is implemented as discrete-time as in [30] with a CMIS mixer employed. The discrete-time design allows the CMIS mixers to be seamlessly integrated, and helps to reduce the complexity for a system intended to operate over a wide range of frequency.

# Appendix A

## Derivation OF Multi-Bit RZ and NRZ DAC Jitter Sensitivity

The jitter sensitivity of  $\Delta\Sigma$  ADCs with single-bit feedback DACs have been well studied in the literature in the past. For this work, a modified derivation from [40] can address the multi-bit feedback case. For any  $\Delta\Sigma$  system in the jitter-free case, it is can be shown as

$$Y_0(z) = H_{NTF}(z)Q_0(z) + H_{STF}(z)X(z) \quad (21)$$

$Y_0(z)$  is the output free from jitter, and  $X(z)$  is the input.  $Q_0(z)$  is the quantization noise.  $H_{NTF}$  and  $H_{STF}$  stand for the noise transfer function and the signal transfer function.

With the impact of the clock jitter, the above equation can be rewritten as

$$Y(z) = H_{NTF}(z)Q(z) + H_{STF}(z)(X(z) + \tilde{Y}(z)) \quad (22)$$

where  $\tilde{Y}(z)$  is the feedback signal modulated by the jitter, and  $Y(z)$  and  $Q(z)$  stands for the output and the quantization noise with the effect of the clock jitter.

To extract the overall effect of the jitter,

$$\begin{aligned} E_y(z) &= Y(z) - Y_0(z) \\ &= H_{NTF}(z)\tilde{Q}(z) + H_{STF}(z)\tilde{Y}(z) \end{aligned} \quad (23)$$

where  $\tilde{Q}(z)$  is the jitter-induced additional quantization noise. Within the low frequency in-band,  $\tilde{Q}(z)$  is suppressed by the huge loop gain from the noise transfer function, therefore, its effect can be neglected. Therefore the above equation simplifies into

$$E_y(z) \approx Y(z) - Y_0(z) \quad (24)$$

From (24), the output jitter-induced noise PSD can be described as

$$S_{e_y}(z) \approx |H_{STF}(z)|^2 S_{\tilde{y}}(z) \quad (25)$$

$S_{\tilde{y}}(z)$  is the discrete-time Fourier transform (DTFT) of the autocorrelation of  $\tilde{Y}(z)$ . Given the fact that the clock jitter is uncorrelated with the quantized output, then

$$R_{\tilde{y}}[k] = E\{\tilde{y}[n]\tilde{y}[n+k]\} \quad (26)$$

where  $\tilde{y}[n] = j[n](y[n] - y[n-1])$ .  $j[n]$  is the small perturbation around the ideal clock edge induced by the jitter. Let  $y_d[n] = y[n] - y[n-1]$ , then  $\tilde{y}[n] = j[n]y_d[n]$ , therefore,

$$\begin{aligned} R_{\tilde{y}}[k] &= E\{y_d[n]y_d[n+k]\}E\{j[n]j[n+k]\} \\ &= \sigma_j^2 P_{y_d} \delta[k] \end{aligned} \quad (27)$$

where  $P_{y_d}$  is the autocorrelation between different  $y_d[n]$ .  $P_{y_d}$  is the key in describing a  $\Delta\Sigma$  modulator's performance under the impact of the clock jitter. From the early discussion, it has been shown that the performance under the jitter is related to the loop dynamic, input signal statistic and the system's nonlinear nature.  $P_{y_d}$  helps to capture all of these essential pieces of information for the jitter analysis of a  $\Delta\Sigma$  system.

From (25) and (27), the jitter-induced in-band noise PSD is

$$S_{e_y}(z) \approx |H_{STF}(z)|^2 \sigma_j^2 P_{y_d} \quad (28)$$

Following the analysis shown in the appendix in [42], near the center of the passband, the signal transfer function can be expressed as

$$|H_{STF}(z)| = \frac{1}{T \left| \text{sinc}\left(\frac{\omega_0 T}{2}\right) \right|} \quad (29)$$

Since the interest here is the low-frequency in-band, the  $\text{sinc}\left(\frac{\omega_0 T}{2}\right) \approx 1$ .

Therefore, the overall in-band jitter-induced noise power is then given by

$$P_e \approx \left(\frac{\sigma}{T}\right)^2 \frac{P_{yd}}{OSR} \quad (30)$$

Equation (30) suggests that the clock jitter is not noise shaped but simply spreading by  $OSR$ , due to the fact that the jitter is injected through the first DAC. The loop filter would treat it in the same way as it does to the input signal, therefore, the jitter noise is not noise shaped. Finally, the SNR of a  $\Delta\Sigma$  modulator with a multi-bit NRZ DAC with a sinusoidal input with amplitude  $A$  can be shown as

$$SNR_{NRZ} \approx 10 \log_{10} \left[ \frac{OSR}{\left(\frac{\sigma_j}{T}\right)^2} \left(\frac{A}{P_{yd}}\right)^2 \right] \quad (31)$$

For the RZ DAC case, equation (27) can be rewritten as

$$R_{\hat{y}}[k] = \sigma_j^2 P_y \delta[k] \quad (32)$$

where  $P_y = \sqrt{2}E\{y[n]y[n+k]\}$ , which is the power in the modulator's output sequence. And the rest of the analysis will follow what has been shown above. Then

$$SNR_{NRZ} \approx 10 \log_{10} \left[ \frac{OSR}{\left(\frac{\sigma_j}{T}\right)^2} \left(\frac{A}{P_y}\right)^2 \right] \quad (33)$$



# Chapter 4

## Experimental Prototype

### 4.1. Introduction to System Implementation

The overall architecture of the receiver is shown in Fig. 4.1. For the sake of clarity, the system diagram is shown as single-ended, while the actual design is fully differential. The  $\Delta\Sigma$  receiver includes both I and Q channels. A low noise transconductance amplifier (LNTA) in each channel converts the input RF voltage into an output RF current. A programmable gain of 20 dB is implemented by changing the bias current in both the LNTA and the feedback DACs. As shown in Fig. 4.1, the output of the LNTA is then split into two interleaved paths for I and Q channels, each of which contains a pair of passive mixers, which are implemented as a pair of CMIS switches. The signal is then processed by a second-order loop filter implemented using a passive switched-capacitor network. A two-bit quantizer is digitizing the filtered signal and its output is fed back to the RF summing node.

With two channels of  $\Delta\Sigma$  ADC's RF feedback signal, an effective bandpass feedback is created at the summing node. This multi-bit bandpass feedback suppresses the RF voltage swing; consequently, it improves the overall linearity performance. In comparison to [31][30], the two-bit network effectively reduces the swing at RF node by a factor of three. However, due to the lack of front-end gain, the reduced swing in the system posed a serious design challenge on the comparator design, which will be thoroughly discussed in this section. The entire system takes in an external clock operating at twice the speed of the carrier frequency. All the necessary clock phases needed are then generated internally.

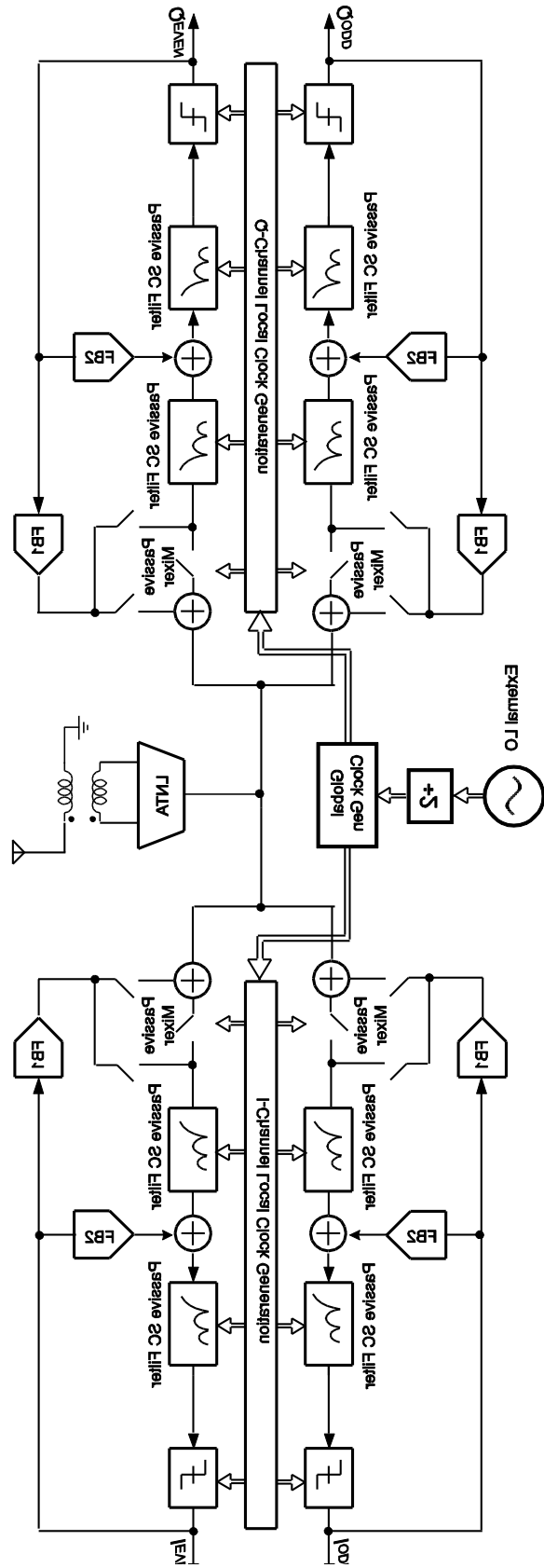


Fig 4.1 Simplified block diagram of the entire receiver

## 4.2 Circuit Design Designs

### 4.2.1 Sub-channel Design

A detailed schematic of the I-channel is shown in Fig. 4.2. Two channels of interleaved  $\Delta\Sigma$  ADCs create a bandpass  $\Delta\Sigma$  feedback on the RF summing junction. The high output impedance of the LNTA forces the output current to flow through the mixer, switched at an externally-supplied  $f_{LO}$ . When the LO signal is high, the output current from the LNTA charges a pair of capacitors ( $C_{1a}$ ,  $C_{1b}$ ) in the top path. When the LO signal is low, these capacitors are isolated from the input, and the signal is held constant. This two-path scheme indirectly implements a sample-and-hold function for the subsequent switched-capacitor circuits. The sample-and-hold feature of the mixer limits the jitter sensitivity to the LOs rising edge only, however, the feedback DAC implementation does impact the SNDR of the receiver.  $C_{1a}$  and  $C_{1b}$  are chosen to be 5 pF to trade off among distortion, noise and power favorably as discussed in [44].



## 4.2.2 Low Noise Transconductance Amplifier

Fig. 4.3 illustrates the design of the front-end LNTA. A class-AB dual common gate (CG) amplifier provides both wide-band input matching and good linearity. To improve both noise performance and power efficiency, the  $g_m$  of the four tail current sources are reused by AC-coupling the RF input signal to their respective gates. The input common-mode voltage is set by two replica biases that mimic the biasing conditions of the NMOS CG and the PMOS CG. The LNTAs differential outputs are AC-coupled to the mixer switches, and the output common mode voltage is set by a common-mode feedback amplifier connected to the mixers. The LNTA provides a transconductance gain of up to 20 dB from a 1.5 V supply with the CMIS circuits. The key feature is that the entire system is based on current mode operation. All the internal nodes are at low impedance (enforced by the cascode devices) except for the output nodes, whose swing is suppressed by the low impedance enforced by the global loop.

One major issue with such a design is how to combine the output current. Since there are two pairs of output currents flowing out of the LNTA, no conventional techniques can be used. One possibility is to borrow the idea of distributive active transformer (DAT) from [16] to create an active transformer current summation network as shown in Fig. 4.4. One nice benefit of transformer-based output combining network is that the transformer network itself, with proper design, can absorb the parasitic capacitor loadings on each side, therefore, it can potentially achieve a low-loss signal combining. Moreover, the common-mode voltage can be easily defined by connecting a desired bias voltage to the center tap on the secondary winding. However, software-define radio system need to operate at a low frequency range, where the transformer design could cost a huge area overhead. In addition, because of the insertion loss requirement, a transformer network could only support a rather limited frequency range. This makes transformer-based design less appealing for software define radio application, where a wide range of frequency of operation is a must. The transformer structure shown in Fig. 4.4 has a size of 200  $\mu\text{m}$  by 200  $\mu\text{m}$ . It can only support a tunable range up to 500 MHz centering around 2 GHz, which is clearly not enough for software-define radio application.

As the result, a capacitor-coupling network is used. To carefully manage the insertion loss, different capacitor layout structures have been studied. Iterations on different layout structures and their extraction results have suggested that avoiding the first and second layers of metal provides the best tradeoff between area overhead and the overall insertion loss. Detail analysis results are listed in Table 4.1. The extracted parasitic capacitor results are also further verified with the aid of 3D simulation cad tools such as EMX, which is also listed in Table 4.1.

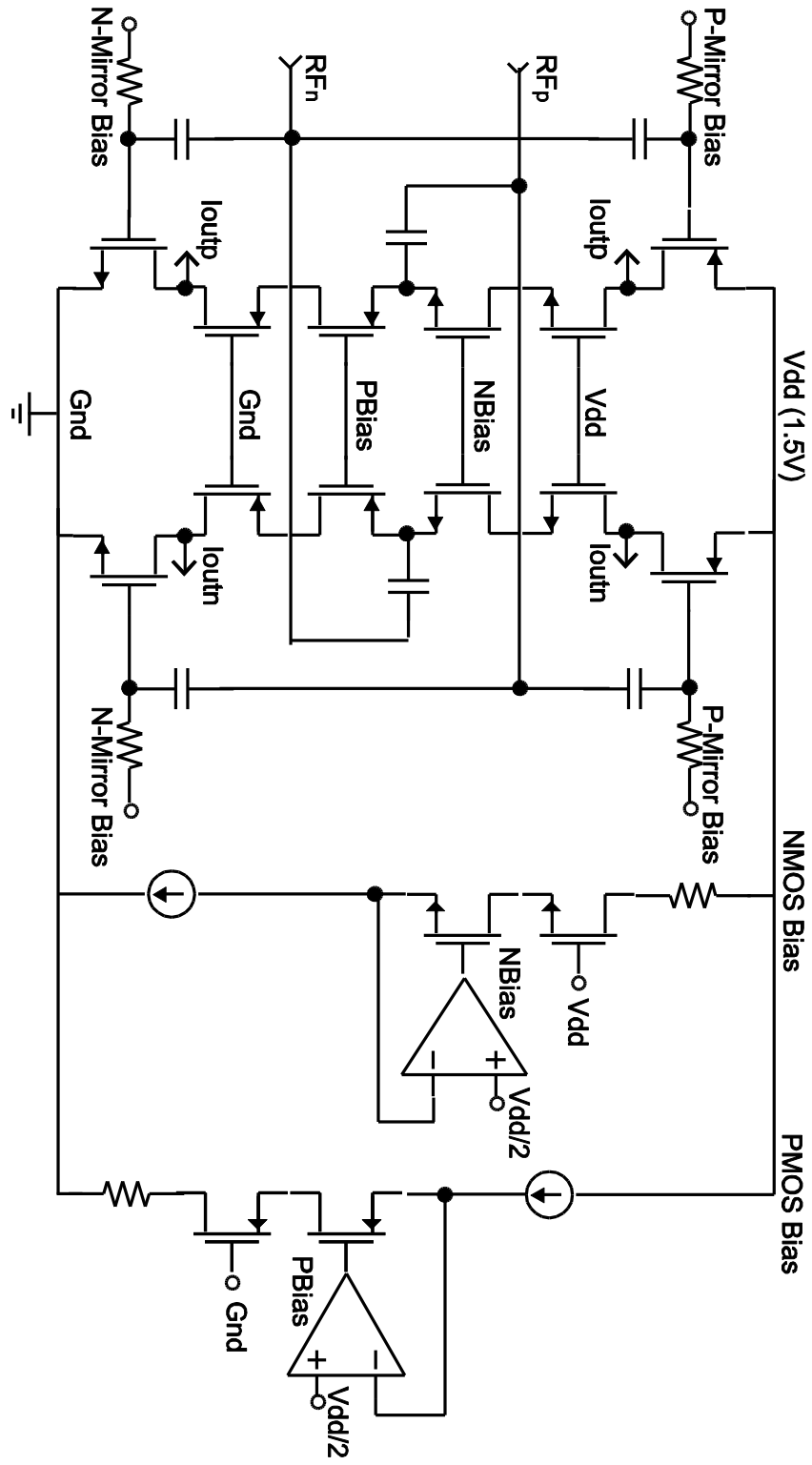


Fig. 4.3. Low noise transconductance front-end design with bias.

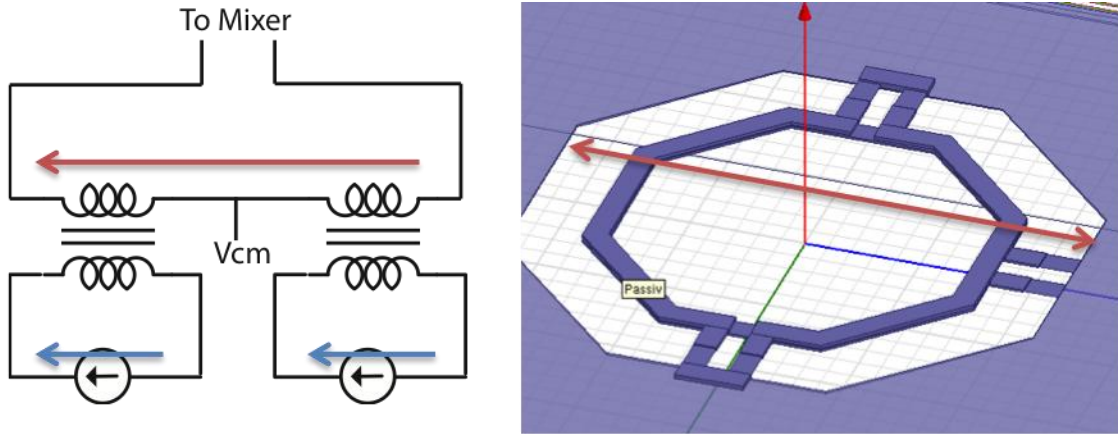


Fig. 4.4. Transformer-based output combining topology.

	<b>TSMC Model</b>	<b>EMX No Polyshield</b>	<b>EMX With Polyshield</b>
M1-M7	4.4 %	4.7 %	2.6 %
M2-M7	2.1 %	2.7 %	2.2 %
M3-M7	1.4 %	2.2 %	2.1 %

Table 4.1 Parasitic capacitor extraction result for different capacitor layout topology.

It can be shown the noise figure for the LNTA design detailed in Fig. 4.3 can be expressed as

$$\overline{v_i^2} = \frac{4kTG_m}{(G_m + G_{mc})^2} \left[ \frac{\gamma}{(1 + G_m R_s)^2} + \frac{G_m R_s}{(1 + G_m R_s)^2} + \gamma \right] \Delta f$$

$$N_f = \frac{G_m}{R_s(G_m + G_{mc})^2} \left[ \frac{\gamma}{(1 + G_m R_s)^2} + \frac{G_m R_s}{(1 + G_m R_s)^2} + \gamma \right] \quad (34)$$

where  $G_m = g_{m_n} + g_{m_p}$  is the overall trans-conductance of the common-source stages, and  $G_{mc} = g_{m_{nc}} + g_{m_{pc}}$  is the overall trans-conductance for the common gate stages.  $R_s$  stands for the loading impedance presented from the next stage.

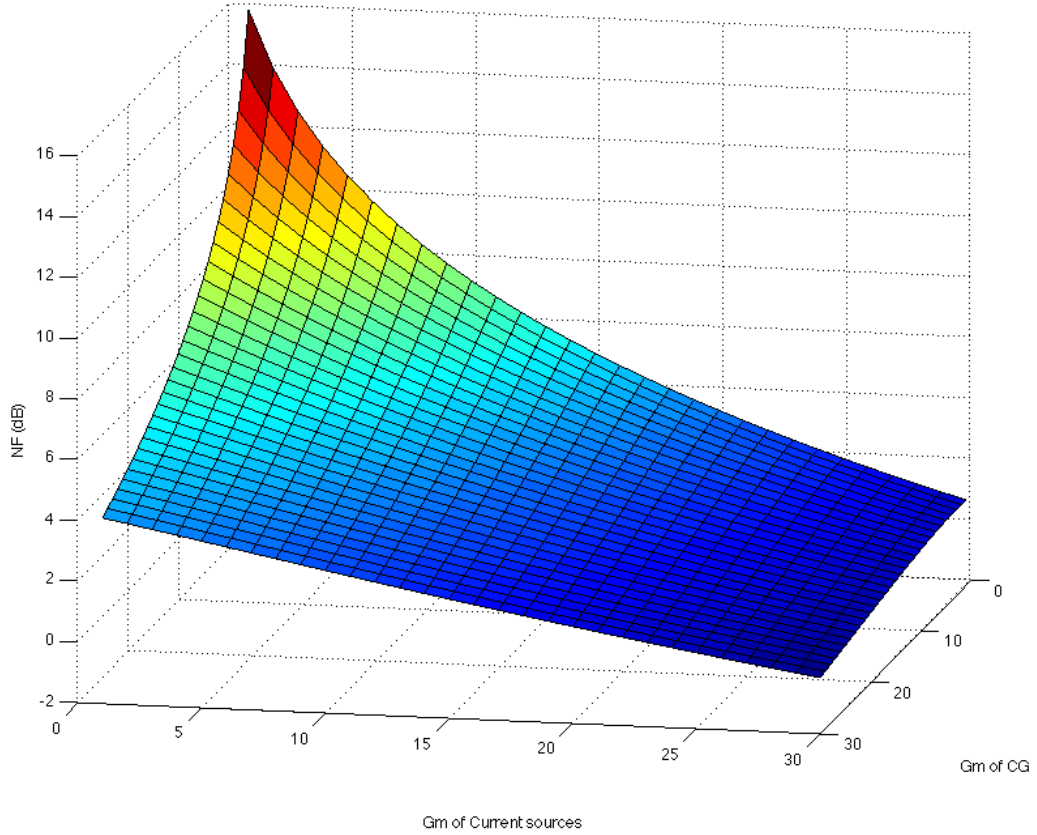


Fig. 4.5. 3-dimentional NF plot and 2-dimentional NF contour.



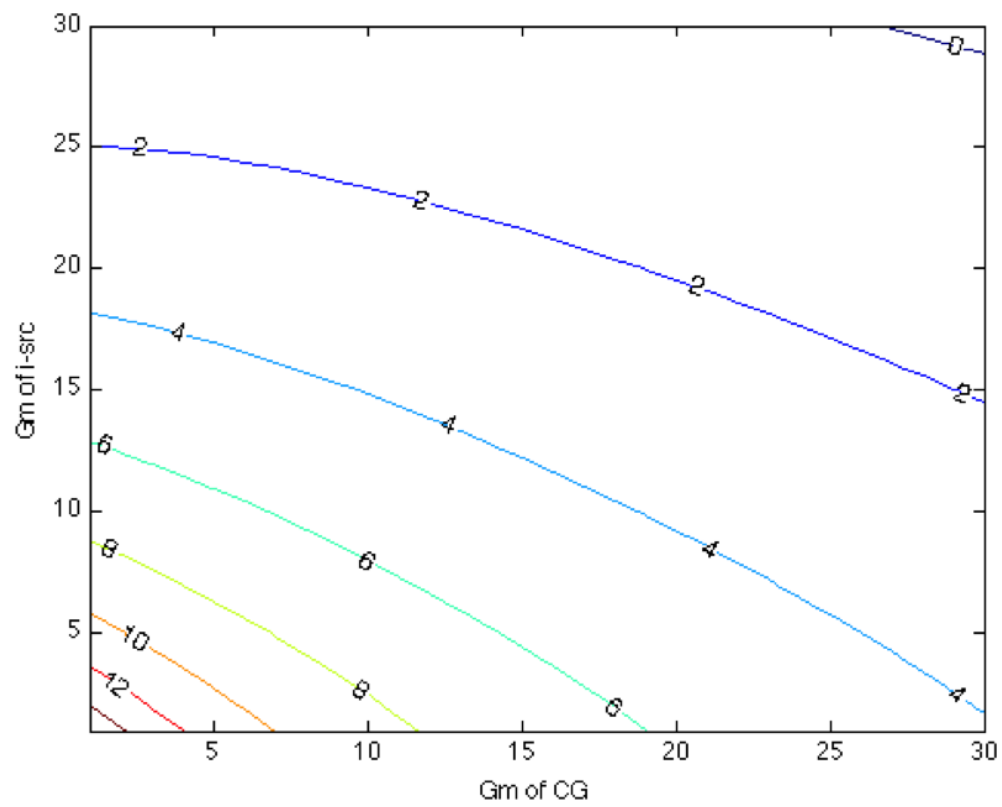


Fig. 4.5. 3-dimensional NF plot and 2-dimentional NF contour.

Noise and linearity simulation results are shown in Fig. 4.5 and Fig. 4.6 respectively. The LNTA can achieve a 2.8 dB NF and an IIP3 close to +20 dBm. The superb linearity of the LNTA design benefit from its class-AB based design. Even though the LNTA can handle large signal transient, its noise figure performance cannot keep up with it. The noise figure measured with 0 dBm blocker level is close to 13 dB as can be seen from Fig. 4.5. The reason can be explained as shown in Fig. 4.7. When the LNTA experiences with large signal transient, its input stages are so heavily tilted to accommodate the large blocker current it needs to supply or sink that the amplifier fails to maintain its differentially. As the result, the noise injected from the bias network such as the NMOS and PMOS bias network can no longer be simply treated as common-mode noise as in the small signal case, as highlighted in Fig. 4.7. The consequence is that the bias network noise would no longer be rejected as the common noise at the differential output, and it leaks into the LNTA and compromises the overall noise figure when there is a large blocker present.

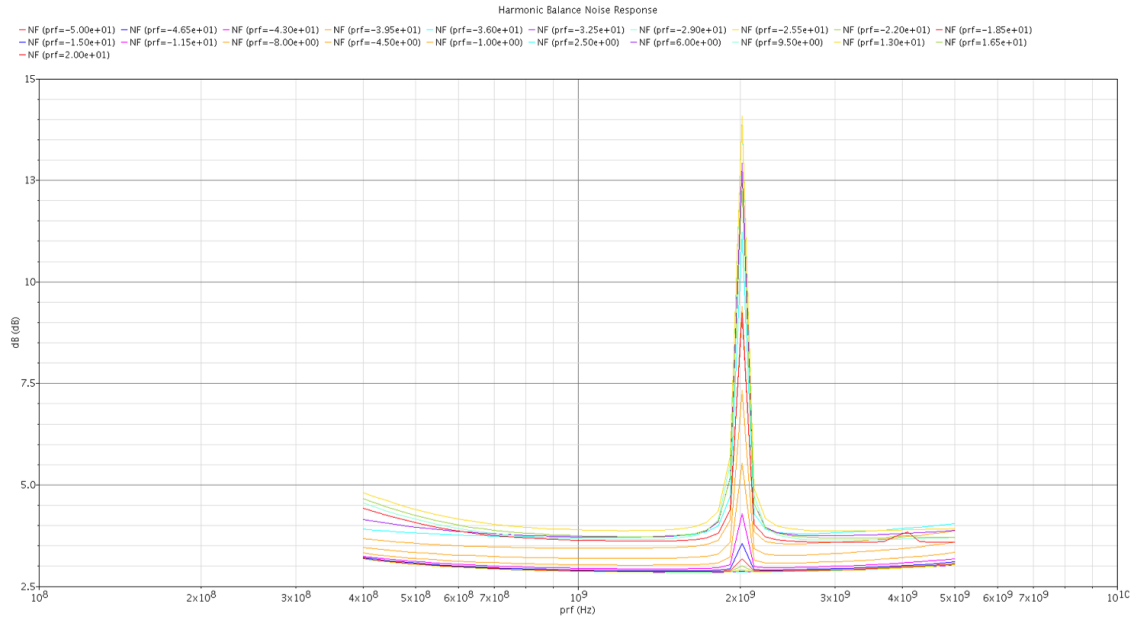


Fig. 4.5. Noise figure simulation result of LNTA under different blocker levels.

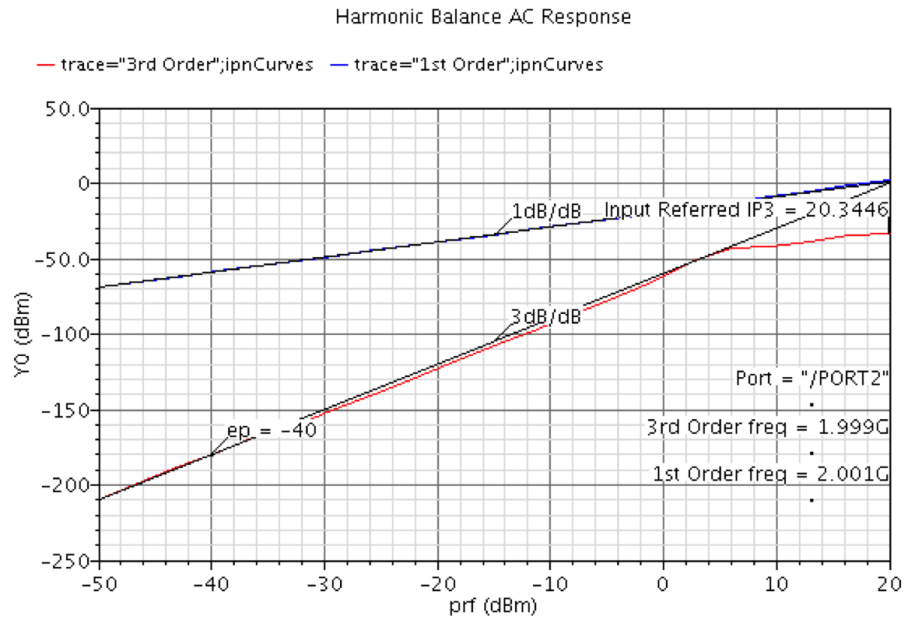


Fig. 4.6. Linearity simulation results for the LNTA.

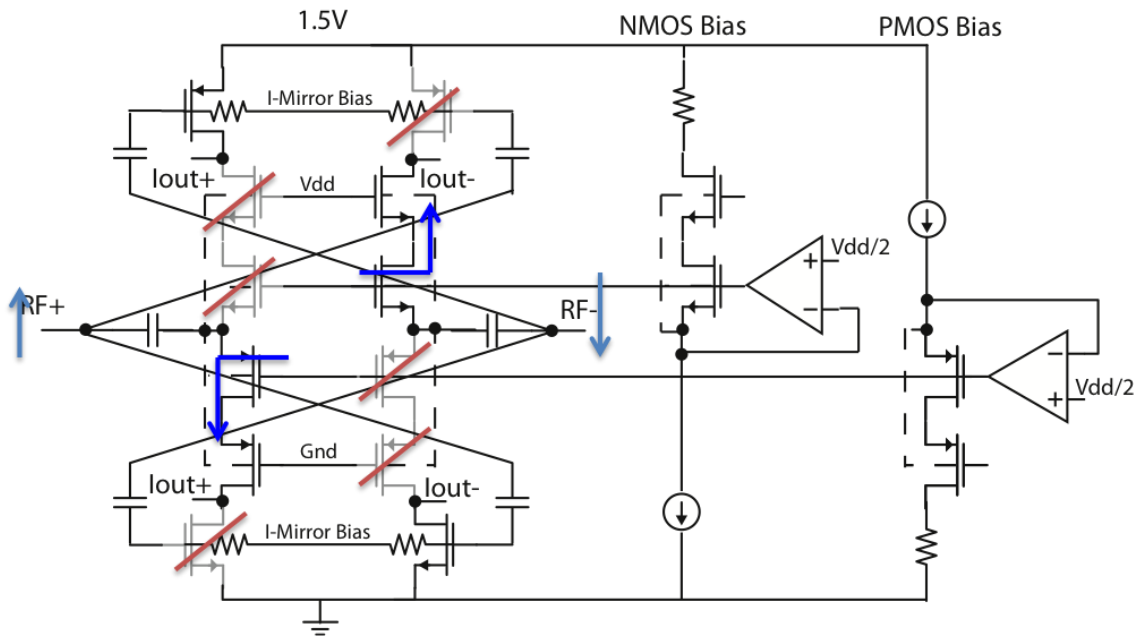


Fig. 4.7. Graphical explanation of the LNTA under large blocker transient

### 4.2.3 Feedback DAC designs

A two-bit NRZ DAC is implemented to favorably trade off jitter immunity with power consumption. The NRZ DAC, (Fig. 4.8), operates in two phases,  $LO\_D$  and  $\overline{LO\_D}$ , derived from the LO. When the mixer switches are on, the feedback DAC is connected to the RF side of the mixer, suppressing the voltage swing at the LNTA and the mixer switches. During the second phase, the switches are off, and the DAC is connected to the baseband (BB) side of the switches, thus preserving the DACs NRZ feature. This scheme is sensitive to the clock jitter during the switching instances at the RF side only (or rising edge of the  $LO\_D$ ), since the timing uncertainties of the exact instance switching to the BB side doesn't change the duration of the feedback DAC pulse.

Inter-sample interference (ISI) is one major issue for the design of NRZ DAC. As noted in [46], ISI is the result of asymmetry between the positive and negative DAC feedback pulses of a NRZ DAC, which is caused by different transition times when switching from the positive to the negative reference and vice versa [46]. Waveform asymmetry can be reduced by shaper transitions and matching of the transition edges, or switching to a RZ DAC design. Due to the jitter sensitivity issue, an RZ DAC design is not a feasible choice. In this design, a pair of fast-switching complementary DFFs are applied within the DAC unit cell to retime the quantizer outputs as shown in Fig. 4.8. The DAC is switching with a slightly delayed clock,  $LO\_D$ , to avoid output leaking into the wrong channels. The PMOS retiming DFF is pre-charged high when  $LO\_D$  is low, and transparent when  $LO\_D$  is high, while the NMOS retiming DFF operates in the opposite way. For the switches connected to the RF terminal, the quantizer output is directly latched by the complementary DFFs. For the switches connected to the BB side, the digital output is first stored by another simple DFF and then this stored value would be supplied to a second pair of retiming DFFs which is ready to drive the DAC on the rising edge of  $LO\_D$ .

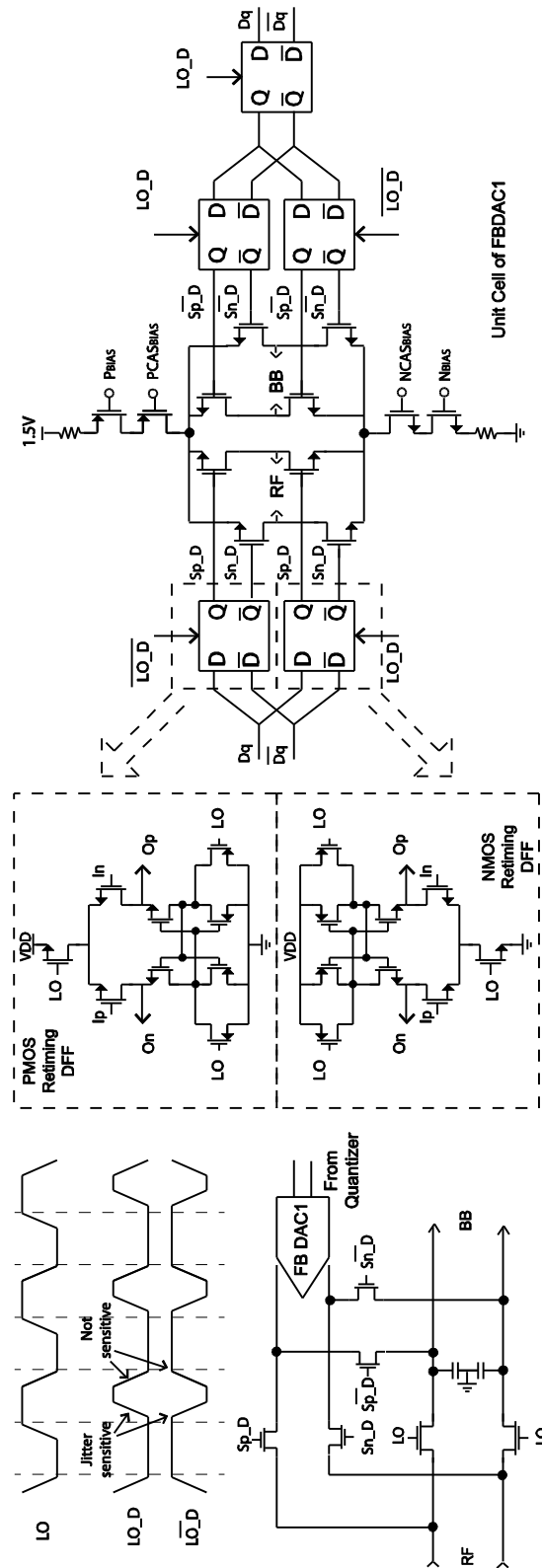


Fig. 4.8. Detail schematic and clocking scheme for FB-DAC1.

Another issue associated with the DAC design, as suggested by [44], is the effect of limited output impedance. Finite output impedance in the feedback DAC would result in second order distortion since it creates a signal-dependent discharge path. In [44], a behavioral model including the effect of finite DAC output resistance is proposed and shown here as Fig. 4.9. RDAC in Fig. 4.9 can be derived as [44]

$$\beta_{DAC} = 1 - \exp\left(\frac{-T_{Ref}}{C_H R_{DAC}}\right) \quad (35)$$

Simulation suggests that the DAC impedance has to be larger than 10 k $\Omega$  to ensure the second-order tone induced by the DAC impedance is always below -80 dBc.

The DAC unit cell is shown in Fig. 4.8. To ensure voltage headroom for all the devices stacked in the unit cell and hence to maintain the desired high output impedance of the DAC, it is connected to the 1.5 V supply. All current source devices are sized up appropriately for the required mismatch performance, and they are further degenerated for better matching and noise performance as reported in [47].

The second feedback DAC design is less critical compared to the first one, since the jitter injected there is noise-shaped by the first integrator. Therefore, it is implemented as a simple RZ DAC.

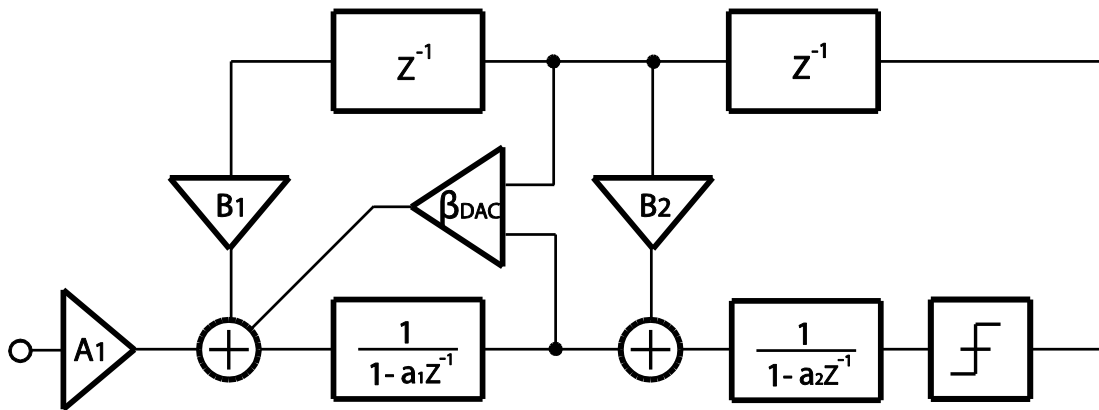


Fig. 4.9. System model including the effects of feedback DAC finite output resistance..

## 4.2.4. Comparator Design

The comparator design is quite challenging due to the speed and precision requirements. The comparator requires a short decision time (200 ps), a small input-referred noise level (200 mV), and low power consumption (4 mW at 2 GHz). As shown in Fig. 4.10, the comparator core is implemented using a calibrated pre-amplifier followed by a sense-amplifier-based latch. The pre-amplifier helps to ease the stringent input-referred noise and mismatch requirements (0.5 mV) posed on the comparator, due to the lack of front-end gain in the system. The mismatch of the core comparators is further suppressed through an integrated calibration DAC to avoid using excessively large devices. To calibrate the mismatch, the comparators' inputs are first disconnected from the loop and tied to a on-chip reference ladder. Then, the optimum codes for each comparator can be found by sweeping through the DAC. Finally, the comparators are connected back to the loop. This is a one time process, and is robust over different frequencies.

To reduce the jitter sensitivity, more feedback levels are preferable. However, it also poses a more stringent requirement on the comparators' mismatch performance. Fig. 4.11 compares the quantizer area with respect to the resolution in the quantizer. To meet the mismatch requirement, the comparators need to be excessively large in conventional design. With calibration, the quantizer can be four times smaller.

To better understand the area overhead of the calibrated quantizer, its area breakdown is shown in Fig. 4.12. At the one bit level, the size of the decoder dominates. At higher resolution, the area of the calibration DAC dominates. At the 2 bit level, the decoder has a similar size as the calibration DAC. It is also worth noting that a 3-bit quantizer has a size that is 10 times larger than a 2-bit quantizer, even with the calibration. For the current design, the quantizer occupies around 10% of the overall area. If a 3-bit design is adopted, the quantizer would have a comparable size to the current system.

Another benefit with calibration is power saving as shown in Fig. 4.13. Without calibration, each comparator cell scales up exponentially with resolution to meet the stringent mismatch requirements. Meanwhile, more unit cells are needed. Hence, the switching power increases more rapidly. With calibration, more cells are still needed, but each cell stays the same size; only the size of the calibration DAC increases exponentially. Therefore, power overhead is less severe than the un-calibrated case.

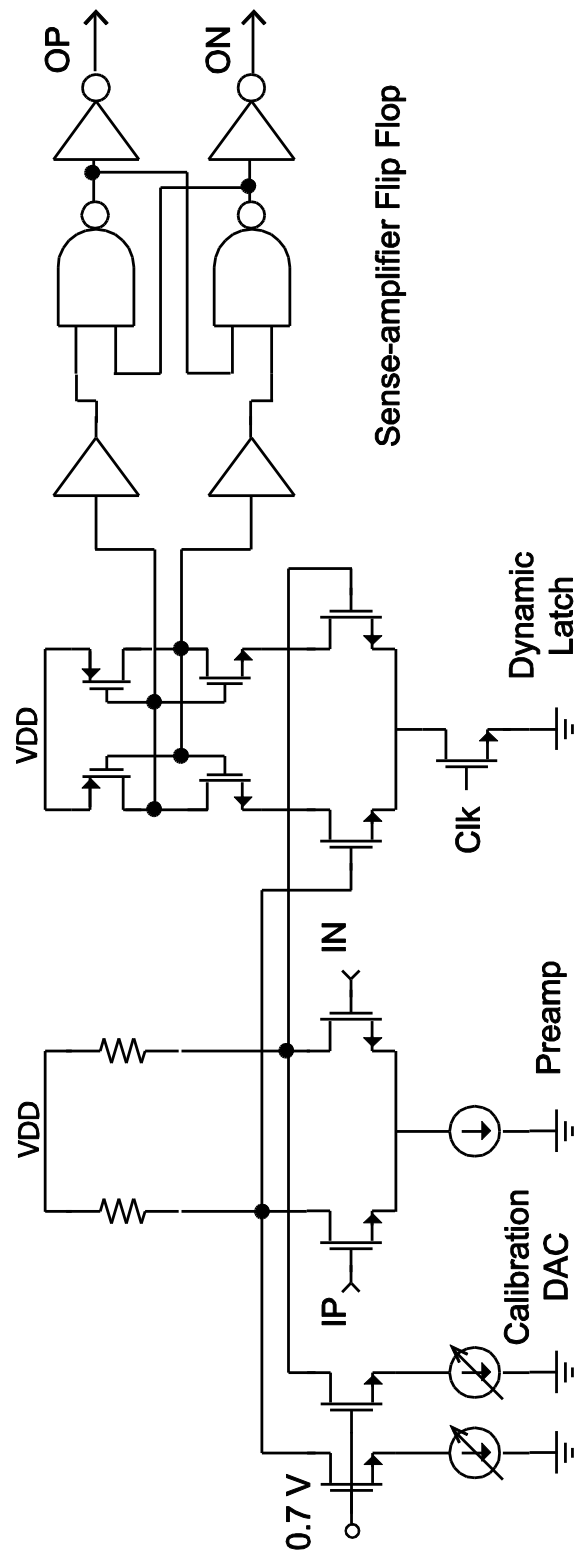


Fig. 4.10. Schematic for the quantizer design.



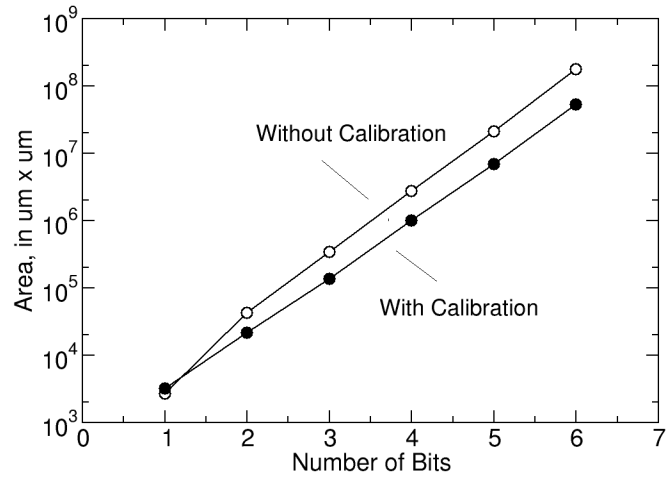


Fig. 4.11. Quantizer area comparison with and without calibration.

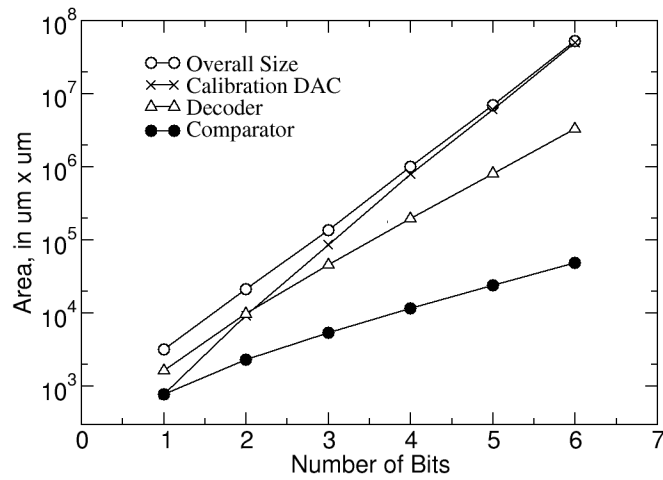


Fig. 4.12. Quantizer area breakdown with calibration.

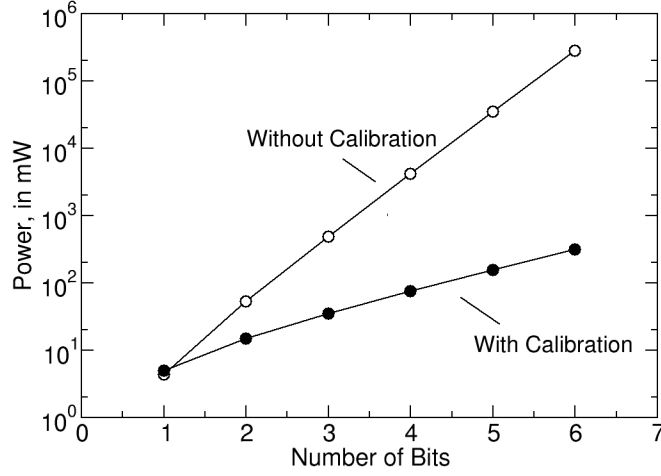


Fig. 4.13. Comparison in power for quantizer with and without calibration.

## 4.2.5. LO generation and distribution

As shown in Fig. 4.14, an external clock operating at twice the carrier frequency is fed to the chip. An on-chip global clock generation circuit brings down the clock speed to the carrier clock frequency and generates four phases of I/Q clocks. These I/Q clocks are then fed to the local clock generation circuit to generate all the needed clock phases, such as the mixer and DAC clock phases shown on the Fig. 4.14.

LO network sets the limit for the power and performance of such a system. It degrades the overall noise floor in two ways: its thermal noise and its flicker noise. According to [48], the added jitter due to the thermal noise can be described as

$$\sigma_{td}^2 = \frac{4kT\gamma\tau_{delay}}{I_{Discharge}V_{Overdrive}} \quad (36)$$

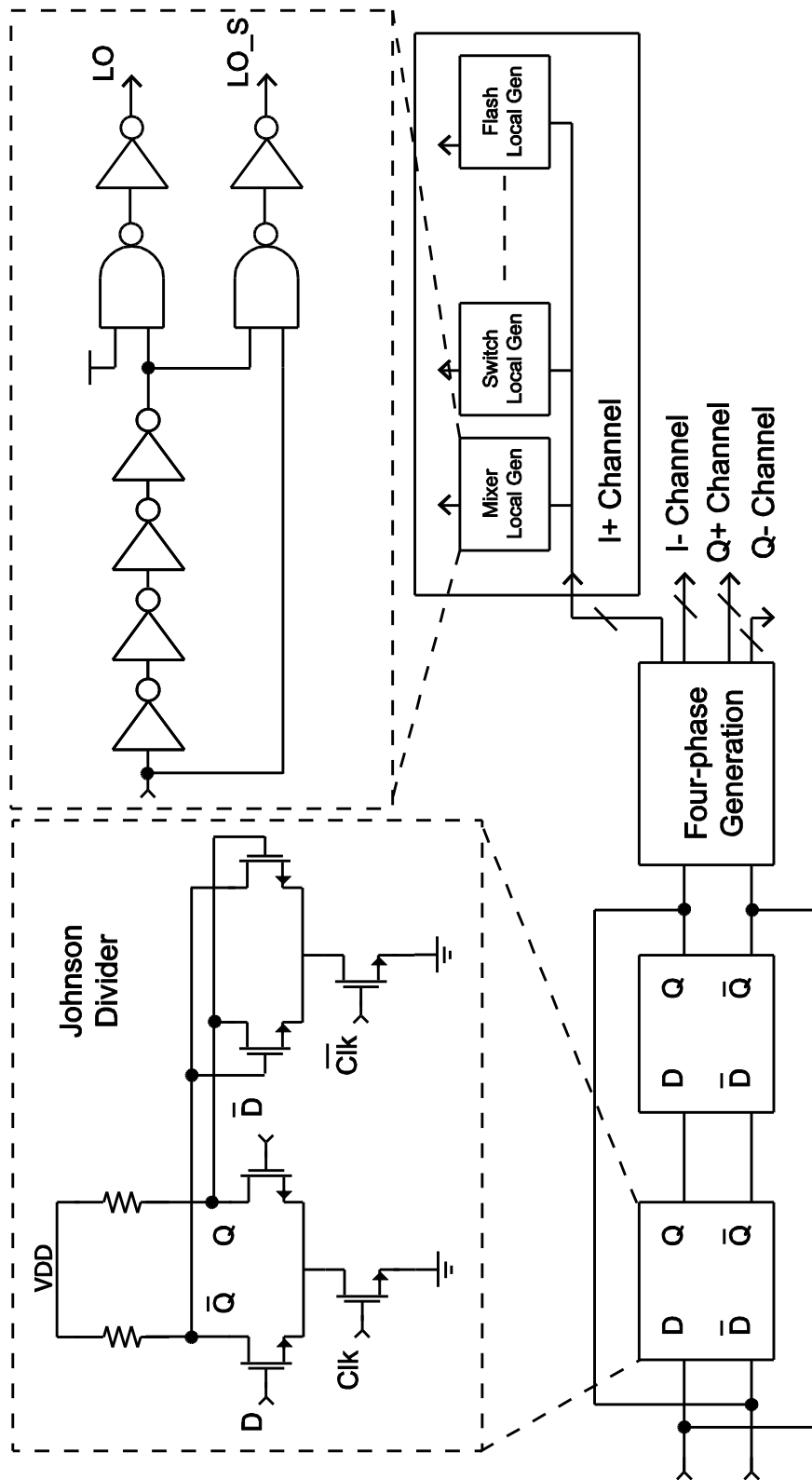


Fig. 4.14. LO generation and distribution network.

This suggests the added jitter can only be reduced by sizing up the discharge current and reducing the delay time, which is just sizing up the devices. For short, sizing up the devices would improve both its edge rate and its flicker noise performance, but it comes with large power penalty. Noise simulations on the Mixer and the first feedback DAC paths have revealed that the added jitter is 920 fs with 9 mW power consumption under 2 GHz operation. The effect of the flicker noise will be later discussed in the next section.

### 4.3. Measurement

The chip is implemented in TSMC's 65nm GP technology. The chip photomicrograph is shown in Fig. 4.15, highlighting that the receiver occupies an area of 850  $\mu\text{m}$  x 650  $\mu\text{m}$ , including the calibration DACs for the comparators as well as the local bypass capacitance.

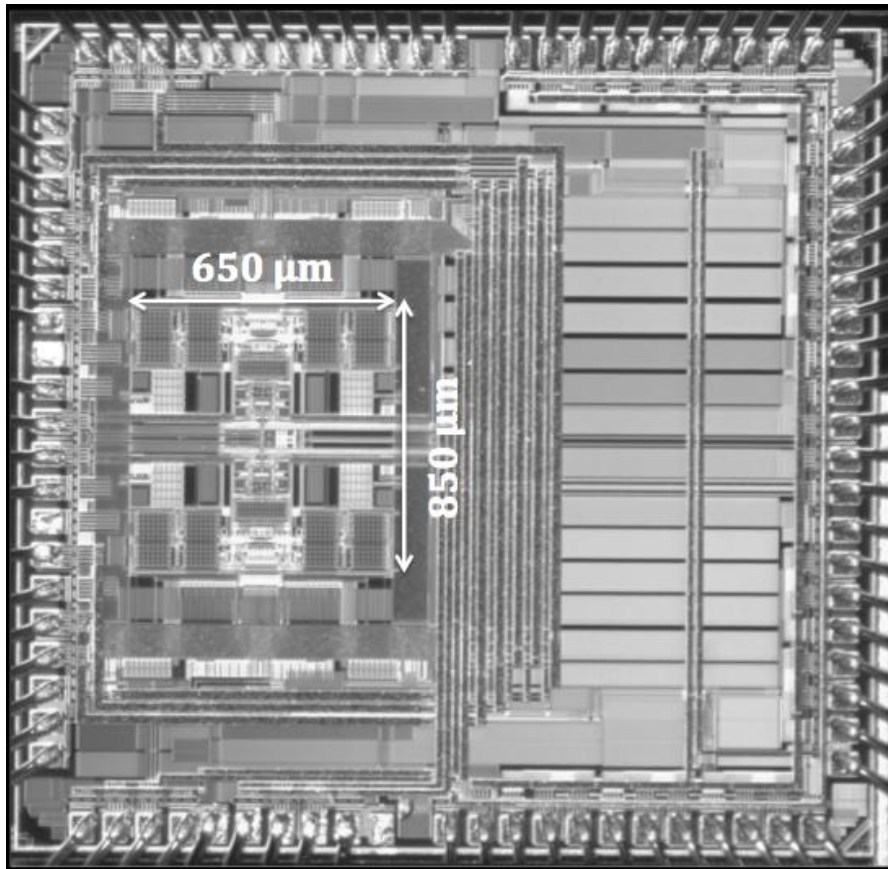


Fig. 4.15. Chip Microphotograph.

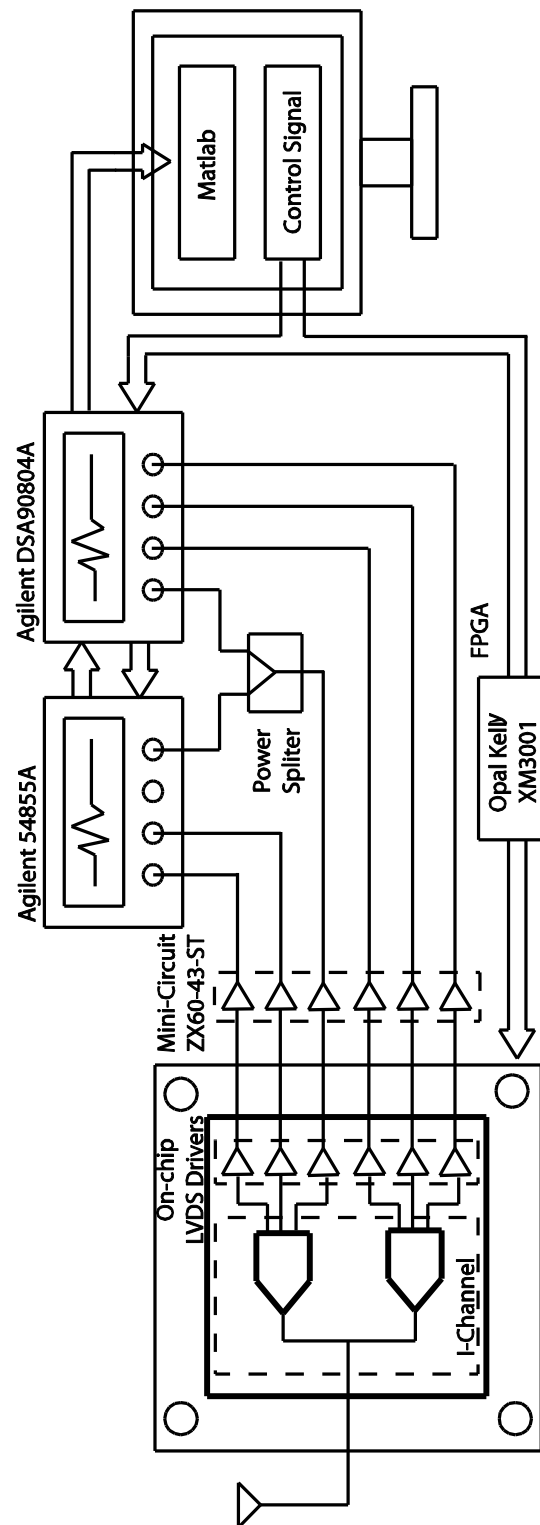


Fig. 4.16. Measurement setup for data capturing and system control .

Fig. 4.16 shows the measurement setup for capturing data. Two real-time 20 GS/s oscilloscopes are used to capture the output digital waveforms, and post processing is performed on a computer. One channel of the digital waveform is power-split and sent to two scopes as the trigger signal for both scopes. The same channel signal is also used for synchronizing digital signals captured from the two scopes.

Fig. 4.17 shows the measured SNDR for 4 MHz and 10 MHz signal bandwidths at 2 GHz. The peak SNDR is 68.86 dB for 4 MHz and 64.83 dB for 10 MHz, respectively. The in-band P1dB is measured at -15 dBm input level, which is because input exceeds the input full-scale of the baseband ADCs, and saturates them. SNDR is higher than 60 dB over the 0.4 GHz to 4 GHz tuning range.

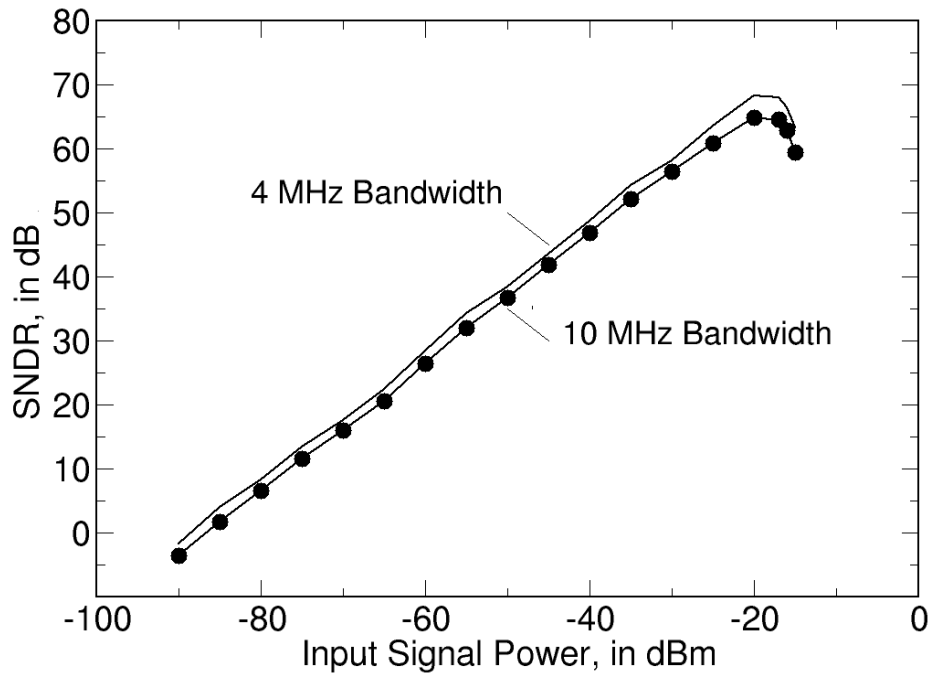


Fig. 4.17. Measured SNR at 2 GHz carrier frequency.

Fig. 4.18 shows the SNR and SNDR for varying signal bandwidths at a 2 GHz center frequency. SNR and SNDR spectra are integrated from 10 KHz to the bandwidth mentioned.

Fig. 4.19 shows the output spectrum for a 2GHz frequency with an input signal at 2.001GHz. The low frequency noise floor is elevated due to the reciprocal mixing of the LO phase noise by the mixer. A closer look at the noise floor in Fig. 4.19 reveals that there are two mechanisms that contribute to the noise floor of the above measurement. All the transistors in the clock generation circuitry contribute flicker noise.

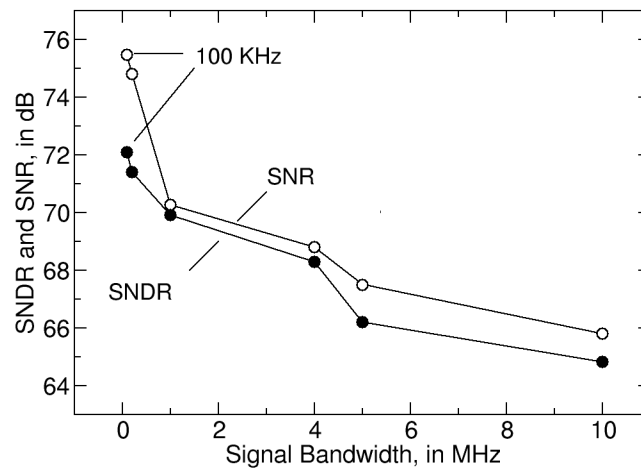


Fig. 4.18. Measured SNR and SNDR at 2 GHz carrier frequency.

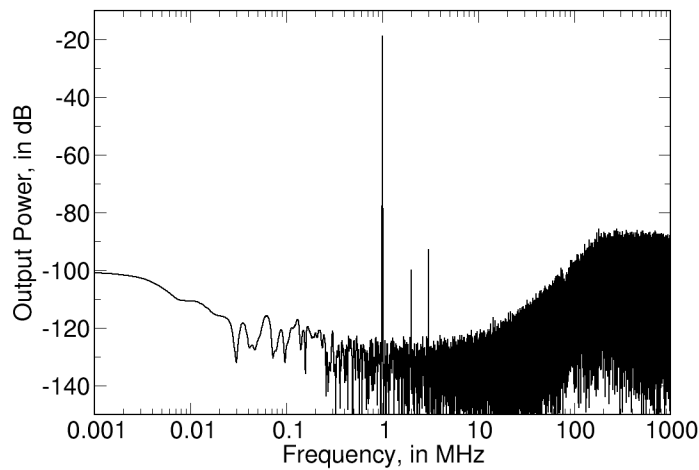


Fig. 4.19. Output spectrum at 2 GHz center frequency with input signal offset by 1 MHz.

As shown in Fig. 4.19, this low frequency flicker noise is first up-converted to the LO frequency by the LO chain. Then, it is down-converted back to baseband by the CMIS mixers, which results a rise in the noise floor in the low frequency. On the other hand, the noise floor on the higher frequency is dominated by the jitter injected though the first feedback DAC. The clock jitter for this system is limited by its LO network. Since the clock source has a jitter as low as 270 fs, while the added jitter from the LO chain is around 900 fs. Therefore, this system would achieve (+10 dB) better SNR performance for narrow band standards, such as GSM, when operating in a low-IF mode.

Fig. 4.21 shows the two tone test result. One Agilent 4438C vector signal generator

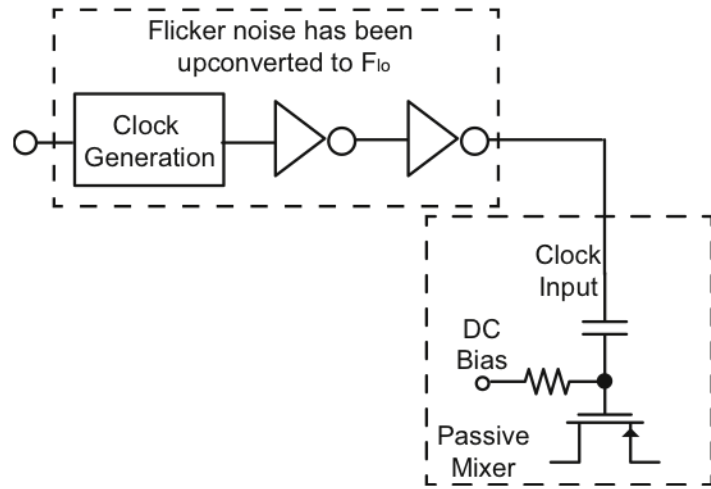


Fig. 4.20. Flicker noise from LO chain upconversion and downconversion.

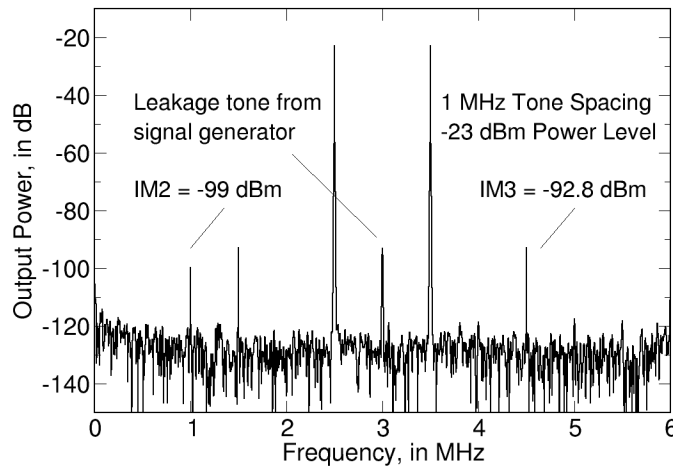


Fig. 4.21. Two tone tests with 1 MHz tone spacing around 2 GHz center frequency.



(VSG) is used to generate the two tones with different spacing. A leakage tone is generated by the VSG right in the middle of the two desired signals. The measured IM2 and IM3 products are -99 dBm and -92.8 dBm respectively.

Fig. 4.22 summarizes the IIP3 performance versus tone spacing. The IIP3 improves with farther spacing between the two tones, since the CMIS network functions in similar manners as the N-path filter proposed in [49]. Overall, the system maintains its high linearity over a wide range of blocker frequencies.

Fig. 4.23 shows the SNR and SNDR for varying signal bandwidths at a 2 GHz

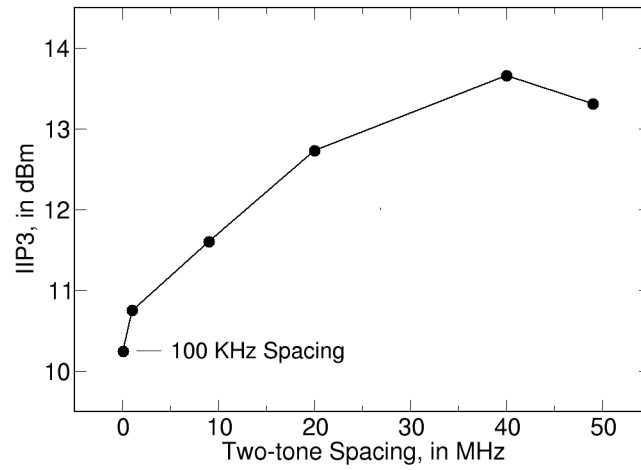


Fig. 4.22. IIP3 versus two-tone spacings at 2 GHz.

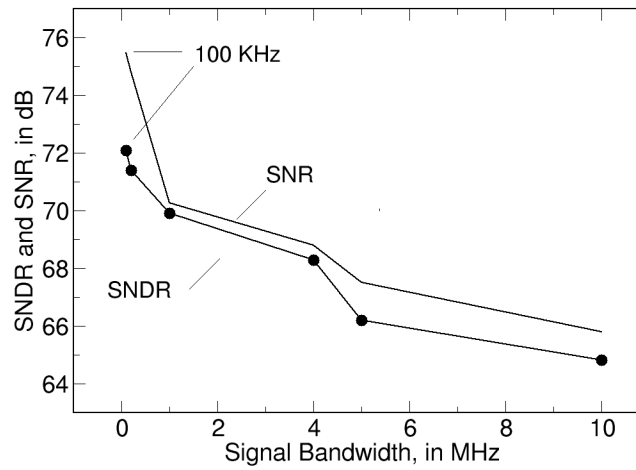


Fig. 4.23. SNR, SNDR vs. Signal Bandwidth.

center frequency. SNR and SNDR spectra are integrated from 10 KHz up. For narrow bandwidth standards, such as GSM, the SNR is severely impacted by the low-frequency noise increase. Therefore, it performs better in low-IF conversion. For a wider bandwidth standards, the clock jitter noise set the dynamic range of the system, which is why a multi-level feedback is used here. Overall, a large SNDR is maintained over a large range.

Fig. 4.24 shows the SNDR performance with the carrier frequency varied from 200 MHz to 4 GHz. The frequency resolution of the plot is limited by the sampling rate of the oscilloscope. At low frequencies, SNDR improves substantially with an increase in carrier frequency, as the in-band noise is dominated by the quantization noise. At higher frequencies, this improvement is offset by the increasing impact of the clock jitter. The clock jitter eventually dominates, so further oversampling only degrades SNDR.

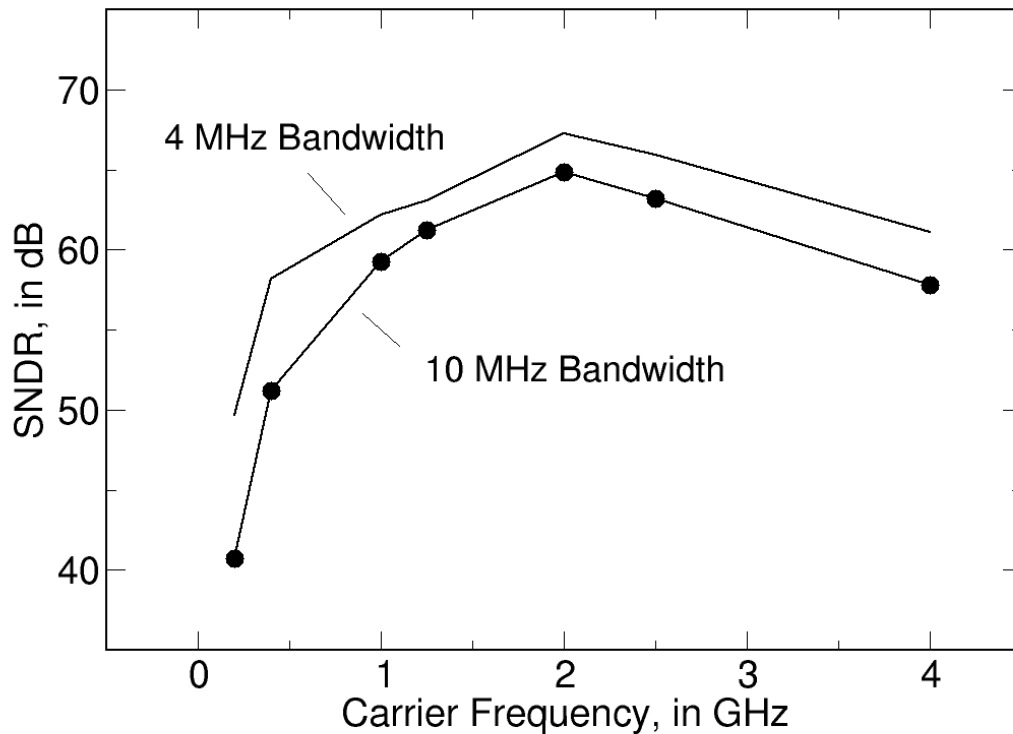


Fig. 4.24. SNDR versus carrier frequency.

Fig. 4.25 shows the power break down among different components in the system.

Finally, Table 4.2 lists the performance summary and comparison other state-of-the-art designs. The proposed receiver is able to achieve the widest tuning range among all the systems. Even compared with a more traditional design, its tuning range is comparable. Linearity performance wise (both in-band and out of band) it is also in line with other state-of-art designs. The noise figure of the system is limited by the clock jitter injected from the first feedback DAC. Compared to [28] which is intended to be a solution for the base station, this system consumes much less power since it avoids the use of active resonators. By avoiding such bulky passives, this design achieves the smallest reported area among all.

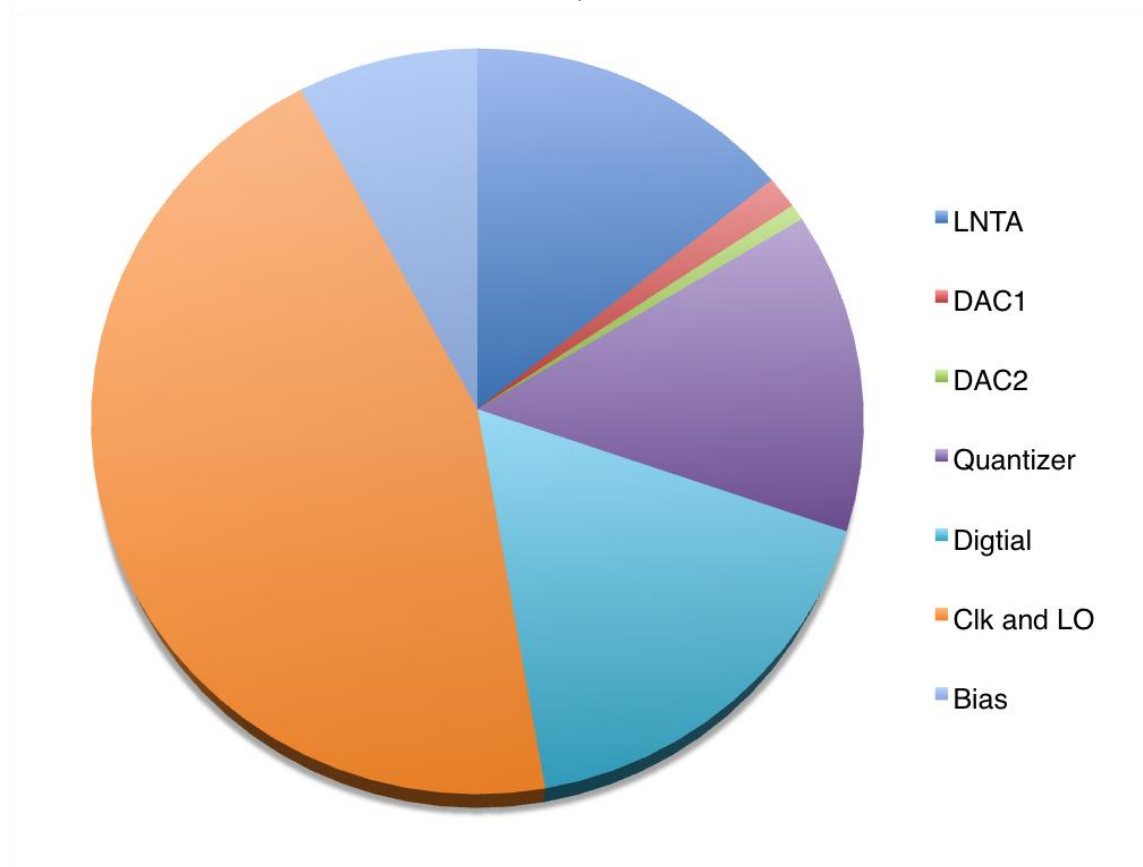


Fig. 4.25. Power breakdown for the entire receiver system.

	[4]	[24]	[5]	[25]	[26]	[27]	[28]	[29]	This work
Architecture	$\Delta\Sigma$ Modulator	Bandpass $\Delta\Sigma$	Lowpass $\Delta\Sigma$	Bandpass $\Delta\Sigma$	Bandpass $\Delta\Sigma$	RX AFE	Bandpass $\Delta\Sigma$ RX	Downconvert $\Delta\Sigma$ RX	RF-Digital $\Delta\Sigma$
RF Freq. [GHz]	0.4-1.7	0.8-2	0.9	0.95	2.4	0.4-6	0-1, 2-4	0.7-2.7	0.4-4
SNDR (dB) <sup>1</sup>	60	50-44 <sup>2</sup>	56	59 <sup>2</sup>	48	N/A	90 (SNR)	44	4 MHz: 68-60 10 MHz: 65-52
IB-IIP3 (dBm)	+19	-5 / -7	-12	N/A	-9	+6	+8	N/A	+10
OB-IIP3 (dBm)	+19	N/A	+4	N/A	N/A	+10	+8	-2	+13.5
Sensitivity (dBm) <sup>3</sup>	N/A	-75 <sup>3</sup>	6.2 dB NF	-77 <sup>3</sup>	N/A	3 dB NF	-97 7 dB NF	5.9-8.8 dB NF	-88 16 dB NF <sup>4</sup>
Power (mW)	50.4	30	80	75	40	30-55	1000	90	40.3 <sup>5</sup> (17-70.5)
Area (mm <sup>2</sup> )	0.8	2.3	1.2	1.36	0.8	2	5.5	1.1	0.56
Supply (V)	1.2	1.2	1.2	1.25	1.0	1.2	1.1/2.5	1.0	1.1/1.5
Technology	90 nm CMOS	0.13 $\mu$ m CMOS	65 nm CMOS	0.25 $\mu$ m BiCMOS	90 nm CMOS	40 nm CMOS	65 nm CMOS	40 nm CMOS	65 nm CMOS

<sup>1</sup> SNDR is normalized for 10 MHz bandwidth.

<sup>2</sup> Reported SNDR is only for 1 MHz bandwidth.

<sup>3</sup> Sensitivity is measured and reported for 10 MHz bandwidth except for [24] and [25], which are measured at 1 MHz Bandwidth.

<sup>4</sup> Noise figure = Dynamic range + LNTA Gain - Thermal noise floor integrated over 10 MHz = 68 dB + 20 dB - (-174 dBm/Hz + 70) = 16 dB

<sup>5</sup> 40.3 mW is measured at 2 GHz, including the divider power. System consumes 17 mW at 400 MHz and 70.5 mW at 4 GHz of operation respectively.

Table 4.2 Performance comparison table

## 4.4. CONCLUSION

This chapter presents an experimental prototype ADC based receiver design that supports a frequency of operation from 400 MHz to 4000 MHz, which covers the entire LTE bands worldwide. An NRZ feedback DAC design reduces the jitter sensitivity of the system, and aids in achieving a high SNDR over the frequency range of interest. It provides a large dynamic range with a low power consumption. It meets the three major criteria of the SDR systems. Without any bulky passives, the design maintains its small footprint, while digital-oriented design methodology enables a truly flexible receiver that is able to adapt to different standards with change of a couple control bits. Finally, the solution can scale naturally with technology.

# Chapter 5

## Mixer-First Receiver Design Considerations

### 5.1 Introduction to the Passive CMOS Mixer

Contradicting the conventional belief that analog/RF circuitry does not scale well with shrinking technology, the CMOS passive mixer is one of the few RF components that have most benefited from the process scaling. Passive mixers based on CMOS technology has been proposed earlier [57][58]. However, they did not attract much attention until the CMOS technology marched into the deep sub-micron region in the late 2000's. The recent improvements to CMOS technology empower the passive mixer designs, as they supersede active mixers designs in industrial designs and academia endeavors [59][60]. Compared to its active mixing peer, a passive mixer has one additional feature which is known as bi-directionality. Ironically, this unique property used to be considered major downside for the passive mixer, since it lacks the reverse isolation ( $S_{21}=S_{12}$ ) as most of the conventional RF circuits can provide. Furthermore, bi-directionality makes the analysis for a passive mixer so obscure that for a fairly long time, engineering intuition was hard to obtain. Fortunately, recent research efforts such as [59] have cleared up the obstacles. It has been shown by multiple sources that this two-way frequency translation feature of passive mixers provides a series of benefits over active mixers, therefore, new opportunities together with unique design challenges arise.

There are two primary differences between a passive mixer and an active mixer design. One is the feature of bi-directionality. Due to the absence of reverse isolation, passive mixers can down-convert the RF signal to the baseband and at the same time up-convert the baseband signal to the RF band. When the passive mixer switches turn on, the switches are transparent, only presenting their on-impedance, and they don't favor one port over the other. This is in contrast to case of an active mixer, where the Gilbert cells behave as the common-gate amplifiers. The passive feature of the passive mixer has long been considered a disadvantage, since the mixer cannot provide any power gain, thus limiting the overall system's noise performance. Moreover, the absence of reverse isolation in a passive mixer often brought up concerns about the robustness of the design. Interestingly, scientific research sometimes takes an unexpected turn, and this "annoying" transparency feature has turned out to be the very reason that the passive mixer is so popular now. The transparent feature allows the signal to translate to different frequencies, as well as allows for impedance frequency translation.

Another major difference between a passive mixer and an active mixer is the absence of DC bias current. The absence of the DC bias current takes away the origin of the low-frequency flicker noise. Therefore, with proper design, RF system with embedded passive mixers can achieve much better tradeoff between power and performance compared to designs adopting active mixers.

Recent research has shown that by utilizing multiple non-overlapping LO waveforms, the passive mixer designs can be better optimized compared with the use of a more traditional sinusoidal or simple square-wave LO waveforms [58][60][63][64][65]. Each of the clock pulses drives a different mixer switch. Together, a series of phase-shifted baseband outputs can be generated, and they can later be summed with the baseband trans-impedance amplifier (TIA) to reconstruct the complete baseband output.

## 5.2 Passive Mixer-First Receiver Design Basics

Back in Chapter 2, the concept of digitally-assisted RF receiver design has been introduced. These designs aim to minimize the component count of the RF front-end design. The passive mixer-first receiver architectures stands at the forefront of the movement towards minimalism in design methodology, which draws upon innovations based on recent studies on the passive mixer. A mixer-first system can be simply described as a receiver topology without the RF amplification stage (LNA or LNTA). Recent research effort has demystified the passive mixer, and the idea of the passive mixer-first design has gained a lot of momentum in different kinds of wireless applications.

To understand the idea of passive-mixer first receiver designs, it is better to start with explaining how a multi-phase passive mixer network operates. Fig. 5.1 shows a simple circuit model for a 4-phase passive mixer network, and Fig. 5.2 shows the four clock waveforms driving each of the four phases in a passive mixer system. One fundamental

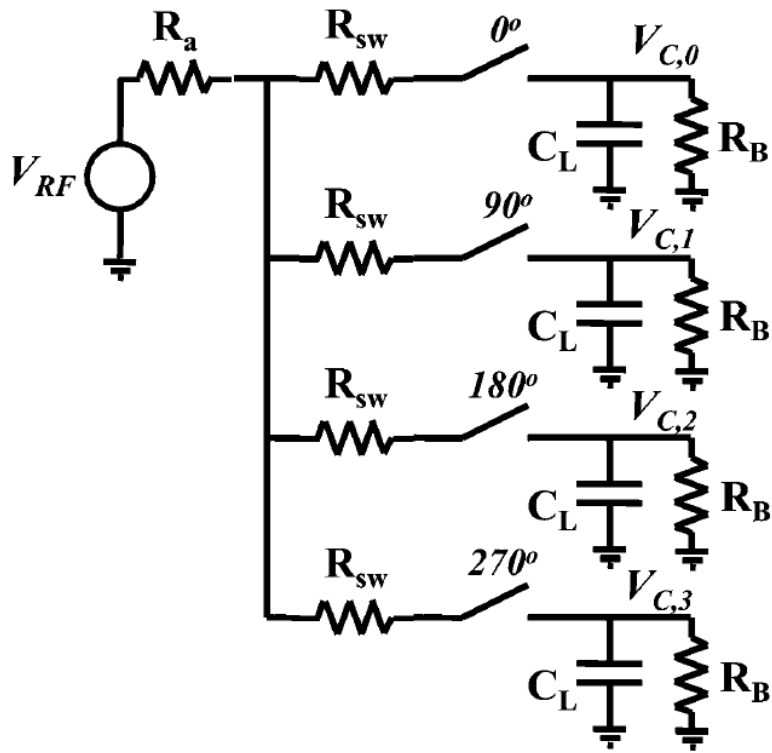


Fig. 5.1. Simplified circuit model of passive mixer.

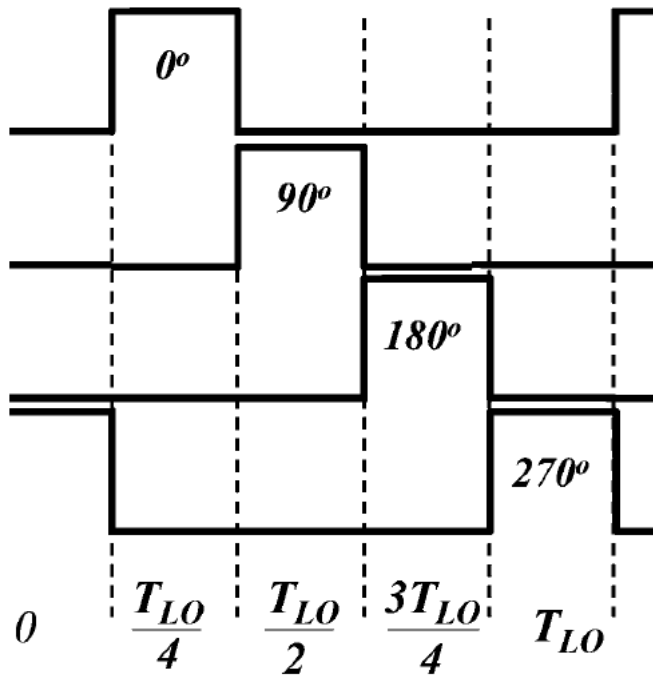


Fig. 5.2. Non-overlapping LO waveforms.



question to be addressed is how to provide the impedance match to the antenna without the LNA. Moreover, the bidirectional nature of the passive mixers might degrade the overall noise figure, since the RF circuits and the IF circuits are very much coupled together. Reference [26] provides an in-depth analysis to address the above questions.

Based on ref. [26], the effective impedance presented to the antenna port can be described as

$$R_{EQ} = \gamma R_B + R_{SW} = R_{SW} + \gamma \frac{R_{FB}}{1 + A} \quad (37)$$

where  $\gamma$  is related to the duty cycle of the LO waveform, and for a 50% duty cycle LO,

$$\gamma = \frac{2}{\pi^2} \approx \frac{1}{5} \quad (38)$$

For an LO with a 25% duty cycle,

$$\gamma = \frac{2}{\pi^2} (2 - \sqrt{2}) \approx \frac{1}{8} \quad (39)$$

Even though neither one of the above expressions is easy to interpret, the end results themselves provide some interesting insight into how the passive mixers work. The input impedance presented to the RF port is roughly inversely proportional to the number of the paths, which is similar to shunting multiple paths with the same impedance together. Qualitatively speaking, passive mixers have different path turned on and off sequentially within a complete clock cycle. From the antenna's perspective, it is like driving all the paths in parallel together within a clock cycle. The overall impedance presented to the antenna is a factor of  $N$  smaller, if there are  $N$  "parallel paths," which is a major benefit of the mixer-first design. Due to the passive mixer's transparency property, the baseband stage can be designed for an input impedance as high as  $50 \times 8 = 400 \Omega$ , to match up to the  $50 \Omega$  antenna impedance when using a 12.5 % duty cycle LO. This leads to a large power reduction in the baseband amplifier design. In addition, the mixer-first topology as shown in Fig. 5.3 doesn't include an LNA in the system, which is often the most power-hungry component in the system budget. As a result, passive mixer-first architecture can be very power efficient.

On the other hand, noise analysis for such a system is not so straightforward. The noise factor of the system noise model detailed in Fig. 5.4 can be written as [25]

$$F = 1 + \frac{R_{SW}}{R_a} + \frac{Z_{sh}}{R_a} \left( \frac{R_a + R_{sw}}{Z_{sh}} \right)^2 + \gamma \frac{R_F}{R_a} \left( \frac{R_a + R_{sw}}{\gamma R_F} \right)^2 \quad (40)$$

$$+ \gamma \frac{Z_{sh}}{4kTR_a} \left( \frac{R_a + R_{sw}}{\gamma R_F} + \frac{R_a + R_{sw} + Z_{sh}}{Z_{sh}} \right)^2$$

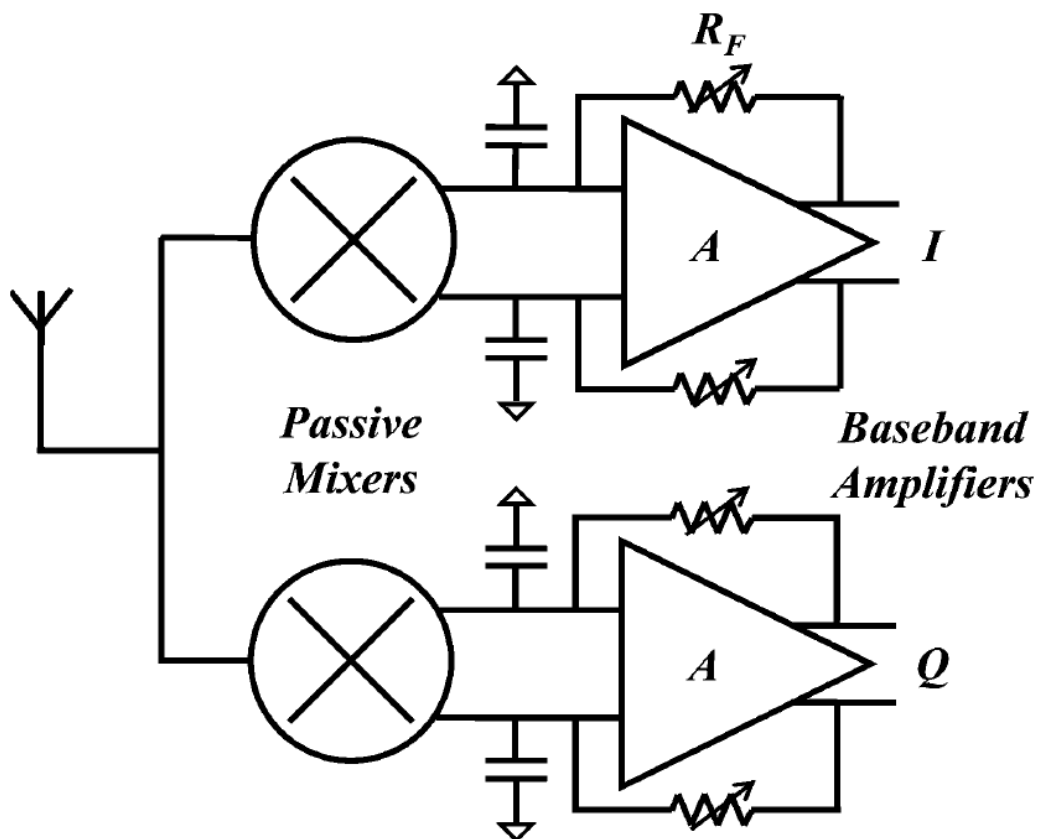
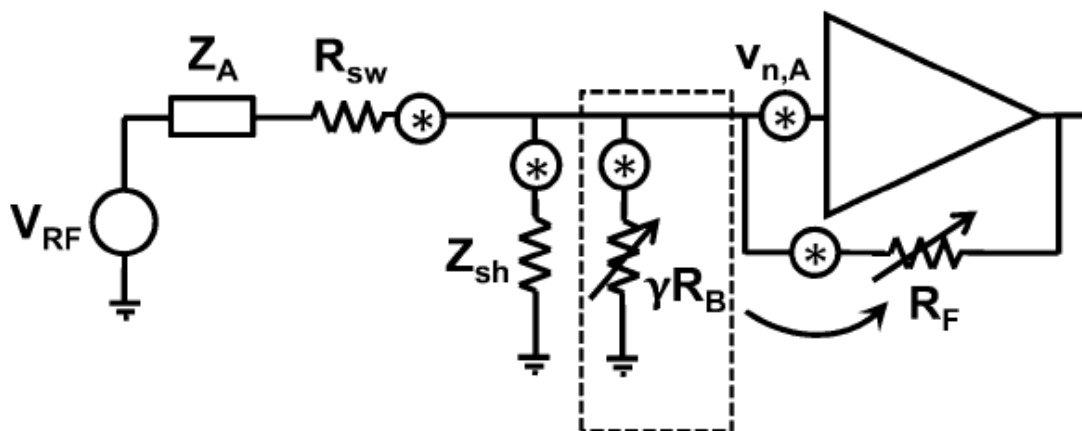


Fig. 5.3. Passive mixer-first receiver with baseband TIA.



Andrews, ISSCC 2010

Fig. 5.4. Equivalent noise model for mixer-first design.

The second term in the above equation comes from the switch on-impedance, while the third term originates from the shunt impedance  $Z_{sh}$ , which is used in Ref. [26] to describe the effect of harmonic noise folding. The fourth term stands for the noise contributing from the feedback resistor  $R_F$ . Finally; the last term represents the noise from the baseband amplifier. To optimize for the noise performance, Ref. [26] proposed to use an 8-phase harmonic rejection architecture to remove most of the noise folded down from the third and the fifth harmonics.

## 5.3 Baseband Trans-impedance Amplifier Design Tradeoff

One of the essential building blocks for a mixer-first design is the baseband trans-impedance amplifier (BB-TIA). Its design seems to be rather benign from the high level perspective; however without careful design; it will limit the overall noise figure performance and linearity performance, as reported in [62]. To understand the design tradeoff behind the BB-TIA, a comparison between popular amplifier choices for BB-TIAs in literature is first presented, followed by detailed discussion about the pros and cons of each design, and finally, the desired topology will be highlighted.

Three amplifier structures which are popular in BB-TIA designs are listed in Fig. 5.5. The first possibility is a two-stage operational amplifier design reported in [62]. The advantage of such a design is that the loop gain of the TIA is unaffected by the feedback resistor, due to the Op-Amp's low output impedance. However, Op-Amp designs tend to be power-hungry.

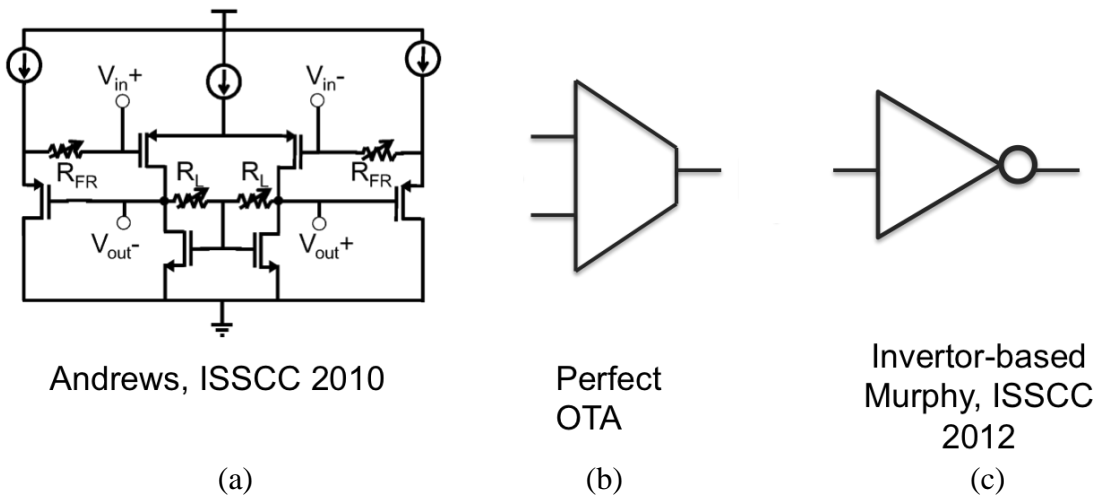


Fig. 5.5. Different amplifier structure candidates for BB-TIA design.

An operational transconductance amplifier (OTA) as shown in Fig. 5.5, on the other hand, would be loaded by the feedback resistors, assuming its output impedance is much larger than the feedback resistors. In this case, the loop gain is set by the feedback resistors. However, for CMOS technology in the deep sub-micron region, the devices' output impedance is quite limited, and hence the loop gain of the BB-TIA is set by the shunt impedance between feedback resistors and the output impedance of the OTA. As shown later in this section, this does have a negative effect on the overall noise performance due to the  $g_m$  noise component.

An inverter-based TIA design was recently reported in [68]. An inverter-based amplifier design has some really interesting properties due to its mid-range output impedance. With a large feedback resistor, the design behaves like an op-amp, while the inverter-based amplifier behaves like an OTA with a smaller feedback resistor. Moreover, the inverter-based amplifier can provide a large dynamic current in the presence of a blocker to maintain its linearity performance over a large signal transient.

Based on the derivations for a general shunt-shunt feedback network from [73], it can be shown that the input impedance of an Op-Amp based TIA like [62] can be expressed as

$$R_{in} = \frac{R_{FB}}{g_m r_o} \quad (41)$$

By a similar analysis, it can be shown that the OTA-based TIA's input impedance can be expressed as

$$R_{in} = \frac{R_{FB}}{g_m R_{FB}} = \frac{1}{g_m} \quad (42)$$

For an inverter-based TIA design, the input impedance can be described as

$$R_{in} = \frac{R_{FB}}{g_m (r_o || R_{FB})} \quad (43)$$

### 5.3.1 Noise Analysis for the BB-TIA

Given the above, the noise figure based on (40) from various designs with different value of  $R_{FB}$  are plotted in Fig. 5.6. For the OTA case, the input impedance is always around the value  $1/g_m$ , especially when  $R_{FB}$  is reasonably large. This would be used to match to the antenna's impedance, which is why the noise figure saturates at the 3dB level beyond certain values of  $R_{FB}$ .

With small  $R_{FB}$ , the Op-Amp needs a smaller  $g_m$  to maintain the same input impedance. This degrades the input-referred noise performance and causes a dramatic increase in the noise figure. This observation makes Op-Amp design unsuitable with smaller  $R_{FB}$ . On the other hand, as  $R_{FB}$  increases,  $g_m$  has to be scaled up to maintain the same impedance. Therefore, the input-referred noise performance of the TIA is improved, and hence the overall NF goes down. Compared to the OTA case, the Op-Amp based design does not rely on  $1/g_m$  for the input matching. This decouples  $g_m$  from the need of input matching at larger  $R_{FB}$  levels, which helps to achieve a much better NF compared to the OTA with a large  $R_{FB}$ . Unfortunately, to achieve the sub-one-dB NF performance,

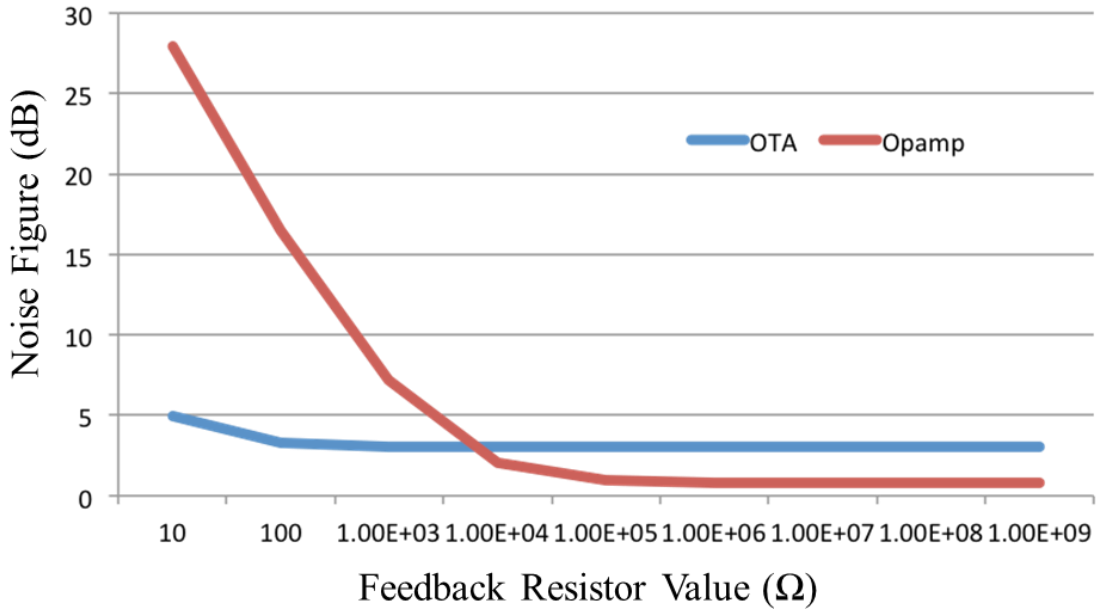


Fig. 5.6. Noise figure for OTA and Op-Amp with different feedback resistors.

a prohibitively large  $g_m$  is required, which makes the Op-Amp way too power hungry. Nevertheless, the analysis provides valuable insight about the baseband design choice.

So far, the trade-off between the choice of OTA or Op-Amp as the BB-TIA amplifier depends on the value of  $R_{FB}$  chosen, or equivalently, the gain allocated to the first baseband stage of amplification. Interestingly, the inverter-based design seems to be a better option: with a smaller  $R_{FB}$ , it behaves like the OTA, and with a larger value of  $R_{FB}$ , it functions as the Op-Amp, therefore its corresponding NF always follows the minimum of the two curves shown in Fig. 5.6.

Most of the reported mixer-first designs such as those in [62] [68] have two stages of baseband amplification. When the noise is referred back into the antenna port, the resulting term in the overall noise figure expression can be written as

$$F_{new} = F + \left(\frac{1}{R_{attn}}\right)\left(\frac{1}{g_m}\right)\left(\frac{100}{R_{FB}}\right)^2 (1 + N_f) \quad (44)$$

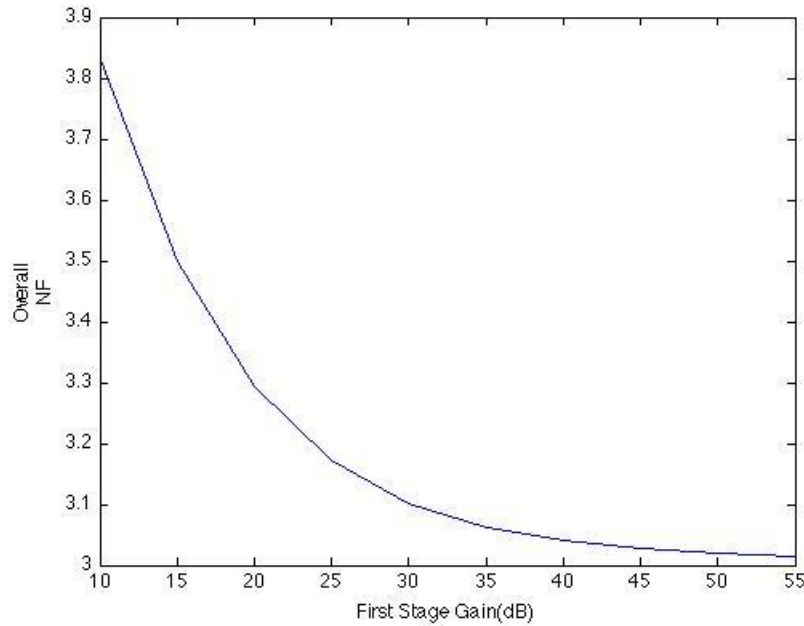


Fig. 5.7. Noise figure with the second amplification stage.

Resistance (ohm)	First Stage Gain(dB)	G <sub>m</sub> (mS)	Amp Gain
316	10	21	6.6
562	15	23	13(inv)
1k	20	24	24
1.7K	25	24.4	41
3.162K	30	24.7	76
5.62K	35	24.8	139(OTA)
10K	40	25	250

Table 5.1. Gain allocation and  $G_m$  requirement for different value of  $R_{FB}$ .

Fig. 5.7 studies the second stage's impact on the overall noise performance. The second stage only has a mild impact on the overall noise figure performance, which should not be surprising at all.

To summarize, an inverter-based or OTA-based BB-TIA design provide the better tradeoff between power and noise performance. In general, it is a bad idea to allocate a large amount of gain to a single stage, in particular, the first stage. Table 4.1 lists different values of  $R_{FB}$  and  $G_m$  required to achieve different gain specifications. For the completeness of this discussion, there is one more type of BB-TIA design that has not been discussed, which is the CG amplifier design reported in [74]. It has the lowest power consumption due to its open loop nature; however its noise and linearity performance also suffer.

### 5.3.1 Analysis for BB-TIA Out-of-Band Linearity

Out-of-band (OOB) linearity performance is one of the key performance metrics in describing the receiver's blocker resilience. As a receiver has no control over its input statistics, when the receiver is jammed by a large interference in a nearby frequency, the receiver is expected to still maintain its functionality with minimum performance degradation. This really stresses the importance of the out-of-band linearity performance of a receiver.

Most of the time, baseband amplifiers set the linearity limits. Due to the mixer-first design's simple topology, the BB-TIA is the first stage to provide amplification; therefore it is also the first stage to experience linearity degradation. The passive CMOS mixer switches, to the first order, are functioning as switches. The signal voltages on the two ends of the switches are retained to their minimum since the switches do not provide any power gain. Therefore, the switches tend to have a good linearity performance.

To improve the out-of-band linearity performance, reducing the OOB blocker as early as possible is essential. Recent passive mixer-first designs [62] [68] rely heavily on  $C_L$  in Fig. 5.1 for attenuating the blocker right after down-conversion so that the large blocker does not make its way into the BB-TIA or the rest of the system. Hence, a good OOB linearity performance can be preserved.

However, the possible frequency locations of the blockers vary drastically from one standard to another. For some standards, such as GSM, a reasonably large interference presented at 40 MHz away from the carrier frequency might easily saturate the receiver system. To accommodate a relatively close-in jammer, the  $C_L$  required for the passive-mixer-first design might be prohibitively large. Ref [62] has reported of using a  $C_L$  as large as 100 pF, which results in a large area overhead and, hence, a large silicon production cost.

To quantify the issue, a design example of the mixer-first design is provided. Assume the baseband amplifier has an in-band IIP3 of -20 dBm, and the CMOS mixer switches have an on-impedance of 20  $\Omega$ . Table 5.2 shows the relationship between OOB filtering and OOB IIP3



Attenuation 80 MHz away (dB)	Out-of-Band IIP3 (dBm)
0	-20
10	-10
20	0
30	10
40	20

Table 5.2. Attenuation requirement for different value of out-of-band IIP3 performance.

To achieve a 0 dBm IIP3 with an 80 MHz frequency offset, the system requires 20dB of filtering at the 80 MHz offset. This implies that the 3dB filter corner needs to be placed around 8 MHz, which results in a  $C_L$  of 663 pF. If an OOB IIP3 of 10 dBm is targeted,  $C_L$  needs to be as big as 6.6 nF.

Fortunately, there is another active component in the system that can share the blocker filtering burden put on the capacitor  $C_L$ . As shown in Fig. 5.8, a first-order filter can be integrated into the BB-TIA with the capacitor  $C_{FB}$ . Due to the Miller effect [73], the effective capacitor presented to the mixer can be boosted by the gain of the amplifier. Therefore, a more area-efficient design is possible.

Fig. 5.9 shows a graphical representation of how the two capacitors  $C_L$  and  $C_{FB}$  influence the input impedance of the BB-TIA. As the frequency increases, the loop gain of the network drops. The OTA is losing control of the feedback network due to its limited unity gain bandwidth. As a result, the input impedance  $R_{IN}$  would increase, while the imaginary part  $C_{IN}$  would diminish. The overall input impedance can then be summarized as  $Z_{IN}$ , shown in Fig. 5.9. There is a noticeable kink just around the unity gain frequency of the OTA. A blocker signal at this frequency would cause a larger voltage swing at the input node of BB-TIA, since the input impedance of BB-TIA is much larger in this frequency. As a result, OOB IIP3 at this frequency would suffer. To mitigate this issue,  $C_L$  can be added to reduce the out-of-band impedance resulting from the limited bandwidth of the BB-TIA as shown in Fig. 5.9 (d).

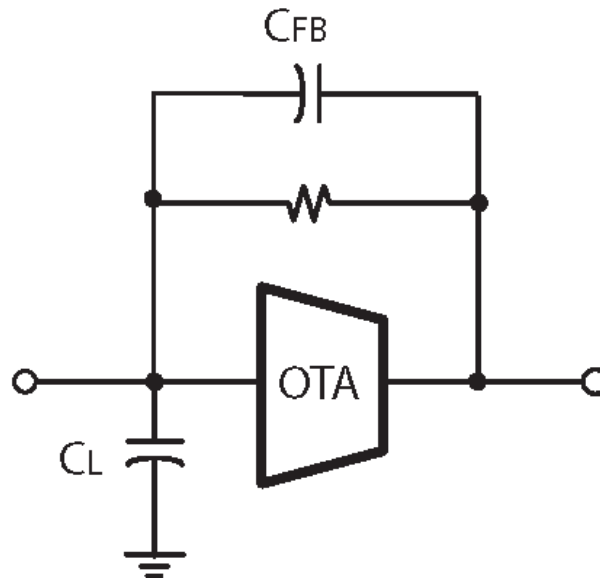


Fig. 5.8. BB-TIA with  $C_L$  and  $C_{FB}$ .

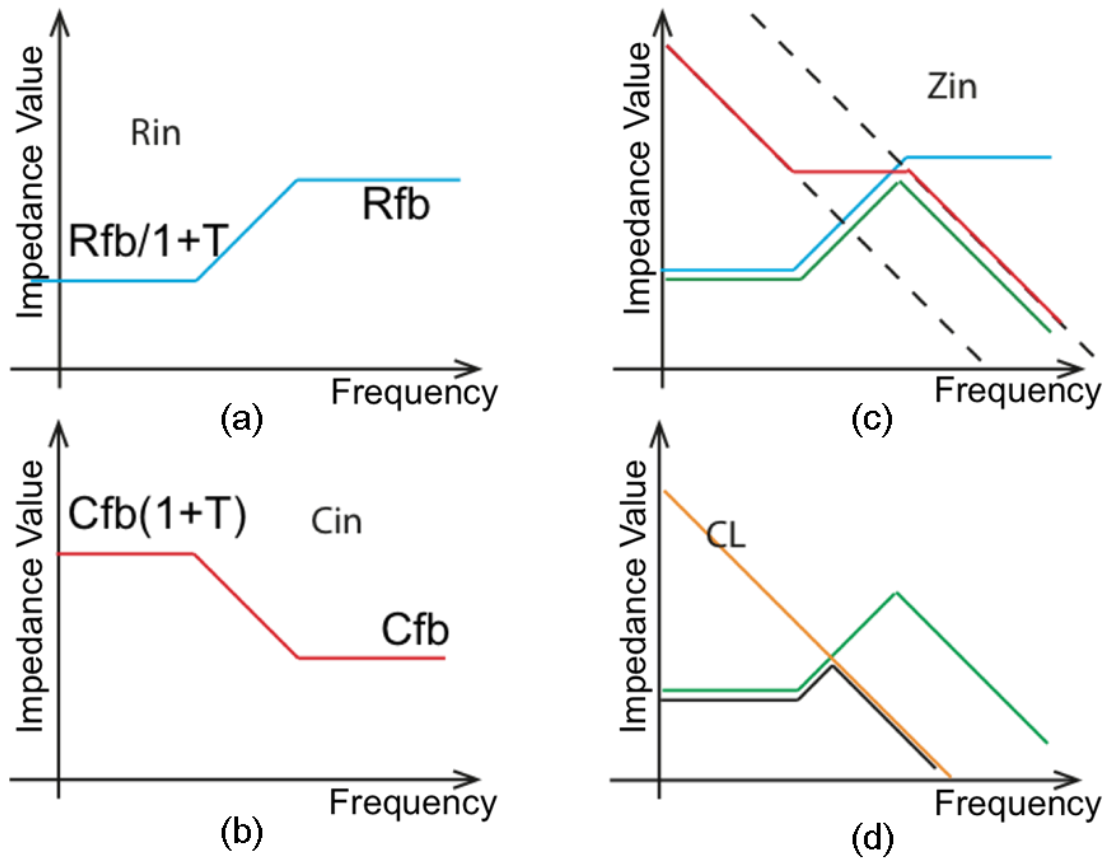


Fig. 5.9. Input Impedance with  $C_L$  and  $C_{FB}$ .

## 5.4 Harmonic Rejection System

### 5.4.1 Harmonic Folding and Its Impact on the Noise Figure Performance

Optimizing the noise performance of a mixer-first design is not a trivial task. Due to the absence of the frontend RF amplifier (such as an LNA or LNTA), the baseband stage input-referred noise is directly reflected on the overall noise figure without any attenuation. Worse still, passive mixers cannot provide any power gain, but only conversion loss, which makes designing a mixer-first receiver with a low noise figure even more challenging.

In section 5.2, an analytical expression for the noise figure is shown as (40). The second term in expression (40),  $\frac{Z_{sh}}{R_a} \left( \frac{R_a + R_{sw}}{Z_{sh}} \right)^2$  is from a fictional noise source  $Z_{sh}$ , which is used by [26] to describe the harmonic noise folding from the high order harmonic frequencies. To achieve a better noise figure performance, [26] proposes to the idea of harmonic rejection to remove noise folding from the third and fifth order harmonic frequencies.

The issue of harmonic noise folding can be explained through Fig. 5.10. According to [75], the output spectrum for a mixer's output can be expressed as

$$\begin{aligned}
 Y(f_{IF}) &= \sum_{n=-\infty}^{\infty} P_{1,n} X(f_{IF} - nf_{LO}) & \begin{array}{l} n=+1 \quad f_{LO}-f_{IF} \\ n=-1 \quad f_{LO}+f_{IF} \\ n=+2 \quad 2f_{LO}-f_{IF} \end{array} \\
 &= \sum_{n=-\infty}^{\infty} P_{1,n} X(nf_{LO} - f_{IF}) & (45)
 \end{aligned}$$

The coefficient  $P_{1,\pm k}$  then represents the conversion gain from frequency  $k \cdot f_{LO} \pm f_{IF}$  to  $f_{IF}$ .

$$P_{1,2k-1} = \frac{1}{\pi(2k-1)} \quad (46)$$

Through some manipulation of the above equations [75], it can be shown that if  $S_{N3}(t) = N_3$  (white), then

$$S_{N3}(f) = N_{N3} \cdot \alpha \quad (47)$$

$$\alpha = \frac{1}{T_{LO}} \int p_1^2(t) dt = \sum_{-\infty}^{\infty} |p_{1,n}|^2$$

Where, for a square wave  $p_1(t)$ ,  $\alpha = 1$ .

The noise for the first pair of sidebands ( $f_{LO} \pm f_{IF}$ ) accounts for  $2 \times (\frac{2}{\pi})^2 = 81\%$  of the overall noise. The noise from the third pair ( $3f_{LO} \pm f_{IF}$ ) accounts for  $2 \times (\frac{2}{3\pi})^2 = 9\%$  of the total noise. The remaining harmonics account for the rest of the noise, which is around 10%. This suggests that removing the noise folding from the third and fifth harmonics can improve the system noise figure performance.

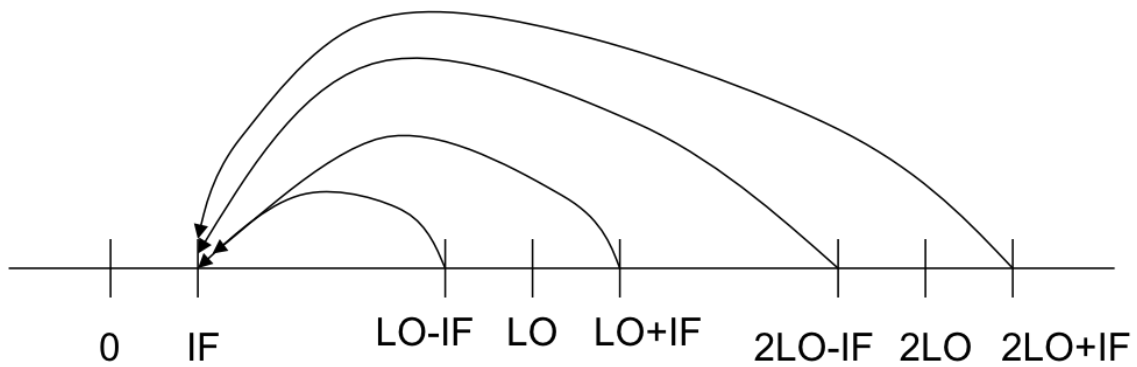


Fig. 5.10. Harmonic noise folding.

## 5.4.2 Harmonic Rejection System Design

The idea of harmonic rejection is detailed in figure 5.11. Multiple phases of the LO are combined, creating a closer approximation of the perfect sinusoidal LO waveform that is free of the third and fifth harmonics. The system implementation diagram is shown in Fig. 5.12.

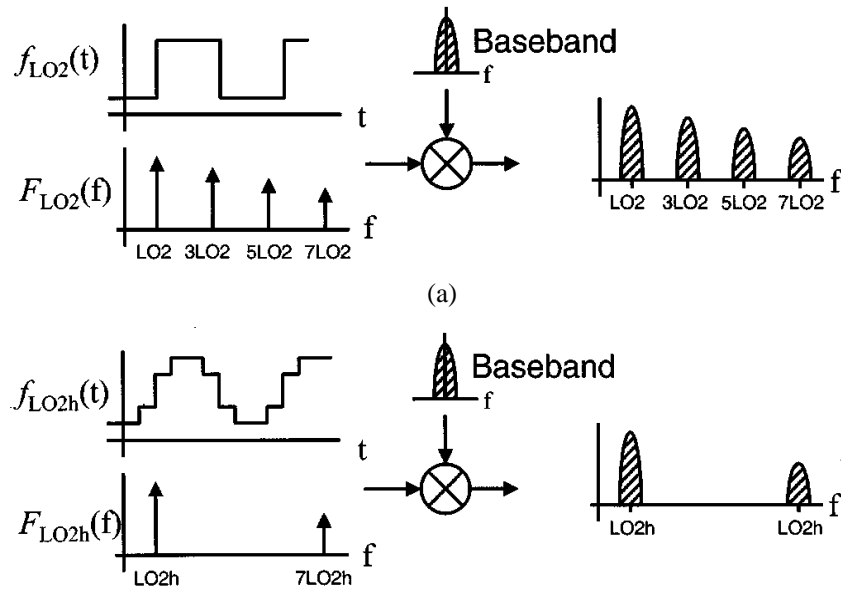
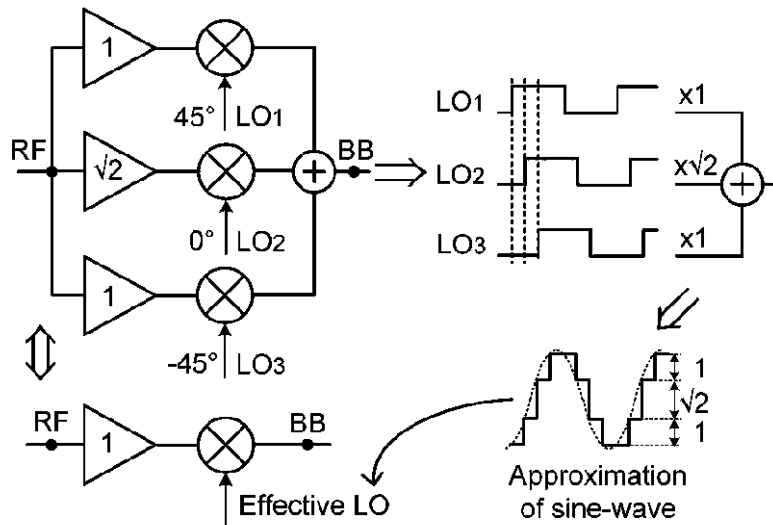


Fig. 5.11. The concept of harmonic rejection.



Ru, ISSCC 2008

Fig. 5.12. System level implementation of harmonic rejection.

Harmonic rejection is actually a form of poly-phase filtering, and it suffers from the same issues that have long plagued poly-phase filter designs. This section is dedicated to discussing the issue associated with harmonic rejection design. It will first compare the 8-phase poly-phase harmonic rejection network to a sampling network that is sampling 8 times faster. Then it will focus on the origins of the issues that degrade the harmonic rejection accuracy.

For Nyquist ADC design, an alternative to oversampling a high-speed input with a faster sampling frequency is to sample the input with multiple ( $n$ ) slower parallel paths. For now, we can assume that we have  $n=8$  number of slower parallel sampling paths, all controlled by different phases of the clock signals running at  $1/n$  of the original speed, as demonstrated in Fig. 5.13. This idea is widely adopted in time-interleaved ADC designs for applications requiring multi-GHz sampling speeds.

The reason time interleaved sampling works is that the 8 paths provide distinct output information within one reference clock cycle. Therefore, comparing just sampling once in every reference clock cycle, now there is eight times more information describing the input signal which is equivalent to oversampling by 8 times. Given this understanding, it is not hard to realize that duty cycle variation of the slower clock doesn't matter at all for a time interleaved system.

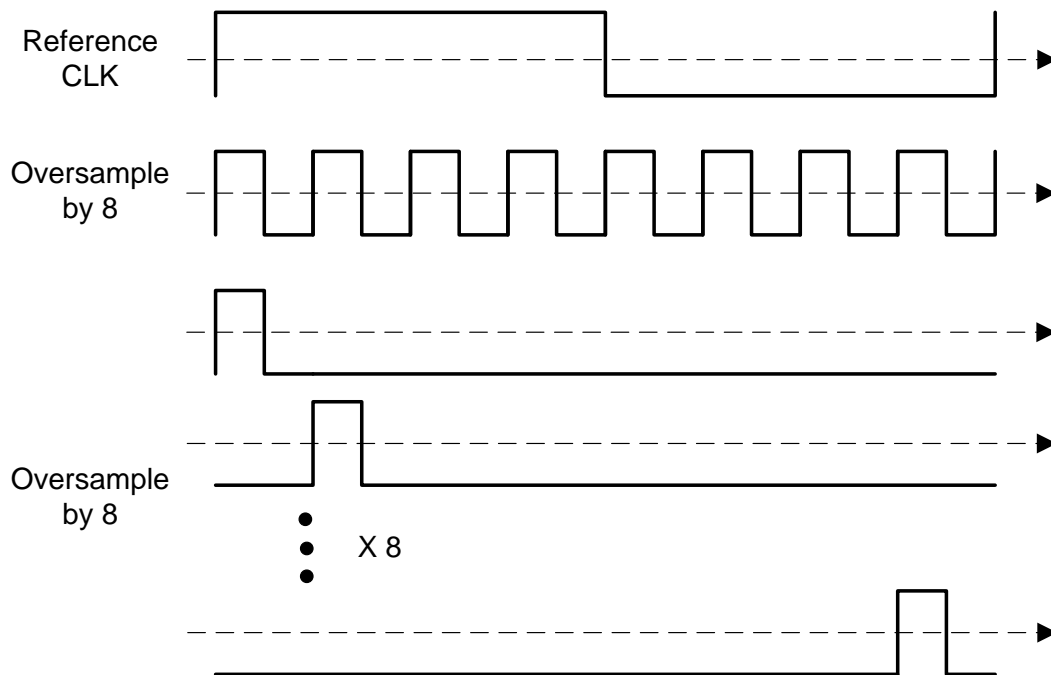


Fig. 5.13 Oversampling and time interleaved sampling.

Since the change in duty cycle of the slower clocks doesn't change the information provided by each of the paths, for a time-interleaved system clocked by two different clock waveforms, shown in Fig. 5.14, the final output would be the same. All discussions about the interleaving system are carried out in the time domain. As a matter of fact, it would be more insightful to examine the problem from the frequency domain perspective.

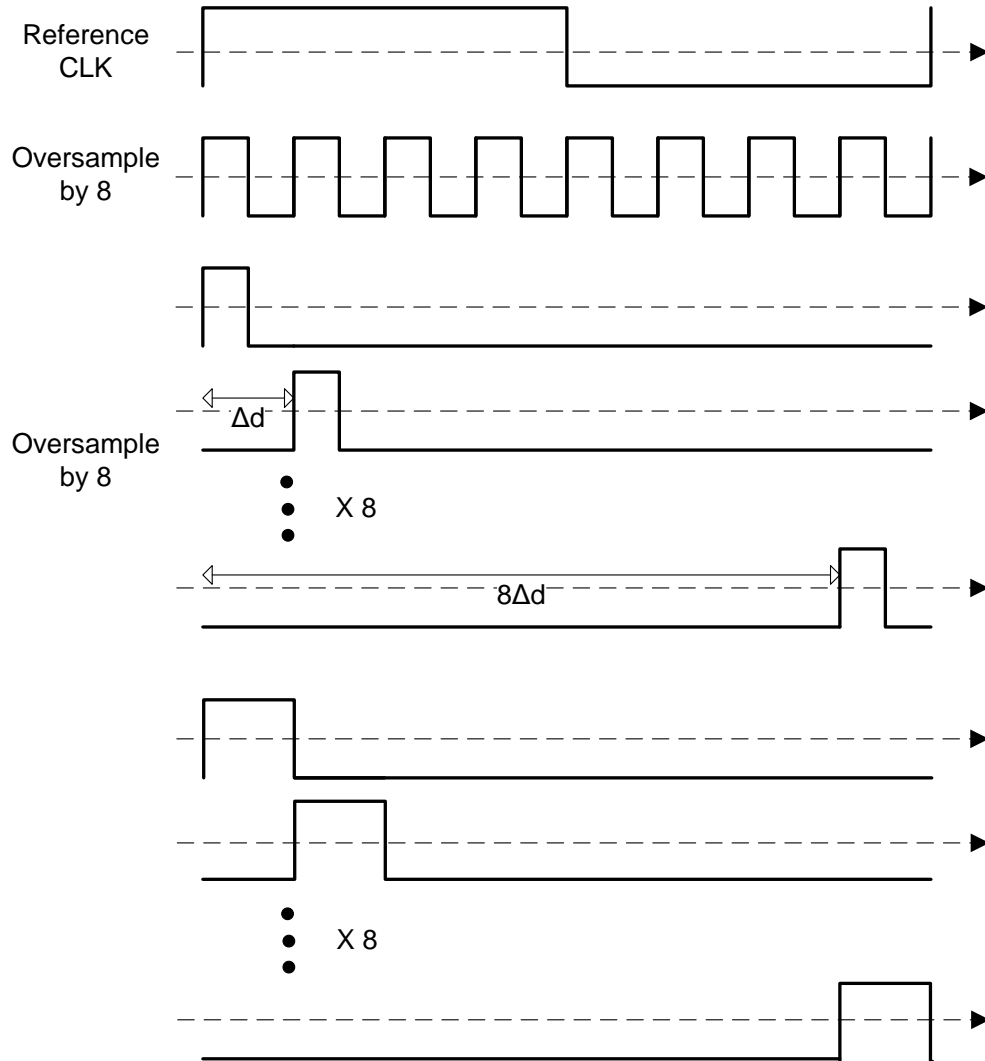


Fig. 5.14 Time-domain interleaving sampling with different duty cycle.

For the sake of simplicity and clarity, discussion will be restricted to 4-path oversampling only, but the conclusion can be easily expanded for a system with more paths. For obvious reasons, there will be aliasing within each of the 4 paths as shown in Fig. 5.15.

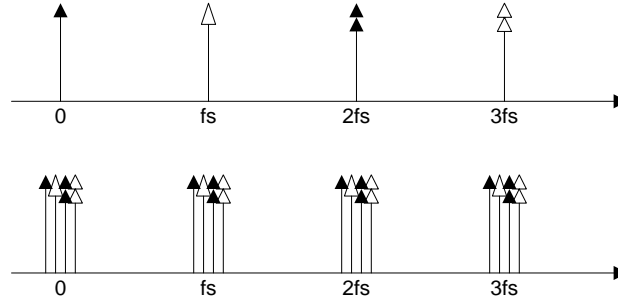


Fig. 5.15. Aliasing content within one slower sampling path.

A close examination into each path would reveal the fact that each path has a slightly different aliasing content, as the aliasing contents are rotated by different phases, which is shown in Fig. 5.16. Therefore, when they are added up, the aliasing content can be removed. Frequency contents at DC,  $f_s$ ,  $2f_s$ , and  $3f_s$  can be cancelled, but not the frequency content at  $4f_s$ , as it experiences the same phase rotation as the frequency content residing at DC.

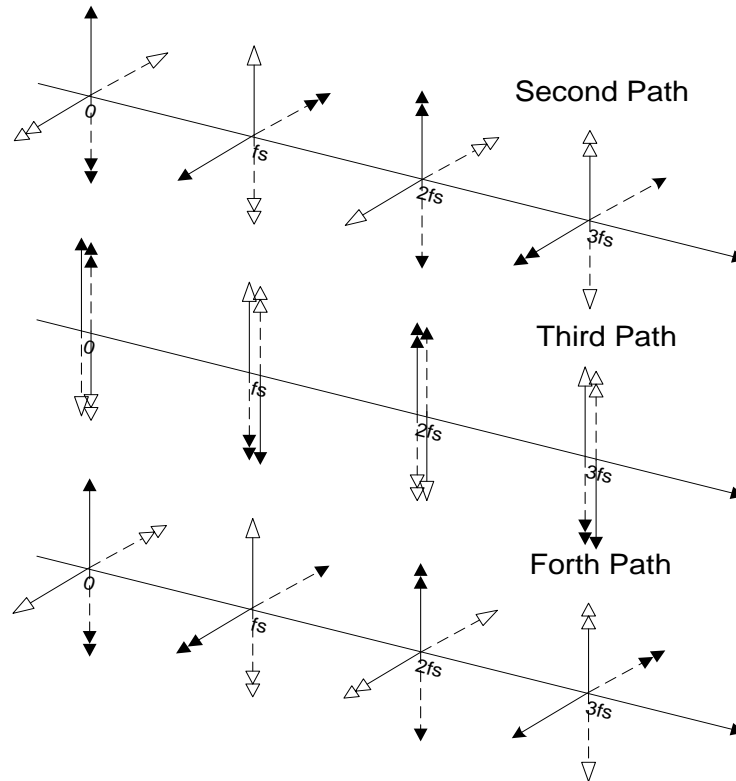


Fig. 5.16 Aliasing contents in each of the paths.



So far, our discussion is only limited to the ideal case. Next, the impact of mismatch is considered. In general, there are two types of mismatches: phase mismatch ( $\alpha$ ), and gain mismatch ( $\Delta d$ ). Because of the mismatches in the system, the vector contents won't be in perfect alignment as in the ideal case as shown in Fig. 5.17. Therefore, when all the paths are summed, there would be residues due to incomplete cancellation as in Fig. 5.18.

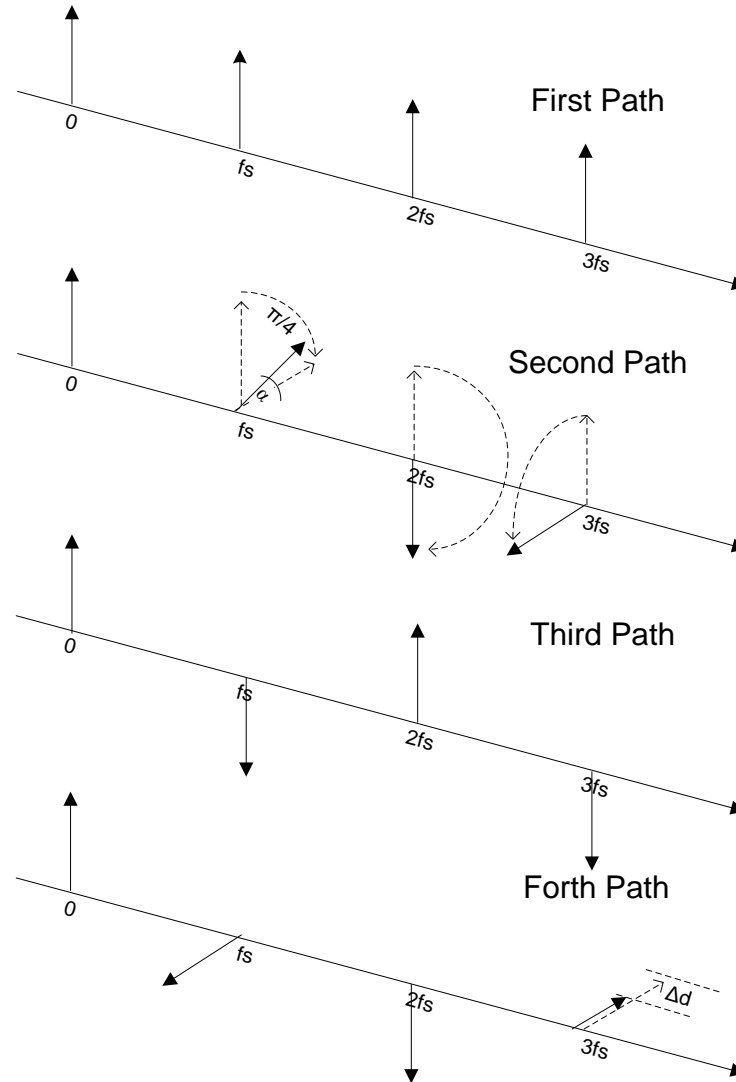


Fig. 5.17. Imperfect alignment due to the presence of mismatch.

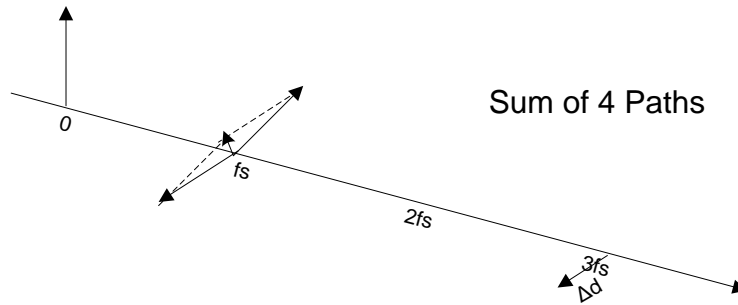


Fig. 5.18 Incomplete harmonic cancellation due to phase and gain mismatch.

Mismatch limits the overall performance (in the case of an ADC, they result in distortion tones) as demonstrated in Fig. 5.19. In general, the resolution is limited to 6-8 bits due to the limited matching between components such as capacitors and resistors (1% element mismatch translates to  $\sim 40$  dB harmonic rejection performance). More paths might help, since the mismatches among all paths tend to average out, but this comes with a huge power and area penalty. Fig. 5.20 provides a behavioral model for studying atime-interleave system under phase and gain mismatches.

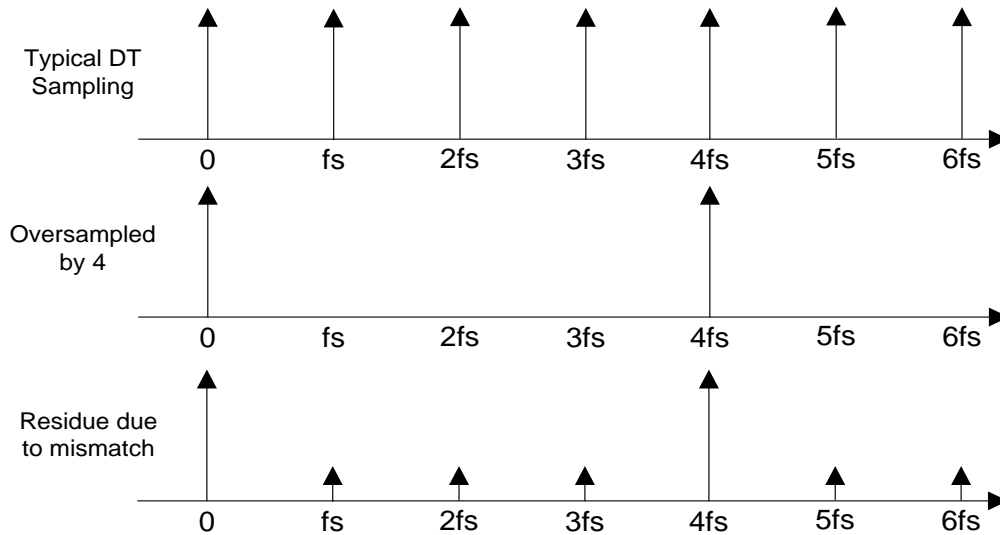


Fig. 5.19 Performance limitation due to mismatches.

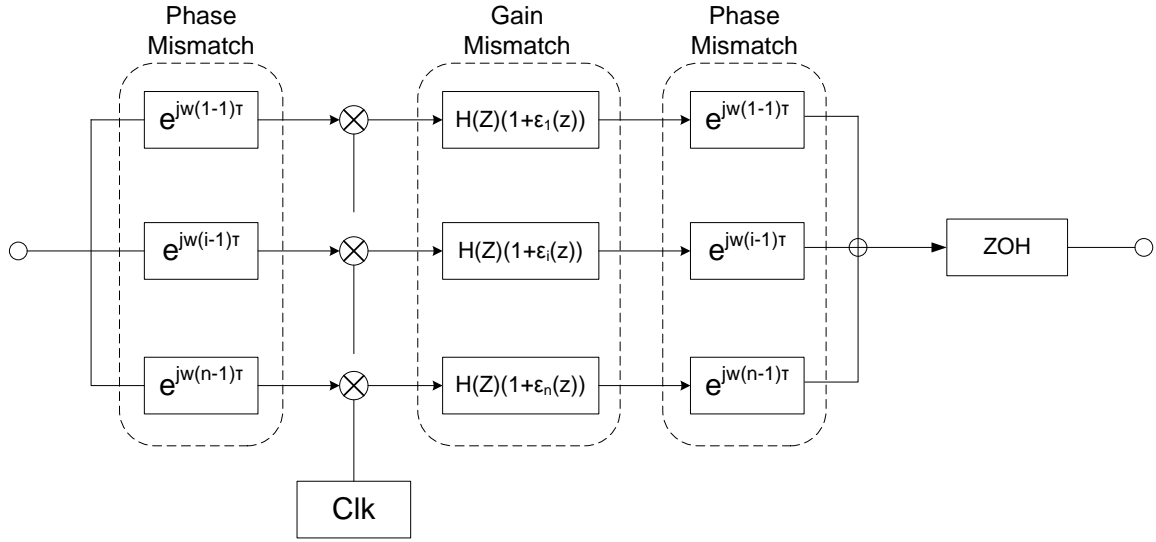


Fig. 5.20 Behavior model for time-interleaved system with phase and gain mismatches.

In Chapter 3, it was established that current-mode sampling is indeed similar and related to continuous-time mixing. This allows us to expand the previous discussions into the time-interleaved sampling to cover a mixing system with a harmonic rejection scheme.

Following a similar reasoning as shown for the time-interleaved sampling network, a harmonic rejection system is sensitive towards phase and gain mismatches. Gain mismatches between different paths scale all the frequency contents in the same way as shown in Fig. 5.21(a). Phase mismatch affects frequency contents differently even within one path as in Fig. 5.21(b). Noticeably, phase mismatch results in more phase shift for the frequency content at high order harmonic. Since this phase winding/unwinding process happens at the same time that the sampling/mixing take place, it cannot be fixed or undone. As a result, gain mismatch can be compensated with techniques like the one reported in [76], but phase mismatches cannot be improved or corrected afterwards.

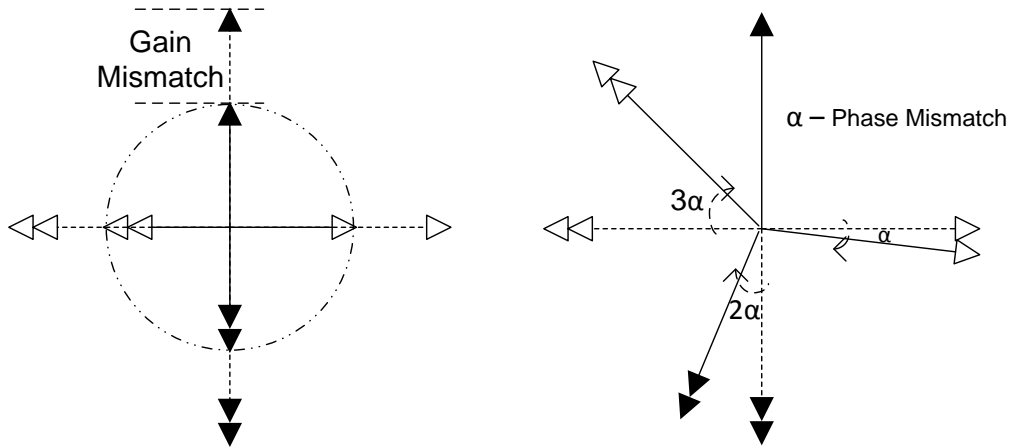


Fig. 5.21. Gain and phase mismatches degrade the harmonic rejection performance.

Based on the model in Fig. 5.20, mismatch sensitivity results can be obtained for different harmonic rejection implementation, which is shown in Fig. 5.22. The simulation result is for a 1.5 GHz LO. The simulation assumes  $0.034^\circ$  phase mismatch among different mixing paths. The phase mismatch used would translate to 62.5 fs timing mismatch among different paths. For comparison, with 1 ps timing mismatch among different paths, the third order rejection ratio drops to 33.7 dB. Phase mismatch has a benign effect on down-converting the signal at the fundamental frequency, while it is critical for rejecting the interferences at multiple harmonic frequencies, since phase mismatch doesn't affect signal vector addition as much as it does to the vector subtraction.

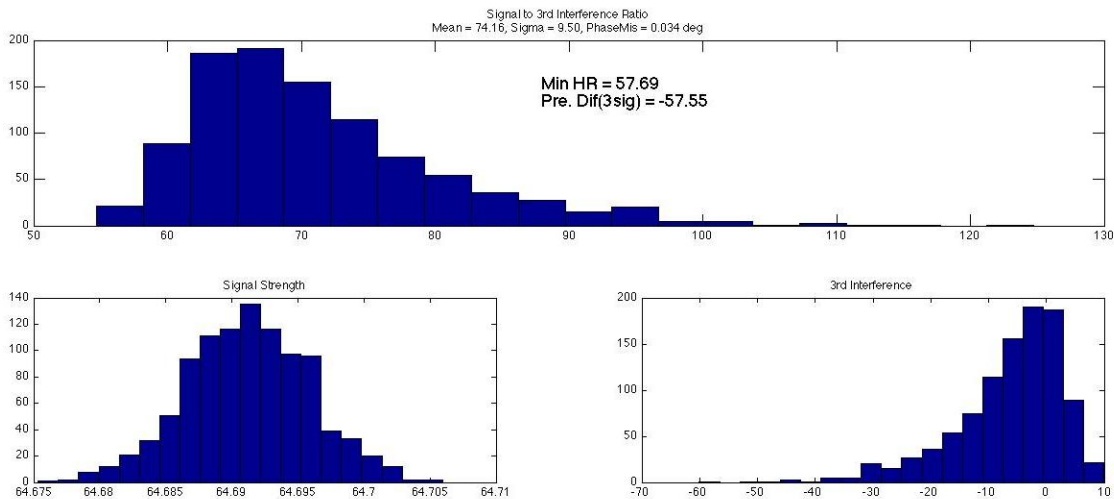


Fig. 5.22. Gain and phase mismatches degrade the harmonic rejection performance

Finally, we expand our study to a harmonic rejection system with clocks of different duty cycles. Simulations suggest that a 50% duty cycle can achieve a better harmonic rejection compared to 25% and 12.5% duty cycle LOs, as shown in Fig. 5.23.

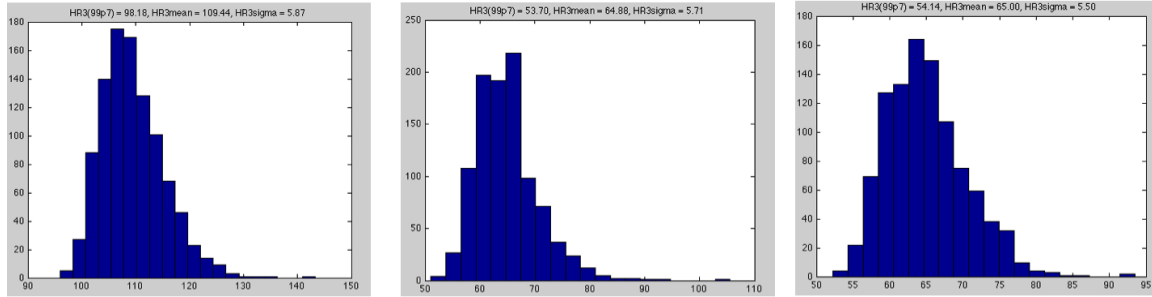


Fig. 5.23. HR ratio measured with 50%, 25% and 12.5% duty cycle LO

This can be explained with Fig. 5.24. For a 50% duty cycle, the 3<sup>rd</sup> harmonic lands on top of the second arc of the sinc function (the green curve), where the slope of the sinc function is close to zero. Therefore, it is the least sensitive to mismatch. For a 25% duty cycle, the third harmonic content lands in a steeper part of the first arc (the blue curve), so it is more sensitive to mismatch. For the 12.5% case, it lands in a steep part of the far-stretching first arc (the red curve). Since the slope at the point of the third harmonic is still larger than the case of 50%, it is still more sensitive to mismatch. In summary, the impact of phase mismatch is related to the slope of the sinc function at the undesired harmonic frequencies. This is a profound observation. By the same reasoning, we should anticipate that a 50% duty cycle LO would outperform the other two LOs for fifth order rejection, which indeed is the case. Moreover, theoretically the magical 33% duty cycle should be free from the 3<sup>rd</sup> order harmonic. However, given this observation, the 33% duty cycle LO would perform extremely poorly in the presence of phase mismatches, given the fact that for a 33% duty cycle LO the third harmonic falls exactly into the null, where the sinc function has the steepest slope. Thus, it is more sensitive to phase mismatch.

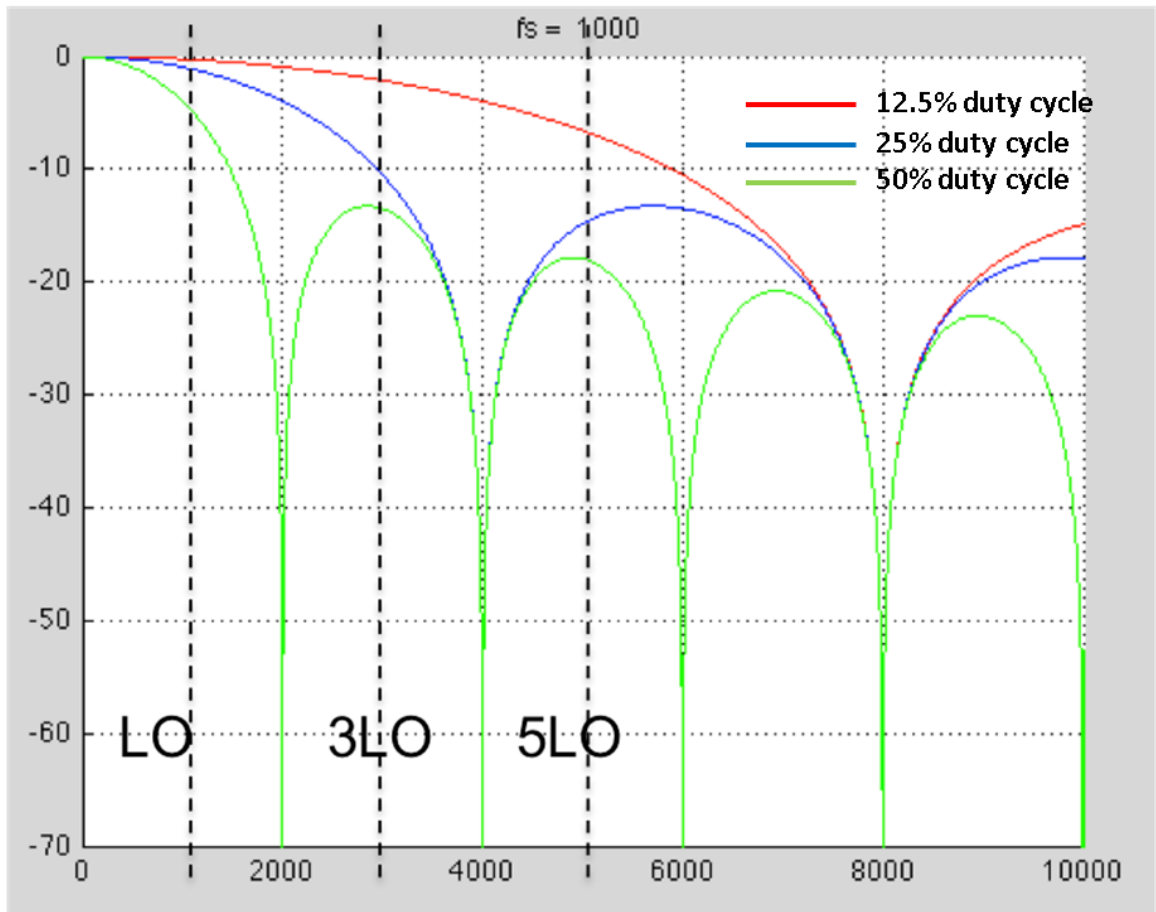


Fig. 5.24 Sinc waveforms for window functions with different duty cycles.

## CHAPTER 5 APPENDIX: Mixer Linearity Analysis

Reference [114] shows a general Volterra analysis for double balanced passive mixer with 50% duty clock. This section intends to extend it to cover the HR case. The signal current content  $i_D$  can be expressed as

$$\begin{aligned} i_D = & g_{ds}(v_d - v_s) \\ & + g_{ds2}v_d^2 + g_{ds3}v_d^3 + \dots \\ & + g_{ds2}v_s^2 + g_{ds3}v_s^3 + \dots \\ & + g_{ds2\_ds}(v_d v_s) + g_{ds3\_ds}(v_d^2 v_s) + g_{ds3\_ds}(v_d v_s^2) \dots \end{aligned}$$

where the  $v_d$  and  $v_s$  are the drain and source voltages respectively of the transistor device. The input and output voltages can be expressed as a converging Volterra series of the source current  $i_{RF}$ . It follows,

$$v_s = H_{1_s}(s) \circ i_{RF} + H_{2_s}(s_1 + s_2) \circ i_{RF}^2 + H_{3_s}(s_1 + s_2 + s_3) \circ i_{RF}^3 + \dots$$

$$v_d = H_{1_d}(s) \circ i_{RF} + H_{2_d}(s_1 + s_2) \circ i_{RF}^2 + H_{3_d}(s_1 + s_2 + s_3) \circ i_{RF}^3 + \dots$$

where  $H_{ns}$  and  $H_{nd}$  are the according nth-order Volterra kernels for the drain and the source nodes of the passive mixer, respectively. The voltage swing at the source node can be written as

$$i_{RF} = [g_s(s) + g_L(s) // g_{ds}]v(s)$$

The first-order Volterra kernels for the source node can be written as

$$H_{1s}(s) = \frac{g_{ds} + g_L(s)}{g_{ds}g_L(s) + g_{ds}g_S(s) + g_L(s)g_S(s)}$$

For the drain node, it can be shown as

$$\begin{aligned} \frac{v(s)}{\lambda i_{RF}} &= \frac{z_s(z_L + r_{ds})}{z_L + z_s + r_{ds} + r_{ds}z_Lz_s} \\ &\approx \frac{z_s z_L}{z_L + z_s + r_{ds}z_Lz_s} \end{aligned}$$

The  $\lambda$  in the above equation is the frequency conversion loss due to the mixing operation, which is related to duty cycle of LO. For a 50% duty cycle clock it can be shown as  $\frac{2}{\pi}$ . While for 25% and 12.5% duty cycle it can be shown as  $\frac{2}{\pi^2}$  and  $\frac{2}{\pi^2}(2 - \sqrt{2})$ . Then, the first-order Volterra kernels at the drain node can be expressed as

$$H_{1d}(s) = \frac{\lambda g_{ds}}{g_{ds}g_L(s) + g_{ds}g_S(s) + g_L(s)g_S(s)}$$

The second order kernels for the drain and source nodes can be

$$\begin{aligned} i_{NL2} &= \frac{1}{\Delta(s_1)\Delta(s_1)} \{ g_{ds2}g_{ds}^2 + g_{ds2}(g_{ds} + g_L(s_1))(g_{ds} + g_L(s_2)) \\ &\quad + g_{ds2}g_{ds}(g_{ds} + \frac{g_L(s_1) + g_L(s_2)}{2}) \} \end{aligned}$$



In a similar fashion, the second order Volterra kenerls can then be shown as

$$H_{2_s}(s_1, s_2) = \frac{g_L(s_1 + s_2)}{\Delta(s_1 + s_2)} \times i_{NL2}(s_1, s_2)$$

$$H_{2_d}(s_1, s_2) = \lambda \frac{g_S(s_1 + s_2)}{\Delta(s_1 + s_2)} \times i_{NL2}(s_1, s_2)$$

The third order of Volterra kernerls can be shown as

$$H_{3_s}(s_1, s_2, s_3) = \frac{g_L(s_1 + s_2 + s_3)}{\Delta(s_1 + s_2 + s_3)} \times i_{NL2}(s_1, s_2, s_3)$$

$$H_{3_d}(s_1, s_2, s_3) = \lambda \frac{g_S(s_1 + s_2 + s_3)}{\Delta(s_1 + s_2 + s_3)} \times i_{NL2}(s_1, s_2, s_3)$$

Now the discussion can be further extended to derive the expressions for IIP2 and IIP3 for a mixer first design. It can be shown that

$$\begin{aligned} IIP_2 &= \frac{P_{out}(\omega_{LO} + \omega_1)}{P_{out}(\omega_1 - \omega_2)} P_{in}(\omega_1) \\ &= \left\{ \frac{v_D(\omega_{LO} + \omega_1)}{v_D(\omega_1 - \omega_2)} \right\}^2 P_{in}(\omega_1) \\ &= \left\{ \frac{v_D(\omega_{LO} + \omega_1)}{v_D(\omega_1 - \omega_2)} \right\}^2 \frac{i_{RF}^2}{50} \\ &\approx \frac{1}{50} \left\{ \frac{g_L(\omega_1)g_L(\omega_1 - \omega_2)}{g_S(\omega_1 - \omega_2)} \right\}^2 [\Delta_2 g_L^2(\omega_1) + \Delta_1 g_L(\omega_1) + \Delta_0]^{-2} \end{aligned}$$

$$\begin{aligned}
IIP_3 &= \left\{ \frac{P_{out}(\omega_{LO} - \omega_1)}{P_{out}(\omega_{LO} - (2\omega_1 - \omega_2))} \right\}^{\frac{1}{2}} P_{in}(\omega_1) \\
&= \left\{ \frac{v_D(\omega_{LO} - \omega_1)}{v_D(\omega_{LO} - (2\omega_1 - \omega_2))} \right\} P_{in}(\omega_1) \\
&= \left\{ \frac{v_D(\omega_{LO} - \omega_1)}{v_D(\omega_{LO} - (2\omega_1 - \omega_2))} \right\} \frac{i_{RF}^2}{50} \\
&\approx \frac{2}{75} \left\{ \frac{g_{ds}^5 g_L^2(\omega_1) g_L(2\omega_1 - \omega_2)}{g_S(2\omega_1 - \omega_2)} \right\} [A_3 g_L^3(\omega_1) + A_2 g_L^2(\omega_1) + A_1 g_L(\omega_1) + A_0]^{-1}
\end{aligned}$$

Also, reference [114] introduces a new metric XM IIP3 for three tone case, by a similar steps, it can be expressed as

$$\begin{aligned}
IIP_{3,XM} &= \frac{K_{XM}}{25} \left\{ \frac{g_{ds}^5 g_L^2(\omega_1) g_L(\omega_1 + \omega_2 - \omega_3)}{g_S(\omega_1 + \omega_2 - \omega_3)} \right\} \\
&\quad \times B_3 [g_L^2(\omega_2) g_L(\omega_1) + B_2 g_L(\omega_1) \{g_L(\omega_2) + 2g_L(\omega_1)\} \\
&\quad + B_1 \{g_L(\omega_2) + 2g_L(\omega_1)\} + B_0]^{-1}
\end{aligned}$$

Now, let's introduce the effect of the source and load impedance which would have a serious impact on mixer' linearity performance.

$$\begin{aligned}
i_{out}(t) &= i_{test}(t) f_{sw}(t) \\
&= \lambda A \sum_{n=1,2n+1,2n+2...}^{\infty} \frac{1}{n} (\sin(n\omega_{LO} + \omega_{in})t + \sin(n\omega_{LO} - \omega_{in})t)
\end{aligned}$$

where  $n = 1/DutyCycle$ . The above equation reveals an important fact that the passive mixer is not immune from high order harmonic content folding.

$$v_{out}(t) = \lambda A \sum_{n=1,2n+1,2n+2...}^{\infty} \frac{1}{n} [2|Z_L(n\omega_{LO} + \omega_{in}) \sin(n\omega_{LO} + \omega_{in})t \\ + 2|Z_L(n\omega_{LO} - \omega_{in}) \sin(n\omega_{LO} - \omega_{in})t]$$

Combining the above two equations, the input impedance can be shown as

$$Z_{L,RF} = \lambda^2 \sum_{n=1,2n+1,2n+2...}^{\infty} \frac{1}{n^2} [Z_L(n\omega_{LO} + \omega_{in}) + Z_L^*(n\omega_{LO} + \omega_{in})]$$

For resistive load, the above equation simplifies into

$$Z_{L,RF} = 2\lambda^2 R_L \sum_{n=1,2n+1,2n+2...}^{\infty} \frac{1}{n^2} = R_L$$

For capacitive load, if we ignore the higher order terms, it can be written as

$$Z_{L,RF} = \begin{cases} \frac{\lambda^2}{j(\omega_{LO} - \omega_{in})C} & \omega_{in} \approx \omega_{LO} \\ -\frac{2\lambda^2\omega_{in}}{j\omega_{LO}^2 C} & \omega_{in} \approx 0 \end{cases}$$

This implies a capacitive load would appear as large reactive impedance close to LO frequency, while it would behave as inductive at the mixer input at much lower frequency. In general, there are large capacitances placed at the mixer output to reduce the out-of-band interferences. Thus previous equation can be simplified into

$$Z_{L,RF} = \lambda^2 Z_L^*(n\omega_{LO} + \omega_{in})$$

What it means is that the load impedance would be scaled and frequency translated by LO at the mixer input, then it follows

$$g_L(\omega) = \frac{1}{\lambda^2 Z_L^*(n\omega_{LO} + \omega_{in})}$$

Hence, the IIP2, IIP3 and XM IIP3 can be expressed as

$$IIP_2 = \frac{1}{50\lambda^2} \left\{ \frac{Z_L(\omega_1)Z_S(\omega_1 - \omega_2)}{Z_L(\omega_1 - \omega_2)} \right\}^2 \left[ \Delta_2 Z_L^2(\omega_{LO} - \omega_1) + \frac{\Delta_1}{\lambda} Z_L(\omega_{LO} - \omega_1) + \frac{\Delta_0}{\lambda^2} \right]^{-2}$$

$$IIP_3 = \frac{2g_{ds}^5}{75\lambda^3} \left\{ \frac{Z_L^2(\omega_{LO} - \omega_1)Z_S(2\omega_1 - \omega_2)}{Z_L(\omega_{LO} - (2\omega_1 - \omega_2))} \right\} \\ \times \left[ A_3 Z_L^3(\omega_{LO} - \omega_1) + \frac{A_2}{\lambda} Z_L^2(\omega_{LO} - \omega_1) + \frac{A_1}{\lambda^2} Z_L(\omega_{LO} - \omega_1) + \frac{A_0}{\lambda^3} \right]^{-1}$$

$$IIP_{3,XM} = \frac{K_{XM}g_{ds}^5}{25\lambda^3} \left\{ \frac{Z_L^2(\omega_{LO} - \omega_1)Z_S(\omega_1 + \omega_2 - \omega_3)}{Z_L(\omega_{LO} - (\omega_1 + \omega_2 - \omega_3))} \right\} \\ \times [B_3 Z_L(\omega_{LO} - \omega_1) + \frac{B_2}{\lambda} Z_L(\omega_{LO} - \omega_2) \times \{Z_L(\omega_{LO} - \omega_1) + 2Z_L(\omega_{LO} - \omega_2)\} \\ + \frac{B_1}{\lambda^2} Z_L(\omega_{LO} - \omega_1)Z_L(\omega_{LO} - \omega_2)\} \times \{Z_L(\omega_{LO} - \omega_1) + 2Z_L(\omega_{LO} - \omega_2)\} \\ + \frac{B_0}{\lambda^3} Z_L^2(\omega_{LO} - \omega_1)Z_L^2(\omega_{LO} - \omega_2)\}]^{-1}$$

The coefficients for the above equations are listed below. For IIP2, we have

$$\Delta_2 = \left( \frac{g_{2S}}{g_{ds}^3} \right)'$$

$$\Delta_1 = \left( \frac{g_{ds2\_ds} + 2g_{2d}}{g_{ds}^2} \right)'$$

$$\Delta_0 = \left( \frac{g_{ds2} + g_{ds2\_ds} + g_{2s}}{g_{ds}} \right)'$$

For IIP3, the coefficients are

$$A_3 = 2g_{2s}^2 + g_{ds}g_{3s}$$

$$A_2 = g_{ds}(3g_{ds2\_ds}g_{2s} + 6g_{2s}^2 + g_{ds}g_{ds3\_ds} + 3g_{ds}g_{ds3})$$

$$A_1 = g_{ds}^2(g_{ds2}^2 + 2g_{ds2}g_{2s} + 6g_{ds2d}g_{2s} + 6g_{2s}^2 + 2g_{ds}g_{ds3d2s} \\ + g_{ds}g_{ds3\_2ds} + 3g_{ds}g_{3s})$$

$$A_0 = g_{ds}^3(g_{2d}g_{ds2ds} + g_{ds2ds}^2 + 2g_{2d}g_{2s} + 3g_{ds2ds}g_{2s} + 2g_{2s}^2 \\ + g_{ds}(g_{3d} + g_{ds3d2s} + g_{ds3\_2ds} + g_{3s}))$$

The coefficients for the Volterra kernel for the XM IIP3 are given by

$$B_3 = 6g_{2s}^2 + 3g_{ds}g_{3s}$$

$$B_2 = g_{ds}(3g_{ds2\_ds}g_{2s} + 6g_{2s}^2 + g_{ds}g_{ds3\_ds} + 3g_{ds}g_{ds3})$$

$$B_1 = g_{ds}^2(g_{ds2}^2 + 2g_{ds2}g_{2s} + 6g_{ds2d}g_{2s} + 6g_{2s}^2 + 2g_{ds}g_{ds3d2s} \\ + g_{ds}g_{ds3\_2ds} + 3g_{ds}g_{3s})$$

$$B_0 = g_{ds}^3(g_{2d}g_{ds2ds} + g_{ds2ds}^2 + 2g_{2d}g_{2s} + 3g_{ds2ds}g_{2s} + 2g_{2s}^2 \\ + g_{ds}(g_{3d} + g_{ds3d2s} + g_{ds3\_2ds} + g_{3s}))$$

# Chapter 6

## Circuit Prototype for Mixer-First RX

### 6.1 Introduction

LTE-Advanced introduces carrier aggregation (CA) to address the demand for further increased data rates. Among many different scenarios, intra-band non-contiguous CA poses the most challenging condition on the receivers' noise figure and linearity performance due to the in-band and out-of-band interferences. A mixer-first design [62][64] offers superb linearity without a large power penalty. However, this kind of designs cannot provide much isolation between the LO port and the antenna port, as a result LO leakage re-radiation is a major issue of such designs. Furthermore, compared to the conventional receiver design, where the LNA or the LNTA provide decent wideband backward isolation, higher order harmonics of the LO in a mixer-first design can leak through the antenna and create undesired out-of-band emission.

In this work, a highly linear wide-band mixer-first receiver to support LTE non-contiguous carrier aggregation is proposed. Moreover, a 5-bit mixer DAC is built into the system to suppress LO leakage re-radiation at the absence of the LNA or LNTA. The overall design achieves a 2.6 dB NF and 16dBm IIP3, while only consuming 55mW power from the nominal 1.1V supply.

### 6.2 System Overview

Figure 6.1. shows the overview of the entire system. The system takes in a single-ended RF input signal. The input signal is first down-converted by an 8-path mixers, where each path is controlled by a 12.5% non-overlapping clock to the baseband. The baseband TIA provides amplification up to 35 dB. The four pairs of output signals are

then combined with proper weighting factors by two on-chip output buffers, which are capable of driving a  $50\ \Omega$  off-chip impedance from the test equipments. The series resistance of the passive mixer switches together with the up-converted input impedance from the baseband amplifiers creates a  $50\ \Omega$  input match. All the baseband amplifiers' supply voltages are generated on-chip through integrated LDOs for better supply rejection performance. An external LO reference running at 4X the carrier frequency is supplied to the system. The on-chip divider brings it down to the LO frequency and generate all the required non-overlapping clock signals. The system is capable of rejecting the third-order and fifth-order harmonics.

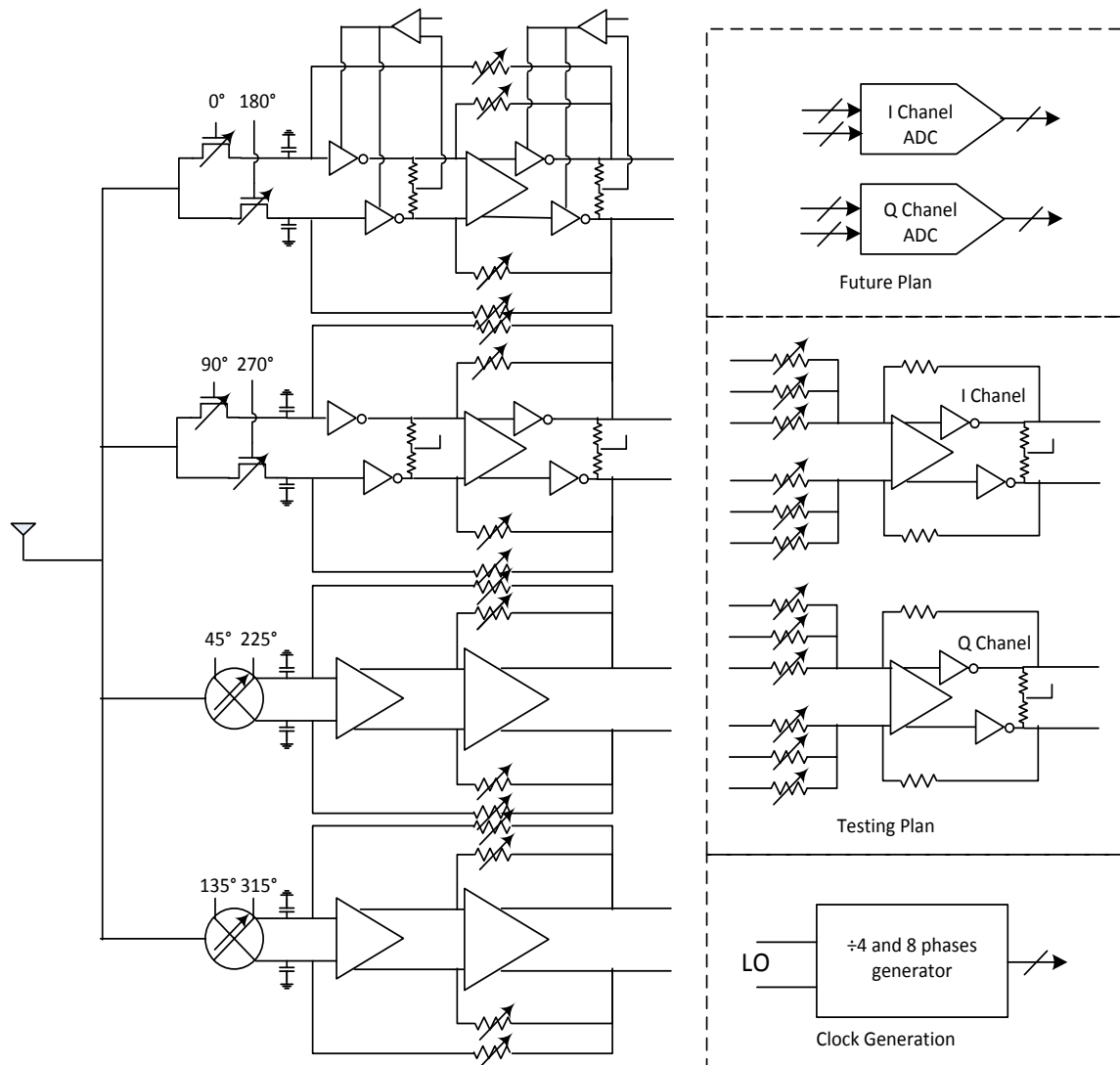


Fig. 6.1 Top-level system overview for mixer-first design.



## 6.3 Circuit Design Details

In this design, each of the eight mixers consists of two parts: a mixer core and a 5-bit mixer DAC (Fig. 6.2.) to provide finer turnability to suppress LO leakage. The origin of LO leakage is the mismatch between different downconverting paths, in particular, the mixer switches and the LO buffers. Mismatches in the size of the switches result in unmatched capacitor loading for the LO buffers, while mismatches in the LO buffers translates to different driving strength for different phases of the LO. Therefore, different phases of LO signals have different edge rates, and this results in LO leakage to the antenna port. The LSB mixer unit in the mixer DAC has a size slightly smaller than 1% of the device in the mixer core. The layout of the 5-bit mixer DAC is shown in Fig. 6.3. Multiple layout design iterations together with careful layout extraction verification ensure the overall parasitic capacitor on the RF node is less than 100 fF. The pitch of the differential mixer unit as shown in Fig. 6.3 is optimized to 120  $\mu\text{m}$  for an overall compact and area-efficient design.

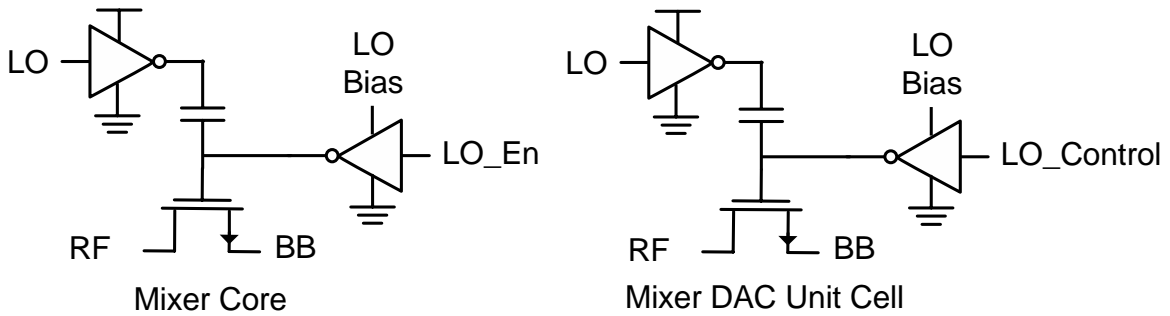


Fig. 6.2 Schematic for the mixer core and unit cell in the mixer DAC.

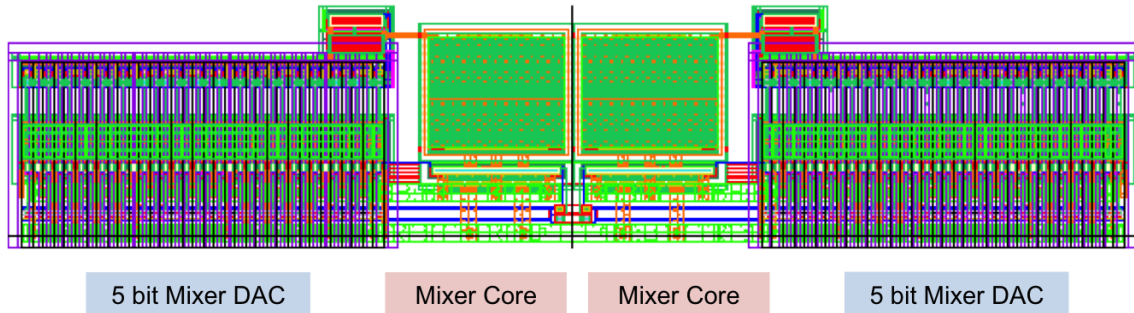


Fig. 6.3 Layout for the differential mixer cells.

The baseband TIA is implemented as two amplifiers in cascade, so it can achieve a wide baseband bandwidth (50MHz) and a high slew rate while maintaining low power consumption. The wide bandwidth is essential to support LTE Advanced, since it allows the receiver to take in the entire RX band of LTE channels. A high slew rate, on the other hand, is necessary to maintain a superb linearity performance in the presence of in-band and out-of-band interferences. Compared to a conventional receiver design, where the RX only processes one narrow band signal, our system aims to handle the entire band. Therefore, interferences can come as out-of-band blockers as well as in-band jammer which are from the other users' signals in the same channels. Therefore, an excellent linearity performance for both in-band and out-of-band frequencies is a must of such a design.

To achieve good linearity performance and maintain a power efficient design, the first amplifier or baseband LNA as described by [62] is an inverter-based design with thick oxide (Fig. 6.4). As discussed in Chapter 5, inverter-based designs can be quite power efficient. Also, its class-AB structure helps to maintain linearity, even in the presence of a large blocker. One major issue of an inverter-based design is its poor power supply rejection performance (PSRP). This inverter design is a pseudo-differential circuit; therefore supply ripple cannot be rejected as the common corruption. To improve the overall PSRP, the common-mode control amplifier is integrated into an on-chip low-dropout (LDO) amplifier with a bandwidth up to 50 MHz. The reference voltage of the LDO is derived from a local replica bias.

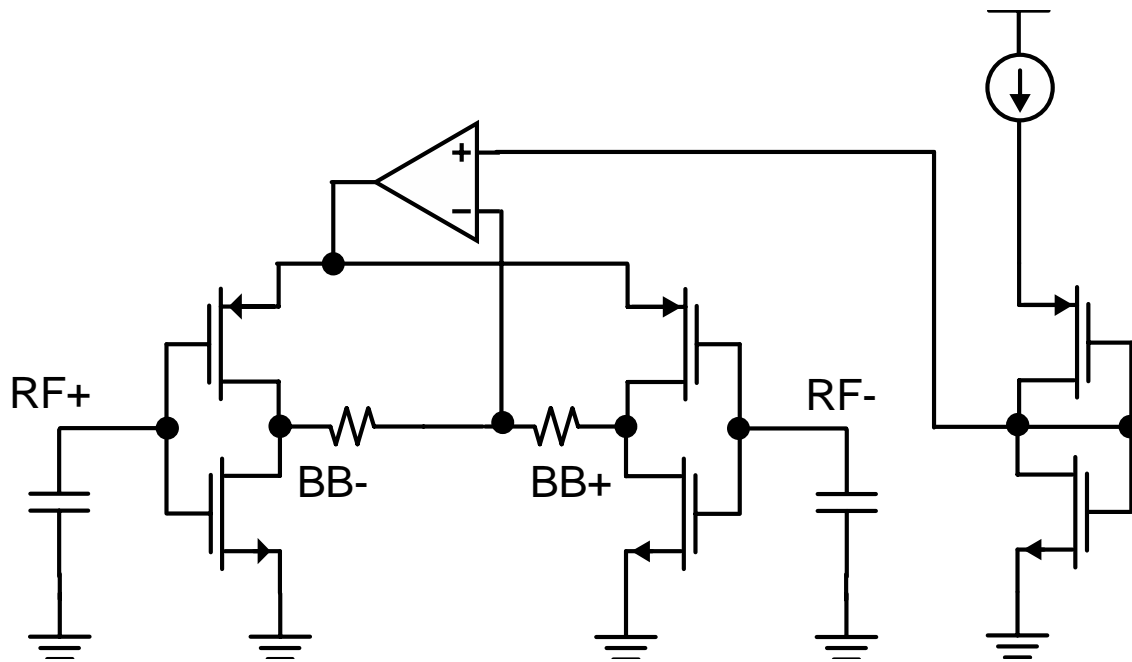
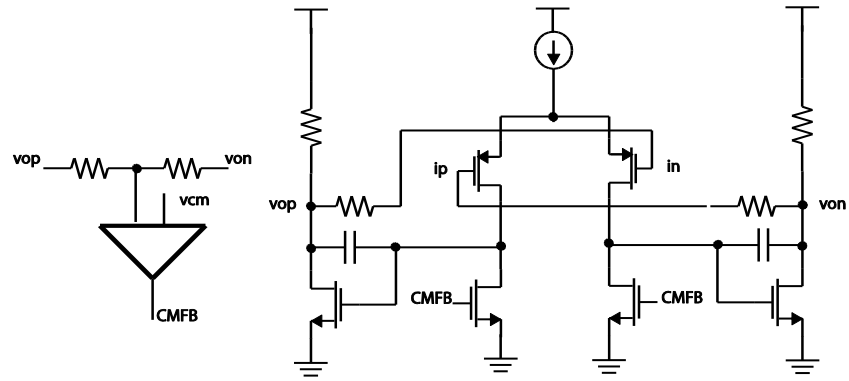


Fig. 6.4. Inverter-based amplifier design with CMFB and its bias scheme.

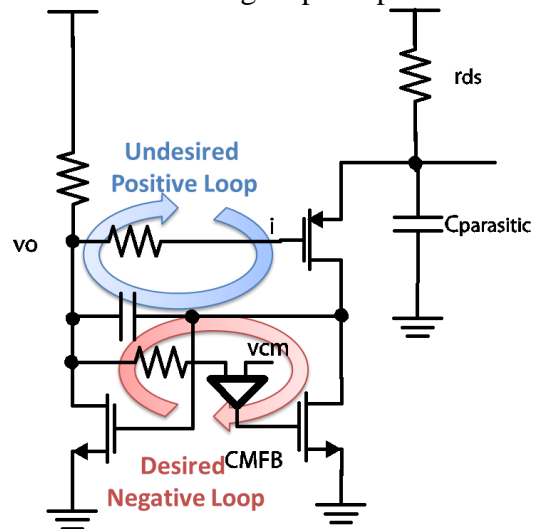
The second amplifier prefers a high gain and a wide bandwidth for accuracy and linearity performance. These are quite challenging to achieve for deep sub-micron CMOS technology, since the supply is limited to 1.1V. Two-stage amplifier design can meet the gain requirement with ease but the bandwidth and the slew rate performance suffer due to the size of the compensation capacitors. Moreover, two-stage amplifier design suffers from a common mode instability issue due to the low supply. Figure 6.5(a)(b) and (c) demonstrate this issue. Figure 6.5(a) shows a simple two-stage amplifier with Miller compensation capacitors. The two-stage amplifier is configured with Shunt-Shunt feedback to function as a trans-impedance amplifier. A common-mode feedback amplifier detects the output common mode voltage and feeds the control signal back to the NMOS loads in the first stage to regulate the common-mode bias conditions.

Due to the low supply, only limited headroom can be allocated for the tail current source, which leads to a poor  $g_{ds}$ , as shown in Fig. 6.5(b). The issue of headroom shortage further forces the input pair and the tail current source to operate with small overdrive voltages, leading to large transistor size. This results in a large parasitic capacitor connected to the virtual ground node. Large parasitic capacitor on the virtual ground together with the smaller  $g_{ds}$  lower the impedance seen by the two input pair devices. This degrades the common-mode rejection at the first stage of the amplifier as it increases the common-mode gain of the differential pair. In the two stage amplifier shown in Fig. 6.5 (a), the two inverted gain stage in series creates an undesired wideband common-mode positive feedback as shown in Fig. 6.5(b). In the usual case, this undesired positive loop tends to have a gain less than one, due to the fact that input pair common-mode gain is heavily degenerated by the tail current source's output impedance. However, as discussed above, the first stage common-mode gain in this case is actually large, and hence the undesired positive feedback would have a strong negative effect on the overall common-mode stability.

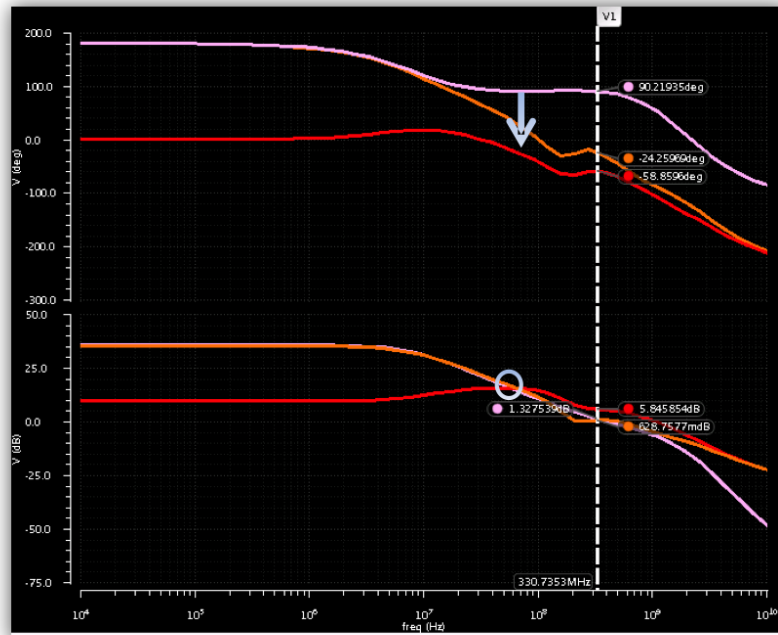
In general, the desirable built-in common-mode control loop, as shown in Fig. 6.5(b) tends to be narrow band due to reasons explained in [73]. Therefore, in low frequency, where the desired negative common-mode loop is still strong, the common-mode signal is well-regulated. However, the undesired positive feedback will take over beyond unity gain frequency of the common-mode loop, where the desired negative common-mode loop begins to fade away as shown in Fig. 6.5(c). As a result, the phase margin of the common-mode loop degrades significantly. In summary, it is difficult to realize a robust two-stage amplifier design over processes and corners in a deep sub-micron CMOS technology due to the limited supply headroom.



a) A fully differential two-stage Op-Amp with feedback and CMFB.



b) Common-mode half-circuit for a two-stage amplifier.



c) AC Frequency response.

Fig 6.5 Common mode instability for a two-stage amplifier design.

An AC-boosting compensation (ACBC) scheme [124] (Fig. 6.6) provides a good alternative to solve the CM stability issue. A major benefit of ACBC design is that it contains three inverting stages; therefore the global CM feedback is always negative. Hence, the global CM feedback never competes against the common-mode control loop, and stability of the CM loops can be ensured with proper design. Also, the input signal is fed forward to the output stage to create a feed-forward zero in the ACBC design, and it allows for a much smaller compensation capacitor ( $\sim 150$  fF) and hence better slew rate performance, essential to maintaining the good linearity performance. Fig. 6.7. shows the details of the second amplifier. PMOS input pairs are adopted for better flicker noise performance. Moreover, the output stage is designed as a class-AB structure which helps to maintain the overall slew rate and linearity performance.

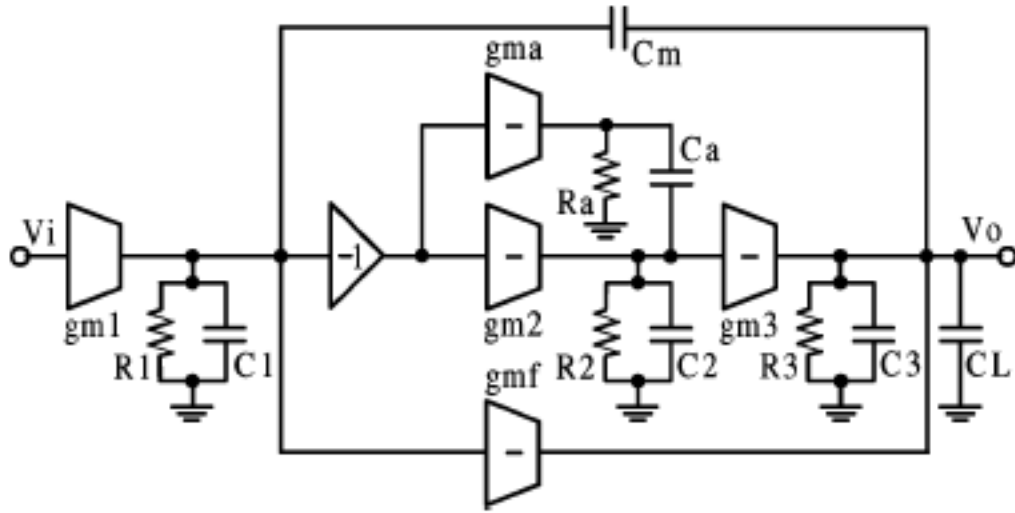


Fig. 6.6. AC-boosting compensation (ACBC) scheme.

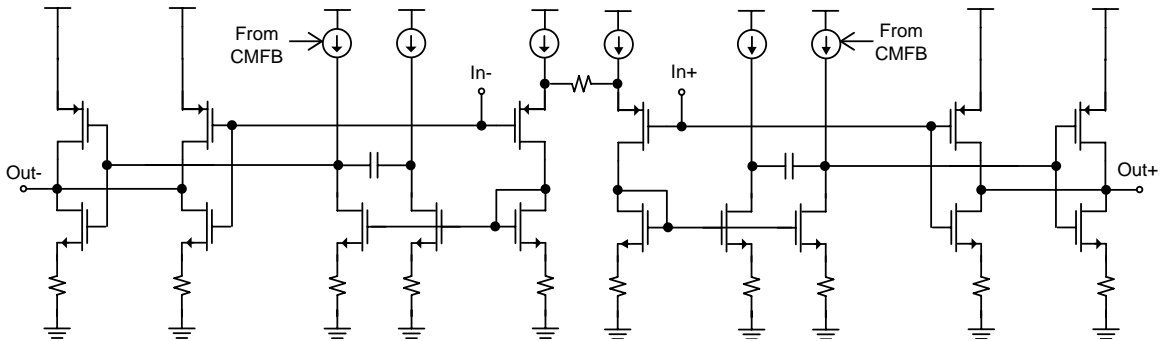


Fig. 6.7. Detailed schematic design for second stage amplifier design.

A single-ended RF signal is down-converted by 8 different paths, each of which is driven by a non-overlapping 12.5% duty-cycle clock. Eight-phase down-conversion rejects the 3<sup>rd</sup> and 5<sup>th</sup> harmonics. Also it helps to reduce the noise folding, and improves the overall NF. A two-stage harmonic rejection (HR) scheme as in [76] is adopted to further improve the accuracy of the HR. The clock generation circuit is similar to [68]. An early version of the floor planning of the entire system is shown in Fig. 6.8. The width of the entire design is carefully designed so that it is entirely set by the pitch of the 8-phases mixer frontends.

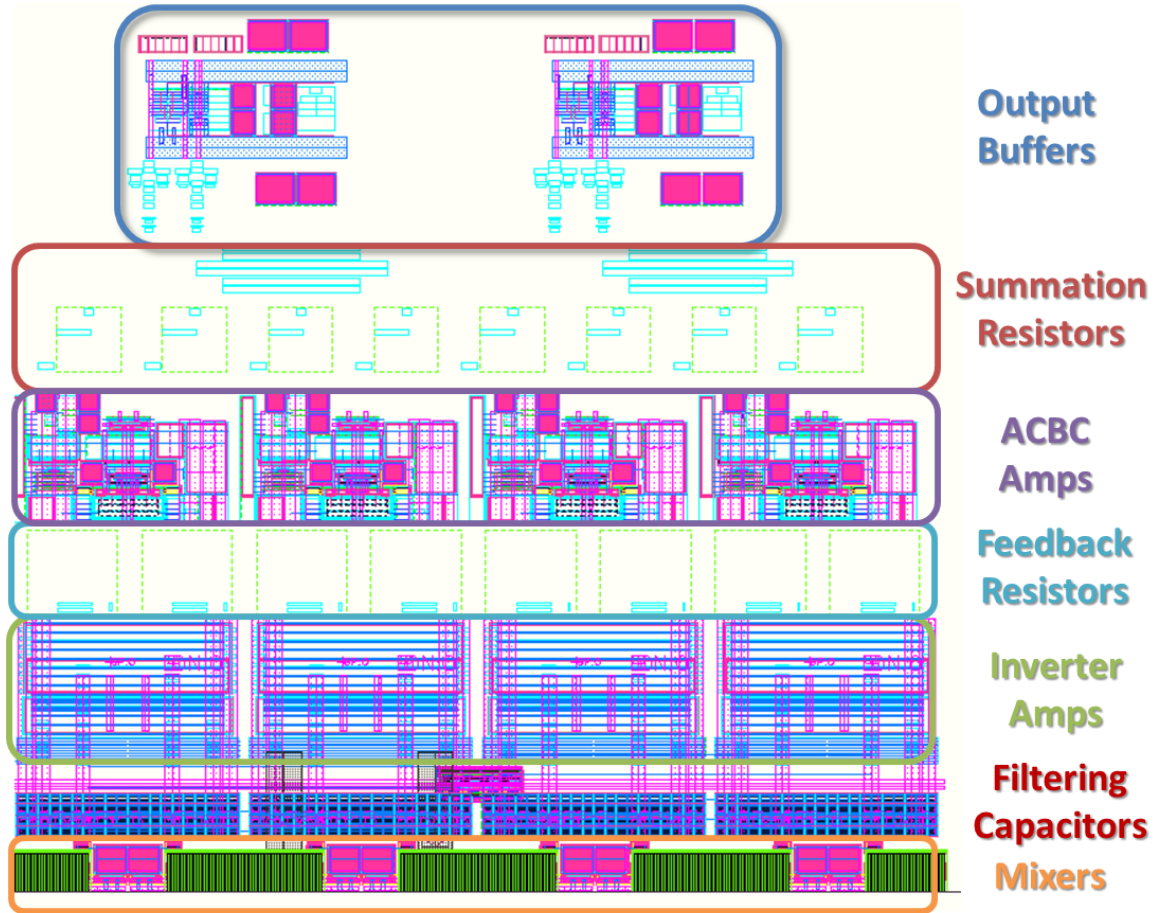


Fig. 6.8. Floor planning for the receiver core.

## 6.4 Optimizing Noise Figure Performance

Mixer-first design tends to have worse noise figure performance, when compared to conventional receiver designs, due to the absence of the RF amplification stage. This makes noise figure optimization even more important. Table 6.1 shows the noise power breakdown for noise integrated over different bandwidths. The analytical expression for the noise figure has been shown as (40) in Chapter 5. This section shall focus on the interpretation of the simulation results, followed by design to achieve the best noise figure in both the small signal and large signal case.

For different integration bandwidths(10 KHz - 100 KHz to 10 KHz - 10 MHz), the baseband LNA, the mixer and the clock generation circuit are always the major noise contributors. In particular, the baseband LNA's flicker noise dominates over a narrower integration bandwidth, while the mixer switches' thermal noise dominates over in a wider integration bandwidth. The noise figure for wireless standards with narrower bandwidth can be improved by sizing up the devices in the baseband LNA while maintaining their width to length ratios. This won't cost any additional power overhead, since the bias current is set by the bias network. The transistors would have the same operating condition, since their overdrive voltages don't change. To reduce the thermal noise contributed by the mixer, the mixer switches need to have a lower on-impedance, which requires a large switch size. Fortunately, the mixer switch is one of the RF components that mostly benefited from process scaling. The 28 nm technology allows for a larger mixer size to be used without severe power penalty.

<b>Int. from 1K to 100K</b>	<b>Int. from 10K to 170K</b>	<b>Int. from 10K to 10M</b>
Flicker-- LNA (21.2%)	Therm-- Mixer (19.6%)	Therm-- Mixer (28.9%)
Flicker-- Clk Gen (14.6%)	Flicker-- LNA (12.2%)	Flicker-- LNA (2.82%)
Therm.- Mixer (12.8%)	Flicker-- Clk Gen (8.36%)	Flicker-- Clk Gen (0.50%)

\*\* Note: around 50% of the noise is from the input port

Table 6.1 Noise power breakdowns for noise integrated over different bandwidths.

Also, the flicker noise from the clock generation circuits shows up in all three categories. The mechanism of the flicker noise up-conversion and down-conversion has been discussed in Chapter 4, and it won't be repeated here. The clock networking is then carefully sized to avoid large power overhead, while the whole system can still achieve a good noise figure performance.

Fig. 6.9 shows the noise power break down among the few major noise contributors. Compared to the smaller signal case, the noise is no longer dominated by the mixer alone. Some of the reference noise from sources such as the common-mode feedback and LDOs would leak into the system. The reason is that during a large signal transient, the baseband amplifiers would need to provide large amount of current to maintain functionality so that the baseband amplifiers are heavily tilted to one side or the other. As a result, the baseband amplifiers fail to maintain their differential feature as in the LNTA discussion back in Chapter 4. Therefore, the reference noise can no longer be treated as the common mode noise, and needs to be considered for noise optimization.

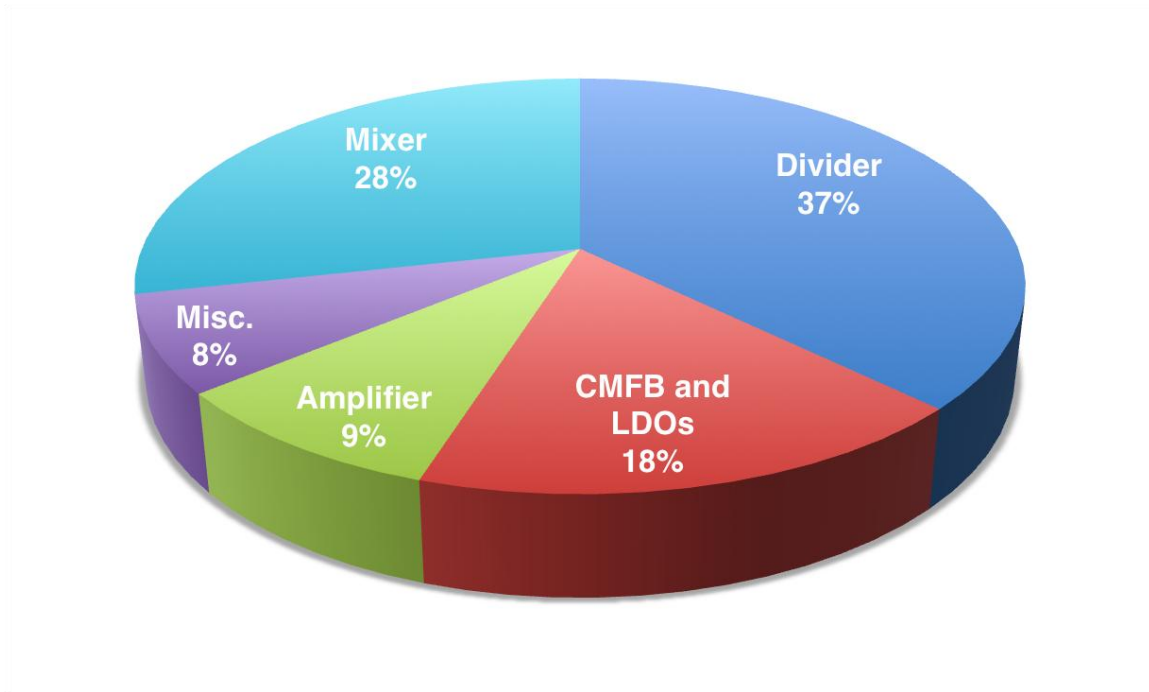


Fig. 6.9. Noise power breakdown during large signal transient.



Also, noise from the clock divider circuit has a serious impact on the noise figure, as shown in Fig. 6.8. Reference [68] claims that only a few transistors in the divider circuit matter in the noise optimization, since noise from other transistors is “correlated.” This claim is valid only for the small signal analysis. During the large signal transient, mixer switches are so heavily tilted that their on-impedance varies a lot. Some of them would be turned on hard, while the others might just barely be on. Therefore, when the once “correlated” divider noise couples into the mixer network and makes its way down the receiver chain, the divider noise would experience different noise transfer functions for each and every one of the 8 paths in the system. Therefore, when the noise finally meets up at the baseband summer TIA at the end of the chain, it cannot be rejected as “common mode” noise as in the small signal case. It is noticeable that most of the noise from the divider network is flicker noise as in the clock generation circuit in the small signal case.

Finally, the mixers become noisier in the presence of a large blocker. As discussed previously, each and every mixer among the 8 mixers would have different turn-on states, and hence different on-impedance. The result is two fold. First, some of the mixer would contribute more thermal noise. Secondly, the input matching to the antenna port is degraded, since the series impedance of the mixer switch and BB-TA is the very thing the mixer-first receiver relies on for input matching. If the bias condition significantly alters either one of them, the input matching might not hold, therefore, signal power cannot be delivered into the receiver but is deflected back to the antenna port (or the air), degrading the overall noise figure.

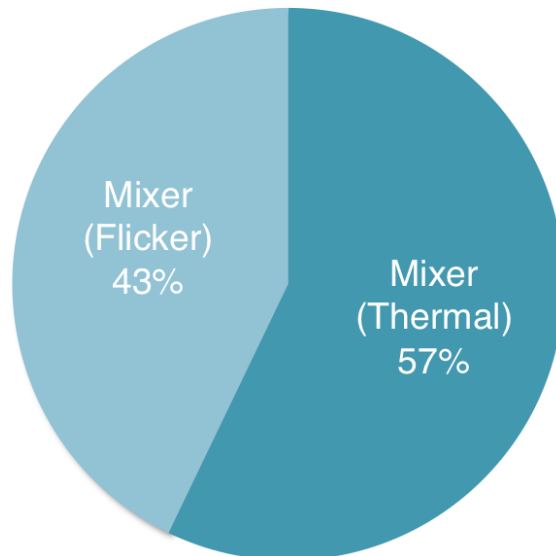


Fig. 6.10 Mixer noise power breakdown during large signal transient.

Fig. 6.10 demonstrates one important point in optimizing the mixer for large signal transient in a receiver like this. More than 40% of the noise from the mixers is flicker noise, which is not present at all in the small signal case. It has been established back in Chapter 5 that passive mixers doesn't require a DC-bias current, and hence they are free of flicker noise. These seemingly contradictory simulation results might cause some confusion to arise. In the small signal case, the input signal is so small that it doesn't disrupt the normal biasing condition of the entire system. Hence, the mixer transistors don't generate any flicker noise. During the large signal transient, the receiver is so heavily tilted to one direction or the other that there will indeed be a DC current passing through the mixers when the switches are turned on. Therefore, optimizing the mixers' flicker noise performance is as important as optimizing their thermal noise number for a mixer-first receiver design.

## 6.5 Measurement Results

The chip is sponsored by the Intel Corporation and fabricated by TSMC. The design is implemented in a general-purpose high-k metal gate 28nm technology with 1.1V nominal supply voltage. The chip micro-photograph is shown in Fig. 6.11. The core area of the design is 460  $\mu\text{m}$  by 500  $\mu\text{m}$ . This includes the 8 paths of passive mixer cells (each contains a mixer core and a 5-bit mixer DAC), four channels of baseband amplification stages, a clock generation circuit for the 8 phases of non-overlapping LO signals, all the local LDOs for the first and second stage of amplifiers together with the digital control unit. The local LDOs are implemented with 1.8V thick-oxide transistors, and they are connected to the high supply voltage. They are designed with the intention to operate over a wide range of supply voltages (1.5V-1.9V).

For testing purpose, two baseband output buffers are also integrated onto the same silicon. They are powered with a high supply voltage (1.5 V – 2 V). These two output buffers are capable of driving an off-chip 50  $\Omega$  impedance presented by the test equipment, which greatly reduces the complexity of testing.

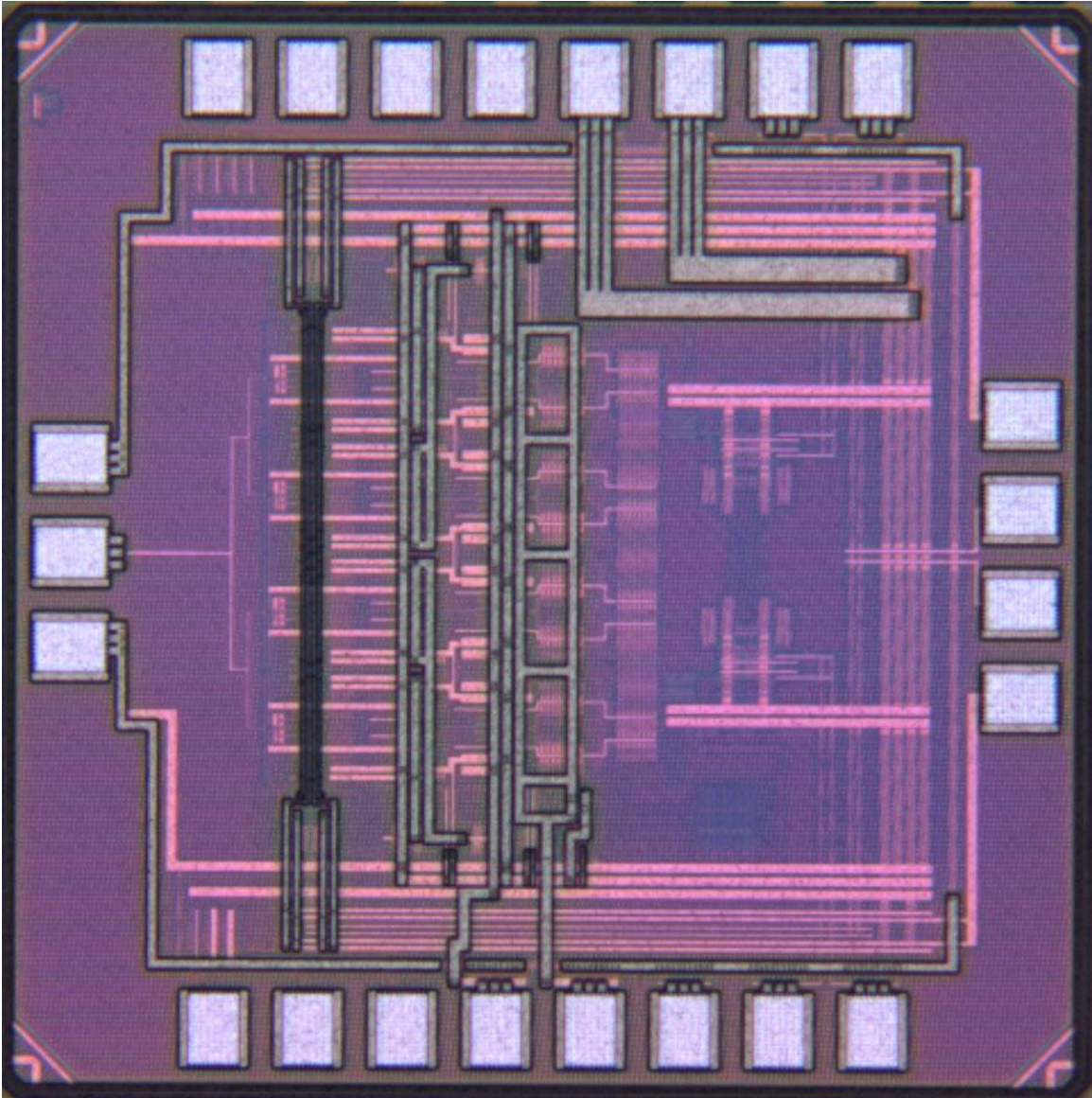


Fig. 6.11 Chip Microphotograph.

Fig. 6.12 shows the LO leakage measured the RF port of one silicon sample prior to calibration. Due to the mismatches among the downconverting paths, multiple harmonics of the LO signal leaked to the antenna port. In this particular measurement, the measured 4<sup>th</sup> harmonic (6 GHz) frequency content is as high as -46 dB. This LO leakage would be radiated to the air through the antenna. Therefore, it is possible that LO leakages might become jammers for other wireless systems operating around those frequencies in the nearby environment.

In this particular example, the fundamental frequency is at 1.5 GHz. Therefore, its 4<sup>th</sup> harmonic, which is at 6 GHz, is still within typical range of wireless commercial communication bands. This is a major limiting issue for a passive mixer-first receiver design. For this design, each mixer comes with a separate 5-bit mixer DAC, which helps to mitigate this issue.

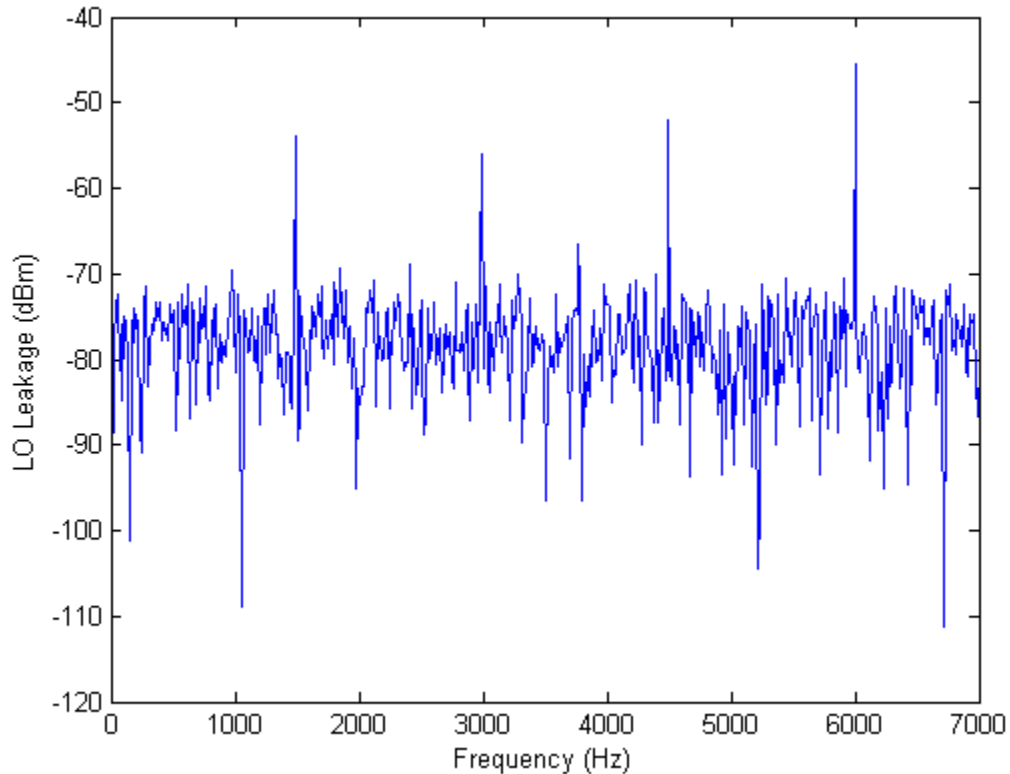


Fig. 6.12. LO leakage before calibration.

The calibration process starts by first measuring the LO leakage prior to the calibration by turning down all of the mixer DACs. Then, all of the bits of one mixer DAC are swept until an optimum codeword is obtained for this mixer cell. This process is then repeated for all of the other mixer units in the system one after another, until first-trial calibration codewords are obtained for all of the mixers. Afterwards, all of the mixer-DACs have to be swept a second time based upon the codewords just obtained. Since the calibration conditions change when more mixer cells are calibrated, the optimum codewords obtain in the first trial would no longer be valid. In particular, the cells calibrated earlier in the process would deviate more from their optimum codewords. Fortunately, experimental results over three silicon samples have verified that two rounds of calibration are sufficient to produce consistent codewords for optimal LO suppression. In some case, additional calibration can potentially provide further improvements, but only marginally.

Fig. 6.13 shows the LO leakage after calibration. All of the leakage harmonics are suppressed below -60 dB. The third harmonic frequency content (4.5 GHz) is measured as low as -62 dB. The experimental data proves that the calibration mixer DAC helps to suppress the LO leakage content in the absence of the LNA or LNTA. This suppression can be as large as 15 dB. For an actual system, all of the peripheral components have limited bandwidth, such as the duplexer, external SAW-filter and the bondwires, so it should be able to meet the coexistence requirement with other wireless systems.

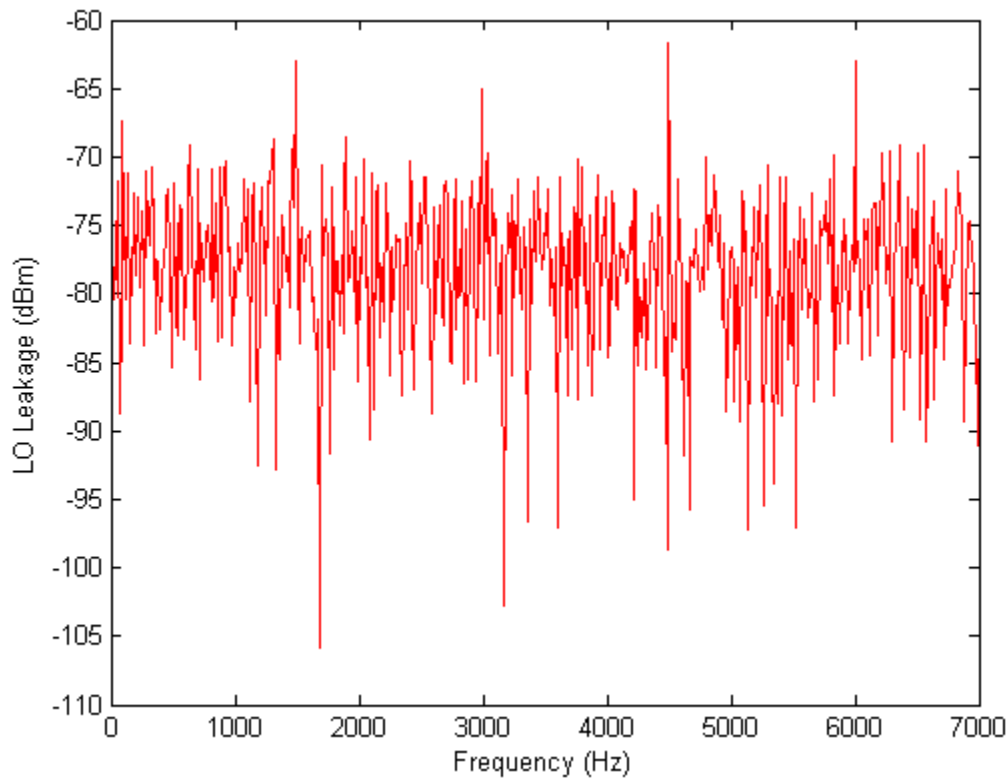


Fig. 6.13 LO leakage after calibration.

Fig. 6.14 shows the measured S11 over a wide frequency range of operation. Given the measurement settings used, the system provided good input matching up to 3.5 GHz. No data is reported here beyond 3.5 GHz, due to the output power limitation of the PSG signal source. As discussed earlier in this chapter, the system takes in an external reference 4 times faster than the desired LO to generate all of the required clock phases. For 3.5 GHz operation, the system requires a 14 GHz external clock reference. Unfortunately, the output power of the PSG used in the measurement setup degrades so significantly beyond 14 GHz that it cannot trigger the on-chip clock receiver. For a noise cancellation design such as [68], where more circuit elements need to be attached to the antenna port, the matter of input matching is complicated. Our system manages to maintain a good input match over a wider range of frequencies

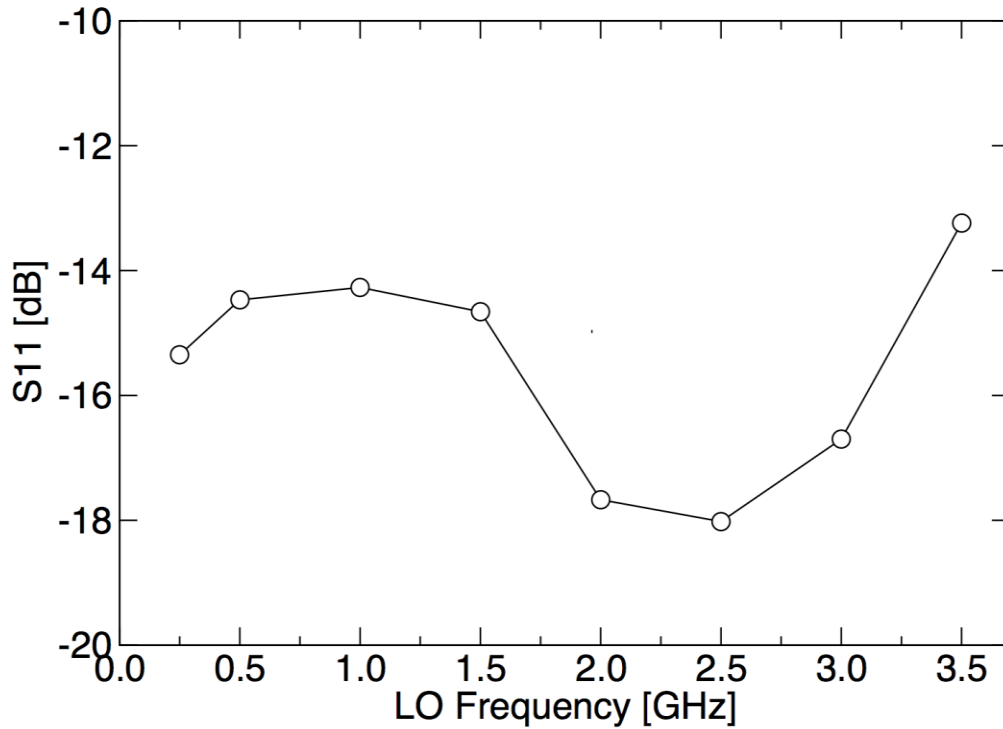


Fig. 6.14 S11 over wide range of frequencies.

Fig. 6.15 shows the measured noise figure over a wide range of frequencies. The lower bound of the measurement is at 250 MHz, which is limited by the lowest operational frequency of the external balun. Based on simulation results, the receiver is capable of functioning at frequencies lower than 250 MHz. The upper bound is at 3.5GHz, which is due to the limited output power of the PSG beyond 14 GHz. Simulation suggests the system can operate up to 4 GHz. Over the range of 250 MHz to 3.5 GHz, the receiver achieves a much better noise figure performance compared to other passive mixer-first designs that have been reported in literature, such as those in [63][66][67]. Our design is not far off from the design aided by the noise cancellation circuitry [68]. The noise figure shape is similar to that of the  $S_{11}$ , where it dips a little between 1.5 – 2 GHz. We suspect this lump around 1.5 GHz to 2 GHz is due to the external baluns on the external LO path. Since no single external balun can cover such a wide frequency range (1 GHz to 14 GHz), two baluns with different operational frequencies are inter-changed in this test, and their handover frequency happens to be around 6 GHz ~ 8 GHz.

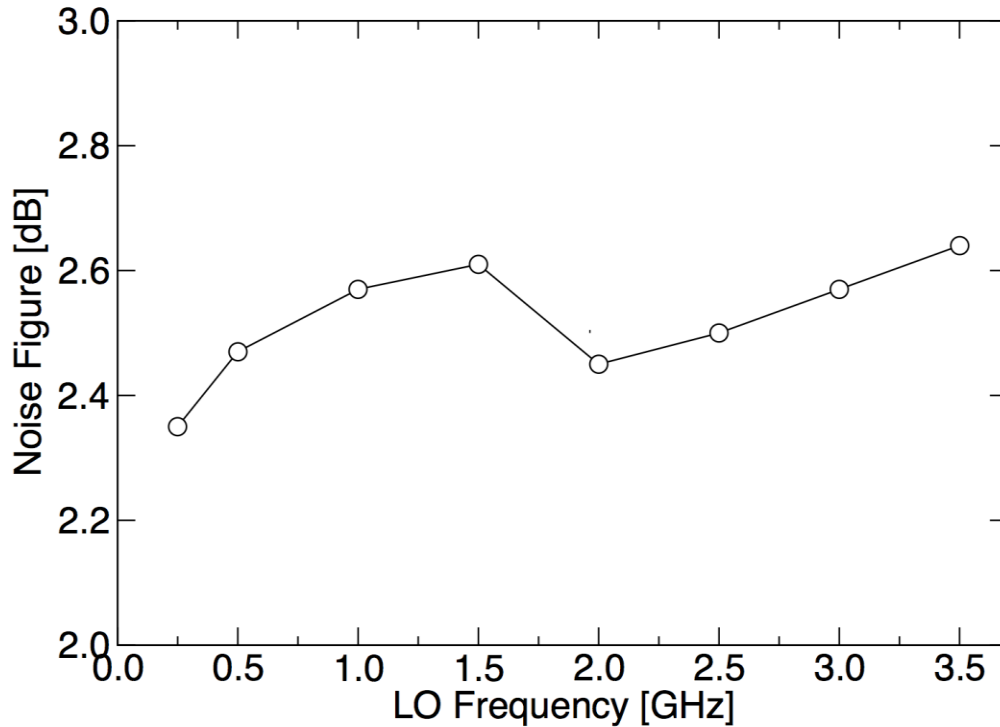


Fig. 6.15 Measured noise figure performance from 250 MHz to 3.5 GHz.

Fig. 6.16 shows the noise figure measured with different baseband bandwidth using a 1.5 GHz carrier frequency. For standards with narrower bandwidth, the noise figure is dominated by the flicker noise. According to table 6.1, this flicker noise is mostly from the baseband LNA, the clock generation (the divider), and the distribution (buffer) network. For standards with wider baseband bandwidth, the noise figure is dominated by the thermal noise of the mixers, therefore the noise figure stays flat from beyond 100 KHz. For far-out frequencies, the noise figure rises again because of the N-path nature of the receiver. The behavior of this in-band matching has been well studied in literature, such as in [49][62]. In short, because of the transparency nature of the passive mixer, the baseband impedance is frequency translated up to the RF carrier frequency, and creates a narrowband input matching around the carrier frequency.

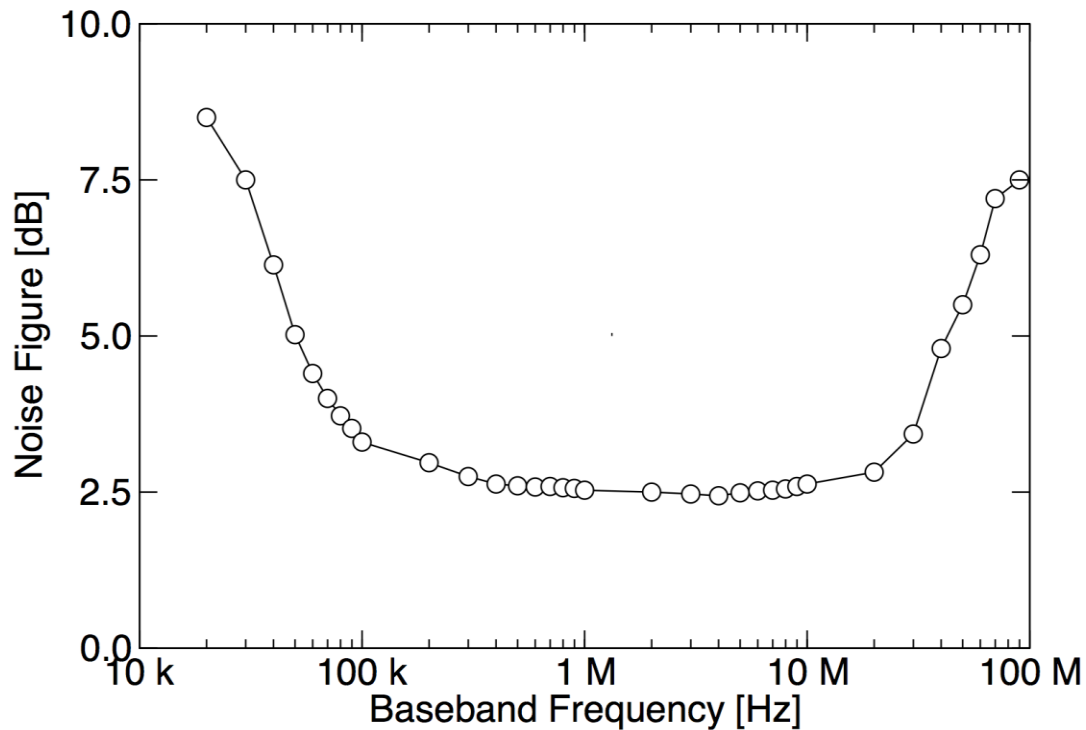


Fig. 6.16 Measured noise figure performance with different baseband bandwidth.



Fig. 6.17 shows the noise performance measured in the presence of a single-tone out-of-band blocker with various power levels. This noise figure test is carried out with a 2 GHz carrier frequency. The receiver system is operating at its highest gain setting with a 50 MHz baseband bandwidth. The blocker signal injected is 50 MHz away from the band edge or 100 MHz offset from the carrier frequency. The blocker is at 2.1 GHz to mimic a strong single-tone leakage from the TX band. The noise figure measured with a -10 dBm blocker is 3.2 dB, while the noise figure measured with a 0 dBm blocker is 6.35 dB. Together with Fig. 6.14 and Fig. 6.15, it has shown that our system can indeed maintain a good noise figure in both the small signal and the large signal environment.

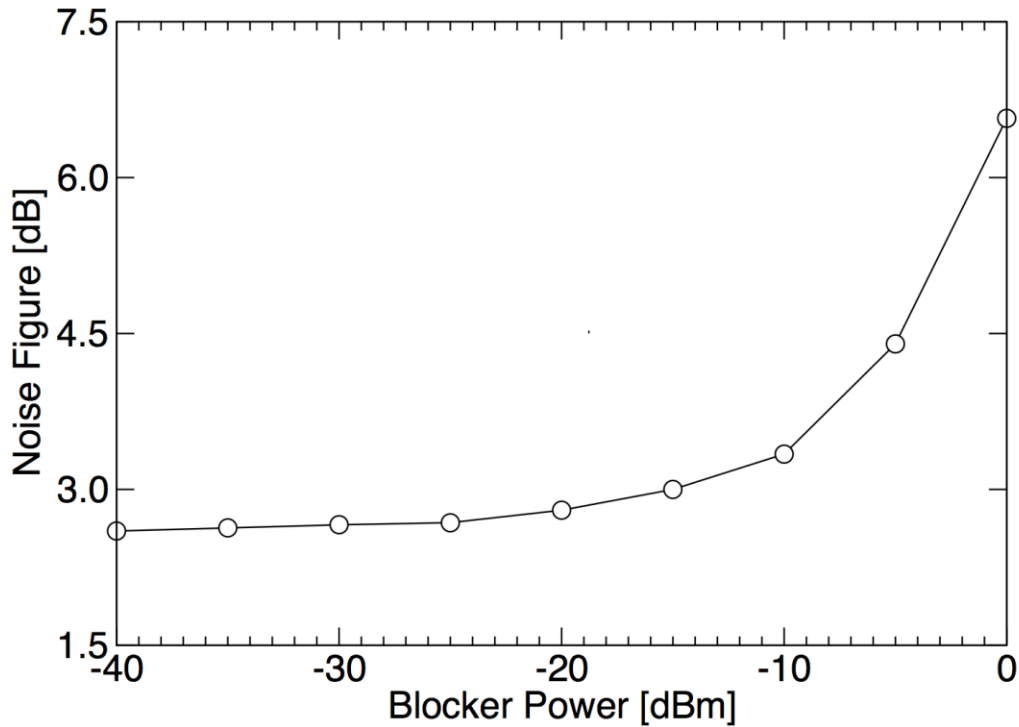


Fig. 6.17 Noise figure measurement result with various blocker power levels.

Fig. 6.18 and Fig. 6.19 describe the test setup for measuring the close-in and far-out IIP3 in detail. For the far-out test, one of the intermodulation contents is set to be at the band edge for measuring the IIP3. In order to do so, the two tones injected have to be placed properly. As shown in Fig. 6.18, one of the two tones needs to move at 1X speed away from the fixed intermodulation product, while the other moves 2X away. As a result, the two tone spacing is given by X. This ensures that the one of the intermodulation products always fall in-band, and it is not a subject to filtering by the system. Therefore, an accurate far-out IIP3 number can be measured.

On the other hand, Fig. 6.19 explains how to measure the close-in IIP3. This time, one of the two tones is fixed at the band edge, which, in this case, is 50 MHz away from the carrier frequency. The other tone can be moved away to measure the close-in IIP3 with a different tone spacing. When the intermodulation product is down-converted by the receiver, it will always fall in band. As the two-tone spacing increases, this intermodulation product moves at move towards the other side of the band edge as shown in Fig. 6.19(a) prior to down-conversion. Fig. 6.19(b) shows the location of the intermodulation product after down-conversion. As the two-tone spacing increases, this intermodulation content first moves towards DC but after it reaches DC, it moves away, as shown in Fig. 6.19(b). Therefore, with careful planning, this IM product can always fall within the signal bandwidth without being attenuated by the baseband filter, and an accurate IIP3 number can be measured.

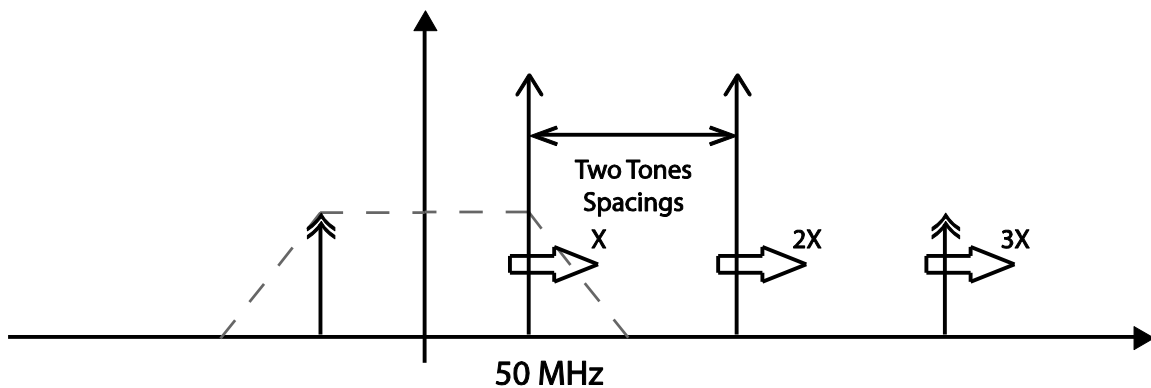
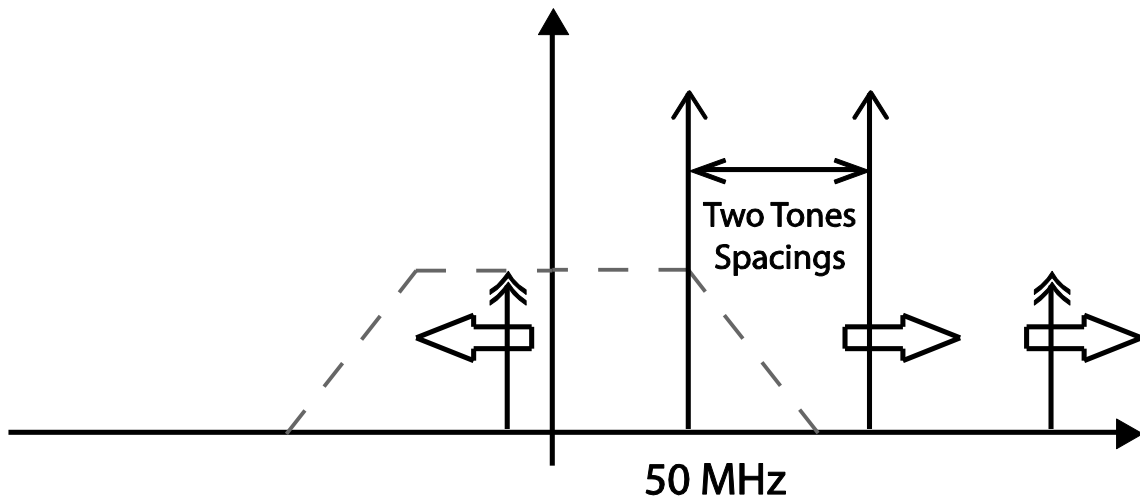
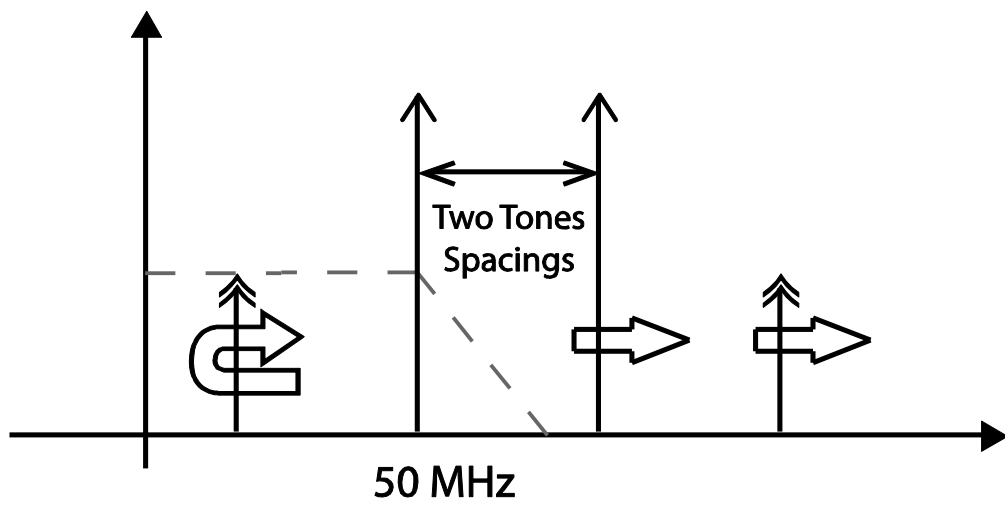


Fig. 6.18 Test setup for measuring far-out IIP3.



(a)



(b)

Fig. 6.19 Test setup for measuring close-in IIP3.

Fig. 6.20 shows the measured IIP3 from close-in and far-out tests around a 2 GHz carrier frequency. The white dots are data points collected from the close-in test, while the black points are from the far-out test. The receiver achieves a  $> +6.4$  dBm IIP3 within the 3dB corner frequency consistently. Moreover, the system achieves an out-of-band IIP3 as high as +20.5 dBm with a 250 MHz tone spacing. The IIP3 measured with a 50 MHz tone spacing (one tone at 2.05GHz, while the other sits at 2.10 GHz) is +15.4 dBm. This is for the test case where the close-in TX leakage could degrade the receiver's performance. The IIP3 is flat close-in, since the linearity is mostly dominated by the baseband amplifiers' linearity performance. As the two tone spacing increases, the IIP3 improves since one of the tones is moving out of band. Eventually, the IIP3 saturates, since the linearity at that point is limited by performance of the intrinsic mixer switches.

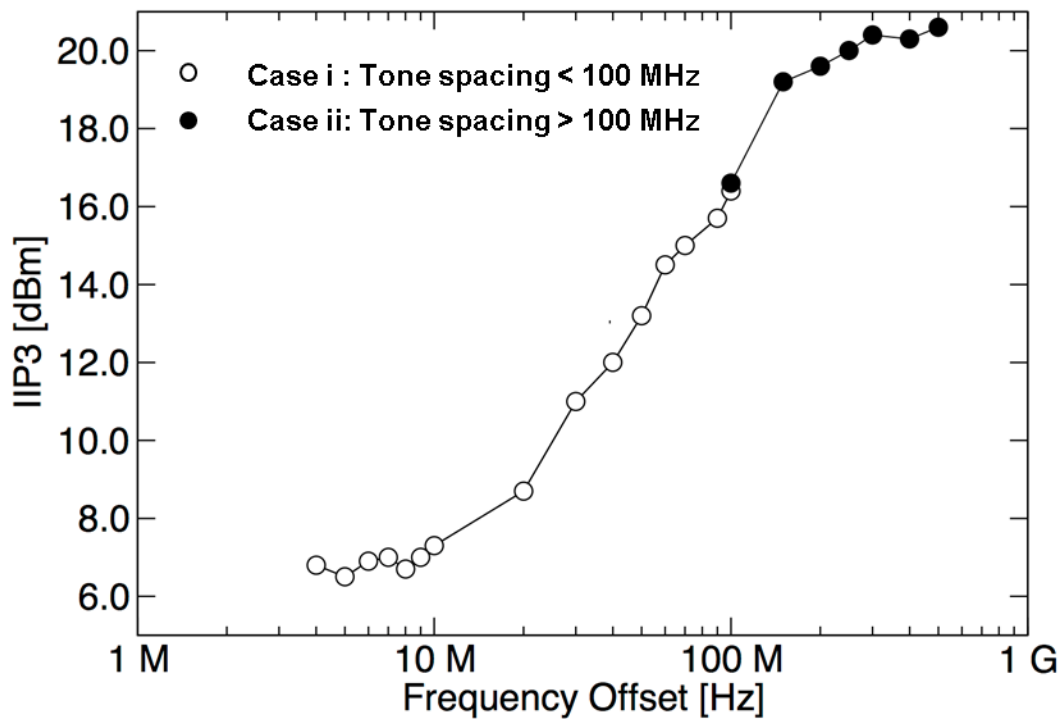


Fig. 6.20 In-band and out-of-band IIP3 measured.

Fig. 6.21 shows the in-band and out-of-band P1dB measured at 2 GHz. The measured in-band P1dB is higher than -15 dB. As the frequency offset increases, the P1dB also improves. However, the P1dB saturates at +4.4 dBm at best. The reason behind this is that the mixer switches cannot be turned on properly at large input level even with greater frequency offset from the carrier frequency. Since most of the filtering happens on the baseband side of the mixer switches, it doesn't help to improve the P1dB performance of the passive mixer on the RF terminal. Therefore, the P1dB input signal power that can be handled by the receiver is limited to +4 dBm. Beyond this power level, the mixer would generate higher order distortion.

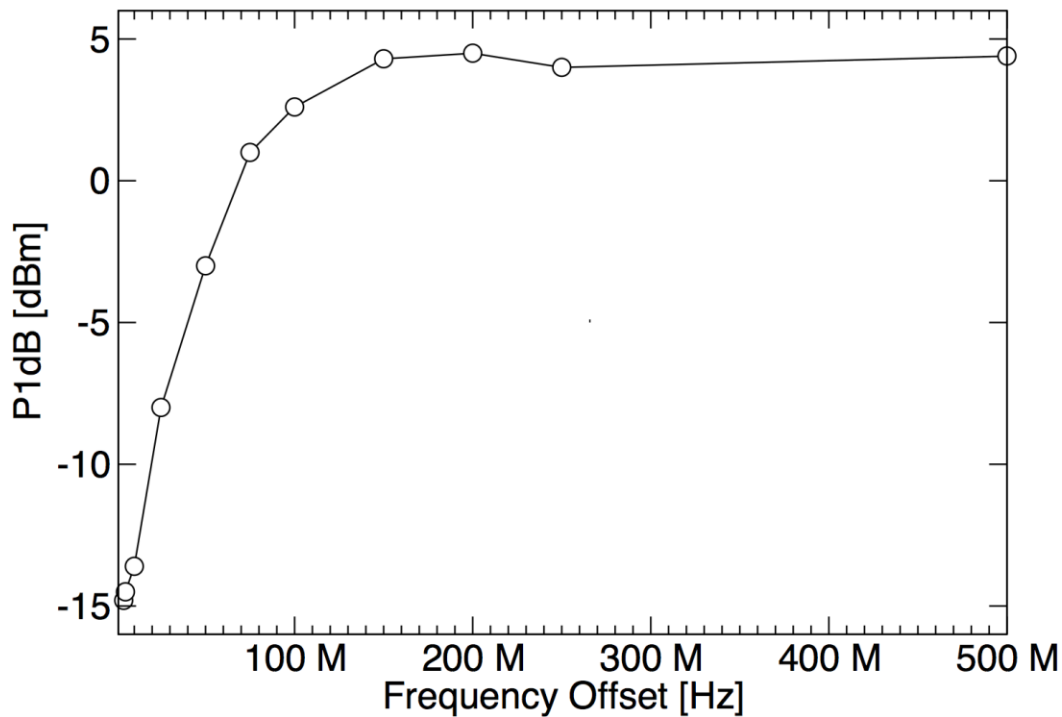


Fig. 6.21 Measured in-band and out-of-band P1dB.

Fig. 6.22 shows the power break down for the entire receiver. The power is more or less evenly distributed among all of the major circuit blocks at 2 GHz. The dynamic power spent by the mixer buffers and the clock generation circuits would scale with the frequency of operation quite linearly. The first amplifier (baseband LNA) and the second amplifier (ACBC amplifiers) draw power from different 1.1 V supplies regulated by separate on-chip LDOs. The measured regulated voltages from the LDOs range from 1.08V to 1.12V across 10 different silicon samples. The LDOs are designed to work with a wide range of supply voltage from 1.5V to 2 V. All of the LDOs draw a total of 2.5 mA from the high supply. The receiver consumes 55 mW from the 1.1 V supplies and the entire system consumes 62 mW from the external 1.1 and 1.5 V supplies.

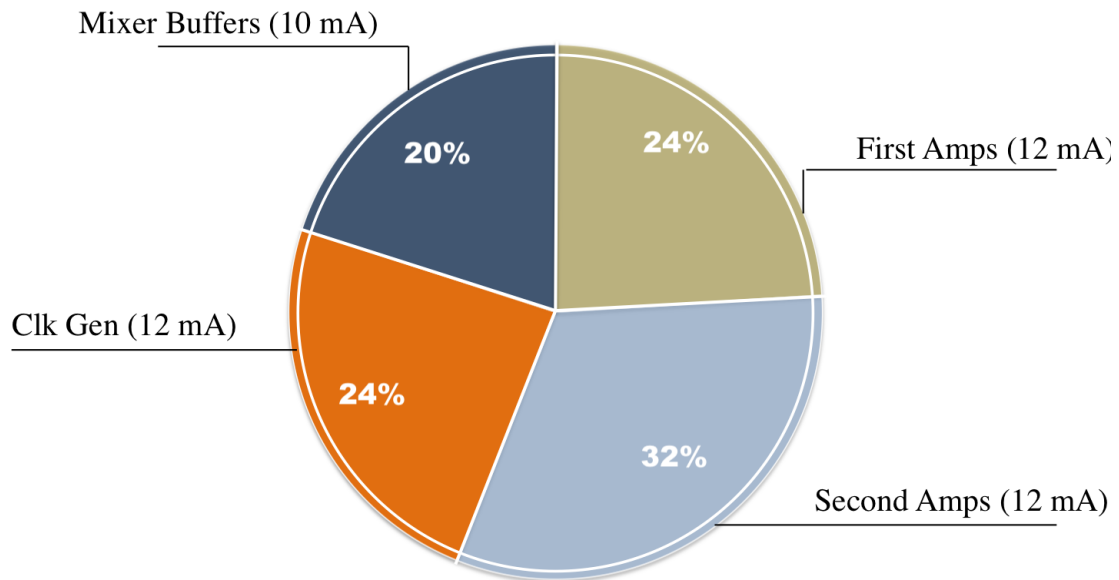


Fig. 6.22 Power breakdown for major circuit blocks.

Table 6.2 compares our work with other state-of-the-art receivers implemented in different architectures. Compared to the other mixer-first receiver designs, our system manages to achieve the widest frequency range, benefiting from the 28 nm technology. Compared to the other state-of-the-art research, our system achieves the widest baseband bandwidth. Also, it maintains a competitive IIP3 performance if it is not better than the others. Even compared to the design with noise cancellation [68], our work is not far off: the measured small signal noise figure is around 2.5 dB while the noise cancellation design can achieve a sub 2 dB noise figure. Moreover, the measured noise figure with an out-of-band 0 dBm blocker present is 6.4 dB including the noise contributed by the five LDOs, compared with 4.1 dB for a design with noise cancellation. On the other hand, our design with integrated LDOs still takes less than half of the area, and consumes less power compared to [68].

Compared to recent research works for the LTE-A standards, our work manages to cover a wide frequency range of operation. It achieves a better noise figure, and it is more linear within the signal bandwidth and out of the signal bandwidth. Also, it achieves a footprint that is far smaller than existing designs, and consumes much less power.

	ISSCC 2010 Andrews	ISSCC 2011 Borremans	ISSCC 2012 Lu	ISSCC 2012 Murphy	VLSI 2013 Borremans	ISSCC 2014 Murphy	ISSCC 2014 Tohidian	ISSCC 2014 Razavi	This Work
Technology	65nm	40 nm	65 nm	40 nm	28nm	28nm	65nm	65nm	28nm
RF Input	Single-ended	Differential	Differential	Single-ended	Differential.	Single-ended	Differential.	Differential.	Single-ended
RF Freq. [GHz]	0.1-2.4	0.4-6	0.85/0.9/1.8/1.9	0.08-2.7	0.4-3	0.6-3	1.8-2.5	0.05-2.5	0.4-3.5
Bandwidth	2MHz	100KHz	100KHz	N/A	N/A	N/A	N/A	0.35-20M	15-50MHz
NF [dB]	5	3	2.7-2.9	1.9	2.3-2.9	1.8 (3)	3.2-4.5	2.9	2.4-2.6
OOB-P1 dB [dBm]	+4	-8	+1	-2	N/A	-6	N/A	N/A	+4.6
IB-P1 dB [dBm]	N/A	N/A	N/A	N/A	N/A	N/A	N/A	N/A	-14.7
NF w/ 0dBm Blocker [dB]	N/A	15	7-8.5	4.1	N/A	13 (9)	N/A	5.1	6.5
NF w/ 3 <sup>rd</sup> HB [dB]	N/A	N/A	N/A	N/A	N/A	9	N/A	N/A	7.4
Supply [V]	1.2/2.5	1.1/2.5	2.8	1.3	0.9	1	1.2/2	1.2	1/1.5 <sup>1</sup>
IB-IIP3 [dBm]	N/A	N/A	0	78mA	N/A	N/A	-7	N/A	+6.7
OOB-IIP3 [dBm]	25	10	N/A	13.5	3	10	N/A	10	20.5
OOB-IIP2 [dBm]	58	70	>50 (44.5)	54	85	49	85	N/A	64
HR (3rd/5th)	35/42	N/A	N/A	42/45	70/55	52/54 (LF)	N/A	N/A	62/65 (0.8M) 47/51(2GHz)
LO Leakage [dBm]	N/A	N/A	N/A	N/A	N/A	N/A	N/A	N/A	-62
Power [mW]	37-70	30-55	58.9 mA <sup>2</sup>	35-78	40 (2GHz)	39-70	55-65	20 (2GHz)	38-75 <sup>3</sup>
Active Area [mm <sup>2</sup> ]	2	2	1.4	1.2	0.6	5	1.1	0.82	0.23 <sup>3</sup>

<sup>1</sup> The high supply is for the five on-chip LDOs, which support a wide range of supply voltage (1.5 V to 2 V).

<sup>2</sup> Power is listed in manner of current in the original publication.

<sup>3</sup> Power and area include five on-chip LDOs.

Table 6.2 Comparison table with other contemporary receiver designs



	<b>Sundstrom ISSCC 2013</b>	<b>Alpman VLSI 2013</b>	<b>This work</b>
Architecture	Double Conv. HR Homodyne	Baseband HR Backend Only	Mixer-first
RF Frequency	Band 25 (1.96GHz)	240 MHz	0.4-3.5 GHz
RF Input	Differential	Differential	Single-ended
Gain [dB]	45	12	35
Bandwidth	100KHz	1.4 MHz	100KHz-50MHz
NF[dB]	4.5+1.2	--	2.6
NF w/ 0dBm Blocker	--	--	6.3 (100MHz@2GHz)
OB-IIP3 [dBm]	2.4	10	20 (50MHz@2GHz)
HR3 [dB]	--	70.4	65 @ 800 MHz
HR5 [dB]	--	70.2	63 @ 800 MHz
Active Area	14.8 mm <sup>2</sup>	0.65 mm <sup>2</sup>	0.23 mm <sup>2</sup>
Supply [V]	1.45/1.8	1.1	1.1 (1.5 for LDO)
Power [mW]	155-435	24	60
Technology	40 nm	32 nm	28 nm

Table 6.3 Comparison table with modern receiver designs for LTE-A.

## 6.6 Summary

A passive-mixer-first receiver designed in 28 nm CMOS is presented in this chapter, where the frontend 5-bit mixer-DAC provides a wide-band tunable impedance match to suppress the LO leakage. The baseband LNA together with the AC-boosting compensation amplifier provides a 50MHz baseband bandwidth. This provides power-efficient support for non-contiguous carrier aggregation in LTE. The circuit achieves  $<3\text{dB}$  NF,  $>15\text{dBm}$  IIP3 and 35dB gain with 55mW power.

# Chapter 7

## Conclusion

In this work, we demonstrated two receiver designs to address two different aspects of future wireless standards. First off, an experimental prototype ADC based receiver design is presented as a direct RF-to-digital converter for software defined radio application. The large difference between the baseband bandwidth and the carrier frequency provide the large oversampling ratio necessary to avoid noise folding. The noise shaping feature provided by the  $\Delta\Sigma$  modulator supplies a high-resolution conversion only in the frequency range of interest such that the desired high-speed and high-resolution conversion can be carried out in a power efficient manner. The integrated CMIS mixer performs the frequency translation in a simple yet elegant manner, which allows the mixer to be easily implemented and better integrated for such a design.

The prototype design supports a frequency of operation from 400 MHz to 4000 MHz, which covers all LTE bands worldwide. An NRZ feedback DAC design reduces the jitter sensitivity of the system, and aids in achieving a high SNDR over the frequency range of interest. It provides a large dynamic range with low power consumption. It meets the three major criteria of SDR systems. Without any bulky passives, the design maintains a small footprint, while a digitally-oriented design methodology enables a truly flexible receiver that is able to adapt to different standards with the change of a few control bits. Finally, the solution can scale naturally with technology.

The second design addresses the challenges presented by carrier aggregation where a passive-mixer-first receiver design is proposed. Avoiding the front-end gain element, such as an LNA or LNTA, the mixer and the baseband circuits only need to process a small signal swing, which helps to maintain the overall linearity. This superb linearity performance makes such a design a perfect candidate for applications like LTE Advanced, where the interferences can come within or out of the receiver bands. The wide-band tunable mixer DAC helps to suppress the LO leakage due to the absence of any reverse isolation of the front end. Moreover, careful noise analysis for both the small signal case and the large signal case allows the receiver to achieve a competitive noise figure compared to conventional designs even with at the absence of the RF gain stage.

An experimental prototype implemented in 28 nm CMOS is presented, where the frontend 5-bit mixer-DAC provides a wide-band tunable impedance match to suppress the LO leakage. The baseband LNA and the AC-boosting compensation amplifier provide a 50MHz baseband bandwidth, which provides support for non-contiguous carrier aggregation for LTE in power efficient manners. The circuit achieves  $<3\text{dB NF}$ ,  $>15\text{dBm IIP3}$  and  $35\text{dB gain}$  with  $55\text{mW power}$ .

## 7.1 Significant Contributions

The key accomplishments of this research are:

- Designed a direct RF to digital  $\Delta\Sigma$  converter supporting over a decade of operating frequencies (400 MHz to 4 GHz), which is better than any related work (such as band-pass  $\Delta\Sigma$ , RF-ADC or  $\Delta\Sigma$  down-converter) reported until now.
- Proposed and implemented a novel feedback DAC switching scheme to alleviate the impact of clock jitter for a multi-gigahertz  $\Delta\Sigma$  modulator design.
- Designed a novel low-power highly linear class-AB low-noise trans-conductance amplifier (LNTA) with wide-band input matching.
- Conducted both analytical and numerical analysis on the high-speed  $\Delta\Sigma$  modulator jitter sensitivity issue, and verified the result with actual silicon samples.
- Proposed and verified techniques effectively mitigating the jitter sensitivity issue for a high-speed  $\Delta\Sigma$  modulator design.
- Designed a highly linear passive mixer-first receiver with up to 50 MHz baseband bandwidth with integrated LDO design.
- Proposed and designed a 5-bit mixer calibration DAC for LO leakage suppression.

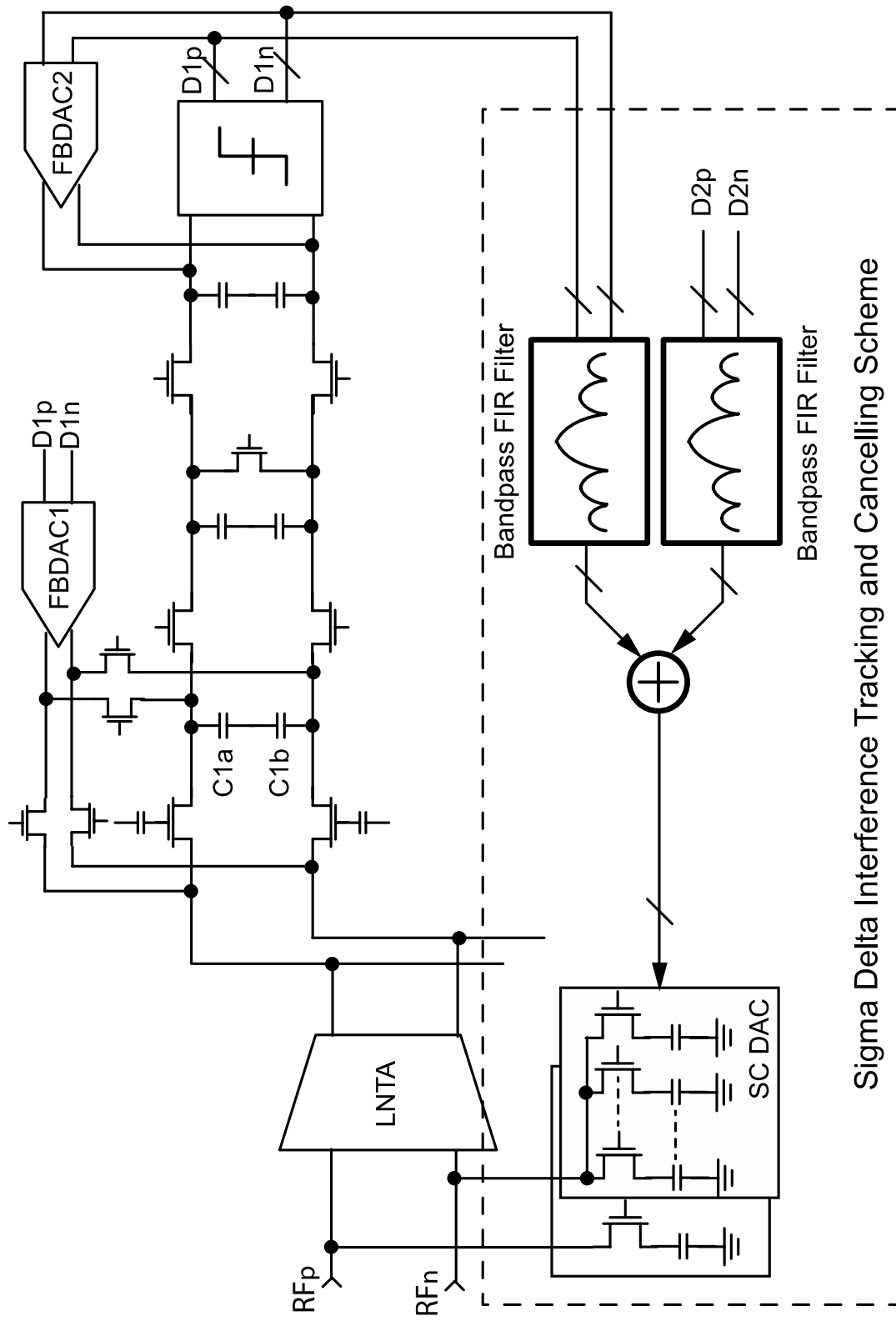
## 7.1 Future Work

We suggest several directions for further research and improvement of our work:

- Improving the operational frequency of the current  $\Delta\Sigma$  converter by re-designing the comparator with a two-way time-interleaved design, which is common in high-speed serializer and de-serializer designs.
- Increasing the front-end gain in the  $\Delta\Sigma$  converter design to achieve a better noise

figure for the overall system.

- An implementation of noise cancelling circuits around the mixer-first design to achieve an even better noise figure performance.
- Attempting a different TX signal injection point the into the mixer-first design to achieve better TX resilience.
- Developing a calibration algorithm for LO leakage suppression.
- Combining the  $\Delta\Sigma$  converter and the passive-mixer's transparency property to achieve a design that is capable of direct down-conversion, while still being resilient to large blockers, as shown in Fig. 7.1.



孤独に歩め...悪をなさず 求めるところは少なく...林の中の象のように

---『ダンマパダ』, 23章にある一節 (330節)

# Bibliography

- [1] Apple Iphone 5c technical spec. Web.
- [2] M. McHenry, D. McCloskey, D. Roberson, and J. MacDonald. Spectrum occupancy Measurements. Chicago, Illinois, November 16-18, 2005. Web.
- [3] J. Mitola, Software Radio: Survey, Critical Evaluation and Future Directions, *Proceedings of National Telesystems Conference. IEEE Press*, May 1992.
- [4] V. Giannini, P. Nuzzo, C. Soens, K. Vengattaramane, M. Steyaert, J. Ryckaert, M. Gooul, B. Debaillie, J. Van Driessche, J. Cranickx, and M. Ingles. A  $2\text{mm}^2$  0.1-to-5GHz SDR Receiver in 45nm Digital CMOS. In *International Solid-State Circuits Conference*, pages 408–409, 2009.
- [5] R. Bagheri, A. Mirzaei, A. Chehrazi, M. Heidari, M. Lee, M. Mikhemar, W. Tang, and A. Abidi. An 800-MHz-6-GHz Software-Defined Wireless Receiver in 90-nm CMOS. *IEEE Journal of Solid State Circuits*, 41(12):2860–2876, December 2006.
- [6] E. Org, R. Cyr, G. Dawe, and J. Kilpatrick. Software Defined Radio Architectures for Mobile Commercial Applications. [online].
- [7] K. Muhammad, D. Leipold, B. Staszewski, Y.-C. Ho, C. Hung, K. Maggio, C. Fernando, T. Jung, J. Wallberg, J.-S. Koh, S. John, I. Deng, O. Moreira, R. Staszewski, R. Katz and O. Friedman. A Discrete-Time Bluetooth Receiver in a 0.13 $\mu\text{m}$  Digital CMOS Process. In *Solid-State Circuits Conference, 2004. Digest of Technical Papers. ISSCC. 2004 IEEE International*, pages 268 Vol. 1, Feb. 2004
- [8] K. Muhammad, Y.-C. Ho, J. Mayhugh, T.L., C.-M. Hung, T. Jung, I. Elahi, C. Lin, I. Deng, C. Fernando, J. Wallberg, S. Vemulapalli, S. Larson, T. Murphy, D. Leipold, P. Cruise, J. Jaenig, M.-C Lee, Staszewski, R.B., R. Staszewski and K. Maggio. The first fully integrated quad-band GSM/GPRS receiver in a 90-nm digital CMOS Process. *IEEE Journal of Solid State Circuits*, 41:1772-1783, August 2006.
- [9] H. Lakdawala, J. Zhan, A. Ravi, S. Anderson, B. Carlton, R. Nicholls, N. Yaghini, R. Bishop, S. Taylor, and K. Soumyanath. Multi-Band (1-6GHz), Sampled, Sliding- IF Receiver with Discrete-Time Filtering in 90nm Digital CMOS Process. In *VLSI Circuits, 2006. Digest of Technical Papers. 2006 Symposium on*, pages 230–231, 0-0 2006.
- [10] J. Yuan. A charge sampling mixer with embedded filter function for wireless applications. In *Proc. 2nd, Int. Conf. Microwave and Millimeter Wave Technology*, pages 315–318, Beijing, China, 2000



- [11] S. Karvonen, T. Riley, and J. Kostamovaara. A cmos quadrature charge-domain sampling circuit with 66-db sfdr up to 100 mhz. *Circuits and Systems I: Regular Papers, IEEE Transactions on*, 52(2):292–304, Feb. 2005.
- [12] S. Karvonen, T. Riley, and J. Kostamovaara. Charge-domain fir sampler with programmable filtering coefficients. *Circuits and Systems II: Express Briefs, IEEE Transactions on*, 53(3):192–196, March 2006.
- [13] S. Karvonen, T. Riley, and J. Kostamovaara. A Low Noise Quadrature Subsampling Mixer. In *Circuits and Systems, 2001. ISCAS 2001. The 2001 IEEE International Symposium on*, volume 4, pages 790–793 vol. 4, May 2001.
- [14] S. Lindfors, A. Parssinen, and K. Halonen. A 3-V 230-MHz CMOS decimation sub-sampler. *IEEE Transactions on Circuits and Systems - II*, 50(3): 105–117, March 2003.
- [15] H. Pekau and J. Haslett. A 2.4 GHz cmos Sub-Sampling Mixer with Integrated Filtering. *Solid-State Circuits, IEEE Journal of*, 40(11): 2159–2166, Nov. 2005.
- [16] R. Schreier. ADCs and DACs: Marching Towards the Antenna. GIRAFE Forum in International Solid State Circuits Conference, February 2003.
- [17] R. Winoto and B. Nikolic ,A highly reconfigurable 400–1700MHz receiver using a down-converting sigma-delta A/D with 59-dB SNR and 57-dB SFDR over 4-MHz bandwidth, *VLSI Circuits, 2009 Symposium*, Page(s): 142 – 143
- [18] L. Breems, E. van der Zwan, and J. Huijsing. A 1.8-mW CMOS sigma-delta modulator with integrated mixer for A/D conversion of IF signals. *Solid-State Circuits, IEEE Journal of*, 35(4): 468–475, Apr 2000
- [19] F. Chen and B. Leung. A 0.25-mW Low-Pass Passive Sigma-Delta Modulator with Built-in Mixer for a 10-MHz IF Input. *Solid-State Circuits, IEEE Journal of*, 32(6):774–782, Jun 1997.
- [20] A. Namdar and B. Leung. A 400-MHz, 12-bit, 18-mW, IF Digitizer with Mixer Inside a Sigma-Delta Modulator Loop. *Solid-State Circuits, IEEE Journal of*, 34(12):1765– 1776, Dec 1999.
- [21] H. Tao and J. Khoury. A 400-Ms/s Frequency Translating Bandpass Sigma-Delta Modulator. *Solid-State Circuits, IEEE Journal of*, 34(12):1741–1752, Dec 1999
- [22] S. R. Norsworthy, R. Schreier, and G. C. Temes. Delta-Sigma data converters: Theory, design, and simulation. IEEE Press, 1997.
- [23] M. Ortmanns and F. Gerfers. Continuous-time sigma-delta A/D conversion: Fundamentals, performance limits and robust implementations. Springer, 2006.
- [24] A. Molnar, B. Lu, S. Lanzisera, B. Cook, and K. Pister, “An ultralow power 900

MHz RF transceiver for wireless sensor networks,” in *Proc. IEEE Custom Integr. Circuits Conf.*, Oct. 2004, pp 401-404.

- [25] C. Andrews and A. Molnar “A Passive Mixer-First Receiver with Digitally Controlled and Widely Tunable RF Interface”, *IEEE Journal of Solid-State Circuits*, vol. 45, no. 12, December 2010.
- [26] C. Andrews and A. Molnar “Implication of Passive Mixer Transparency for Impedance Matching and Noise figure in Passive Mixer-first Receivers”, *IEEE Trans on Circuits and System-I*, vol. 57, no. 12, December 2010.
- [27] A. A. Abidi, “Software-defined radio receiver: Dream to reality”, *IEEE Communications Magazine*, pp. 111-118, 2006.
- [28] F. Rivet, Y. Deval, J-B. Begueret, D. Dallet, P. Cathelin, D. Belot, “The experimental demonstration of a SASP-based full Software Radio Receiver”, *IEEE J. Solid-State Circuits*, vol. 45, no. 6, pp. 979-988, Jun. 2010
- [29] F. Chen and B. Leung, “A 0.25-mW low-pass passive sigma-delta modulator with built-in mixer for a 10-MHz IF input”, *IEEE J. Solid-State Circuits*, vol. 32, no. 6, pp. 774-782, Jun. 1997.
- [30] R. Winoto and B. Nikolic, “A highly reconfigurable 4001700MHz receiver using a down-converting sigma-delta A/D with 59-dB SNR and 57-dB SFDR over 4-MHz bandwidth”, *IEEE Symposium on VLSI Circuits*, pp. 142-143, Jun. 2009.
- [31] K. Koli, J. Jussila, P. Sivonen, S. Kallioninen and A. Parssinen, “A 900 MHz Direct Receiver in 65nm CMOS”, in *IEEE ISSCC Dig. Tech. Papers*, Feb 2010, pp 64-65.
- [32] A. K. Ong and B. A. Wooley, “A Two-path Bandpass  $\Delta\Sigma$  Modulator for Digital IF Extraction at 20 MHz”, *IEEE J. Solid-State Circuits*, vol. 32, no. 12, pp. 1920-1934, Aug. 1997.
- [33] R. Schreier and G. C. Temes, *Understanding Delta-Sigma Data Converters*. New York: IEEE 2005.
- [34] J. Gealow, M. Ashburn, C. H. Lou, S. Ho, P. Riehl, A. Shabra, J. Silva and Q. Yu, “A 2.8 mW  $\Delta\Sigma$  ADC with 83 dB DR and 1.92 MHz BW Using FIR Outer Feedback and TIA-Biased Integrator”, *IEEE Symposium on VLSI Circuits*, pp. 42-43, Jun. 2011.
- [35] Y. S. Shu, J. Y. Tsai, P. Chen, T. Y. Lo and P. C. Chiu, “A 28 fJ/conv CT  $\Delta\Sigma$  Modulator with 78 dB DR and 18 MHz BW in 28 nm CMOS Using a Highly Digital Multibit Quantizer”, in *IEEE ISSCC Dig. Tech. Papers*, Feb, 2013, pp 268-269.
- [36] P. Shettigar and S. Pavan, “A 15 mW 3.6 GS/s CT  $\Delta\Sigma$  ADC with 36 MHz Bandwidth and 83 dB DR in 90 nm CMOS”, in *IEEE ISSCC Dig. Tech. Papers*,

Feb, 2012, pp 156-157.

- [37] P. Shettigar and S. Pavan, "Design Techniques for Wideband Single-Bit Continuous-Time  $\Delta\Sigma$  Modulators with FIR Feedback DACs", IEEE J. Solid-State Circuits, vol. 47, no. 12, pp. 2865-2879, Dec 2012.
- [38] J. A. Cherry and W. M. Snelgrove, "Clock Jitter and Quantizer Metability in Continous-Time Delta-Sigma Modulators", IEEE Tran. Circuits Syst. II, Analog digit. Signal Process., vol. 46, no. 6 pp. 661-676, Jun 1999.
- [39] PG. R. Silva, L. J. Breems, KA. A. Makinwa, R. Roovers and J. H. Huijsing, "An IF-to-Baseband  $\Delta\Sigma$  Modulator for AM/FM/IBOC Radio Receiver with 118 dB Dynamic Range", IEEE J. Solid-State Circuits, vol. 42, no. 5 pp. 1076-1089, Dec 2007.
- [40] N. Beilleau, H. Aboushady, F. Montaudon and A. Cathelin, "A 1.3V 26mW 3.2GS/s undersampled LC bandpass ADC for a SDR ISM-band receiver in 130nm CMOS", IEEE RFIC Symposium, pp. 383-386, Jun. 2009.
- [41] B. Ovidiu and J. H. Huijsing, "Systematic design of Sigma-Delta analog-to-digital converters", Boston: Kluwer Academic Publishers, 2004.
- [42] H. Tao, L. Toth and J. M. Khoury, "Analysis of timing jitter in bandpass sigma-delta modulators", IEEE Tran. Circuits Syst. II, Analog digit. Signal Process. vol. 46, no. 8 pp. 991-1001, Aug 1999.
- [43] J. Yuan, "A charge sampling mixer with embedded filter function for wireless applications", in Proc. 2nd, Int. Conf. Microwave and Millimeter Wave Technology, pages 315318, Beijing, China, 2000.
- [44] R. Winoto, Downconverting Sigma-Delta A/D Converter for a Reconfigurable RF Receiver, Technical Report, EECS Department, University of California, Berkeley. 2009
- [45] I. Aoki, S.D. Kee, D.B. Rutledge, A. Hajimiri, "Distributed active transformer-a new power-combining and impedance-transformation technique", IEEE Tran. Microwave Theory and Techniques, vol. 50, no. 1 pp. 316-331, 2002.
- [46] L. Breems and J.H. Huijsing, "Cotinous-Time Sigma-Delta Modulation for A/D Conversion in Radio Receivers", Kluwer Academic, Boston, MA, 2002.
- [47] M. Bolatkale, L.J. Breems, R. Rutten, K.A.A. Makinwa, "A 4-GHz Continuous-Time D! ADC with 70-dB DR and -74 dBFS THD in 125-MHz BW, IEEE Journal of Solid State Vol. 46, Issue. 12, Dec, 2011.
- [48] A. Abidi, "Phase Noise and Jitter in CMOS Ring Oscillator, IEEE Journal of Solid State Vol. 41, Issue. 8, Aug, 2006.

- [49] A. Mirzaei and H. Darabi, "Analysis of Imperfections on Performance of 4-Phase Passive-Mixer-Based High-Q Bandpass Filters in SAW-Less Receivers", *IEEE Tran. Circuits Syst. I, Analog digit. Signal Process.*, vol. 58, no. 5 pp. 879-892, May 2011.
- [50] S. Gupta, D. Gangopadhyay, H. Lakdawala, J.C. Rudell and D.J. Allstot, "A QPLL-timed direct-RF sampling band-pass ADC with a 1.2 GHz tuning range in 0.13 m CMOS," *Proc. IEEE Radio Frequency Integrated Circuits Symp.*, pp.25 -28 2008
- [51] K. Koli, J. Jussila, P. Sivonen, S. Kallioinen, and A. Parssinen "A 900MHz direct receiver in 65nm CMOS, " in *IEEE ISSCC Dig. Tech. Papers*, Feb 2010, pp 64-65.
- [52] B.K. Thandri and J. Silva-Martinez, "A 63 dB SNR, 75-mW Bandpass RF  $\Delta\Sigma$  ADC at 950 MHz Using 3.8-GHz Clock in 0.25-m SiGe BiCMOS Technology" *IEEE J. Solid-State Circuits*, vol. 42, no. 2, pp. 269-279, Feb. 2007.
- [53] J. Ryckaert, J. Borremans, B. Verbruggen, L. Bos, C. Armiento, J. Craninckx and G. Van der Plas, "A 2.4 GHz Low-Power Sixth-Order RF Bandpass  $\Delta\Sigma$  Converter in CMOS" *IEEE J. Solid-State Circuits*, vol. 44, no. 11, pp. 2873-2880, Nov. 2009.
- [54] J. Borremans, G. Mandal, V. Giannini, T. Sano, M. Ingels, B. Verbruggen and J. Craninckx, "A 40nm CMOS highly linear 0.4-to-6GHz receiver resilient to 0dBm out-of-band blockers" in *IEEE ISSCC Dig. Tech. Papers*, Feb 2011, pp 62-64.
- [55] H. Shibata, R. Schreier, W. Yang, A. Shaikh, D. Paterson, T.C. Caldwell, D. Alldred and P. Lai "A DC-to-1 GHz Tunable RF  $\Delta\Sigma$  ADC Achieving DR = 74 dB and BW = 150 MHz at  $f_0 = 450$  MHz Using 550 mW," *IEEE J. Solid-State Circuits*, vol. 47, no. 12, pp 2888-2897, Dec 2012.
- [56] M. Englund, K.B. Ostman, O. Viitala, M. Kaltiokallio, Kari. Stadius, K. Koli and J. Ryyanen "A programmable 0.7-to-2.7 GHz Direct  $\Delta\Sigma$  receiver in 40 nm CMOS," *IEEE ISSCC Digest*, pp 470-471, Feb 2014.
- [57] Geffroy, V.; De Astis, G.; Bergeault, E "RF mixers using standard digital CMOS 0.35  $\mu\text{m}$  process" *Microwave Symposium Digest*, vol. 1, 2001,pp. 83–86.
- [58] D. Tayloe. "A Low-noise, High-performance Zero IF Quadrature Detector/Preamplifier" *RF Design*, Mar. 2003,
- [59] A. Mirzaei, H. Darabi, J. Leete, X. Chen, K. Juan, and A. Yazdi, "Analysis and optimization of current-driven passive mixers in narrowband direct conversion receivers," *IEEE J.Solid-State Circuits*, pp. 2678–2688, Oct. 2009.
- [60] N. Kim, L. Larson, and V. Aparin, "A highly linear SAW-less CMOS receiver using a mixer with embedded Tx filtering for CDMA," *IEEE J.Solid-State Circuits*, pp. 2126–2137, Aug. 2009.
- [61] M. Soer, E. Klumperink, Z. Ru, F.E. van Vliet, and B. Nauta, "A 0.2-to-2.0GHz 65nm CMOS receiver without LNA achieving 11dbm IIP3 and 6.5 dB NF," *IEEE*

*ISSCC Dig. Tech. Papers*, vol. 52, Feb. 2009, pp. 222-223.

- [62] C. Andrews and A.C. Molnar, "A Passive Mixer-First Receiver with Digitally Controlled and Widely Tunable RF Interface," *IEEE J. Solid-State Circuits*, vol. 45, 2010.
- [63] C. Andrews and A.C. Molnar, "Implications of Passive Mixer Transparency for Impedance Matching and Noise Figure in Passive Mixer-First Receivers," *Transactions on Circuits and Systems I: Regular Papers*, vol. 57, 2010.
- [64] H. Khatri, L. Liu, T. Chang, P. Gudem, and L. Larson, "A SAW-less CDMA receiver front-end with single-ended LNA and single-balanced mixer with 25% duty-cycle LO in 65nm CMOS," *IEEE Radio Frequency Integrated Circuits Symp.*, pp. 13–16, Jun. 2009.
- [65] Soer, M.C.M.; Klumperink, E.A.M.; de Boer, P.-T.; van Vliet, F.E.; Nauta, B., "Unified Frequency-Domain Analysis of Switched-Series- RC Passive Mixers and Samplers," *Circuits and Systems I: Regular Papers, IEEE Transactions on*, Vol. 57, pp. 2618-2631, 2010
- [66] J. Borremans, et al. "A 40nm CMOS highly linear 0.4-to-6GHz receiver resilient to 0dBm out-of-band blockers," *ISSCC 2011*.
- [67] I.S. –C.Lu, et al. "A SAW-less GSM/GPRS/EDGE receiver embedded in a 65nm CMOS SOC," *ISSCC 2011*
- [68] D. Murphy, A.A Hafez, A. Mirzaei, M. Mikhemar, H. Darabi, M.F. Chang and A.A. Abidi "A Blocker-Tolerant Wideband Noise-Cancelling Receiver with a 2dB Noise Figure," *ISSCC 2012*.
- [69] C. Liu and M Damgaard, "IP2 & IP3 Nonlinearity Spec for 3G/WCDMA Receivers," *High Frequency Electronics*, June 2009.
- [70] X. Peng and W. Sansen, "AC Boosting Compensation Scheme for Low-Power Multistage Amplifiers," *JSCC Vol 39, NO. 11*, Nov, 2004
- [71] L. Sundstrom, et al., "A Receiver for LTE Rel-11 and Beyond Supporting Non-Contiguous Carrier Aggregation," *ISSCC 2013*
- [72] E. Alpman, et al., "Two-Channel Receiver Back-End Using Statically Calibrated HRM with > 70dB 3<sup>rd</sup> and the harmonic Rejection for Carrier Aggregation in 32nm CMOS," *VLSI 2013*
- [73] P.G. Gray, P.J. Hurst, S.H. Lewis and R.G. Meyer "Analysis and Design of Analog Integrated Circuit" Wiley; 5<sup>th</sup> Edition, Jan, 2009.
- [74] M. Mikhemar, A. Mirzaei, A. Hadji-Abdolhamid, J. Chiu and H. Darabi "A 13.5mA sub-2.5dB NF multi-band receiver," *VLSI Circuit Symposium 2012*. Page(s): 82-83

- [75] A. Niknejad, EE242 Advanced Analog/RF Circuit Design Lecture slides, UC Berkeley, 2007
- [76] Z. Ru, E.A.M. Klumperink, C.E. Saavedra, B. Nauta, "A 300–800 MH Tunable Filter and Linearized LNA Applied in a Low-Noise Harmonic-Rejection RF-Sampling Receiver," *Solid-State Circuits, IEEE Journal of* Volume: 45 , Issue: 5 Publication Year: 2010, Page(s): 967- 978.
- [77] B. Marholev, M. Pan, E. Chien, L. Zhang, R. Roufoogaran, S. Wu, I. Bhatti, T.- H. Lin, M. Kappes, S. Khorram, S. Anand, A. Zolfaghari, J. Castaneda, C. Chien, B. Ibrahim, H. Jensen, H. Kim, P. Lettieri, S. Mak, J. Lin, Y. Wong, R. Lee, M. Syed, M. Rofougaran, and A. Rofougaran. A Single-Chip Bluetooth EDR Device in 0.13 $\mu$ m CMOS. In *Solid-State Circuits Conference, 2007. ISSCC 2007. Digest of Technical Papers. IEEE International*, pages 558–759, Feb. 2007.
- [78] L. Nathawad, D. Weber, S. Abdollahi, P. Chen, S. Enam, B. Kaczynski, A. Kheirkhahi, M. Lee, S. Limotyrakis, K. Onodera, K. Vleugels, M. Zargari, and B. Wooley. An IEEE 802.11a/b/g SoC for Embedded WLAN Applications. In *Solid-State Circuits Conference, 2006. ISSCC 2006. Digest of Technical Papers. IEEE In- ternational*, pages 1430–1439, Feb. 2006.
- [79] Y. Palaskas, A. Ravi, S. Pellerano, B. Carlton, M. Elmala, R. Bishop, G. Banerjee, R. Nicholls, S. Ling, S. Taylor, and K. Soumyanath. A 5GHz 108Mb/s 2x2 MIMO Transceiver with Fully Integrated +16dBm PAs in 90nm CMOS. In *Solid-State Circuits Conference, 2006. ISSCC 2006. Digest of Technical Papers. IEEE International*, pages 1420–1429, Feb. 2006.
- [80] A. Behzad, K. Carter, E. Chien, S. Wu, M. Pan, C. Lee, T. Li, J. Leete, S. Au, M. Kappes, Z. Zhou, D. Ojo, L. Zhang, A. Zolfaghari, J. Castanada, H. Darabi, B. Yeung, R. Rofougaran, M. Rofougaran, J. Trachewsky, T. Moorti, R. Gaikwad, A. Bagchi, J. Rael, and B. Marhoiev. A Fully Integrated MIMO Multi-Band Direct-Conversion CMOS Transceiver for WLAN Applications (802.11n). In *Solid-State Cir- cuits Conference, 2007. ISSCC 2007. Digest of Technical Papers. IEEE International*, pages 560–622, Feb. 2007.
- [81] O. Degani, M. Ruberto, E. Cohen, Y. Eilat, B. Jann, F. Cossoy, N. Telzhensky, T. Maimon, G. Normatov, R. Banin, O. Ashkenazi, A. Ben Bassat, S. Zaguri, G. Hara, M. Zajac, E. Shaviv, S. Wail, A. Fridman, R. Lin, and S. Gross. A 1x2 MIMO Multi-Band CMOS Transceiver with an Integrated Front-End in 90nm CMOS for 802.11a/g/n WLAN Applications. In *Solid-State Circuits Conference, 2008. ISSCC 2008. Digest of Technical Papers. IEEE International*, pages 356–619, Feb. 2008.
- [82] S. Tadjpour, E. Cijvat, E. Hegazi, and A. Abidi. A 900-MHz Dual-Conversion Low-IF GSM Receiver in 0.35 $\mu$ m CMOS. *Solid-State Circuits, IEEE Journal of*, 36(12):1992– 2002, Dec 2001.
- [83] O. Erdogan, R. Gupta, D. Yee, J. Rudell, J.-S. Ko, R. Brockenbrough, S.-O. Lee, E. Lei, J. L. Tham, H. Wu, C. Conroy, and B. Kim. A Single-Chip Quad-Band

GSM/GPRS Transceiver in 0.18  $\mu\text{m}$  Standard CMOS. In Solid-State Circuits Conference, 2005. Digest of Technical Papers. ISSCC. 2005 IEEE International, pages 318–601 Vol. 1, Feb. 2005.

- [84] Y. Le Guillou, O. Gaborieau, P. Gamand, M. Isberg, P. Jakobsson, L. Jonsson, D. Le Deaut, H. Marie, S. Mattisson, L. Monge, T. Olsson, S. Prouet, and T. Tired. Highly Integrated Direct Conversion Receiver for GSM/GPRS/EDGE with On-Chip 84-dB Dynamic Range Continuous-Time  $\Delta$  ADC. Solid-State Circuits, IEEE Journal of, 40(2):403–411, Feb. 2005.
- [85] H. Darabi, A. Zolfaghari, H. Jensen, J. Leete, B. Mohammadi, J. Chiu, T. Li, Z. Zhou, P. Lettieri, Y. Chang, A. Hadji, P. Chang, M. Nariman, I. Bhatti, A. Medi, L. Serrano, J. Welz, K. Shoarinejad, S. Hasan, J. Castaneda, J. Kim, H. Tran, P. Kilcoyne, R. Chen, B. Lee, B. Zhao, B. Ibrahim, M. Rofougaran, and A. Rofougaran. A Fully Integrated Quad-Band GPRS/EDGE Radio in 0.13 $\mu\text{m}$  CMOS. In Solid-State Circuits Conference, 2008. ISSCC 2008. Digest of Technical Papers. IEEE International, pages 206–607, Feb. 2008.
- [86] V. Aparin, N. Kim, G. Brown, Y. Wu, A. Cicalini, S. Kwok, and C. Persico. A Fully- Integrated Highly Linear Zero-IF CMOS Cellular CDMA Receiver. In Solid-State Circuits Conference, 2005. Digest of Technical Papers. ISSCC. 2005 IEEE International, pages 324–601 Vol. 1, Feb. 2005.
- [87] D. Kaczman, M. Shah, N. Godambe, M. Alam, H. Guimaraes, L. Han, M. Rachedine, D. Cashen, W. Getka, C. Dozier, W. Shepherd, and K. Couglar. A Single-Chip Tri- Band (2100, 1900, 850/800 MHz) WCDMA/HSDPA Cellular Transceiver. Solid-State Circuits, IEEE Journal of, 41(5):1122–1132, May 2006.
- [88] B. Tenbroek, J. Strange, D. Nalbantis, C. Jones, P. Fowers, S. Brett, C. Beghein, and F. Beola. Single-Chip Tri-Band WCDMA/HSDPA Transceiver without External SAW Filters and with Integrated TX Power Control. In Solid-State Circuits Conference, 2008. ISSCC 2008. Digest of Technical Papers. IEEE International, pages 202–607, Feb. 2008.
- [89] J. Zipper, R. Vazny, L. Maurer, M. Wilhelm, T. Greifeneder, and A. Holm. A single-Chip Dual-Band CDMA2000 Transceiver in 0.13 $\mu\text{m}$  CMOS. In Solid-State Circuits Conference, 2007. ISSCC 2007. Digest of Technical Papers. IEEE International, pages 342–607, Feb. 2007.
- [90] Z. Li, W. Ni, J. Ma, M. Li, D. Ma, D. Zhao, J. Mehta, D. Hartman, X. Wang, K. O, and K. Che. A Dual-Band CMOS Transceiver for 3G TD-SCDMA. In Solid-State Circuits Conference, 2007. ISSCC 2007. Digest of Technical Papers. IEEE International, pages 344–607, Feb. 2007.
- [91] D. Sahu, A. Das, Y. Darwhekar, S. Ganesan, G. Rajendran, R. Kumar, B. Chandrashekar, A. Ghosh, A. Gaurav, T. Krishnaswamy, A. Goyal, S. Bhagavatheeswaran, K. M. Low, N. Yanduru, S. Dhamankar, and S. Venkatraman.

- A 90nm CMOS Single- Chip GPS Receiver with 5dBm out-of-band IIP3 2.0dB NF. In Solid-State Circuits Conference, 2005. Digest of Technical Papers. ISSCC. 2005 IEEE International, pages 308–600 Vol. 1, Feb. 2005.
- [92] V. Delia Torre, M. Conta, R. Chokkalingam, G. Cusmai, P. Rossi, and R. Svelto. A 20mW 3.24mm<sup>2</sup> Fully Integrated GPS Radio for Cell-Phones. In Solid-State Circuits Conference, 2006. ISSCC 2006. Digest of Technical Papers. IEEE International, pages 1902–1911, Feb. 2006.
  - [93] Broadcom Corp. BRCM2075 Product Brief.
  - [94] Broadcom Corp. BRCM4329 Product Brief.
  - [95] L. Lin, N. Wongkomet, Y. D., C. Lin, M. He, B. Nissim, S. Lyuee, P. Yu, T. Sepke, S. Shekarchian, L. Tee, P. Muller, J. Tam, and T. Cho. A Fully Integrated 2x2 MIMO Dual-Band Dual-Mode Direct-Conversion CMOS Transceiver for WiMAX/WLAN Applications. In International Solid-State Circuits, 2009.
  - [96] D. Kaczman, M. Shah, M. Alam, M. Rachedine, D. Cashen, L. Han, and A. Raghavan. A SingleChip 10-Band WCDMA/HSDPA 4-Band GSM/EDGE SAW-less CMOS Receiver with DigRF 3G Interface and +90 dBm IIP2. Solid-State Circuits, IEEE Journal of, 44(3):718–739, March 2009.
  - [97] B. Bakkaloglu, P. Fontaine, A. Mohieldin, S. Peng, S. J. Fang, and F. Dulger. A 1.5- V multi-mode quad-band RF receiver for GSM/EDGE/CDMA2K in 90-nm digital CMOS process. Solid-State Circuits, IEEE Journal of, 41(5):1149–1159, May 2006.
  - [98] T. Sowlati, J. Agarwal, J. Cho, T. Obkircher, and M. El Said. Single-Chip Multi-band WCDMA/HSDPA/HSUPA/EGPRS Tranceiver with Diversity Receiver and 3G DigRF Interface without SAW Filters in Transmitter/3G Receiver Paths. In International Solid State Circuits Conference, pages 116–117, 2009.
  - [99] A. Hadjichristos, A. Cassia, H. Kim, and C. Park. Single-Chip RF CMOS UMTS/EGSM Transceiver with Integrated Receive Diversity and GPS. In International Solid-State Circuits Conference, pages 118–119, 2009.
  - [100] V. Giannini, P. Nuzzo, C. Soens, K. Vengattaramane, M. Steyaert, J. Ryckaert, M. Goffioul, B. Debaillie, J. Van Driessche, J. Craninckx and M. Ingels, "A 2mm<sup>2</sup> 0.1-to-5GHz SDR receiver in 45nm digital CMOS," In International Solid-State Circuits Conference, pages 409–410, 2009.
  - [101] Q. Huang, J. Rogin, X. Chen, D. Tschopp, T. Burger, T. Christen, D. Papadopoulos, I. Kouchev, C. Martelli, T. Dellsperger, "A tri-band SAW-less WCDMA/HSPA RF CMOS transceiver with on-chip DC-DC converter connectable to battery," In International Solid-State Circuits Conference, pages 60–61, 2010.



- [102] T. Dellsperger, D. Tschopp, J. Rogin, Y. Chen, T. Burger and Q. Huang "A quad-band class-39 RF CMOS receiver for evolved EDGE," In International Solid-State Circuits Conference, pages 56–57, 2010.
- [103] H. Moon, L. Sangyoub, S. Heo, H. Yu, J. Yu, J. Chang, S. Choi, B. Park "A 23mW fully integrated GPS receiver with robust interferer rejection in 65nm CMOS," In International Solid-State Circuits Conference, pages 68–69, 2010.
- [104] C. Lee, A. Behzad, B. Marholev, V. Magoon, I. Bhatti, Li, D. ; Bothra, S. ; Afsahi, A. ; Ojo, D. ; Roufoogaran, R. ; Li, T. ; Yuyu Chang ; Rao, K.R. ; Au, S. ; Seetharam, P. ; Carter, K. ; Rael, J. ; MacIntosh, M. ; Lee, B. ; Rofougaran, M. ; Rofougaran, R. ; Hadji-Abdolhamid, A. ; Nariman, M. ; Khorram, S. ; Anand, S. ; Chien, E. ; Wu, S. ; Barrett, C. ; Lijun Zhang ; Zolfaghari, A. ; Darabi, H. ; Sarfaraz, A. ; Ibrahim, B. ; Gonikberg, M. ; Forbes, M. ; Fraser, C. ; Gutierrez, L. ; Gonikberg, Y. ; Hafizi, M. ; Mak, S. ; Castaneda, J. ; Kim, K. ; Zhenhua Liu ; Bouras, S. ; Chien, K. ; Chandrasekhar, V. ; Chang, P. ; Li, E. ; Zhimin Zhao "A multistandard, multiband SoC with integrated BT, FM, WLAN radios and integrated power amplifier, " In International Solid-State Circuits Conference, pages 455–456, 2010.
- [105] Deguchi, J. ; Miyashita, D. ; Ogasawara, Y. ; Takemura, G. ; Iwanaga, M. ; Sami, K. ; Ito, R. ; Wadatsumi, J. ; Tsuda, Y. ; Oda, S. ; Kawaguchi, S. ; Itoh, N. ; Hamada, M. "A fully integrated 2×1 dual-band direct-conversion transceiver with dual-mode fractional divider and noise-shaping TIA for mobile WiMAX SoC in 65nm CMOS," In International Solid-State Circuits Conference, pages 456–457, 2010.
- [106] Lu, I.S. ; Chi-Yao Yu ; Yen-Horng Chen ; Lan-Chou Cho ; Sun, C.E. ; Chih-Chun Tang ; Chien, G. "A SAW-less GSM/GPRS/EDGE receiver embedded in a 65nm CMOS SoC," In International Solid-State Circuits Conference, pages 356–357, 2011.
- [107] Nilsson, M. ; Mattisson, S. ; Klemmer, N. ; Anderson, M. ; Arnborg, T. ; Caputa, P. ; Ek, S. ; Lin Fan ; Fredriksson, H. ; Garrigues, F. ; Geis, H. ; Hagberg, H. ; Hedestig, J. ; Hu Huang ; Kagan, Y. ; Karlsson, N. ; Kinzel, H. ; Mattsson, T. ; Mills, T. ; Fenghao Mu ; Mårtensson, A. ; Nicklasson, L. ; Oredsson, F. ; Ozdemir, U. ; Park, F. ; Pettersson, T. ; Pålsson, T. ; Pålsson, M. ; Ramon, S. ; Sandgren, M. ; Sandrup, P. ; Stenman, A. ; Strandberg, R. ; Sundström, L. ; Tillman, F. ; Tired, T. ; Uppathil, S. ; Walukas, J. ; Westesson, E. ; Xuhao Zhang ; Andreani, P. "A 9-band WCDMA/EDGE transceiver supporting HSPA evolution," In International Solid-State Circuits Conference, pages 354–355, 2011.
- [108] Cicalini, A. ; Aniruddhan, Sankaran ; Apte, R. ; Bossu, F. ; Choksi, O. ; Filipovic, D. ; Godbole, K. ; Tsai-Pi Hung ; Komninakis, C. ; Maldonado, D. ; Narathong, C. ; Nejati, B. ; O'Shea, D. ; Xiaohong Quan ; Rangarajan, R. ; Sankaranarayanan, J. ; See, A. ; Sridhara, R. ; Bo Sun ; Wenjun Su ; van Zalinge, K. ; Gang Zhang ; Sahota, K. "A 65nm CMOS SoC with embedded HSDPA/EDGE transceiver,

- digital baseband and multimedia processor," In International Solid-State Circuits Conference, pages 366–367, 2011.
- [109] X. He and H. Kundr "A compact SAW-less multiband WCDMA/GPS receiver front-end with translational loop for input matching," In International Solid-State Circuits Conference, pages 373–374, 2011.
- [110] Beffa, F. ; Tze Yee Sin ; Tanzil, A. ; Ivory, D. ; Tenbroek, B. ; Strange, J. ; Ali-Ahmad, W. "A receiver for WCDMA/EDGE mobile phones with inductorless front-end in 65nm CMOS," In International Solid-State Circuits Conference, pages 370–371, 2011.
- [111] Yuan-Hung Chung; Min Chen ; Wei-Kai Hong ; Jie-Wei Lai ; Sheng-Jau Wong ; Chien-Wei Kuan ; Hong-Lin Chu ; Chihun Lee ; Chih-Fan Liao ; Hsuan-Yu Liu ; Hong-Kai Hsu ; Li-Chun Ko ; Kuo-Hao Chen ; Chao-Hsin Lu ; Tsung-Ming Chen ; YuLi Hsueh ; Chunwei Chang ; Yi-Hsien Cho ; Chih-Hsien Shen ; Yuan Sun ; Eng-Chuan Low ; Xudong Jiang ; Deyong Hu ; Weimin Shu ; Jhy-Rong Chen ; Jui-Lin Hsu ; Chia-Jui Hsu ; Zhan, J.-H.C. ; Shana'A, O. ; Guang-Kaai Dehng ; Chien, G. "A 4-in-1 (WiFi/BT/FM/GPS) connectivity SoC with enhanced co-existence performance in 65nm CMOS," In International Solid-State Circuits Conference, pages 172–174, 2012.
- [112] Kumar, R.; Krishnaswamy, T. ; Rajendran, G. ; Sahu, D. ; Sivadas, A. ; Nandigam, M. ; Ganeshan, S. ; Datla, S. ; Kudari, A. ; Bhasin, H. ; Agrawal, M. ; Narayan, S. ; Dharwekar, Y. ; Garg, R. ; Edayath, V. ; Suseela, T. ; Jayaram, V. ; Ram, S. ; Murugan, V. ; Kumar, A. ; Mukherjee, S. ; Dixit, N. ; Nussbaum, E. ; Dror, J. ; Ginzburg, N. ; EvenChen, A. ; Maruani, A. ; Sankaran, S. ; Srinivasan, V. ; Rentala, V. "A fully integrated 2×2 b/g and 1×2 a-band MIMO WLAN SoC in 45nm CMOS for multi-radio IC," In International Solid-State Circuits Conference, pages 328–329, 2013.
- [113] Chun Geik Tan; Fei Song ; Tieng Yi Choke ; Ming Kong ; De-Cheng Song ; Chee-Hong Yong ; Weimin Shu ; Zong Hua You ; Yi-Hsien Lin ; Shanaa, O. "A universal GNSS (GPS/Galileo/Glonass/Beidou) SoC with a 0.25mm<sup>2</sup> radio in 40nm CMOS," In International Solid-State Circuits Conference, pages 334–335, 2013.
- [114] H. Khatri, P.S. Gudem and L.E. Larson, "Distortion in Current Commutating Passive CMOS Downconversion Mixers," *IEEE Transaction on MTT*, Vol, 57, No. 11, Nov. 2009.
- [115] Federal Communication Commission. "History of Communications," Last modified November, 11, 2005. <http://transition.fcc.gov/omd/history/>
- [116] Abdollahi-Alibeik, S. ; Weber, D. ; Dogan, H. ; Si, W.W. ; Baytekin, B. ; Komijani, A. ; Chang, R. ; Vakili-Amini, B. ; MeeLan Lee ; Gan, H. ; Rajavi, Y. ; Samavati, H. ; Kaczynski, B. ; Sang-Min Lee ; Limotyakis, S. ; Hyunsik Park ; Chen, P. ; Park, P. ; Chen, M.S. ; Chang, A. ; Oh, Y. ; Yang, J.J. ; Lin, E.C. ; Nathawad,

- L. ; Onodera, K.; Terrovitis, M. ; Mendis, S. ; Kai Shi ; Mehta, S. ;Zargari, M. ; Su, D. “A 65nm dual-band 3-stream 802.11n MIMO WLAN SoC,” In International Solid-State Circuits Conference, pages 170–172, 2011.
- [117] Ming He ; Winoto, R. ; Xiang Gao ; Loeb, W. ; Signoff, D. ;Wai Lau ; Yuan Lu ; Donghong Cui ; Kun-Seok Lee ;Sai-Wang Tam ; Godoy, P. ; Yung Chen ; Sanghoon Joo ;Hu, C. ; Paramanandam, A.A. ; Xiaoyue Wang ;Chi-Hung Lin ; Li Lin, “A 40nm Dual-Band 3-stream 802.11a/g/n/ac MIMO WLAN SoC with 1.1Gb/s Over the Air Throughput,” In International Solid-State Circuits Conference, pages 350–351, 2014.
- [118] Ming-Da Tsai ; Chih-Fan Liao ; Chi-Yun Wang ; Yi-Bin Lee ;Tzeng, B. ; Guang-Kaai Dehng, “A Multi-Band Inductor-Less SAW-Less 2G/3G-TD-SCDMA Cellular Recevier in 40nm CMOS,” In International Solid-State Circuits Conference, pages 354–355, 2014.
- [119] T. Lee, The Design of CMOS Radio-Frequency Integrated Circuits. Cambridge, U.K.: Cambridge Univ. Press, 2004.
- [120] S. Zhou and M.-C. Chang, “A CMOS passive mixer with low flicker noise for low-power direct-conversion receiver,” IEEE J. Solid-State Circuits, vol. 40, no. 5, pp. 1084–1093, May 2005.
- [121] D. Manstretta and F. Svelto, “Analysis and optimization of IIP2 in CMOS direct down-converters,” in Proc. IEEE Custom Integrated Circuits Conf., 2002, pp. 243–246.
- [122] M. Lehne, J. Stonick, and U. Moon, “An adaptive offset cancellation mixer for direct conversion receivers in 2.4 GHz CMOS,” in Proc. IEEE Int. Circuits Syst. Symp., 2000, vol. 1, pp. 319–322.
- [123] W. Redman-White and D. M. W. Leenaerts, “1/f noise in passive CMOS mixers for low and zero IF integrated receivers,” in Proc. IEEE Eur. Solid-State Circuits Conf., Sep. 18–20, 2001, pp. 41–44
- [124] W. Sansen, Analog Design Essentials. Dordrecht, The Netherlands: Springer, 2006.